Sound Printing

Document status and date:
Published: 21/06/2024

Document Version:
Publisher's PDF, also known as Version of Record (includes final page, issue and volume numbers)

Please check the document version of this publication:

• A submitted manuscript is the version of the article upon submission and before peer-review. There can be important differences between the submitted version and the official published version of record. People interested in the research are advised to contact the author for the final version of the publication, or visit the DOI to the publisher's website.
• The final author version and the galley proof are versions of the publication after peer review.
• The final published version features the final layout of the paper including the volume, issue and page numbers.

[Link to publication](#)

Download date: 07. Jul. 2024

Sound Printing:
From Laser to Ultrasound

Frank van Berlo

Sound Printing:
From Laser to Ultrasound

Frank van Berlo

Sound Printing:
From Laser to Ultrasound

PROEFSCHRIFT

ter verkrijging van de graad van doctor aan de Technische Universiteit Eindhoven, op gezag van de rector magnificus prof. dr. S.K. Lenaerts, voor een commissie aangewezen door het College voor Promoties, in het openbaar te verdedigen op vrijdag 21 juni 2024 om 11:00 uur

door

Frank Petrus Adrianus van Berlo

geboren te Lieshout

Dit proefschrift is goedgekeurd door de promotoren en de samenstelling van de promotiecommissie is als volgt:

voorzitter: prof.dr.ir. M.G.D. Geers
1$^{\text{e}}$ promotor: prof.dr.ir. P.D. Anderson
2$^{\text{e}}$ promotor: dr.ir. L.C.A. van Breemen
leden: dr.ir. R.G.P. Lopata
                   prof.dr.-ing. K. Wudy (Technische Universität München)
                   prof.dr. J.H. Hattel (Danmarks Tekniske Universitet)
                   prof.dr.ir. P. van Puyvelde (Katholieke Universiteit Leuven)
                   prof.dr.ir. H.C. de Lange

Contents

Summary

Powder-based additive manufacturing is often used to produce products cost-effectively and efficiently. Combined with near-net density, these techniques are best suited for high-end applications. Yet, in conventional power-based methods, like selective laser sintering (SLS), the delicate interplay between process parameters, material properties, and temperature control still poses open challenges that necessitate thought. This lack of knowledge imparts adversities to controlling the temperature while processing and, consequently, the ultimate properties of the materials produced. This thesis explores the complex interplay between process parameters and intrinsic material properties by introducing new concepts involving SLS printing or a newly developed ultrasound-based 3D printing technique called selective acoustic sintering (SAS).

In **Chapter 2**, the temperature control in SLS is addressed, followed by an experimental study on predicting part properties based on processing conditions. Integrating an infrared camera improves the temperature control of a commercial SLS printer. Process parameters were defined using the ratio of laser energy to the energy required for melting (AMR), including a range of bed temperatures, laser powers, and scan velocities. A printability map is proposed, and tensile test results are used to find relations between AMR, part density, and mechanical properties of PA12. It was found that processing parameters and mechanical properties are related by percolation theory.

A finite element model is used to further investigate the role of processing parameters on part quality, as described in **Chapter 3**. A proposed model incorporates temperature-dependent thermal properties and porosity-induced shrinkage during melting. The thermal history of a multi-layer part is simulated for different process conditions. This illustrates that inaccurate prints due to the sagging of layers are related to the combination of the initial porosity of the powder bed and the laser power. The average-lamellar thickness (ALT) crystallization model is introduced, which describes the crystallization and melting kinetics. Utilization of this model provides insights into space-filling evolutions during SLS printing and, finally, lamellar thickness distributions, which are coupled to the yield stress of PA12 end-products.

In **Chapter 4**, the SAS 3D printing approach for processing powder-based materials is studied. First, the benefits of switching from a laser to an acoustic source are discussed, wherein enabling in-volume 3D printing and powder compaction is most distinctive. Subsequently, a mathematical framework is proposed to determine the feasibility of volumetric SAS 3D printing in a spherically shaped build volume. The framework demonstrates that selective temperature increase near the printer's center is affected by energy input, energy gain from geometrical focusing, and energy loss due to attenuation. Additionally, the framework establishes relationships between printer size, acoustic and thermal material properties, and transducer properties on temperature increase and focal spot diameter. For application

purposes, the study analyses a diverse dataset of printable materials and concludes that optimization enables volumetric printing for various materials, including metals, polymers, and ceramics.

Chapter 5 presents an extension of the SAS framework by numerically modeling different transducer configurations and building volume shapes using the k-space pseudospectral method. Both two-dimensional and three-dimensional simulations are performed to study the effect of phased array configuration on intensity amplitudes and spot dimensions within these build volumes. Herein, the transducer properties (amount, size, positions, and frequency) are varied, demonstrating that focusing on specific positions within the build volume is possible. A time-reversal method is presented to predict the delays between transducers and amplitudes of the transducers that result in the desired focusing location. Finally, the acoustic-thermal coupling via finite difference simulations of the energy balance is used to find the ultrasound-induced heating within the build volume.

As data on the acoustic properties of powders used in the SAS system are lacking, an ultrasound setup for characterizing powder compacts is designed. In **Chapter 6**, the design of this setup is elaborated upon. It is demonstrated through numerical simulations that a combined echo and through-transmission setup with a focused ultrasound transducer can be used to characterize various materials acoustically. Next, the realization of the setup is shown, and speed of sound and attenuation measurements are performed on PMMA and PBT disks as validation. Finally, unfilled and filled, powder-based samples are compacted to study the effect of porosity and liquid fraction on the acoustic properties.

The framework and the results of the ultrasound heating experiments on powder compacts are the first step to proving the practical applicability of SAS. With this perspective, it is aimed to incite scientists to explore the field of powder-based ultrasound 3D printing further and advance this discipline toward functional prototypes of the SAS printers.

Chapter 1

Introduction

Additive manufacturing (AM) translates computer-aided design (CAD) virtual 3D models into physical objects. Additive manufacturing processes, often called 3D printing, are widely used for producing models, prototypes, tools, and even end products cost-effectively and efficiently. Parts can be manufactured using different materials, such as metals, metal alloys, polymers, and ceramics [1]. Chemical and physical processes create these products directly from computer-generated models, using shapeless (liquids, powders, etc.) or shape-neutral (e.g., strip-shaped or wire-shaped) starting materials. Standard ISO/ASTM52900 [2] has defined seven categories of additive manufacturing (AM) processes: Binder jetting, Directed energy deposition, Material extrusion, Material jetting, Powder bed fusion, Sheet lamination, and Vat photopolymerization (see Figure 1.1).
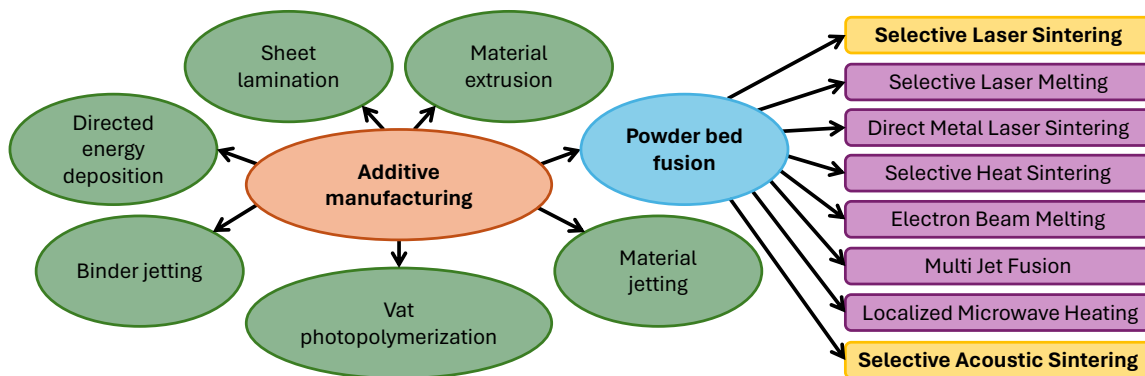
Figure 1.1: Additive manufacturing technologies and different powder bed fusion methods.

This thesis focuses on the powder bed fusion (PBF) additive manufacturing processes. In PBF, a heat source is used to fuse powdered materials. It generally distinguishes itself from other AM techniques by requiring no external support, wide material choice, relatively high part complexity, and excellent mechanical properties [3]. Powder-based 3D printing techniques have an enormous potential for developing and manufacturing prototypes and customized products since components with near-net-density and near-net-shape can be produced from fine powders [4]. The most significant PBF-based processes include Selective Laser Sintering, Selective Laser Melting, Direct Metal Laser Sintering, Selective Heat Sintering, Electron Beam Melting, Multi Jet Fusion, and Localized Microwave Heating [4, 5], as

shown in Figure 1.1. The PBF methods can be subdivided based on their heat source.

The laser-assisted PBF process, which includes Selective Laser Sintering (SLS), Selective Laser Melting (SLM), and Direct Metal Laser Sintering (DMLS), is widely used in the field of additive manufacturing (AM) [4, 6]. SLS implements a high-power laser to sinter metallic or thermoplastic powder in a heated powder chamber [5]. As shown in Figure 1.2, a laser heats and sinters powder evenly distributed by a roller on a build platform and repeats this process until the entire part is finished. SLS is mainly an industrial PBF method, as it is relatively expensive. However, desktop-sized SLS printers are available (e.g. [7]). SLM is like SLS in form but achieves complete melting when heating metallic powder [5]. The surface quality of SLM-based products is superior to that of SLS but requires support structures and has restricted build capacity [5]. DMLS uses the same technical principles as SLS/SLM but achieves exceptional accuracy and precision with smaller layer thicknesses (20 - 40 μm). Nevertheless, the drawbacks of DMLS are its high expense and long production times.
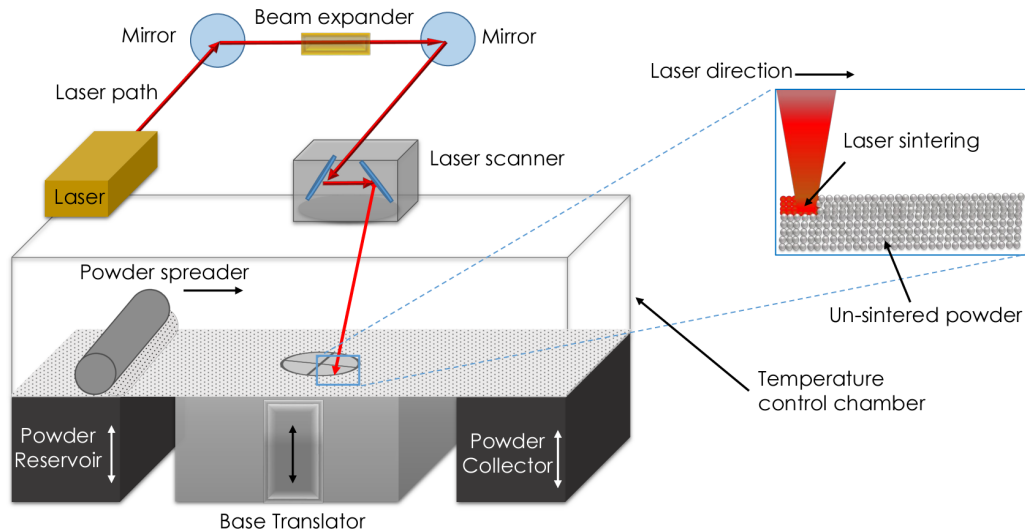
Figure 1.2: Schematic representation of the selective laser sintering (SLS) 3D printing process [8].

Other energy sources used in PBF methods are heaters, electron beams, lamps, and microwaves [4]. In Selective Heat Sintering (SHS) or Micro Heater Array Powder Sintering (MAPS), powdered materials are fused using a thermal printhead [9, 10]. Electron Beam Melting (EBM), just as the name implies, deploys a high-energy electron beam to melt the powder. Although costly as a vacuum enclosure is required, EBM is much faster than SLS and SLM, and nearly solid part densities can be achieved [4]. A different fusion approach is used in Multi Jet Fusion (MJF) [1] and High-Speed Sintering (HSS) techniques [11]. An inkjet head selectively applies to fuse and detail agents across the powder layer, which is solidified upon the second pass with a thermal energy source. Microwave sources can also induce the fusion of powder particles, as described in the Localized Microwave Heating (LMH) Based Additive Manufacturing method by Jerby et al. [12].

1.1   Intricacies of selective laser sintering

While sintering can result in near-net-density and near-net-shape products [4], especially using thermoplastic materials drastically complicates the process. Fundamental research within our group has shown that the sintering of two polymer particles is related to the complex interplay between material properties and processing conditions. Development of a unique two-particle sintering setup has demonstrated that the sintering kinetics is determined by a complex interplay between the transient rheology caused by the finite relaxation times of the polymer and the time-dependent temperature profile, which also affects the polymer viscosity [13]. Using numerical simulations, the effects of material properties on the flow behavior of these single particles are shown [14]. Expansion of these numerical simulations to 2D SLS simulations shows the effects of crystallization of PA12 during printing [15]. Additionally, the humidity, part porosity, and temperature history are determinants for the mechanical properties of PA12 SLS-parts [16–18]. An overview of the material parameters relevant to SLS, depicted in Figure 1.3, is given in the work of Schmid [19]. This figure shows the complexity of the SLS print process and highlights the importance of understanding the material characteristics to control final part properties.
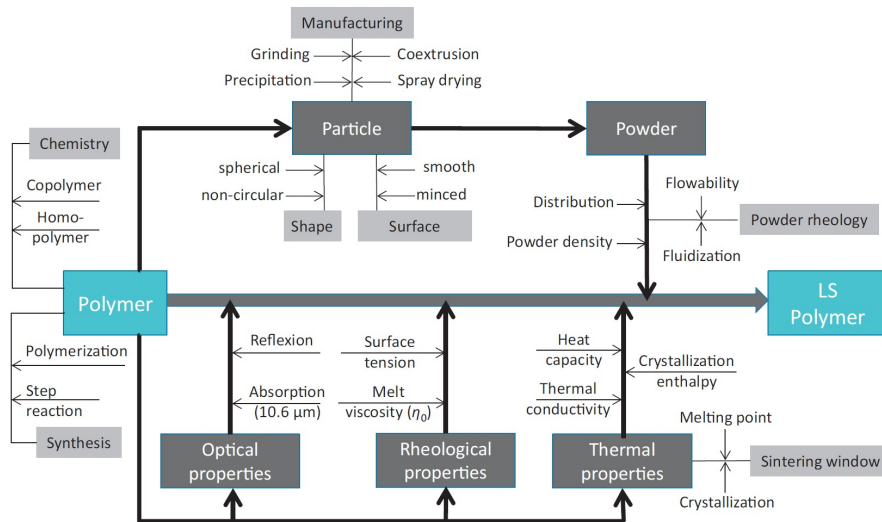
Figure 1.3: Key material properties in a powder-based laser sintering process [19].

The material and process complexity result in limitations of the SLS technique. For example, SLS requires powders with uniform sizes and good flowability to produce dense parts [4]. Hence, processing various materials becomes limited due to the availability of materials in the desired powder form. Another limitation of SLS printing is the rapid sintering of particles that involves high heat transfer and (moving) components with temperature gradients, which require a high level of control [4]. The absorption of laser energy at the polymer powder surface is one of the core aspects of the SLS process, as sufficient laser penetration is required for stable bonding of multiple layers [19]. Therefore, the laser type must be matched to the material's absorption spectrum, which limits the choice of materials in an SLS machine. Controlling the laser absorption of the powders is crucial to increase the number of possible materials that can be printed in a single SLS system and to increase the process efficiency [20].
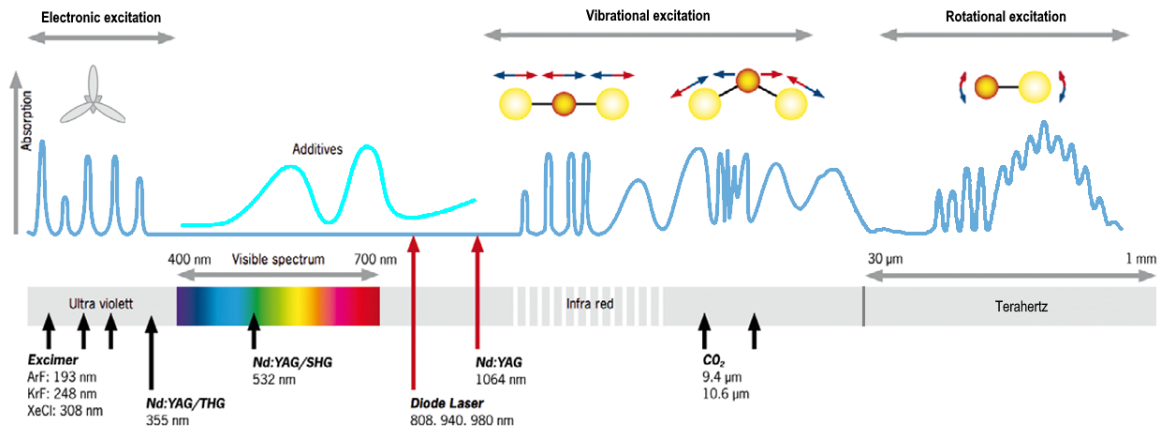
Figure 1.4: Laser absorption spectrum of polymers for several laser sources. Absorption in the infrared and terahertz regime is dominated by molecular vibration and rotation transitions, whereas X-ray and UV radiation couples to electronic transitions. Additives are required to enable absorption in the visible spectrum (edited from [26, 27]).

1.2 Laser absorption

The absorption as a function of the wavelength of a laser is given for polymers in Figure 1.4 and for various metals in Figure 1.5. The spectrum of thermoplastic materials shows that molecular vibrations determine laser absorption at wavelengths in the infrared and terahertz regimes. However, no absorption is seen near the visible spectrum [21]. Thus, yttrium aluminum garnet (YAG) or diode lasers (DL) are incompatible with standard polymers. Thermoplastic materials can absorb excimer lasers ($\lambda < 0.3~\mu$m), but the high energy densities of these lasers can cause cyclic chemical reactions that result in photodegradation of the polymer [22]. Lazare and Benet [23] report that photochemical reactions are possible in addition to photothermal effects since excimer lasers operate at UV wavelengths with photon energies higher than specific bond energies in polymers. For lasers in the terahertz gap $0.03 < \lambda < 1$ mm, typically, powers (and resolutions) required in SLS printing cannot be reached [24] (except for combinations of high-power CO_2 lasers with polar gasses [25]). Most commercial
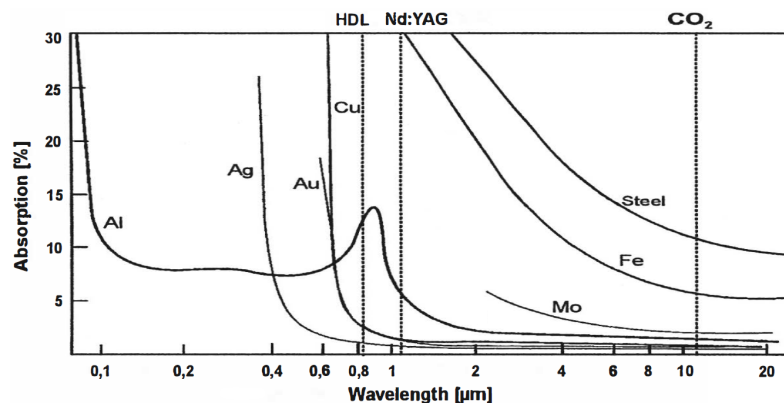
Figure 1.5: Comparison between the laser absorption of different metals and several laser sources [20].

SLS machines use high-power 10 µm carbon dioxide (CO_2) laser beams [4], with absorption for thermoplastic materials (see Figure 1.4). Additives, e.g., titanium dioxides whiteners in PA12 [28], could be used to color the powders, increase their flowability and laser absorption [19, 29].

The metals in Figure 1.5 absorb laser energies at wavelengths near the visible spectrum but almost entirely reflect laser light with wavelengths in the far-infrared region [20]. Hence, a ytterbium (Yb) fiber laser at a wavelength of 1 µm is mainly used in metal sintering processes [30].

Multiple or tunable high-power laser sources in the visible and infrared regime (e.g., 400 nm to 6 µm) would be required to print different polymers and metals in a single working system. Other laser types are compared in Table 1.1 to find those suitable for absorption control in SLS printing. These lasers can be classified based on the lasing medium, which may be solid (i.e., ER/TM/ND:YLF/YAG laser crystals) or gas (i.e., CO or CO_2) [4]. A quantum cascade (QC) laser can tune the wavelength over the entire infrared regime. However, QC lasers have a limited power supply, generally below 1 W. An alternative to the laser could be an Optical Parametric Oscillator (OPO). Herein, wavelength tuning is achieved by influencing the phase-matching conditions. The efficiencies of these systems are low, and even with a high-power amplifier, only powers of about 1 W are achieved. Both these tunable sources are expensive and hence disregarded as an option for SLS printing. Therefore, alternative energy sources are required.

Table 1.1: Commercially available lasers with various wavelengths and powers relevant for SLS printing. These lasers are mostly single wavelength but are available within a wavelength and power range. However, some tunable lasers can span the wavelength range without changing the working system.

Laser	λ [µm]	P [W]	M_2 [-]	D_0 [mm]	Reference
CO_2	9.20 - 10.6	400	<1.3	3.5	[31]
CO_2 tunable	9.10 - 10.9	50 - 180	<1.5	7.5 - 11	[25]
CO	5.50	250	<1.3	4	[32]
ER:YLF/YAG	2.81 - 2.94	5 - 80	<10 - <50	1.6	[33]
TM:YAG	2.02	2 - 100	<5 - <40	1.6	[33]
Y/E/R/T Fiber*	1.00 - 2.05	100-500	<1.1	<1	[34, 35]
ND:YAG	0.53 - 1.06	10 - 90	<15	1 - 2	[36]
QC	2.00 - 12.0	1 - 5	<1.5	4	[37]
QC tunable	3.80 - 10.2	<0.3	<1.5	4	[38]
FS/OPA tunable	1.50 - 16.0	10 - 0.1**	<1.3	2	[39]

* Ytterbium[1.04], Erbium[1.56], Raman[1.15−1.8] and Thulium[1.9−2.05] ($x^{\lambda \text{ in µm}}$)

** Power scales with wavelength: $P \approx 21.8\lambda^{-1.8}$ (1.5<λ<16 µm)

1.3   What about an acoustic energy source?

A possible alternative to the laser source in SLS could be an acoustic source. Acoustic sources benefit from mechanical oscillations being tuned easily to cover a wide range of frequencies (i.e., wavelengths). Therefore, instead of a laser, acoustic energy sources could potentially be used to control the absorption of materials. The idea of using acoustics for 3D printing originates from a game called Command and Conquer, in which a fictional acoustic tank uses a high-intensity acoustic canon to destroy objects, as depicted in Figure 1.6a. Similarly,

concentrating acoustic energy was envisioned to fuse powder particles. Later, it was realized
that high-intensity focused ultrasound (HIFU) probes are used in medical treatments, such
as liver cancer ablation [40] (see Figure 1.6b). Focussing the ultrasound energy results in
specific ablation of the solid tumor, as the temperature increases rapidly at the focal spot
while keeping surrounding tissue intact [40]. In addition, with phased array ultrasound probes,
it is possible to electronically adjust the focus distance and direction of the ultrasound beam.
This phased array principle enables tumor ablation by volumetric scanning of the focal spot
throughout the liver without moving the ultrasound probe. The existing knowledge on phased
array systems and tissue ablation is a good starting point for investigating the feasibility of
ultrasound-assisted powder bed fusion.

(a) Fictional acoustic cannon on a tank [41]   (b) Tumor heating and ablation with HIFU [42, 43]
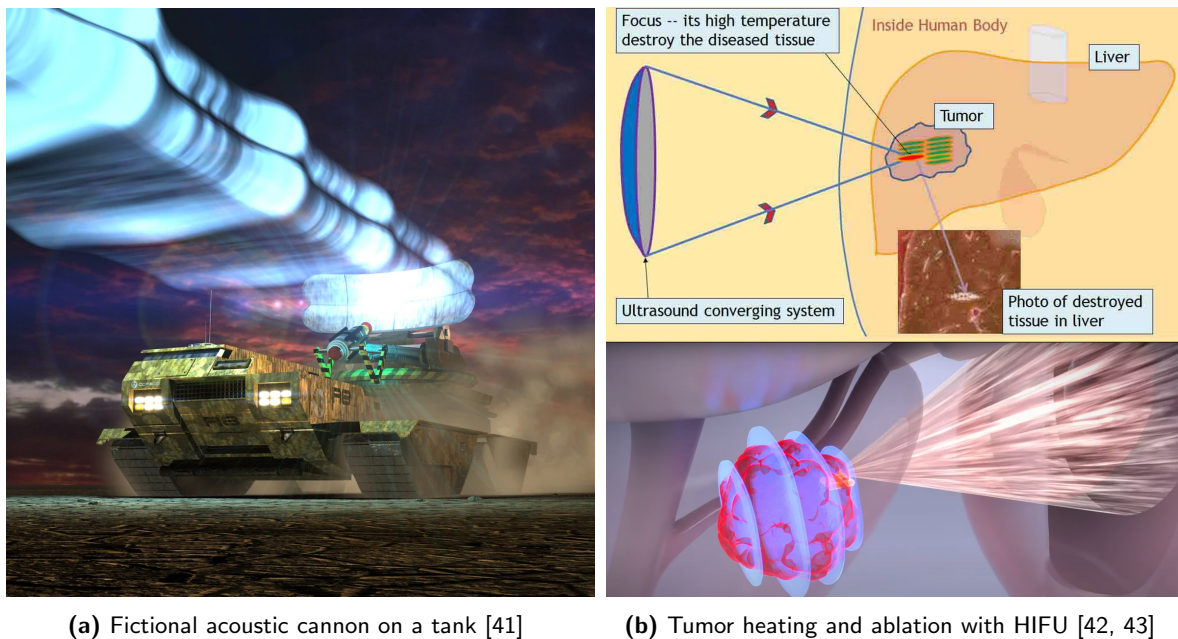
Figure 1.6: Examples of acoustic energy sources that initialized the idea of using focused ultrasound
transducers as an alternative to a laser in powder-based 3D printing.

Despite the various printing techniques available, no powder-bed fusion methods exist that
could potentially use a volumetric scanning approach. Therefore, a new type of powder-based
3D printing method, which we named Selective Acoustic Sintering (SAS), is developed in this
thesis. This new subcategory of PBF 3D printing (see Figure 1.1) uses many acoustic sources
to fuse powder particles. The transducers are positioned on the sides of an enclosure and create
a focal spot within a material volume. Using the phased array principle, the position of this
one or multiple focus spots can be moved through the volume. This enables volumetric 3D
printing and combining multiple focal spots in holographic shapes (see, e.g., [44, 45]) can lead
to homogeneous acoustic energy fields instantly forming 3D parts. In this multi-transducer
design, no moving components are required to spread or sinter the powder, and volumetric
printing renders layer-by-layer deposition obsolete. This shows great potential for overcoming
the limitations of current PBF methods related to layer-by-layer manufacturing (i.e., printing
speed, layer adhesion, inhomogeneous part qualities, etc.).

1.4 Objectives and outline of the thesis

Since the processing capabilities, deposition of powders, surface quality, and sintering capabilities are the essential factors to study for processing newly developed materials, finding the optimal parameters for processing these materials is an aspect that needs further attention [4]. This thesis explores the complex interplay between process parameters and intrinsic material properties by introducing new concepts in selective laser sintering (SLS) 3D printing and by studying, for the first time, an ultrasound-based 3D printing technique called selective acoustic sintering (SAS). The objective of this thesis is threefold:

- Determining the relevant process parameters and their coupling with final part quality to improve the selective laser sintering process.

- Developing a powder-based 3D printing system that can be used to print high-performance (thermoplastic) materials.

- Studying the feasibility of using selective acoustic sintering as an alternative powder-based 3D printing technique for high-performance materials.

In this dissertation, the first part focuses on laser-assisted 3D printing. **Chapter 2** discusses the prediction of the final product properties in SLS by controlling the temperature during printing. It demonstrates the modifications to a commercial SLS printer by adding infrared camera-assisted temperature control. Additionally, theories on the ratio of input laser energy to the energy required for melting (AMR) and percolation are used to propose a printability map and predict the relation between the process parameters and material properties of SLS prints.

In **Chapter 3**, a finite element model is presented to investigate the role of various processing parameters on part quality in SLS printing. The chapter introduces the combined melting and crystallization model for PA12, providing insights into space-filling evolution during SLS printing and lamellar thickness distributions. This results in a prediction for yield kinetics and SLS-part accuracy.

The second part of this dissertation focuses on the newly developed ultrasound-based 3D printing. **Chapter 4** introduces the SAS 3D printing technique for processing powder-based materials. The chapter discusses the benefits of using an acoustic energy source instead of a laser. It presents a mathematical framework to determine the feasibility of volumetric SAS 3D printing in a spherically shaped build volume. The printability of various materials, including metals, polymers, and ceramics, is also analyzed.

Chapter 5 extends the SAS framework by numerically modeling different transducer configurations and building volume shapes using the k-space pseudospectral method. The study conducts simulations to study the effect of phased array configuration on intensity amplitudes and spot dimensions within these build volumes. A time-reversal method is presented to predict the delays between transducers and amplitudes of the transducers that result in the desired focusing location.

The design of an ultrasound setup for characterizing powder compacts, presented in **Chapter 6**, demonstrates that combined echo and through-transmission experiments with a focused ultrasound transducer can characterize various materials acoustically. Speed of sound and attenuation measurements are performed on PMMA and PBT disks as validation. Finally, unfilled and filled, powder-based samples are compacted to study the effect of filler fraction (i.e., porosity) and filler material on the acoustic properties.

Lastly, **Chapter 7** summarizes the main conclusions and makes recommendations for future work on laser- and sound-based 3D printing with powder-based materials.

Chapter 2

Selective Laser Sintering: Predictive Analysis of Process Parameters Impact on Intrinsic Material Properties

Abstract

Selective laser sintering (SLS) is a widely used 3D printing method that produces high-quality objects using various materials. In this study, we investigate how different printing parameters affect the material properties of SLS-printed parts. Modifying a commercial desktop SLS printer shows that controlling the bed temperature is crucial because it affects porosity and mechanical properties through the energy melt ratio. The energy melt ratio links print parameters and powder melting physics. We find that increasing energy melt ratios improves the mechanical properties of the prints, such as Young's modulus, elongation at break, and tensile strength. Our results also show that percolation theory applies to the prints, which can be used to predict the mechanical properties from the density of sintered parts. The findings of this study provide a valuable guide to estimating material properties of SLS printed parts from process parameters.

2.1 Introduction

Selective laser sintering (SLS) is a 3D printing method that generally uses a high-power CO_2 laser to fuse powder particles and form a 3D-printed object. SLS has several advantages compared to other 3D printing methods, including the availability of machines from multiple retailers and a wide range of available materials, including metals, ceramics, and plastics [46]. The most commonly used polymer for SLS is the semi-crystalline polymer polyamide 12 (PA12), which holds about 95% of the total laser sintering polymer market [47]. PA12 has a

---

relatively large sintering window of approximately 25 °C compared to other semi-crystalline polymers, making it ideal for SLS 3D printing [19]. However, the range of available polymer materials is relatively limited compared to competitive processes such as injection molding [48].

Controlling printing parameters like laser power, layer thickness, and bed temperature is crucial for producing high-quality parts in SLS printing. An equation to describe the printing quality based on these parameters was derived by Nelson et al. [49, 50]. They found that combinations of laser power, scan speed, and hatch spacing could be used to estimate the area energy density E_D, a measuring unit used to evaluate print quality based on several mechanical properties. The energy density, defined as the laser power P divided by the product of laser speed v and laser beam spacing h_{space}, is given by the following equation:

$$E_D = \frac{P}{v h_{\text{space}}}. \tag{2.1}$$

The study found that the part density and bending strength of PMMA-coated SiC particles increase nonlinearly with increasing energy density. In another study by Caulfield et al. [51] on PA12, a nearly linear relationship was found between energy density and density up to degradation temperatures, suggesting that energy input and particle fusion are directly related to each other in PA12. The equation that describes the relationship between energy density and material property is a good guide for estimating the material property value of polyamide parts [51].

The energy density relation used does not consider the temperature of the bed or the properties of particles and materials. However, controlling the bed temperature is crucial as it affects porosity and mechanical properties as it is controlled by the rheological properties of the polymers at low deformation rates, specifically the temperature dependence of viscosity [48, 52]. Additionally, it is essential to keep the bed temperature within the sintering region, preferably near the melting peak, to avoid uncontrolled crystallization processes that can cause defects and warpage [19].

A relation that includes additional print parameters is introduced to compare different processing parameters, including powder bed temperature, porosity, and thermal material properties. The energy melt ratio (EMR) compares the laser energy at the powder bed surface to the energy required to melt the powder, making it a more extensive and practical method than the energy density formula [46, 48]. The attenuation melt ratio (AMR) is a reformulation of the energy melt ratio that includes the reflection coefficient and attenuation of the powder bed. It is considered the most fundamental form of the energy melt ratio given by the equation [53]:

$$\text{AMR} = e_l / e_{\text{M}}, \tag{2.2}$$

with the specific energy input and energy for melting given by:

$$e_l = a(1 - R)E_D/\rho_0, \tag{2.3}$$

$$e_{\text{M}} = c_p(T_m - T_b) + \Delta H, \tag{2.4}$$

respectively. Here, a, R, ρ_0, c_p, T_m, T_b, ΔH are the attenuation coefficient, reflection coefficient, solid density, specific heat capacity, onset melting temperature, bed temperature, and heat of fusion, respectively.

The energy melt ratio helps link print parameters and the physics of powder melting. It was found in previous studies that an increase in EMR results in a rising powder sintering temperature, increasing mechanical properties including Young's modulus, elongation at break, and yield stress [46, 48]. Although stated that increasing the bed temperature reduces the energy needed to melt the powder, thus reducing the amount of laser energy required to achieve improved mechanical performance, the effect of the bed temperature on mechanical properties is not examined experimentally in the works of Starr et al. [46] and Vasquez et al. [48]. Other literature studies have shown that this trend exists for PA12 [54, 55], but perform process parameter optimizations rather than studying fundamental process-material relations via, for example, the energy melt ratio. Experimental studies are necessary to understand how the temperature of the powder bed affects the quality of the printed parts. These studies should be systematic and based on fundamental process-material relations.

In this study, we aim to predict the impact of process parameters on the mechanical properties of materials used in selective laser sintering. Our objective is to develop a general method that can be used to predict part quality based on the intrinsic material properties of PA12. Instead of focusing on optimizing printing parameters, the relationship between part quality and energy melt ratio will be explored. In this paper, for the first time, the energy melt ratio is combined with percolation theory to predict the mechanical properties of SLS-printed PA12 parts with varying densities. Section 2.2 describes the materials and methods used to perform these experiments in SLS 3D printing. This involves modifying a desktop SLS printer by installing an infrared camera and calibrating laser power and scan velocity. Section 2.3 discusses the performance of the modified system and presents the results of part property measurements, including Young's modulus, strain at break, and yield stress, which are compared to the print process parameters and percolation theory. Finally, Section 2.4 offers conclusions and recommendations based on our findings.

2.2   Materials and methods

The Sharebot SnowWhite 1 SLS printer is used to print single-layer parts from a laser sintering grade of PA12 (type: PA2200, supplier: EOS PA2200), with a material density of 1020 kg/m^3 [7, 28]. This printer uses a 14W CO_2 laser with a 200 µm focal spot diameter to sinter powders selectively, creating three-dimensional objects through a layer-by-layer process.

Table 2.1: Fixed process parameter settings in the Sharebot SnowWhite 1.

Parameter	Value	Unit
Border laser speed	40000	points/s
Border power	20	%
Powder layer	800	µm
Layer thickness	200	µm
Waiting time	1200	s
Hatching space	100	µm
Warming layers	20	-
Env. Temperature	155	°C

2.2.1 System control and process parameters

Some process parameters are kept constant in this work, as listed in Table 2.1. Three process parameters are varied: the bed temperature, laser power, and scan speed.

(a) Temperature drift in the powder bed compared to the inaccurate pyrometer measurement

(b) Undiserd fusion within the powder bed after a few layers of printing
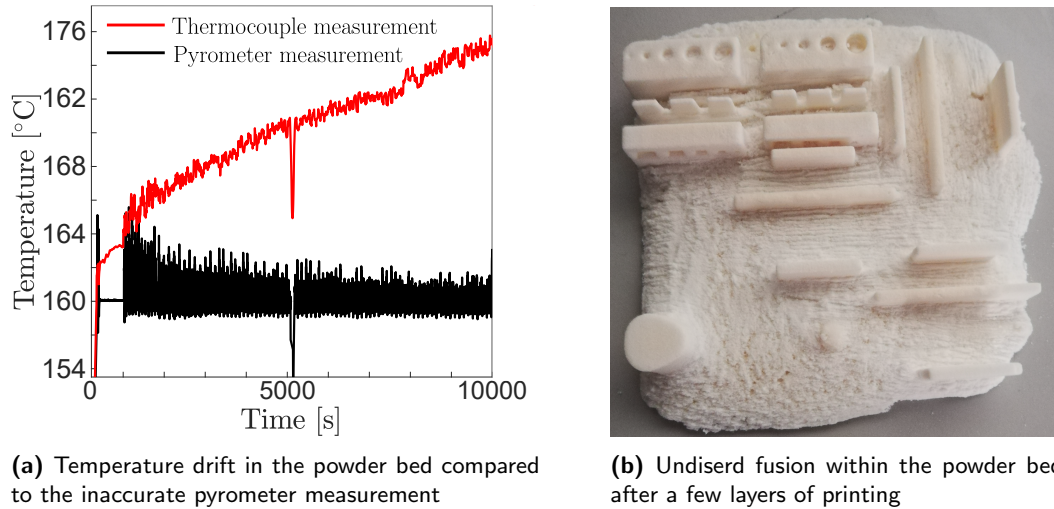
Figure 2.1: The pyrometer controls the bed temperature in the SnowWhite 1 SLS printer. However, due to the malfunctioning of this pyrometer, the actual bed temperature measured with a thermocouple increases over time. Hence, at some point in time, premature melting of the powder bed occurs, and the print job fails. This indicates the importance of process control in the SLS printer.

Bed temperature

The SnowWhite SLS printer has a temperature control unit that uses a pyrometer positioned outside the build chamber that points onto the powder bed to measure the temperature. Unfortunately, the pyrometer resulted in insufficient control to produce multi-layer parts, as shown in Figure 2.1a. Figure 2.1b shows the resulting part, where parts of the powder bed are molten after a few layers. A malfunction in the pyrometer readings is found when the temperature in the powder bed is measured with a thermocouple. This resulted in a drift in set temperature over actual bed temperature, as shown in Figure 2.1, melting undesired parts of the powder bed during printing.

To improve the control of the powder bed temperature, an infrared (IR) camera is mounted on the door depicted in Figure 2.2A. An Optris 640PI IR camera with a 33° lens and a temperature range option of 0-250 °C is utilized [56]. As the camera could not be placed at the top of the build chamber, a polished steel mirror is used to visualize the temperature of the powder bed (see Figure 2.2B-E). To allow temperature measurements of wavelength between 1 and 20 µm while the CO_2 laser is active, a long wave pass filter (>11 µm transmission) is installed in the IR camera. In addition, a potassium bromide (KBr) window is integrated into the door of the build chamber (0.25 - 26 µm transmission) [57]. This window is 90% transparent and serves as a heat shield for the camera (up to 400 °C). For safety, the camera is placed in an aluminum box to contain possible reflections of the laser beam, and a forced air flow is applied to keep the camera below 50 °C.

A white polymer block of polybutylene terephthalate (PBT), with a thermocouple inside of it, is placed just above the bed in the view of the camera (see bottom square area 1 in Figure 2.2C). Matching the temperature readings of the thermocouple with the camera readings of

this block is done by tuning the transmittance and emissivity settings of the IR camera. PBT is chosen since it has comparable emissivity to PA12 but a higher melting temperature of 220 °C. Hence, it does not melt during the printing of PA12 parts. This calibration is repeated before each print at temperatures close to the desired bed temperature setting.
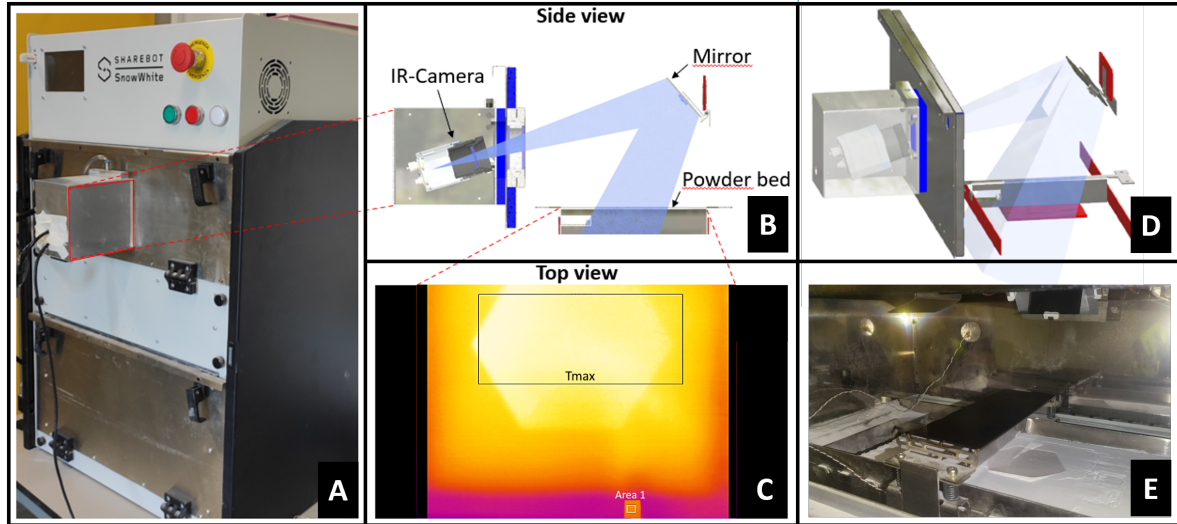
Figure 2.2: The Sharebot SnowWhite 1 SLS 3D printer has been modified with an infrared (IR) camera to enhance process control. To house the IR camera, an aluminum box has been mounted to the front of the door of the build chamber (see A). The camera captures visual information of the temperature field of the print bed, which is reflected by a steel mirror mounted to the ceiling of the build chamber (see B-E).

An Arduino Mega is connected to the SnowWhite SLS printer. It converts analog temperature readings from the IR camera to an I^2C communication signal for the control system of the SnowWhite. The Optris pix software is utilized to select an area of the IR camera view and export the maximum temperature as an analog signal to the Arduino. In Figure 2.2C, the maximum temperature in the T_{max}-area is used for the analog temperature output. The pyrometer is disconnected and bypassed by the Arduino by sending this IR camera-based I^2C signal to the SnowWhite. This means that the regular control procedure of the SnowWhite remains intact, but the Optrix pix software and the Arduino now control the temperature measure of the bed. In Arduino software, the temperature is read every millisecond, and a moving median function is utilized to prevent temperature readings from passing the recoater blade.

Laser power and scan velocity
In the SnowWhite SLS printer, the power is set in percentage, which the manufacturer calibrates according to specifications. Therefore, logically, one would convert the power to Watts by taking the percentage set on the printer and multiplying this by the maximum power of the 14W laser such that $P = \frac{P_{in}}{100} 14$ W. However, this is not the laser fraction that reaches the powder bed, as the laser is reflected on mirrors and passes windows before it reaches the powder bed. Close to maximum power, the performance of a laser starts to drop. The laser power at the powder bed surface is recorded with a Gentec UP19K-30H-H5-D0 (CO_2 laser calibrated) laser power detector [58]. To accurately measure the power and prevent damage to the laser power detector, the detector is placed as close as possible to the laser window,

resulting in beam diameters of about 6 mm. A range from 0 to 100 % laser power is measured with increments of 5 %.

The scan velocity of the laser is set in points/s, with a maximum of 64000 points/s. According to specifications, a conversion factor of 0.046875 mm/points can be used to find the print velocity in mm/s. The laser power detector is used to see if the SnowWhite SLS printer performs as specified. Laser powers of 20 % are used to prevent damage to the detector as print speed decreases. The spot is moved over the sensor by drawing circles at print speeds between 800 and 51200 points/s. More details on the laser power and scan velocity measurement methods are provided in Appendix 2.A.1.

2.2.2   Experimental strategies

Powder properties such as size distribution, sphericity distribution, surface morphology, microstructure, thermal properties, molecular weight, flowability, and rheological properties determine, amongst others, the printability of a powder material [59]. Aging and reuse of the powder can cause significant changes to these powder properties and affect the resulting part quality [18]. Therefore, to minimize the difference in powder properties between prints, a single batch of 100% virgin PA12 powder is used. Before every print, the powder is filtered so there are no lumps, and no powder is reused or mixed.

Maintaining a constant initial thermal history of the powder in the feeders and the build volume is crucial for getting similar powder properties between consecutive prints. Therefore, after starting the printer, a pre-heating step for 2 hours at 164 °C is performed to bring the printer and air in the build chamber to a constant temperature. Then, the first print is started, which starts with 20 warming layers of 200 μm and ends with one extra top layer to reduce the cooling rate of the part to the environment. After a print, the printer is cooled to far below the crystallization temperature (100 °C), and the part is removed. Afterward, pre-heating towards 164 °C is performed, followed by a 20-minute waiting time before the second print starts.

Single-layer hexagonal parts are produced, shown in Figure 2.3a. Single-layered parts are made to understand the SLS process, as they are not affected by the thermal history of previous layers and the thermal exposure of the following layers. The laser scan path is from the top to the bottom of the part, moving from the left to the right corner. The Slic3r software is utilized in the production of these scan paths [60]. The recoating cycle starts from left to right and returns to its original position. The use of this hexagonal geometry has some implications. The left and right corners, with smaller scan lengths, can represent minor features, while the mid-section (40 mm wide), with constant scan lengths of 69.3 mm, represents large (flat) surfaces. At constant scan velocity, the time between consecutive line scans at the hexagon's corners is smaller than in the midsection. So, due to the overlap of the scan lines, the temperature increase at the left and right corners is expected to be larger than the midsection of the hexagon.

2.2.3   Characterization methods

Standard tensile test specimens (as shown in Figure 2.3b) are punched from the mid-section of the hexagon (random orientation). These samples' neck width and thickness are measured with a micrometer to determine the cross-sectional area. Tensile data is recorded on two tensile machines (Linkam TST350 and ZwickRoell) with a 200 N and a 1 kN force cell for at

(a) Hexagon geometry   **(b)** Tensile bar   **(c)** Tensile test
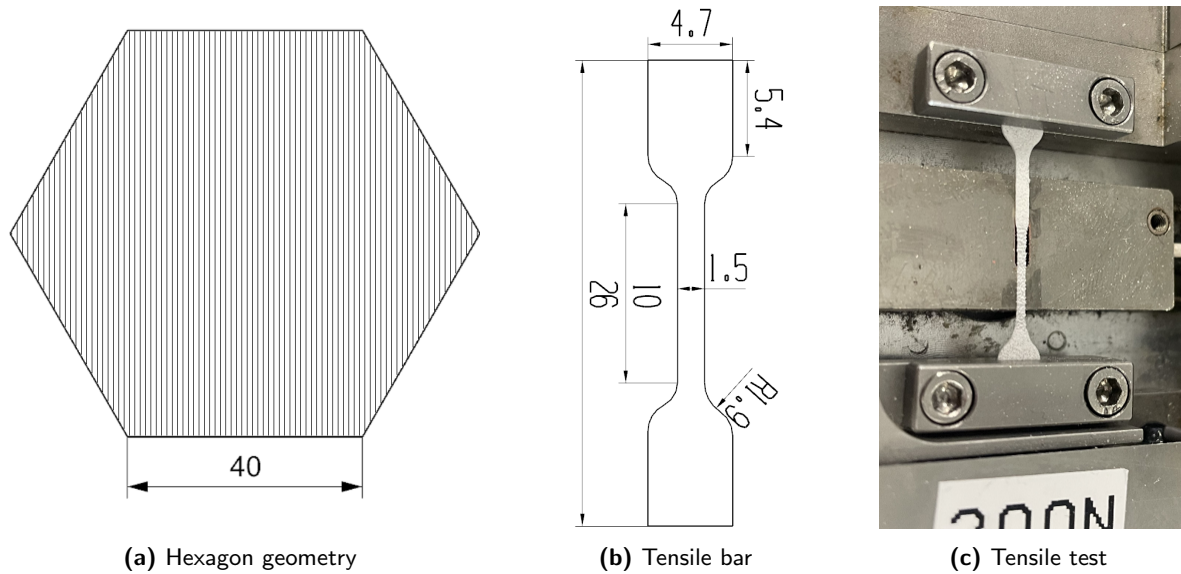
Figure 2.3: The hexagonal part shape with a midsection width of 40 mm is visualized in a). Successive vertical scan lines are drawn, and the scan direction is from left to right. In b), the tensile bar geometry is given, with an area of 78.58 mm^2. Mechanical characterization is performed by tensile experiments as shown in c).

least five tensile specimens extracted from the same hexagon. Results for Young's modulus, elongation at break, and yield stress are recorded for a constant strain rate of 0.001 1/s at room temperature. An example of an elongated sample in the Linkam TST350 is given in Figure 2.3c.

The single-layer hexagon part is prone to curling due to its large length-to-width ratio. Therefore, the warpage of the sharp corner and the midsection can be visually analyzed using a camera. This analysis is performed ex-situ after printing and can only be used to indicate warpage that could lead to printing failures. Refer to Appendix 2.A.2 for more details.

Before conducting tensile tests on the samples, the density of each sample is determined by weighing all the samples and dividing the mass by the volume of each sample. The volume is found from the area and thickness of the tensile specimen. The thickness is measured individually for each tensile specimen. The surface area of the tensile specimen is determined from a reference sample with known thickness and density (0.2 mm, Teflon) that is punched and weighted. The surface area of the tensile bar in Figure 2.3b follows to be 78.58 mm^2.

Differential scanning calorimetry (DSC) measurements are performed to determine the powders' thermal properties. Contact between the measuring pan and the powder is ensured by pre-compacting the powder between two glass plates. Two properties are obtained from these measurements: the onset of melting and the latent heat of melting. The measurements are performed with a constant rate of 10 °C/min and from 25°C to 220°C. The material starts to melt in the first stroke up to 220 °C, and the endothermic peak is formed. When the material cools down, it crystallizes, and an exothermic peak is formed. The temperature range between these two peaks is the sintering region.

2.3   Results and discussion

This section assesses the effect of processing parameters on print quality by performing controlled printing experiments for single-layer hexagon parts and measuring the tensile properties of dogbone-shaped tensile specimens punched from these hexagons. In total, 82 hexagonal parts were printed, and 5-10 tensile tests were performed per hexagon. The corresponding print settings are listed in Table 2.3 in Appendix 2.A.4. Equation 2.2 is used to calculate AMR for each of the prints using a value for $c_p = 2.35$ kJ/(kg K) [28]. The onset of melting temperature is used in Equation (2.4). DSC measurements of PA12 shown in Appendix 2.A.3 find the onset of melting temperature and latent heat of melting values of $T_m = 180$ °C and $\Delta H = 110.78$ kJ/kg, respectively. Attenuation, reflection coefficient and solid density of PA12 are $a = 17$ 1/mm, $R = 0.05$, and $\rho_0 = 1020$ kg/m^3 [53], respectively.

2.3.1   Temperature control

The modified SLS 3D printer is equipped with an IR camera that can be used to control the temperature. The print temperature is directly coupled to the energy required for melting and is thus related to the quality of the final product. To study this effect, the temperature control of the SLS printer is improved by replacing the pyrometer with an IR camera. With this camera, the maximum temperature of a specific area of the powder bed can be selected as the temperature control area. Two control strategies are used, which are called $T_{\max}$ control and T_{bed} control. In the case of $T_{\max}$ control, the maximum temperature of the hexagon part is used as the control temperature (see Figure 2.4a). The top IR heaters of the SLS printer are only active in the case that the maximum temperature of the hexagon ($T_{\max}$) falls below the desired bed temperature ($T_{\text{bed,desired}}$). Conversely, in the case of T_{bed} control, the maximum bed temperature next to the hexagon is used as the control area. The entire bed is heated by the IR heaters if the measured maximum bed temperature (T_{bed}) becomes smaller than the desired bed temperature. Therefore, the heaters can warm up the entire bed, even if the maximum temperature of the hexagon is larger than the desired bed temperature. The effects of both control strategies are shown in Figure 2.4b and 2.4c.

Figure 2.4b shows the temperature evolution over the center line of the hexagon for a scan velocity of $v = 1.3$ m/s. The laser from left to right irradiates the hexagon geometry. Initially, a significant temperature increase is visible at the left corner of the hexagon (area 11), resulting from the short scanning distance. Consecutive vertical scan lines overlap, and the time between first heating and second heating t_{12} of a point on subsequent scan lines scales with $t_{12} \sim L_{\text{scan}}/v$. At short scan lengths L_{scan}, this time is short, and the superposition of overlapping line scans results in a more significant temperature increase, as seen here. This indicates that controlling scan velocity is crucial for limiting the maximum temperature in complex parts with small features. The energy melt ratio (AMR) does not correctly account for this effect. Recent works have added a multiplication of the energy density with an overlay ratio [61, 62] to account for the beam size to the hatch spacing ratio. However, this does not include the time effect based on the scan length and scan velocity.

The middle part of the hexagon, with a constant scan length of 69.28 mm, shows a relatively constant maximum temperature over time (± 3 °C). As a result of the $T_{\max}$ control, the heaters are inactive if the laser scans the part. Therefore, the temperature of surrounding powder (i.e., the bed temperature) slightly drops with -0.1 °C/s. The cooling rate of the bed depends on the environmental temperature, which is not controlled by the SLS printer.
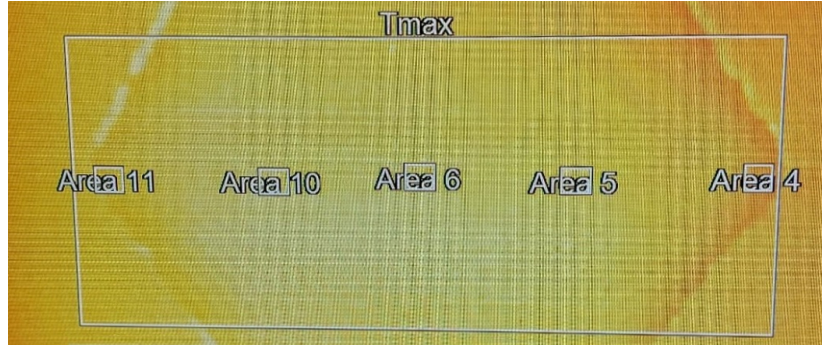
(a) IR camera image and temperature measurement areas
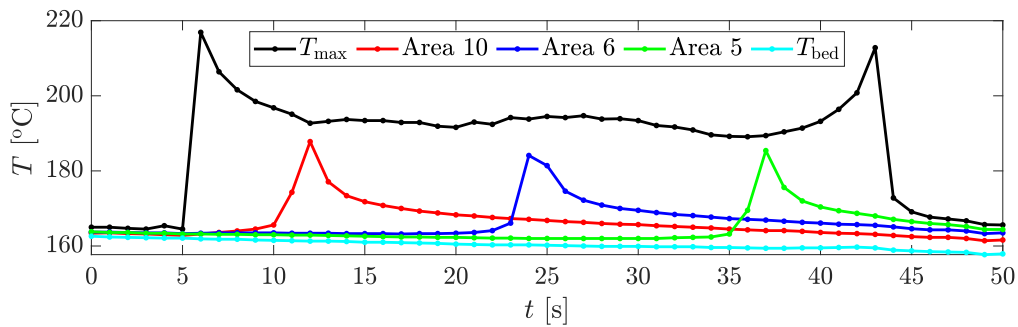
(b) Temperature profile of points the hexagon geometry for print 81 (T_{max} control)
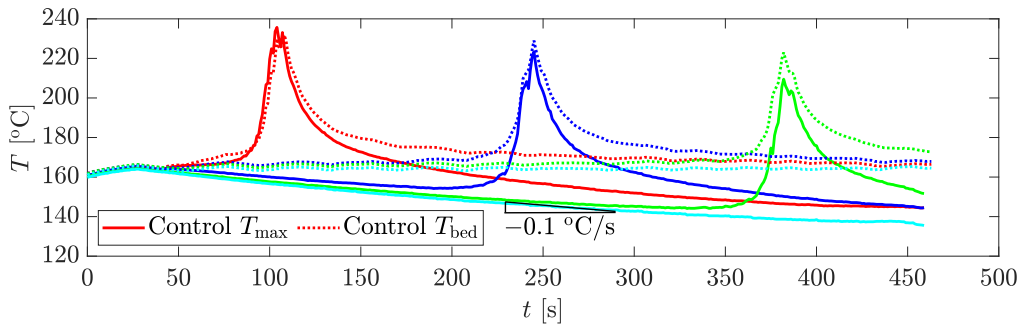
(c) Temperature profile differences: control of T_{max} (print 78) versus control of T_{bed} (print 82)

Figure 2.4: Temperture control in the modified Snowwhite Sharebot SLS 3D printer using an infrared camera and two control strategies. Data acquisition is performed at 1 Hz.

Figure 2.4c shows that this drop in bed temperature is crucial if the print speed is reduced to 0.12 m/s. The bed temperature and the maximum temperature of areas 6 and 10 drop below 150 °C, which results in crystallization-induced warpages of the hexagonal PA12 part during printing. However, by switching the control strategy to T_{bed} control, a nearly constant bed temperature is achieved (cyan dashed line, ±1.5 °C). Also, the peak value of the maximum temperature in area 5 is increased > 10 °C by this control method. Before irradiation, the proposed bed temperature control method produces a stable 164 °C bed temperature in each area. This shows the capability of the IR camera in a temperature control system and the effectiveness of the modifications to the SLS 3D printer.

2.3.2   Laser power and scan velocity
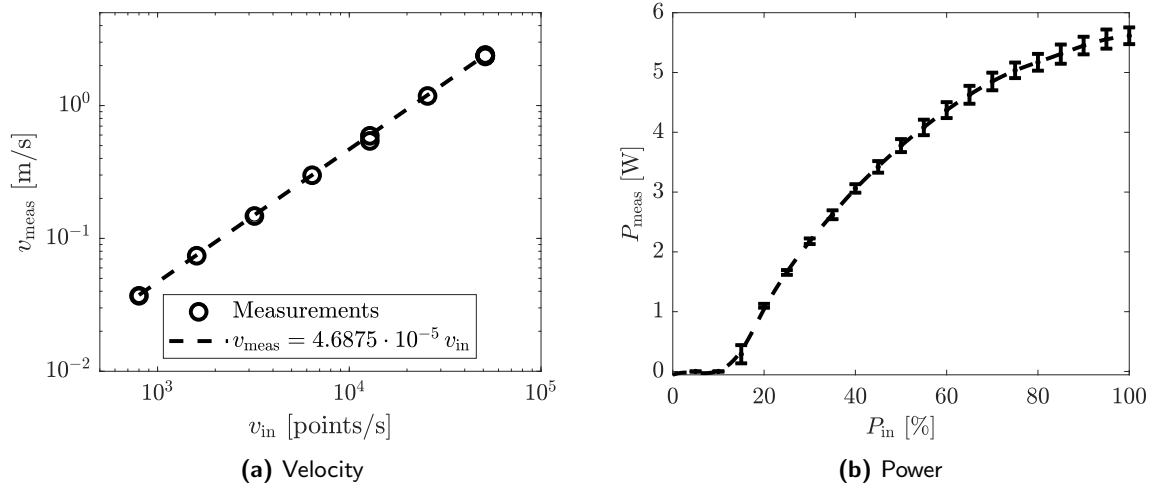
Figure 2.5: Resuliting scaling between input velocity and power versus output velocity and power.

The value of AMR depends on the energy absorption at the surface of the powder bed. The laser power and the scan velocity at this surface are directly coupled to this energy absorption via the energy density. Control over these parameters is required to investigate the effect of energy density on print quality. Details on the power and scan speed calibration measurements are provided in Appendix 2.A.1. The calibration measurements for the scan speed have resulted in Figure 2.5. The input scan velocity and power are in points/s and %, respectively. In Figure 2.5a, fitting results in a linear equation of the scan velocity $v_{\text{scan}} = 4.6875 \cdot 10^{-5} \, v_{\text{in}}$, as specified by the manufacturer. However, the measured power in Figure 2.5b shows two interesting phenomena about the input power. Firstly, the user manual describes that powers below 20% are unsuitable, as the laser is unstable below certain power values. Secondly, while expected from its unit, the power in percentage does not scale linearly with the power in Watt. The slope of the measured power decreases with increasing laser power, resulting in a maximum power of 5.6 W. The measured maximum power is more than a factor 2 smaller than expected for the 14 W laser tube. So, incorrect calibration can significantly affect the reported AMR. Hence, reporting proper calibration of scan velocity and power is advised for any research on SLS 3D printing.

2.3.3   Printability map

In Figure 2.6, the data points of the 82 hexagonal prints are collected in a printability map. The increase in thermal energy per unit mass required to melt the material (e_M) is shown on the vertical axis. Values of the energy input e_l are presented on the horizontal axis. According to the AMR theory, the range in which a material can be printed is defined as [53]:

$$d\varphi a + 1 < \text{AMR} < \frac{e_{\text{deg}}}{e_{\text{M}}} + 1, \tag{2.5}$$

with d the layer thickness, φ the porosity, and $e_{\text{deg}} = c_p \left(T_{\text{deg}} - T_m \right) + \frac{A_{\text{deg}}}{M_w} = 356$ J/g the specific energy of degradation of PA2200, wherein the degradation onset temperature, activation

energy for degradation, and molecular weight are given as $T_{\deg} = 325$ °C, $A_{\deg} = 280$ kJ/mol and $M_w = 18.8$ kg/mol, respectively [53]. In the case of AMR< 1, no melting can occur, and if AMR$< d\varphi a + 1$, the laser does not fully penetrate the desired layer thickness. However, as single-layer prints are performed, the latter is not of concern here, and AMR< 1 is the limiting factor in the printability map in Figure 2.6. At an input energy that exceeds the melting energy by more than the thermal degradation limit $e_l - e_M > e_{\deg}$, the material degrades. Following the definition of Bierwisch et al. [53], degradation of PA2200 is expected for AMR values of 3-4, depending on the bed temperature. Nonetheless, the onset of degradation in the single-layer prints is found for AMR$_{\deg} > 10$, which far exceeds the theoretical value. Density measurements and mechanical characterization are used to determine the onset of degradation in the following sections. Recent works of Lupone et al. [63] and Vande Ryse et al. [62] show that the theoretical prediction of degradation results in an underprediction of the degradation energy, as porosity is not included. For a more qualitative prediction of the onset of degradation, calorimetry measurements could be performed [62]. Next to limits
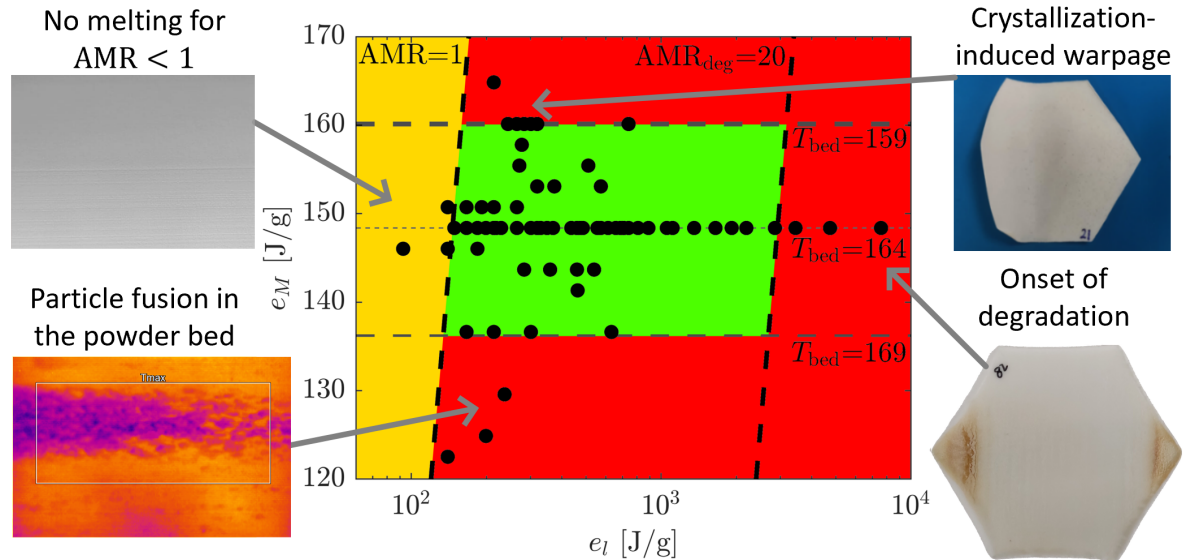
Figure 2.6: The printability map of the PA12 hexagonal parts. The solid black markers are the printed samples in this study, at corresponding specific energy input e_l and energy required for melting e_M. The green area indicates the printable area where parts can be successfully printed. No melting is expected for samples with AMR<1, indicated by the yellow area. The bottom red area shows the region where pre-melting occurs, and warpage occurs in the upper red area. Additionally, at AMR values above 20, the right red area shows the region where degradation occurs.

in the print settings related to the AMR and layer thickness, the bed temperature is also a critical parameter. Prints performed at average bed temperatures above 169 °C failed, as pre-melting of small lamellar structures in the powder resulted in sticking of powder in the powder bed. Therefore, the spreadability of the powder reduces, and the powder can stick to the recoater blade, causing distortions in the powder bed (see Figure 2.6). On the contrary, if the powder bed temperature is below 159 °C, crystallization-induced warpage can distort the printing processes. The onset of crystallization of virgin PA2200 powder is at 153 °C (see Appendix 2.A.3). As the relatively cold powder is applied to the just molten hexagonal part, the part starts to crystallize, decreasing volume. Resulting internal stresses cause the

hexagonal part to warp. The returning recoater blade can wipe or bend the curling part.

2.3.4 Tensile test results

Tensile experiments are performed to evaluate the mechanical characteristics of the hexagonal prints. The evaluated mechanical properties are Young's modulus E, strain at break $\varepsilon_{\text{break}}$ and yield stress σ_y, as depicted in Figure 2.7a. Figure 2.7b shows the typical stress-strain curves of samples processed at varying printing conditions. The tensile curves are ordered from low AMR (print 28) to high AMR (print 76). Necking occurs for the prints with the higher AMR value, while low AMR prints result in brittle failure at small strains.

(a) Mechanical properties

(b) Typical tensile curves
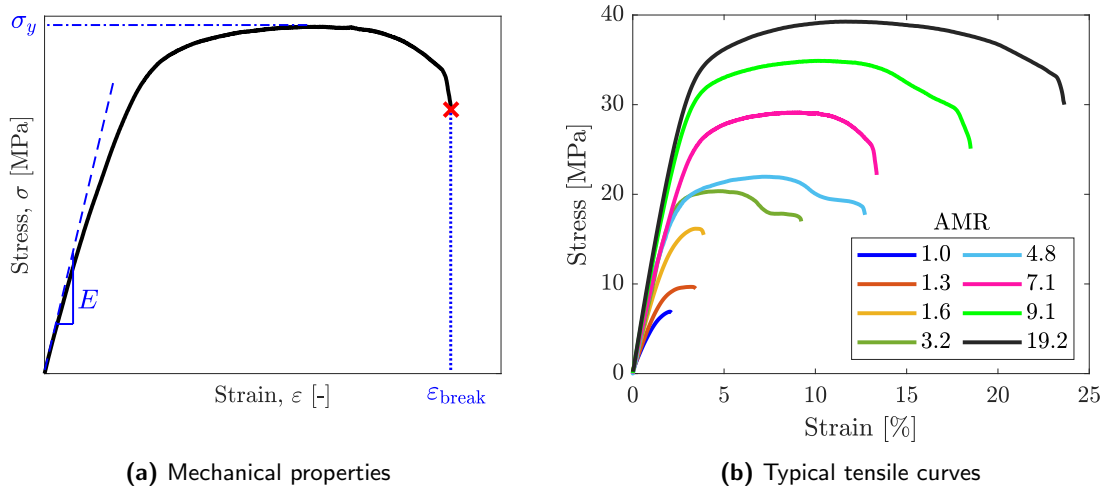
Figure 2.7: Tensile curves, and the determination of Young's modulus E, strain at break $\varepsilon_{\text{break}}$ and yield stress σ_y of sintered PA12 samples with varying AMR values.

2.3.5 Processing-density relation

Besides the mechanical properties, the density of each tensile bar is also measured. In Figure 2.8a, the effect of the bed temperature on the sintering of particles can be seen. The density ρ is used as an indicator of sintering degree. A constant density is measured for nearly constant AMR values of 1.5-1.7, while the bed temperature varies from 159 to 169 °C. This indicates that bed temperature is not a good indicator of sintering degree. An increase in AMR clearly shows an increase in density. Figure 2.8b shows the correlation between density and AMR for all prints. Density values are plotted with error bars indicating the standard deviation of measuring 5 to 10 samples. Again, an increase in AMR results in increased sample density. As the value for AMR increases through higher power, longer irradiation times (i.e., lower scan speed), or increasing bed temperature, more energy is put into the material, and the maximum temperature is increased. As a result, particles reach a molten state with a lower viscosity, contributing to forming parts with increased density. In Figure 2.8b, the density increase with AMR seems to follow an empirical power-law relation with an exponent of 0.22. The guide through the eye (dashed line) shows that the density decreases at AMR>20. This point is taken as the onset of degradation of the PA12 part, $\text{AMR}_{\text{deg}} = 20$. Therefore, we

(a) Bed temperature versus density   **(b)** AMR versus density
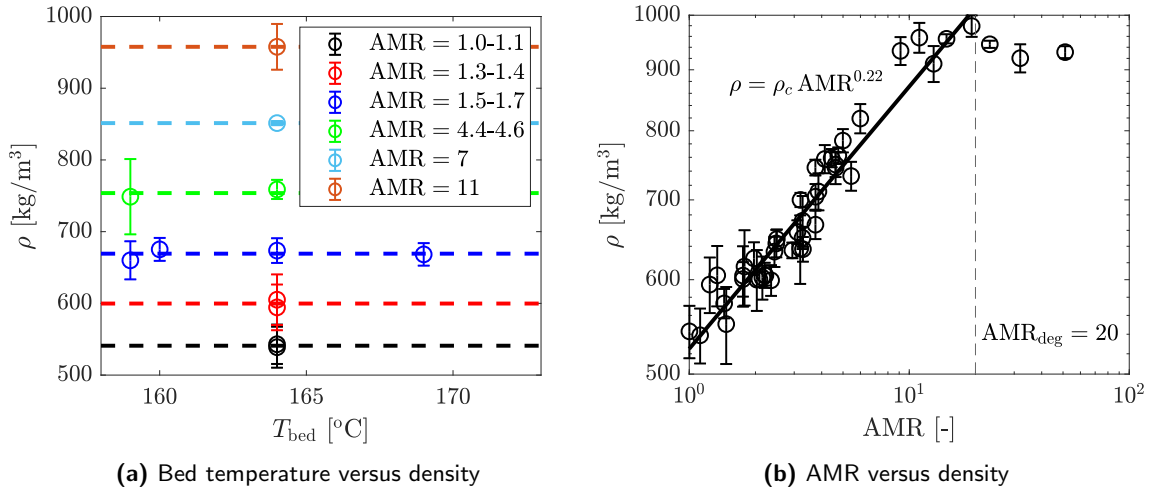
Figure 2.8: Effect of the process parameters on the density of the hexagonal part. In a) the bed temperature is varied for constant AMR (blue dashed line), or the energy density is varied for constant bed temperature (164 °C). In b), the correlation between AMR and density is given.

define the relation between density and AMR as follows:

$$\rho = \rho_c \, \mathrm{AMR}^y \quad \text{for AMR} < \mathrm{AMR}_{\mathrm{deg}}, \tag{2.6}$$

with the critical density $\rho_c \approx 509$ kg/m^3 and the power-law exponent $y = 0.22$.

2.3.6 Material properties and percolation theory

Predictions of the mechanical properties of porous materials over a certain porosity range can be performed using percolation theory (see Landauer [64], and the references therein). The percolation equation, which strictly speaking is only valid near the critical fraction p_c (where the particles first form a continuous percolation path across the medium), has the form $Y = Y_0(p_c - p)^{f_Y}$. Here, Y is the effective material property (e.g., modulus or conductivity), Y_0 a proportionality constant, p the fraction of the highest property component (e.g., high-modulus or high-conductivity component), and f_Y the critical exponent of the effective material property [65]. This relationship is often found to cover the entire composition range [66–69], but only if the ratio of the matrix and pore properties (e.g., low- versus high-modulus) is large and finite, as shown theoretically by Straley [70].

The effective material properties (Y) retrieved from the tensile experiments in Figure 2.7 are the Young's modulus (E), the strain and break ($\varepsilon_{\mathrm{break}}$) and the yield stress ($\sigma_y$). In the sintered powder materials, there is complete percolation at the solid density ρ_0, and no percolation, i.e., the material property becomes zero at the critical density ρ_c. The mechanical properties of air within the pores are significantly smaller than the mechanical properties of the sintered polymer particles. Hence, the percolation theory is expected to hold for the three material properties over the entire porosity range.

As the density ρ of the material decreases, i.e., the porosity $\varphi = 1 - \rho/\rho_0$ increases, the modulus, strain at break, and yield stress deteriorate because fewer connected particles carry the stress. Following polymer physics nomenclature, clumps of connected particles form so-called blobs, and the load-bearing particles resemble strings attached at nodes [71]. Near

percolation, the strength of an elastic medium is determined by the modulus of the backbone represented by the continuous path of links across the particles that carry the stress. The total strain is the strain in each particle times the total number of particles. A 2D lattice representing a thin sample or film implies that the backbone modulus would scale linear, i.e., $f = 1$ [71]. The effect of the strength of the blobs increases the exponent to $f = 1.3$. This exponent is similar to the percolation theory for 2D (electrical) conductivity [68]. Likewise, for connections in an infinite 3D lattice, a theoretical exponent of $f \approx 2.1$ can be derived [72]. This exponent is universal; however, it can be affected by the finite size of the system [73]. Therefore, experiments and given percolation exponents are rather characteristic of the used material than universally applicable [74]. In addition, the value of the percolation threshold and exponent is a function of the powder size, shape, their distributions, and the preparation method [72, 74].

In Figure 2.9, the resulting mechanical tensile properties of the SLS prints, Young's modulus, strain at break, and yield stress are shown as a function of the density of the parts. All samples are plotted with error bars indicating the standard deviations of a measurement. EOS GmbH [28] reports Young's modulus of 1.65 GPa, strain at break of 18%, and yield stress of 48 MPa at $\rho = 930$ kg/m^3 for PA2200. Modulus and strain at break are within the error of the presented measurements. The yield stress is a rate-dependent property not provided in the data sheet [28]. Paolucci et al. [16] show that at a strain rate of 0.001 1/s, the yield stress of sintered PA2200 is $\sim$41 MPa, which agrees with yield stress values at near-solid densities.

(a) Young's modulus versus density   **(b)** Strain-at-break versus density   **(c)** Yield stress versus density

Figure 2.9: The effects of the density increase on Young's modulus, strain at break, and yield stress of PA12 prints. The solid line is the theoretical percolation prediction.

The percolation equation, rewritten to a relative density formulation as [74, 75]:

$$Y = Y_0 \left(\frac{\rho - \rho_c}{\rho_0 - \rho_c} \right)^f \tag{2.7}$$

is fitted simultaneously to the three mechanical properties using a nonlinear least-square method. As the three mechanical properties are measured using the same powder, experimental conditions, and tensile specimen, a universal characteristic exponent f is assumed. The solid density is fixed at $\rho_0 = 1020$ kg/m^3 [53], while characteristic density ρ_c, the exponent f and solid Young's modulus (E_0), strain at break ($\varepsilon_{\text{break0}}$), and yield stress ($\sigma_{y0}$) are used as fitting parameters. The percolation theory fitting results are given by the solid lines in Figures 2.9a (Young's modulus), 2.9b (strain at break), and 2.9c, (yield stress). Optimal

fitting is achieved for a critical exponent $f = 0.608$, a critical density $\rho_c = 525.8$ kg/m^3 and solid modulus, strain at break, and yield stress of $E_0 = 1.869$ GPa, $\varepsilon_{\text{break0}} = 18.5$ %, and $\sigma_{y0} = 39.4$ MPa, respectively, with coefficients of determination of $R_E^2 = 0.893$, $R_\varepsilon^2 = 0.7368$, and $R_\sigma^2 = 0.96051$.

The percolation equation especially predicts the yield stress very well, and it is clear that a percolation type of equation fits the data, as the material properties deteriorate to zero near the critical density $\rho_c \approx 525$ kg/m^3. The fits are in good agreement at small densities for the modulus and strain at break; however, the mechanical properties level off at nearly solid densities. A similar plateau at large densities (i.e. large energy densities) has been reported for SLS-printed PA12 parts (see e.g., [53, 76, 77]) and is attributed to the onset of degradation of the polymer [53, 76]. Print 78 ($\rho = 931$ kg/m^3), produced with the highest energy melt ratio (AMR=51), shows most discoloration and severe degradation as modulus, strain at break and yield stress drop in Figure 2.10. This point is also visible in Figure 2.9 and has lower mechanical properties than prints with similar densities of $\rho = 930$ kg/m^3. Therefore, this point is excluded from the fitting procedure.

To study the sensitivity to the fitting parameters of the percolation theory, the exponent f is varied from 0.44 to 1.3. The resulting fitting parameter and coefficients of determination are listed in Table 2.2. The coefficients of determination R_Y^2 are the first indicator for describing the material properties by the percolation equation. Increasing the percolation exponent $f > 0.61$ results in a drop in coefficients of determination of all three material parameters while lowering the exponent to $f = 0.5$ gives a slight increase in R_E^2 and R_ε^2, and a minor decrease in R_σ^2. As the latter differences in R^2 are small, the coefficients of determination are only indicative of the goodness of the fit. Therefore, next to the coefficient of determination, the resulting fitting parameters are also examined to determine the correctness of the percolation equation fit. The critical percolation density originates from the density of unsintered powder,

Table 2.2: Fitting results of percolation equation to the tensile material properties for different characteristic exponents f. The first rows are the fitting parameters, while the last three are the coefficients of determination of Young's modulus, strain at break, and yield stress, respectively.

Parameter [unit]	**f=0.44**	**f=0.5**	**f=0.61**	**f=0.77**	**f=1.00**	**f=1.30**
ρ_0^* [kg/m^3]	1020	1020	1020	1020	1020	1020
ρ_c [kg/m^3]	537.6	536.5	525.7	487.2	418.3	321.7
φ_c [-]	0.473	0.474	0.485	0.522	0.590	0.685
E_0 [GPa]	1.663	1.749	1.869	1.939	1.982	2.013
$\varepsilon_{\text{break0}}$ [%]	16.44	17.31	18.51	19.15	19.53	19.801
σ_{y0} [MPa]	34.90	36.79	39.43	40.92	41.84	42.50
R_E^2 [-]	0.89504	0.90201	0.89266	0.88142	0.86729	0.85432
R_ε^2 [-]	0.72391	0.74004	0.73680	0.70931	0.68126	0.66020
R_σ^2 [-]	0.91033	0.94014	0.96051	0.95804	0.94906	0.94040

* fixed parameter

which equals the powder's untapped or tapped bulk density. For PA2200, this value is between 420 and 530 kg/m^3 [78]. Besides, Young's modulus of solid PA2200 is expected to be close to 1.95 GPa [79], strain at break approximately 20 %, and yield stress close to 40 MPa. Compared to injection molded samples, this relatively small strain at break originates from the increased void fraction of sintered SLS parts, inducing cavitations during tensile tests [16].

Comparing the fitting parameters in Table 2.2 to the expected values shows that exponents between 0.61 and 0.77 meet the proposed critical density criterion, and the solid material properties are close to the expected values. So, the measured tensile material properties are directly coupled to the percolation theory with an exponent of $0.61 \leq f \leq 0.77$ and an optimum of $f = 0.61$.

2.3.7 Processing and material property pedictions

To capture and predict the processing parameters' relation to material properties of SLS-printed parts, Equations (2.6) and (2.7) are combined to the following process-property relation:

$$Y = Y_0 \left(\frac{(\text{AMR}^y - 1)(1 - \varphi_c)}{\varphi_c} \right)^f \quad \text{for AMR} < \text{AMR}_{\text{deg}}, \tag{2.8}$$

with $\varphi_c = 1 - \rho_c/\rho_0$ the critical porosity. Figure 2.10 shows the results of Young's modulus, strain at break, and yield stress measured with tensile tests as a function of the AMR. The prediction of the process-material relation for $\varphi_c = 0.485$, $y = 0.23$, $f = 0.608$, $E_0 = 1.869$ GPa, $\varepsilon_{\text{break0}} = 18.5$ %, and $\sigma_{y0} = 39.4$ MPa, are added as solid lines. In Figure 2.10a, the modulus increases gradually towards a maximum value for increasing AMR. This can be explained by a growing degree of particle fusion for increasing energy inputs. Also, the maximum temperature is higher, resulting in a decrease in viscosity. This enhances the fluidability for particles to flow towards porous parts in the bed and decreases sintering times, increasing Young's modulus. However, at AMR>20, the degradation is causing the modulus to drop below the maximum value. Up to the degradation AMR value, it can be concluded that an increasing AMR increases Young's modulus, making it a good measure for predicting Young's modulus. Figure 2.10b shows the relation between strain at break

(a) Young's modulus versus AMR (b) Strain-at-break versus AMR (c) Yield stress versus AMR

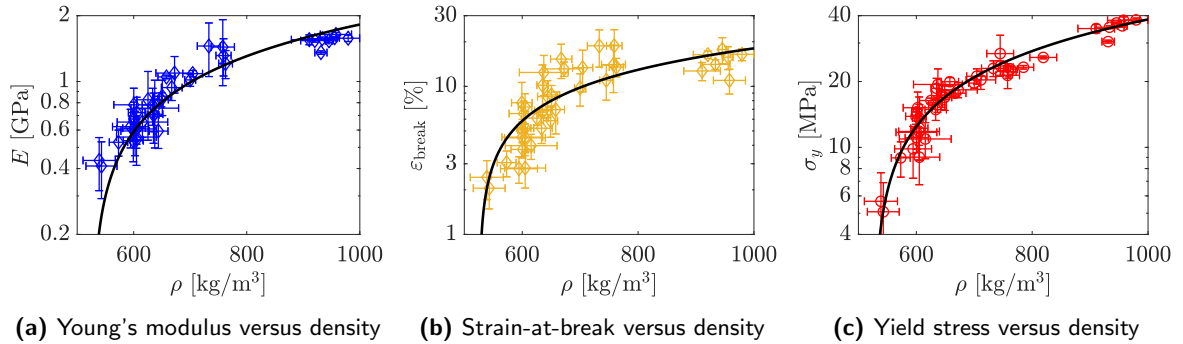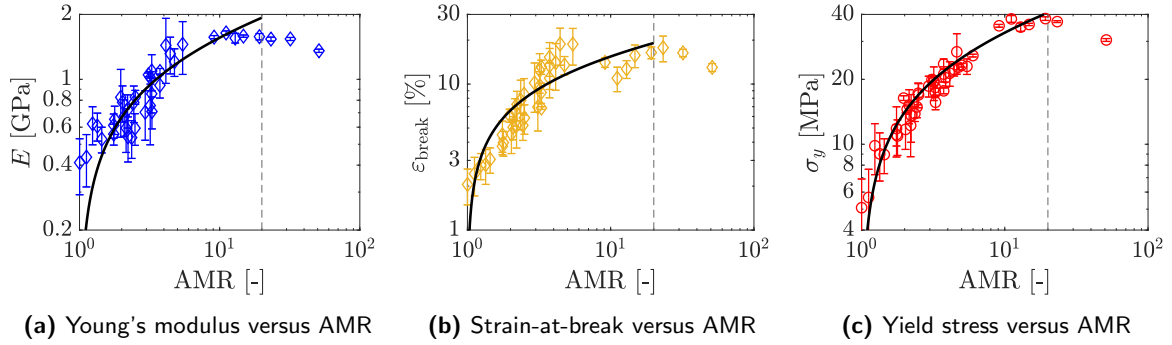**Figure 2.10:** The effects of an AMR increase on Young's modulus, strain at break, and yield stress of PA12 prints. Solid lines represent the process-property relation based on the percolation theory with a characteristic exponent of $f = 0.61$.

and AMR. This figure shows that for higher values of AMR, the samples will break at larger strains. This can be explained by the samples becoming less porous and, thus, more ductile for higher AMR values. In Figure 2.10c the yield stress increases with AMR, showing excellent agreement with the predictions of the process-density relation. After degradation, the yield stress drops to about 30 MPa and deviates from the proposed relation with the density. The findings here show that the material properties of PA12 can be directly linked to AMR. As AMR is a material-dependent relation, it is hypothesized that the proposed material-process

relation applies to other thermoplastic polymers in SLS. Combining these findings with the printability map gives operators of SLS printers an easy way of choosing process parameters for new materials without performing endless trial-and-error optimization experiments.

2.4   Conclusions

Single-layer SLS-printed PA12 samples were produced to investigate mechanical properties under various process parameters. To ensure consistent results, the temperature control of a desktop SLS printer was improved by adding an infrared camera, which regulated the bed temperature within $\pm 3^{\circ}$C.

The attenuation melt ratio (AMR) was varied by choosing different bed temperatures, laser powers, and scan velocities. The attenuation melt ratio (AMR) is the ratio of energy input to the required energy for melting PA12 powder. It was utilized to construct a printability map, wherein printing limits are identified for no melting (AMR < 1) and degradation at large energy ratios (AMR > 20). Additionally, a lower temperature limit was determined at ∼159°C, where the bed temperature is close to the onset of crystallization. Below this temperature, the crystallization-induced warpage caused the printed parts to fail. On the other hand, a higher temperature limit was found at 169°C, where the bed temperature is close to the onset of melting temperature. At this temperature, premature melting of the powder bed caused distortions in the prints. These limits were visualized in a printability map that can be used to predict printing parameters.

Increased attenuation melt ratio improved the prints' mechanical properties, including Young's modulus, elongation at break, and tensile strength. The effectiveness of AMR theory was demonstrated by keeping the energy melt ratio constant and varying the bed temperature. The densification of parts with increasing AMR in a power-law type of relation proved the usefulness of AMR in predicting the part quality of SLS prints. Furthermore, percolation theory was studied to predict the mechanical properties from the density of the part. It was concluded that a uniform critical exponent could be applied to predict the three investigated mechanical properties simultaneously. The universality of this equation resulted in a new process-material relationship for predicting the mechanical characteristics of SLS-printed parts.

2.A   Additional information

2.A.1   Calibration

Both laser power and scan velocity are measured to calibrate the system. The power sensor is positioned near the focusing lens of the SLS printer. In this way, the beam size at the detector is about 4-7 mm, preventing damage to the sensor. The results of the calibration measurements are given in Figure 2.5. For the scan velocity calibration, the laser irradiates N_{circ} times a circle with a diameter of 1 mm. The total path length L_{tot} follows from $L_{\mathrm{tot}} = N_{\mathrm{circ}}\pi D_{\mathrm{circ}}$. An input power of 15 % is used, resulting in startup effects (power overshoot to 0.6 W at times below 10 s) in some of the measurements in Figure 2.11a. Measuring the time at which the power drops to zero (i.e., the scan time t_{scan}) results in the scan velocity using $v = L_{\mathrm{tot}}/t_{\mathrm{scan}}$. This procedure is repeated for different input scan velocities and rotation amounts, as shown in Figure 2.11a.

(a) Velocity measurements

(b) Power measurements
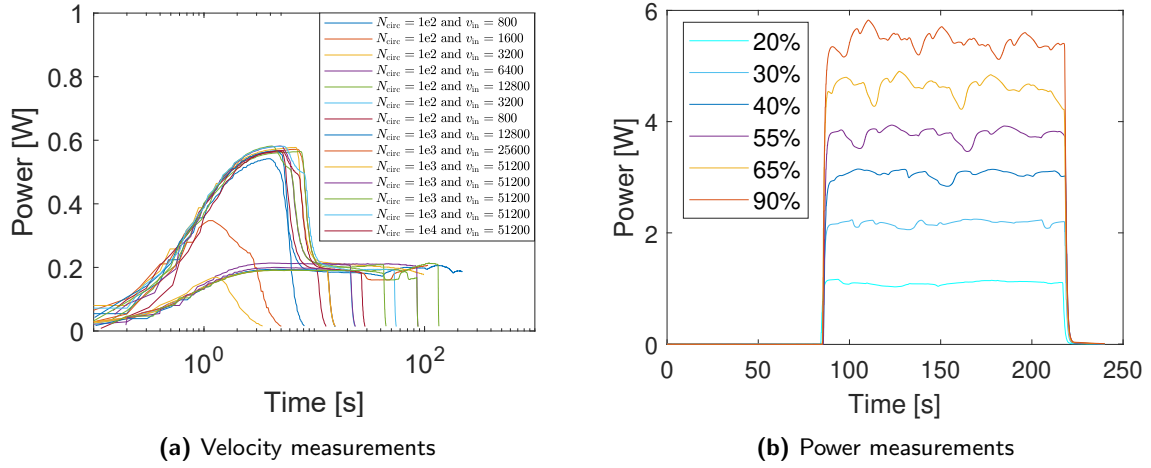
Figure 2.11: Scan velocity and laser power measurements used for system calibration.

The power is also measured using the rotating circles. The plateau values of the power are given in Figure 2.11b. The laser stability decreases as the power increases, resulting in larger power fluctuations. The mean value and standard deviation of the measured powers are reported in the main text of this paper.

2.A.2   Edge curling and printabilty

The edge of a part can curl upwards, depending on the temperature and power of the print. This has been studied by measuring the curling height w as illustrated in Figure 2.12a. This measurement has been performed for small AMR values. Figure 2.12b shows that the warpage is minimal at 164 °C. However, at smaller bed temperatures, crystallization-induced warpage can curl the edges. As this can occur during printing, warpage can cause the part to be wiped from the bed, resulting in printing failure. The markers in red indicate hexagonal prints that warped too much and were wiped from the bed. Particles start to stick at larger temperatures

(a) Warpage measurement

(b) Warpage and printability map
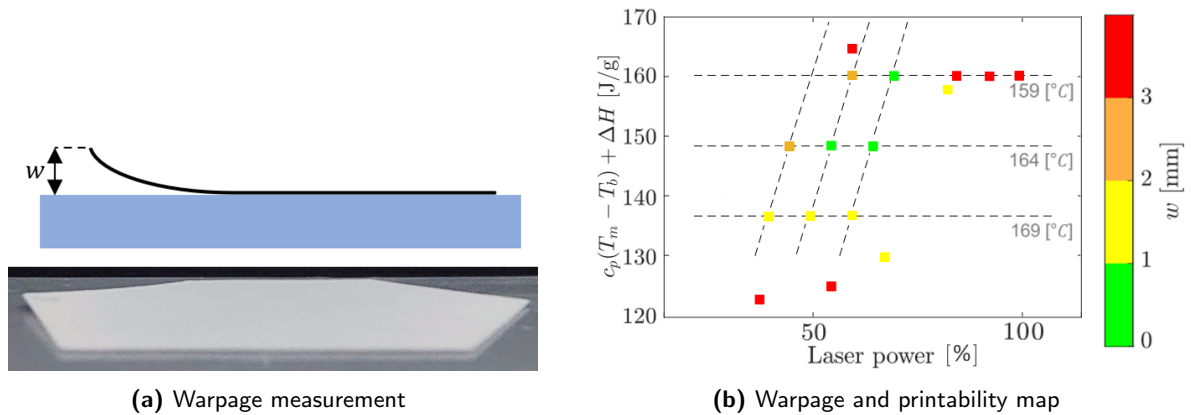
Figure 2.12: Measurement results of the effect energy melt ratio on edge curling height w at a constant scan velocity of 1.875 m/s.

due to premature melting. As a result, the part may also stick to the recoating device, causing the folding of the edges of the hexagon. This curling of edges is thus not a result of warpage. The part starts to sag into the build plate at higher powers due to volume changes during melting. This will also result in raised edges of the hexagon. As the warpage is minimal for 164 °C, this is regarded as the optimal temperature to print at large values of AMR.

2.A.3 DSC measurements of PA12

The DSC measurements of virgin PA2200 powder are given in Figure 2.13. The first cycles of 5 measurements are shown for a heating and cooling rate of 10 °C/min ranging from 25 °C to 220 °C. These measurements result, on average, in the heat of fusion of $\Delta H = 110.78$ kJ/kg and an onset of melting temperature of $\sim$180 °C.
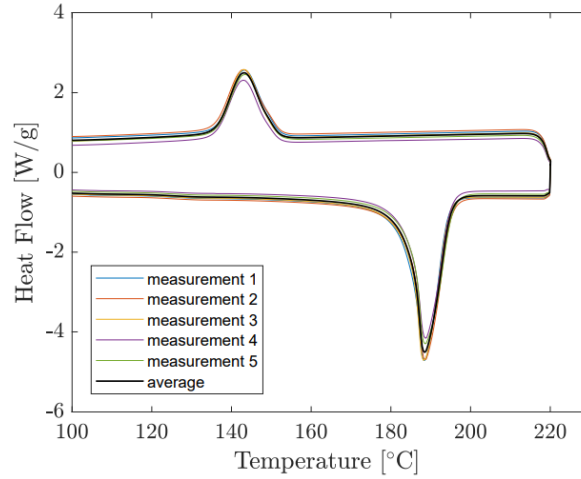
Figure 2.13: First cycle DSC measurements of virgin PA2200 powder for a heating and cooling rate of 10 °C/min ranging from 25 °C to 220 °C.

2.A.4 Print settings and AMR values

Table 2.3 gives the print settings and corresponding AMR values for the 82 hexagonal prints.

Table 2.3: Print numbers, process parameters and corresponding E_D, e_l, e_M and AMR values.

Print	P_{in} [%]	P [W]	T_{bed} [°C]	v_{in} [points/s]	v [m/s]	E_D [J/mm^2]	e_l [J/g]	e_M [J/g]	AMR [-]
1	20	1.099	165	40000	1.875	0.00586	92.76	146.03	0.635
2	25	1.656	165	40000	1.875	0.00883	139.84	146.03	0.958
3	30	2.178	165	40000	1.875	0.01162	183.92	146.03	1.259
4	20	1.099	165	40000	1.875	0.00586	92.76	146.03	0.635
5	25	1.656	165	40000	1.875	0.00883	139.84	146.03	0.958
6	34	2.532	163	40000	1.875	0.01351	213.84	150.73	1.419
7	31	2.267	163	40000	1.875	0.01209	191.40	150.73	1.270
8	28	1.969	163	40000	1.875	0.01050	166.29	150.73	1.103
9	25	1.656	163	40000	1.875	0.00883	139.84	150.73	0.928

Print	P_{in}	P	T_{bed}	v_{in}	v	E_D	e_l	e_M	AMR
10	25	1.656	175	40000	1.875	0.00883	139.84	122.53	1.141
11	31	2.267	163	40000	1.875	0.01209	191.40	150.73	1.270
12	28	1.969	169	40000	1.875	0.01050	166.29	136.63	1.217
13	34	2.532	157	40000	1.875	0.01351	213.84	164.83	1.297
14	38	2.885	159	40000	1.875	0.01539	243.62	160.13	1.521
15	36	2.709	164	40000	1.875	0.01445	228.75	148.38	1.542
16	34	2.532	169	40000	1.875	0.01351	213.84	136.63	1.565
17	37	2.797	172	40000	1.875	0.01492	236.19	129.58	1.823
18	43	3.277	160	40000	1.875	0.01748	276.74	157.78	1.754
19	50	3.778	159	40000	1.875	0.02015	318.99	160.13	1.992
20	47	3.564	159	40000	1.875	0.01901	300.95	160.13	1.879
21	44	3.349	159	40000	1.875	0.01786	282.83	160.13	1.766
22	44	3.349	159	40000	1.875	0.01786	282.83	160.13	1.766
23	42	3.205	161	40000	1.875	0.01709	270.66	155.43	1.741
24	34	2.532	164	40000	1.875	0.01351	213.84	148.38	1.441
25	32	2.355	164	40000	1.875	0.01256	198.88	148.38	1.340
26	30	2.178	164	40000	1.875	0.01162	183.92	148.38	1.240
27	28	1.969	164	40000	1.875	0.01050	166.29	148.38	1.121
28	26	1.760	164	40000	1.875	0.00939	148.66	148.38	1.002
29	32	2.355	174	40000	1.875	0.01256	198.88	124.88	1.593
30	30	2.178	164	40000	1.875	0.01162	183.92	148.38	1.240
31	41	3.133	159	40000	1.875	0.01671	264.57	160.13	1.652
32	41	3.133	163	40000	1.875	0.01671	264.57	150.73	1.755
33	44	3.349	166	40000	1.875	0.01786	282.83	143.68	1.968
34	50	3.778	162	40000	1.875	0.02015	318.99	153.08	2.084
35	50	3.778	164	40000	1.875	0.02015	318.99	148.38	2.150
36	52	3.899	164	40000	1.875	0.02079	329.24	148.38	2.219
37	56	4.139	164	40000	1.875	0.02208	349.53	148.38	2.356
38	60	4.371	164	40000	1.875	0.02331	369.12	148.38	2.488
39	80	5.171	164	40000	1.875	0.02758	436.65	148.38	2.943
40	100	5.614	164	40000	1.875	0.02994	474.08	148.38	3.195
41	47	3.564	164	40000	1.875	0.01901	300.95	148.38	2.028
42	47	3.564	169	40000	1.875	0.01901	300.95	136.63	2.203
43	90	5.451	164	40000	1.875	0.02907	460.26	148.38	3.102
44	61	4.422	162	40000	1.875	0.02359	373.44	153.08	2.440
45	58	4.255	166	40000	1.875	0.02269	359.32	143.68	2.501
46	90	5.451	166	40000	1.875	0.02907	460.26	143.68	3.203
47	100	5.614	164	21333	1.000	0.05614	888.90	148.38	5.991
48	100	5.614	164	25600	1.200	0.04678	740.75	148.38	4.992
49	100	5.614	164	28800	1.350	0.04159	658.44	148.38	4.438
50	100	5.614	164	30933	1.450	0.03872	613.03	148.38	4.132
51	100	5.614	164	33067	1.550	0.03622	573.48	148.38	3.865
52	100	5.614	164	34133	1.600	0.03509	555.56	148.38	3.744
53	100	5.614	162	33067	1.550	0.03622	573.48	153.08	3.746
54	100	5.614	166	35200	1.650	0.03402	538.73	143.68	3.749
55	55	4.081	164	17067	0.800	0.05101	807.72	148.38	5.444

Print	P_{in}	P	T_{bed}	v_{in}	v	E_D	e_l	e_M	AMR
56	100	5.614	164	39040	1.830	0.03068	485.74	148.38	3.274
57	100	5.614	161	37120	1.740	0.03226	510.86	155.43	3.287
58	55	4.081	164	19520	0.915	0.04460	706.20	148.38	4.759
59	100	5.614	167	40960	1.920	0.02924	462.97	141.33	3.276
60	43	3.277	160	40000	1.875	0.01748	276.74	157.78	1.754
61	41	3.133	164	40000	1.875	0.01671	264.57	148.38	1.783
62	41	3.133	164	40000	1.875	0.01671	264.57	148.38	1.783
63	43	3.277	160	40000	1.875	0.01748	276.74	157.78	1.754
64	100	5.614	164	21333	1.000	0.05614	888.90	148.38	5.991
65	100	5.614	164	17067	0.800	0.07018	1111.12	148.38	7.488
66	100	5.614	164	25600	1.200	0.04678	740.75	148.38	4.992
67	25	1.656	164	25600	1.200	0.01380	218.50	148.38	1.473
68	100	5.614	164	18000	0.844	0.06654	1053.51	148.38	7.100
69	100	5.614	159	25600	1.200	0.04678	740.75	160.13	4.626
70	50	3.778	164	18000	0.844	0.04477	708.86	148.38	4.777
71	100	5.614	164	11500	0.539	0.10415	1648.97	148.38	11.113
72	100	5.614	164	14000	0.656	0.08555	1354.51	148.38	9.129
73	100	5.614	164	11500	0.539	0.10415	1648.97	148.38	11.113
74	100	5.614	164	9900	0.464	0.12098	1915.47	148.38	12.909
75	100	5.614	164	8650	0.405	0.13846	2192.28	148.38	14.775
76	100	5.614	164	6650	0.312	0.18010	2851.61	148.38	19.218
77	100	5.614	164	5500	0.258	0.21776	3447.85	148.38	23.237
78	100	5.614	164	2500	0.117	0.47907	7585.27	148.38	51.121
79	100	5.614	164	4000	0.188	0.29942	4740.80	148.38	31.950
80	100	5.614	169	30000	1.406	0.03992	632.11	136.63	4.626
81	100	5.614	164	27630	1.295	0.04335	686.33	148.38	4.625
82	100	5.614	164	2500	0.117	0.47907	7585.27	148.38	51.121

Chapter 3

Selective Laser Sintering: Numerical Modeling of Porosity and Crystallization Effects

Abstract

Selective Laser Sintering (SLS) is a widely used additive manufacturing process involving specially developed polymer powders that are selectively fused using a laser beam to create a solid three-dimensional (3D) object. However, the properties of the final product are highly dependent on the processing conditions, including the temperature history and the type of polymer powder used. In this context, numerical modeling has emerged as a valuable tool for predicting the effects of various processing parameters on the final product. This study presents a numerical model to explore the impact of initial porosity, crystallization, and melting on SLS-produced products' accuracy and mechanical properties. A porosity-induced shrinkage model and a combined crystallization and melting kinetics model are introduced. The effectiveness of these models is demonstrated through finite element simulations in two case studies. The first use case models the effect of initial porosity on shrinkage and accuracy of PA12 parts. In contrast, the second use case quantifies the impact of microstructural changes on the yield stress characteristics of PA12 parts. The results of this work can be used to evaluate and predict the quality of SLS-produced products, which is crucial for optimizing the manufacturing process and ensuring high-quality products.

3.1 Introduction

Selective Laser Sintering (SLS) is a widely used additive manufacturing process that has gained significant attention due to its ability to produce complex, high-quality products with high accuracy and mechanical strength. The process involves using specially developed polymer powders, most commonly polyamide-based, selectively fused using a laser beam to create

a solid three-dimensional (3D) object. However, the properties of the final product are highly dependent on the processing conditions, including the temperature history and the type of polymer powder used.

Several studies have investigated the effect of structural properties on the mechanical properties of semi-crystalline polymers like polyethylene (PE) [80–82], polypropylene (PP) [83, 84], and polyamides (PA) [17, 85, 86]. Investigating these structure-property relations in combination with processing is crucial for evaluating and predicting part quality.

In this context, numerical modeling has emerged as a useful tool for predicting the effects of various processing parameters on the final product. Many studies have been carried out to investigate the effects of material and powder properties on SLS-produced products. Mechanical properties are related to energy density and energy melt ratio formulations (see e.g. [48, 50, 53, 62, 76, 77]). The impact of the powder layer properties on the optical properties of the material is discussed by Schmid [19], and Heinl et al. [87] studied the influence of the laser scanning strategy on the mechanical properties of SLS-produced products.

This work provides a numerical model to investigate the effects of initial porosity, crystallization, and melting on SLS-produced products' accuracy and mechanical properties. The model is an extension and modification of a previously developed numerical model for SLS as presented in the work of Balemans [15]. Models for porosity-induced shrinkage and newly developed kinetics models for crystallization and melting will be given. The effectiveness of these models is demonstrated through two case studies. In the first use case, the goal is to model the effect of initial porosity on the shrinkage behavior of PA12 powder and to determine their combined impact on the accuracy of parts produced with SLS. Secondly, in use case two, the yield kinetics of a simple 2D product made out of PA12 will be used to quantify the effect of microstructural changes on the yield stress characteristics of PA12 parts. In the latter, the lamellar thickness is related to modified Ree-Eyring equations [88], as presented in the works of Van Erp et al. [83], Caelers et al. [84], and Parodi et al. [85, 86].

Section 3.2 explains the model and the material parameters of PA12 used in the numerical simulations. The experimental methods necessary to find some of the required material properties are shown in Section 3.3. The linkage of the lamellar thickness to the yield kinetics via the rate constants and the modified Ree-Eyring Equation is herein discussed. Section 3.4 explains the numerical method to solve the general equations with finite element simulations. Subsequently, Section 3.5 demonstrates the here extended and modified numerical model based on the two use cases. In the final section, conclusions and recommendations are formulated.

3.2   Problem description

A 2D geometry is generated within the simulation domain Ω shown in Figure 3.1a to model the SLS sintering process. The domain is sliced into layers with constant height. To build a geometry, the domain is translated, and a layer is added as described in the study of Balemans et al. [15] (see Figure 3.1b). A mesh that consists of $n_x = 200$ mesh elements in the x-direction and $n_y = 2$ elements in the y-direction is generated for each layer.

A laser scans selectively parts of each layer to produce a product with SLS. To determine which parts of the domain must be scanned, an image of a 2D part is converted to binary format. Subsequently, this image is projected on the domain mesh to determine the scan

(a) Simulation domain   **(b)** Layer addition
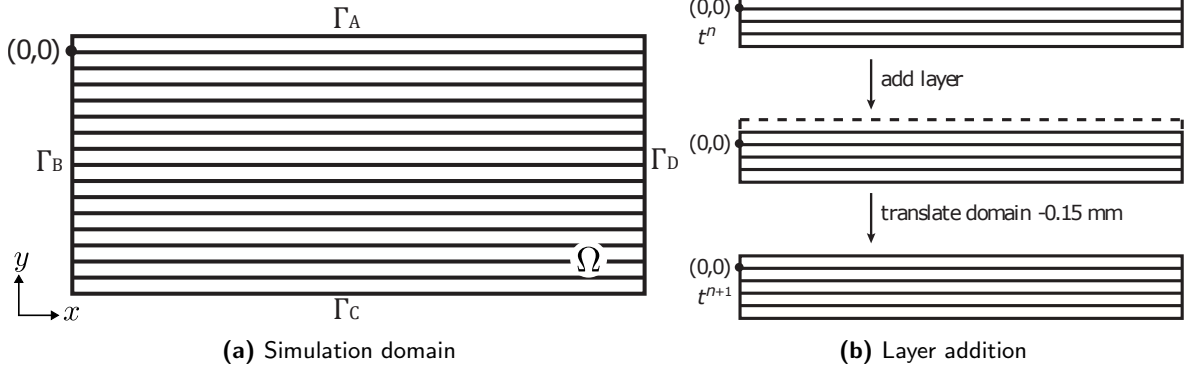
Figure 3.1: Schematic drawing of the simulation domain and the procedure of adding layers [15].

path. The laser is turned on at the image's black (1) regions and off at the white (0) regions. In this work, two use cases of printing a 30 x 1.5 mm rectangular product are studied, shown in green in Figure 3.2. Here, the domain has a width of $l_x = 50$ mm. The rectangular part is sliced into ten layers by selecting a layer height of $l_y = 150$ µm. Before printing, ten warming layers are put below the part, and six cooling layers are deposited after the last scan. This results in a total of twenty-six layers and a final domain height of 3.94 mm. In use case one, the effect of accuracy is studied by modeling the porosity-induced shrinkage in SLS. In use case two, the effect of crystallization and melting on the yield stress of parts processed by SLS is discussed. Simulation results of printing a more complex geometry, the TU/e logo, are also presented in the second use case.
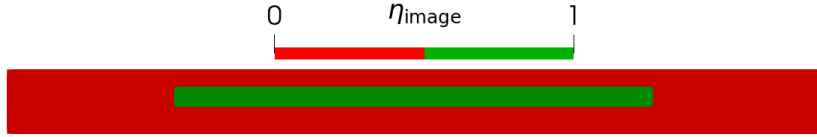
Figure 3.2: The position of the rectangular product (30 x 1.5 mm) in the simulation domain generated from a binary image. Ten warming layers are deposited in green before the scanning of the product, and six cooling layers are deposited after the last scan.

3.2.1   Balance equation

To describe the sintering process in SLS, Balemans et al. [15] concluded that the flow of particles could be neglected and that only temperature history is required to describe the crystallization kinetics on timescales relevant to the SLS process. Therefore, in both use cases, flow is neglected, and the energy balance is given by:

$$\rho c_p \frac{\partial T}{\partial t} = \nabla \cdot (K \cdot \nabla T) + \rho \chi_\infty \Delta H \frac{\partial \xi}{\partial t} + Q(x, y, t) \quad \text{in } \Omega, \tag{3.1}$$

with T the temperature, ρ the density, K the thermal conductivity, ξ the total space-filling, ΔH the crystallization enthalphy and χ_∞ the final crystallinity of the polymer. The volumetric heat source following laser irradiation is given by:

$$Q(x, y, t) = \alpha(1 - \mathcal{R}) \frac{P}{\sqrt{\pi W^2/2}} \exp\left(-2\frac{(x - x_b - vt)^2}{W^2}\right) \exp\left(-\alpha(y_{\Gamma_A} - y)\right). \tag{3.2}$$

Here, α is the absorption coefficient, $\mathcal{R}$ the surface reflectively, x_b the x-coordinate of the center of the beam, W the beam radius, v the laser scan velocity, t the time, P the effective laser power, defined per unit length, and $y_{\Gamma_A} - y$ the depth of penetration with respect to the scan boundary Γ_A, with $y_{\Gamma_A} = l_y$.

The effective laser power is given by $P = \eta_{\text{image}} P_0$, where P_0 is the laser power, defined per unit length, and η_{image} a value between 0 (off) to 1 (on) following from the binary image that determines the geometry of the part and scan path (see Figure 3.2). The density, specific heat capacity, and thermal conductivity are treated as temperature- and porosity-dependent material properties depicted in Figure 3.3a-3.3c.

(a) Density

(b) Specific heat capacity

(c) Thermal conductivity

(d) Transmission and attenuation coefficient
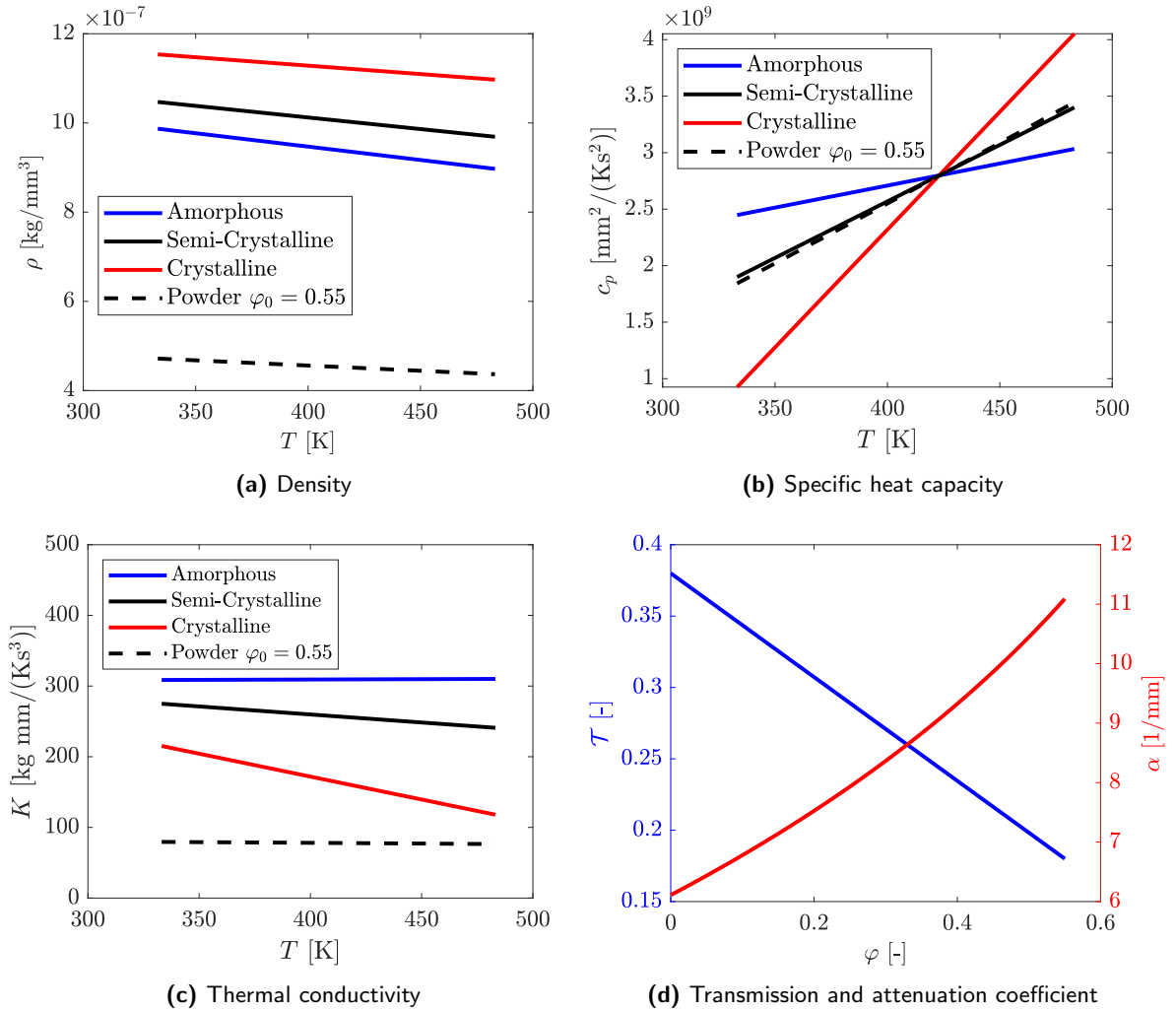
Figure 3.3: Thermo-physical properties of PA12 used to solve the energy balance. In a) density, b) specific heat capacity, and c) thermal conductivity are shown as functions of the temperature, crystallinity, and porosity, while in d) the transmission and attenuation are modeled as solely porosity-dependent.

The effective density and specific heat capacity are calculated using the mixing law that depends on the porosity φ (i.e., gas fraction) and the crystallized volume fraction χ of the semi-crystalline polymer. An empirical correlation based on the exact Maxwell model is used for effective thermal conductivity. This model offers the possibility of calibrating the predicted

values by the particle geometric factor d, which is related to the shape of the powder particles. Hence, the thermo-physical relations are given by [89–92]:

$$
\begin{aligned}
\rho &= (1 - \varphi)[\chi\rho_s + (1 - \chi)\rho_l] + \varphi\rho_{\mathrm{gas}} \\
c_p &= [(1 - \varphi)[\chi\rho_s c_{p,s} + (1 - \chi)\rho_l c_{p,l}] + \varphi\rho_{\mathrm{gas}} c_{p,\mathrm{gas}}]/\rho \\
K &= K_{\mathrm{gas}}[1 + \vartheta(d - 1)(1 - \varphi)]/[1 - \vartheta(1 - \varphi)],
\end{aligned}
\tag{3.3}
$$

with $\vartheta = [K_p - K_{\mathrm{gas}}]/[K_p + (d-1)K_{\mathrm{gas}}]$ and $K_p = \chi K_s + (1-\chi)K_l$. The crystallized volume fraction is found from the space-filling ξ according to $\chi = \chi_\infty\xi$. The subscripts s, l, and gas indicate the crystal, amorphous, and gas phases, respectively. For example, if the space-filling after melting is zero, this results in only a (liquid) amorphous phase. To model the temperature dependence, the crystal and amorphous phases of a thermo-physical property $\mathcal{X}$ are assumed to depend linearly on the temperature, following:

$$
\mathcal{X}_i = \mathcal{X}_{i,0} + \mathcal{X}_{i,1}(T - 273.15) \quad \text{for } i = s, l.
\tag{3.4}
$$

In the energy balance equation, the absorption coefficient is modeled as a function of the effective transmission coefficient of a layer. This relation reads [93]:

$$
\alpha = \ln\left(\mathcal{T}/(1 - \mathcal{R})\right)/l_y,
\tag{3.5}
$$

where $\mathcal{T}$ is the effective transmission coefficient. The effective transmission coefficient depends on the material state and the porosity. In this work, the following mixing rule is proposed to model the effect of porosity on the effective transmission coefficient of a powder-based material:

$$
\mathcal{T} = (1 - \varphi/\varphi_{\mathrm{powder}})\mathcal{T}_p + (\varphi/\varphi_{\mathrm{powder}})\mathcal{T}_{\mathrm{powder}},
\tag{3.6}
$$

where $\varphi_{\mathrm{powder}}$ is the porosity of the powder used in the optical experiment, $\mathcal{T}_{\mathrm{powder}}$ the transmission coefficient of this powder, and $\mathcal{T}_p$ the transmission coefficient of the solid polymer (no pores). This equation is based on the work of Heinl et al. [87], where an increase in transmission is seen after melting and crystallizing the powder. This indicates that the reduction in scattering results in a larger beam penetration. However, no information about thickness reduction is given, which could also explain the transmission change [87]. There is only a small scattering effect from crystals with respect to the amorphous phase; a 4% difference between molten state and crystallized solid in the work of Heinl et al. [87]. Therefore, this is neglected in the model. The resulting attenuation and transmission, as a function of porosity, is shown in Figure 3.3d. The values for the parameters linked to the thermo-physical and optical properties of the energy balance are listed in Table 3.1.

3.2.2   Coalescence and porosity evolution

Above the onset of melting temperature, the particles in contact tend to form interfaces and to decrease their total area by surface forces [101]. This phenomenon is called coalescence. The time evolution of the coalescence radius has been modeled by Pokluda et al. [102], and the resulting coalescence angle θ follows the relation:

$$
\frac{\mathrm{d}\theta}{\mathrm{d}t} = \frac{\gamma}{2^{5/3}\eta r_0} \frac{\cos\theta \sin\theta (2 - \cos\theta)^{1/3}}{(1 - \cos\theta)(1 + \cos\theta)^{1/3}} \quad \text{for } \varphi \geq 0.06.
\tag{3.7}
$$

Here, η is the viscosity, r_0 is the particle radius, and γ is the surface tension. Initially, a coalescence angle θ_0 is used, and the angle cannot become larger than $\pi/2$. Due to coalescence, the porosity decreases, and pores can be fully closed. However, the densification mechanism becomes different at porosity lower than 0.06. The time evolution of porosity is then determined by air diffusion (disappearance of air bubbles). Therefore, the coalescence angle does

Table 3.1: Thermo-physical, laser, and optical parameters of PA12 used in the energy balance.

Parameter	Symbol	Value	Reference
Density constant of crystal phase	$\rho_{s,0}$	1176 kg/m^3	[91, 94, 95]
Density slope of crystal phase	$\rho_{s,1}$	-0.378 kg/(Km^3)	[91, 94, 95]
Density constant of amorphous phase	$\rho_{l,0}$	1023 kg/m^3	[91, 94, 95]
Density slope of amorphous phase	$\rho_{l,1}$	-0.6 kg/(Km^3)	[91, 94, 95]
Density of air	ρ_{gas}	1.0 kg/(m^3)	[91, 96, 97]
Specific heat capacity constant of crystal phase	$c_{p,s,0}$	-325 J/(Kkg)	[91, 94, 95]
Specific heat capacity slope of crystal phase	$c_{p,s,1}$	20.8 J/(K^{2}kg)	[91, 94, 95]
Specific heat capacity constant of amorphous phase	$c_{p,l,0}$	221.4 J/(Kkg)	[91, 94, 95]
Specific heat capacity slope of amorphous phase	$c_{p,l,1}$	3.9 J/(K^{2}kg)	[91, 94, 95]
Specific heat capacity of air	$c_{p,\mathrm{gas}}$	1049 J/(Kkg)	[91, 96]
Thermal conductivity constant of crystal phase	$K_{s,0}$	0.254 W/(Km)	[91, 98]
Thermal conductivity slope of crystal phase	$K_{s,1}$	-6.5·10^{-4} W/(K^{2}m)	[91, 98]
Thermal conductivity constant of amorphous phase	$K_{l,0}$	0.308 W/(Km)	[91, 98]
Thermal conductivity slope of amorphous phase	$K_{l,1}$	1·10^{-5} W/(K^{2}m)	[98]
Thermal conductivity of air	K_{gas}	0.033 W/(Km)	[91, 96, 97]
Particle geometric factor	d	3	[91]
Maximum crystallinity	χ_∞	0.36	[99]
Heat of fusion	ΔH	53.2·10^3 J/kg	[15]
Laser beam radius	W	125 µm	
Laser scan velocity	v	0.5 m/s	
Laser power*	P_0	5.5·10^3 to 40·10^3 W/m	
Porosity of powder in optical experiment	$\varphi_{\mathrm{powder}}$	0.55	[100]
Transmittance of powder**	$\mathcal{T}_{\mathrm{powder}}$	0.18	[87]
Transmittance of solid ($\varphi = 0$)	$\mathcal{T}_p$	0.38	[87]
Surface reflectivity	$\mathcal{R}$	0.05	[87]

* depends on the use case

** for a layer thickness of $l_{y,0} = 150$ µm

not change, $d\theta/dt = 0$, for $\varphi < 0.06$. Correspondingly, the relation of porosity with the neck growth evolution is found by [103]:

$$\varphi = 1 - \frac{1 - \varphi_0}{[1 - (\sin(\theta)/2)^2]^3} \quad \text{for } \varphi \geq 0.06,$$
$$\frac{d\varphi}{dt} = -\frac{3\gamma}{2r_0\eta}\varphi \qquad \text{for } \varphi < 0.06. \tag{3.8}$$

To prevent numerical difficulties, the porosity cannot drop below 10^{-8}. Besides, the evolution of coalescence angle and porosity are only calculated for material that has undergone melting (i.e., $T \geq T_{m,\text{onset}}$). The temperature corresponding to the onset of melting is modeled as follows:

$$T_{m,\text{onset}} = T_m - \Delta T_{m,1/2}. \tag{3.9}$$

Here, T_m is the peak melting temperature, $\Delta T_{m,1/2}$ the half-width of the melting region in DSC measurements, and $T_{m,\text{onset}}(l_c)$ the onset of melting.

Childs and Tontowi [104] proposed that the ratio $\frac{\gamma}{r_0\eta}$ in Equation (3.7) and (3.8) should be multiplied by a temperature shift factor a_T and a crystallization shift factor a_ξ to take the effects of temperature and crystallization into account. Similar to multiplying the ratio $\frac{\gamma}{r_0\eta}$ with these shift factors, in this work, the viscosity is shifted with temperature and crystallization according to [15]:

$$\eta = \eta_0 \exp\left(\frac{E_a}{R}\left(\frac{1}{T} - \frac{1}{T_{\text{ref}}}\right)\right) \exp(-\beta_\xi \xi^{n_\xi}), \tag{3.10}$$

where η_0 is the viscosity at the reference temperature T_{ref}, E_a is the activation energy, R the universal gas constant, $n_\xi = 1$ a power-law constant, and $\beta_\xi = -2.5$ a fit parameter to describe the effect of space-filling on viscosity. The surface tension is calculated from the mixing law such that:

$$\gamma = \chi\gamma_s + (1 - \chi)\gamma_l, \tag{3.11}$$

(a) Surface tension and viscosity

(b) Coalescence and porosity evolution
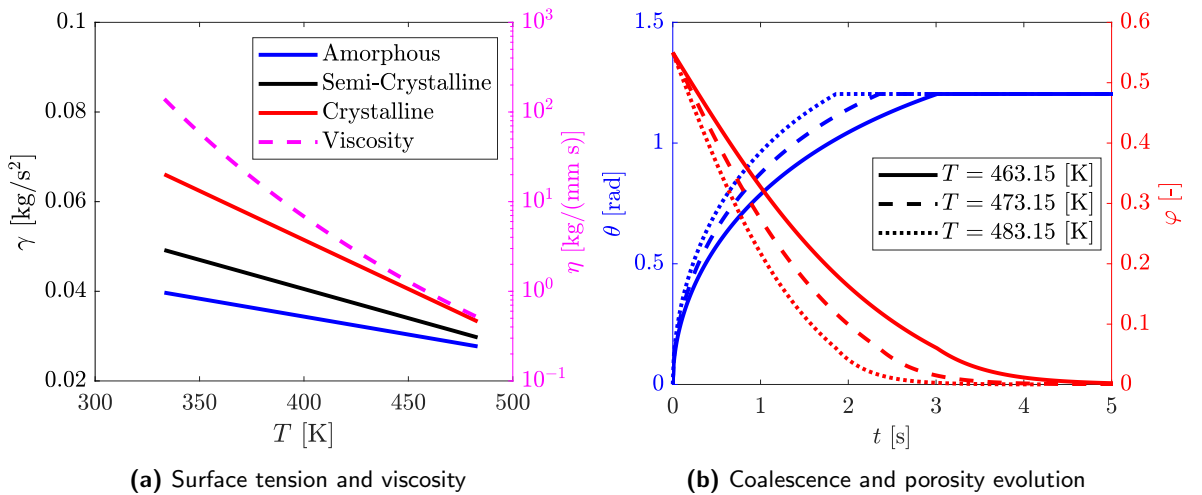
Figure 3.4: Thermo-physical properties related to coalescence and porosity evolution, and the effect thereon. In a) the surface tension and viscosity functions are visualized for PA12, and b) gives an example of coalescence and porosity evolution with $\varphi_0 = 0.55$.

where, again, the liquid and solid phases are linearly dependent on the temperature according to Equation (3.4), as shown in Figure 3.4a. Herein, also the temperature-dependent viscosity is visualized for $\xi = 0$. The coalescence and porosity evolution is modeled for temperatures above the melting point according to Equation (3.7) and (3.8). This evolution is shown in Figure 3.4b for the temperatures $T = 190$, 200, and 210 °C. Herein, increasing temperature results in a faster coalescence as both viscosity and surface tension decrease. Decreasing the initial porosity also leads to a reduction of the coalescence time. The values for the parameters linked to coalescence and porosity are listed in Table 3.2.

The evolution of porosity is directly related to the shrinkage of the part, as pores are filled with molten powder. In the first use case, this effect is considered by adjusting the vertical position of the mesh points so that volume is preserved as porosity decreases. The layer thickness after melting the initially unmolten layer becomes:

$$l_y = l_{y,0}\frac{1 - \varphi_0}{1 - \varphi},\qquad(3.12)$$

where $l_{y,0}$ is the layer thickness of the initially unmolten layer (see Table 3.2).

Table 3.2: Parameters used for the coalescence and porosity evolution of PA12.

Parameter	Symbol	Value	Reference
Initial coalescence angle	θ_0	0.001	
Initial porosity of powder bed*	φ_0	0.55	[100]
Initial layer thickness	$l_{y,0}$	150 μm	
Particle radius	r_0	30 μm	[29, 100]
Viscosity at reference temperature	η_0	400 Pa s	[15, 29]
Reference temperature	T_{ref}	493 K	[15, 29]
Activation energy	E_a	50 kJ/mol	[15, 29]
Exponent in space-filling shift factor	n_ξ	1	[15]
Pre-constant in space-filling shift factor	β_ξ	-2.5	[15]
Surface tension constant of crystal phase	$\gamma_{s,0}$	0.0792 kg/s^2	[105]
Surface tension slope of crystal phase	$\gamma_{s,1}$	$-2.2 \cdot 10^{-4}$ kg/(Ks^2)	[105]
Surface tension constant of amorphous phase	$\gamma_{l,0}$	0.0445 kg/s^2	[105]
Surface tension slope of amorphous phase	$\gamma_{l,1}$	$-8 \cdot 10^{-5}$ kg/(Ks^2)	[105]

* use case one: $\varphi_0 = (0.15 \ 0.35 \ 0.55 \ 0.75)$

3.2.3 Crystallization and melting kinetics

For quiescent isothermal conditions, the space-filling evolution during crystallization as a function of time and temperature can be described by the following equation based on the Avrami theory [106–108]:

$$\xi = 1 - \exp(-k_{\mathrm{crys}}(T)t_{\mathrm{crys}}^{n_a}).\qquad(3.13)$$

Herein, $k_{\mathrm{crys}}(T)$ is the crystallization rate, which is a function of temperature, t_{crys} the time from the start of crystallization, and n_a is the Avrami exponent that stands for the (homogeny or heterogenic) nucleation mode and dimensionality of crystal growth. More general nonisothermal models are required to capture nonconstant cooling rates, as in SLS. In use

case one, the crystallization model proposed by Balemans et al. [15] is used, wherein Schneider rate equations are solved to describe the crystallization kinetics of PA12. Besides, in use case one, the instant melting of crystals is assumed above T_m. For use case two, the crystallization model developed by Nakamura [110, 111] is implemented, and a model for melting is developed. The nonisothermal space-filling evolution of crystallization is given by:

$$\xi = 1 - \exp\left(-\left(\int_0^{t_{\text{crys}}} K_{\text{crys}}(T)\mathrm{d}\tau\right)^{n_a}\right). \tag{3.14}$$

where n_a equals to the Avrami exponent and $K_{\text{crys}}(T)$ is a modification of the isothermal crystallization rate parameter $k_{\text{crys}}(T)$. Mathematically, they are related as follows:

$$K_{\text{crys}}(T) = k_{\text{crys}}(T)^{\frac{1}{n_a}} = \ln(2)^{\frac{1}{n_a}} \left(\frac{1}{t_{1/2}}\right). \tag{3.15}$$

Here, $t_{1/2}$ denotes the temperature-dependent crystallization half time, which is the time taken for half of the crystallization to take place in the case that the crystallization was to be isothermal [112]. Hoffman-Lauritzen's theory assumes that $1/t_{1/2}$ is proportional to the growth rate G. Here, the additional assumptions are made that the number of heterogeneous nuclei is independent of temperature and that all nucleation sites activate simultaneously. In this way, the crystallization half-time can be expressed as [112, 113]:

$$\left(\frac{1}{t_{1/2}}\right) = K_0 \exp\left(-\frac{U^*}{R(T - T_\infty)}\right) \exp\left(-\frac{K_G}{T(T_m^{\text{eq}} - T)f}\right) \quad \text{with} \quad f = \frac{2T}{T_m^{\text{eq}} + T}, \tag{3.16}$$

where U^* is the activation energy for crystallization, and T_∞ is the temperature limit below which the crystallization process is terminated, which can be calculated as $T_\infty = T_g - 30$. Here, T_g is the glass transition temperature, K_0 the growth rate constant, K_G the nucleation rate constant, and T_m^{eq} the equilibrium melting temperature. The factor f is a correction for

(a) Isothermal crystallization

(b) Nonisothermal crystallization
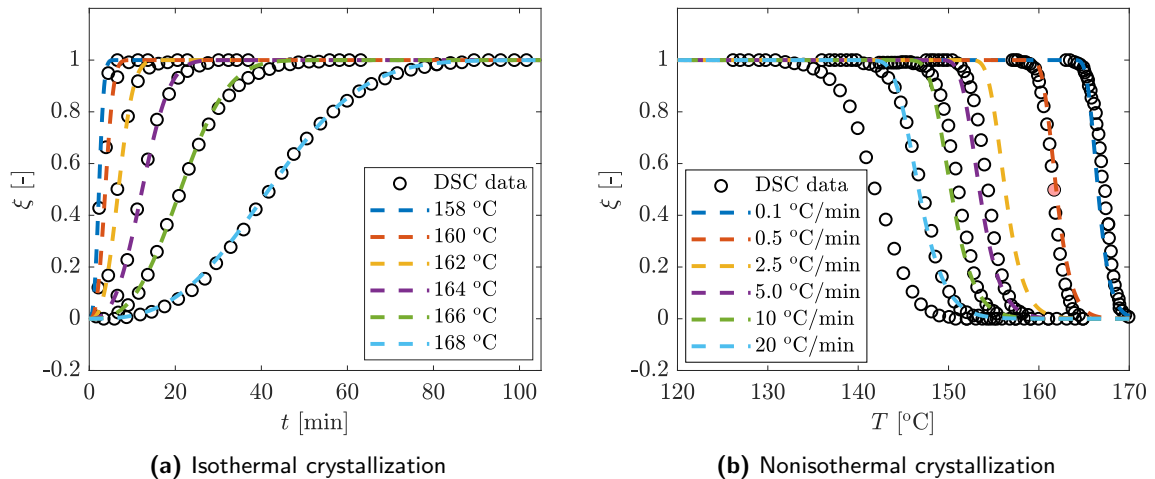
Figure 3.5: Space-filling evolution of PA2200, extracted from DSC measurements by Neugebauer et al. [109] (markers), and the results of the crystallization model for a) isothermal and b) nonisothermal crystallization (dotted lines).

Table 3.3: Parameters used for the crystallization kinetics of PA12.

Parameter	Symbol	Value	Reference
Equilibrium melting temperature	T_m^{eq}	500 K	[16, 114, 115]
Activation energy for crystallization	U^*	6270 J/mol	[109]
Growth rate constant	K_0	$4.089 \cdot 10^{11}$ $1/s$	
Nucleation rate constant	K_G	$7.089 \cdot 10^5$ K^2	
Glass transition temperature	T_g	333 K	[109]
Avrami exponent	n_a	2.82	[109]

the decrease in latent heat of fusion with decreasing temperature [112]. Since crystallization can only occur below T_m^{eq} and above T_∞, $K_{\text{crys}}(T)$ is set to zero elsewhere.

The isothermal and nonisothermal crystallization kinetics of PA12 and the model predictions are given in Figure 3.5. These kinetics are derived from DSC data of PA2200 from Neugebauer et al. [109] by fitting and using $T_m^{\text{eq}} = 500$ K as explained in Appendix 3.A.1. The resulting parameters used for the crystallization kinetics of PA12 are listed in Table 3.3

The dependence of melting temperature on isothermal crystallization temperature T_c follows from combining Gibbs-Thomson equation and Lauritz-Hoffman theory, as proposed by Hoffman and Weeks [116–119]. Herein, the depression from T_m^{eq} of the melting point of a crystalline polymer of high molecular weight has been attributed generally to imperfections in the crystals. Based on the assumption that the main reason for the depression is the high surface-to-volume ratio, which is caused by the lamellar structure, the relation between the melting point depression, $T_m^{\text{eq}} - T_m$, and the thickness, l_c, follows the thermodynamic formula [116, 117]:

$$T_m(l_c) = T_m^{\text{eq}} \left[1 - \frac{2\sigma_e}{\Delta h_f l_c} \right]. \tag{3.17}$$

with σ_e the surface free energy, Δh_f the enthalpy of fusion. Note that this implies that the onset of melting in Equation (3.9) depends on the lamellar thickness. The melting point depression can be rewritten by using the Hoffman–Weeks method to relate T_c and T_m [118]:

$$T_c = T_m \gamma_c + T_m^{\text{eq}}(1 - \gamma_c), \tag{3.18}$$

with γ_c the thickening coefficient, which relates the lamellar thickness to the initial lamellar thickness $l_c = \gamma_c l_{c,\text{ini}}$. Resulting in an expression for lamellar thickness as a function of isothermal crystallization temperature T_c:

$$l_c = \frac{2\gamma_c \sigma_e T_m^{\text{eq}}}{\Delta h_f (T_m^{\text{eq}} - T_c)}. \tag{3.19}$$

The modeled lamellar thickness function for PA12 parameters is shown in Figure 3.6. Lamellar thickness measurements of PA12 are given in Plummer et al. [114], Paolucci et al. [16], and Verkinderen et al. [115], and $T_m^{\text{eq}} = 500K$ is used following the ATHANS value for PA12 [120, 121], as this resulted in the best fit. Note that the previously mentioned relations with lamellar thickness, crystallization, and melting temperature are only used in use case two.

In use case two, an exponential reduction of space-filling is proposed to model the melting of the crystalline phase, opposite to the exponential increase in space-filling during crystal-
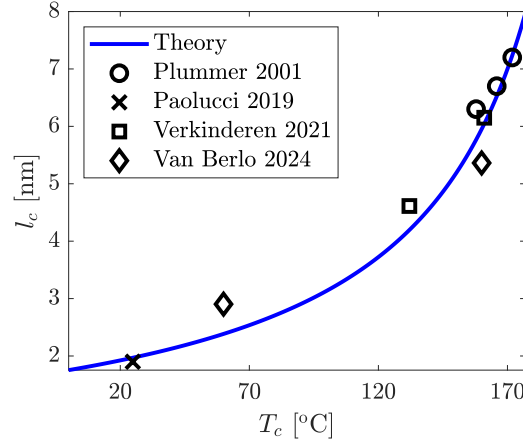
Figure 3.6: Lamellar thicknesses as a function of crystallization temperature for PA12. The Lauritz-Hoffman theory prediction is fitted on the data from Plummer et al. [114], Paolucci et al. [16], and Verkinderen et al. [115]. This study has yielded two measured lamellar thicknesses, which have been added for comparison .

lization. Mathematically, this decrease in space-filling is modeled as follows:

$$\xi = \exp\left(-\left(\int_0^{t_{\text{melt}}} K_{\text{melt}}(T)d\tau\right)^{n_a}\right), \tag{3.20}$$

where $K_{\text{melt}}(T)$ is the melting rate parameter, t_{melt} is the time from the start of melting, and n_a is equal to the Avrami exponent. DSC measurements in Figure 3.7 show that the melting of PA2200 is not instantaneous and that the melting temperature increases with increasing crystallization temperature [122].

(a) DSC curves for melting PA2200 [122]

(b) Space-filling evolution for melting PA2200
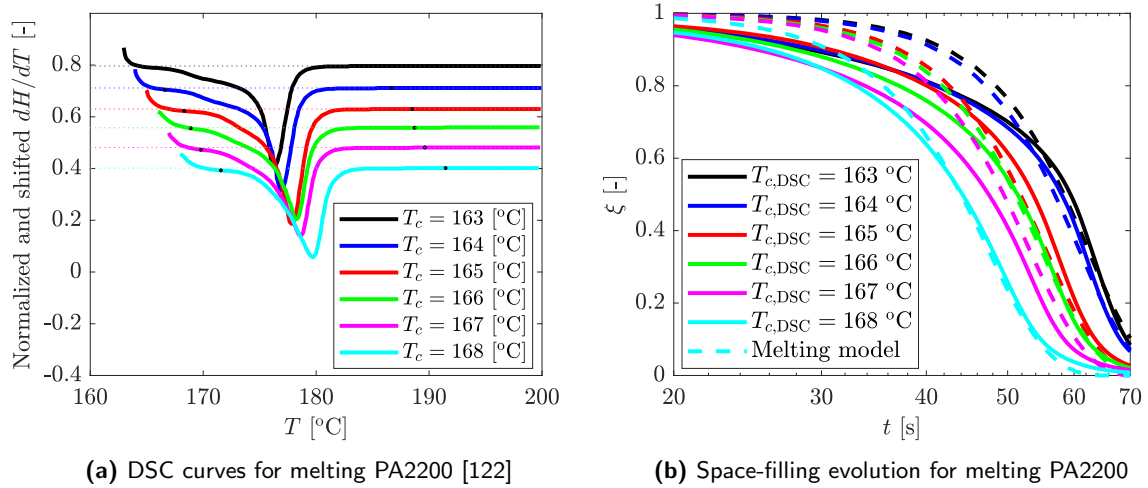
Figure 3.7: DSC curves of PA2200 for a heating rate of 10 K/min at isothermal crystallization temperatures ranging from 163 to 168 °C. Space-filling evolution is extracted from the DSC curves in a), and in b) these experimental results (solid lines) are compared to the melting model prediction (dashed lines).

To capture the effects of noninstantaneous melting and this shift in melting peak with lamellar thickness (i.e., isothermal crystallization temperature), it is assumed that melting rate $K_{\mathrm{melt}}(T)$ can be described by the logistic function:

$$K_{\mathrm{melt}}(T) = \frac{K_{\mathrm{melt,max}}(T)}{1 + \exp[-S(T - T_m(l_c))]}, \tag{3.21}$$

where $K_{\mathrm{melt,max}}(T)$ is a temperature-dependent maximum melting rate, $T_m(l_c)$ the lamellar thickness-dependent melting temperature, S the parameter determining the steepness of the transition from zero to $K_{\mathrm{melt,max}}$.

The melting kinetics accelerate at higher temperatures because of the increased mobility of the chains. Therefore, a temperature-dependent $K_{\mathrm{melt,max}}(T)$ is proposed that follows an exponential increase with temperature:

$$K_{\mathrm{melt,max}}(T) = K_{\mathrm{melt,max,0}} \exp\left(K_{\mathrm{melt,max,1}}T\right). \tag{3.22}$$

Here, $K_{\mathrm{melt,max,0}}$ is the exponential constant, and $K_{\mathrm{melt,max,1}}$ the exponential growth factor.

To provide more insight into the effects of the crystallization and melting model on the space-filling evolution, the above-given relations for $K_{\mathrm{crys}}(T)$ and $K_{\mathrm{melt}}(T)$ are shown in Figure 3.8a for PA12. At large under cooling, $T < 160\,°C$, the rate constant K_{crys} is dominant and space-filling increases due to crystallization. At small undercooling, $T > 160$, lamellar structures are molten following the rate constant K_{melt}. The lamellar thickness determines the melting temperature; hence, a positive shift in temperature is seen with increasing lamellar thickness. At large temperatures $T > T_m + \Delta T_{m,1/2}$, the melting kinetics accelerate, and the effect of lamellar thickness is rendered obsolete.

Figure 3.8a shows an overlap region between crystallization and melting for all lamellar thickness functions. Here, relatively large lamellar structures are formed during crystallization, and small lamellar structures are melting simultaneously. This results in a gradual

(a) Rate constants for crystallization and melting   (b) Melting temperature shift with lamellar thickness
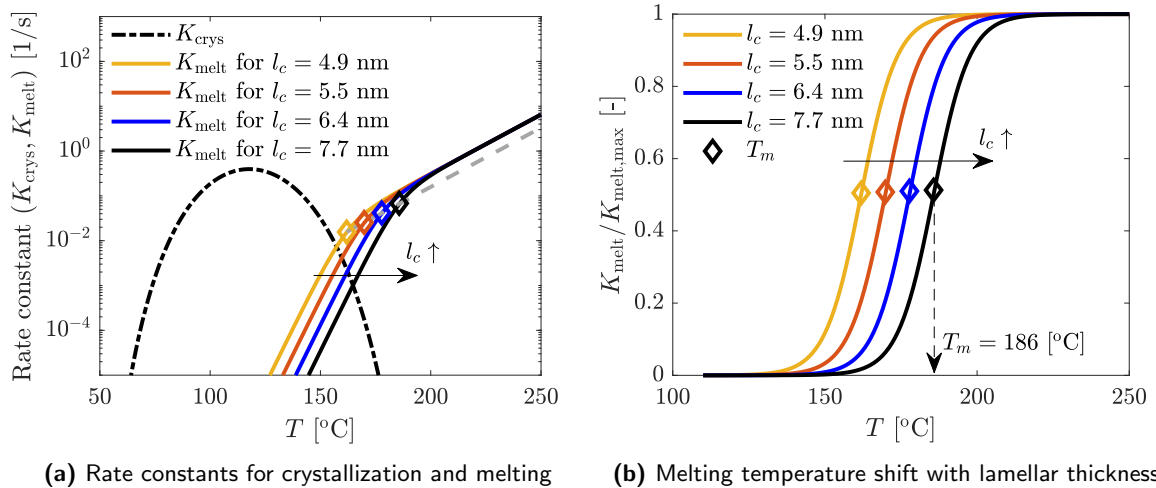
Figure 3.8: Rate constants for crystallization K_{crys} and melting K_{melt}, and the effect of lamellar thickness on the melting temperature. In a) the melting kinetics shift with lamellar thickness, and increasing temperature accelerates the melting kinetics. Suppressing the temperature effects of T_m (grey dashed line), b) shows the smooth transition of melting, where T_m is positioned at the center of the transition and shifts with the lamellar thickness l_c.

increase in average lamellar thickness and a positive shift of T_m. In the case of a space-filling of one, this phenomenon results in crystal perfection, following the increase of the average lamellar thickness in the spherulites.

In Figure 3.8b, the temperature-induced accelerated melting is disregarded by dividing K_{melt} with $K_{\text{melt,max}}$. This results in the sigmoidal function in Equation (3.21), representing the smooth melting transition. The markers represent T_m at half the transition, which shifts with lamellar thickness. So, the melting process is hypothesized to follow a smooth melting transition, which shifts with lamellar thickness, while increasing temperature accelerates melting kinetics. In addition, the effect of heating rate $\mathrm{d}T/\mathrm{d}t$ on the melting temperature of polymers can be introduced following the scaling $\Delta T_m \cong \tau_c \mathrm{d}T/\mathrm{d}t \propto (\mathrm{d}T/\mathrm{d}t)^{1-x}$ as proposed by Toda et al. [123], with τ_c the characteristic time and the power $x < 1$ for iPP and LLDPE. Additionally, Toda et al. [123] elaborate on a physical derivation wherein both lamellar thickness and heating rate are included by assuming a two-dimensional nucleation-controlled transition. However, this results in a T_m-independent heating rate with $T_m \propto l_c$ [123]. Therefore, although experimentally observed for PA2200 by Laumer et al. [124], the heating rate effects on T_m are not included in this work.

The model assumes that lamellae melt from small to large thicknesses. However, while heating powder particles, a temperature gradient exists from the outside to the inside of the particle. It has been shown by Moeskops et al. [125] that kernels of powder particles can remain while the outer shell of the particle melts and then crystallizes into spherulites. Hence, this changes the melting sequence and the distribution of the lamellar thickness within a particle. To avoid this complexity, in use case two, relatively high laser powers that far exceed the melting temperature of the powder are used, such that particles are fully molten. Nevertheless, the results presented in terms of lamellar thickness and corresponding yield stress are indications of structure formation and intrinsic material properties, disregarding geometrical effects on the temperature field of particles. The parameters used to study the melting kinetics of PA12 are listed in Table 3.4.

Table 3.4: Parameters for lamellar thickness and melting rate model for PA12.

Parameter	Symbol	Value	Reference
Lamellar thickening coefficient	γ_c	1.26	[122]
Enthalpy of fusion	Δh_f	$2.17 \cdot 10^8$ J/m^3	
Surface free energy	σ_e	0.0686 J/m^2	
Half width of the melting region	$\Delta T_{m,1/2}$	10 K	[122]
Maximum melting rate constant	$K_{\text{melt,max,0}}$	10^{-13} 1/s	
Maximum melting rate growth factor	$K_{\text{melt,max,1}}$	0.0608 1/K	
Steepness of transition melting rate	S	0.17 1/K	

3.2.4 Boundary- and initial conditions

In the first use case, the laser power values of 5.5, 8.25, 11, and 13.75 W/mm are used to study the effect of shrinkage. However, in the second use case, relatively large laser power values up to 40 W/mm are applied, respectively. On each boundary Γ_i of the simulated powder bed shown in Figure 3.1a, it is assumed that the powder loses heat due to convection and radiation according to:

$$-K\nabla T \cdot \boldsymbol{n} = h(T - T_{\text{amb}}) + \sigma_B \epsilon (T^4 - T_{\text{amb}}^4) \text{ on } \Gamma_i, \qquad (3.23)$$
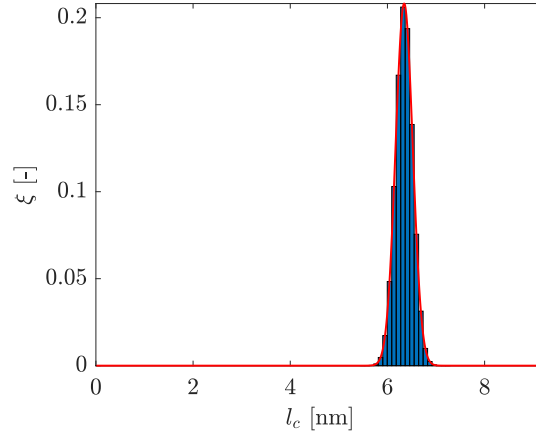
Figure 3.9: Initial distribution and discretization of the lamellar thickness of PA12 powder used in the simulations. The mean lamellar thickness $\bar{l}_{c,0}$ follows from X-ray measurements in Appendix 3.A.2.

with $i =$ A, B, C, and D. Here, $\boldsymbol{n}$ is the outward directed surface normal vector, h the convective heat transfer coefficient, T_{amb} the ambient temperature, $\sigma_B = 5.67 \cdot 10^{-8}$ W/(m^{2}K^4) the Stefan-Boltzmann constant and ϵ the surface emissivity. At the top side of the powder bed, Γ_A, the ambient temperature, convective heat transfer, and emissivity are given by $T_{\mathrm{amb,top}}$, h_{top} and ϵ_{top}. On the remaining side boundaries, Γ_{B-D}, $T_{\mathrm{amb,side}}$, h_{side} and ϵ_{side} are used. Each deposited powder layer has an initial temperature of $T_0 = 435.0$ K. For the coupling of heat transfer between individual layers, a constraint is used wherein:

$$[\nabla T \cdot \boldsymbol{n}]_j = [\nabla T \cdot \boldsymbol{n}]_{j+1}, \tag{3.24}$$

with j the layer number.

A spherulite contains lamellar structures with varying thicknesses. Therefore, the PA12 powder initially consists of a distribution of lamellar thicknesses. Figure 3.9 shows the modeled initial lamellar thickness distribution of PA12 powder. The initial lamellar thickness distribution of the powder is assumed to be Gaussian with the initial average lamellar thickness $\bar{l}_{c,0} = 6.34$ nm determined from X-ray measurements (Appendix 3.A.2) and the standard

Table 3.5: Input parameters used for initial and boundary conditions for PA12.

Parameter	Symbol	Value	Reference
Ambient temperature (top boundary)	$T_{\mathrm{amb,top}}$	435 K	
Convective heat transfer coefficient (top boundary)	h_{top}	2.4 kg/s^3	[126]
Emissivity (top boundary)	ϵ_{top}	0.95	[126]
Ambient temperature (side boundaries)	$T_{\mathrm{amb,side}}$	415 K	
Convective heat transfer coefficient (side boundaries)	h_{side}	200 kg/s^3	
Emissivity (side boundaries)	ϵ_{side}	0.0	
Initial temperature of deposited powder	T_0	435 K	
Average lamellar thickness of powder	$\bar{l}_{c,0}$	6.34 nm	
Standard deviation of lamellar thickness distribution	σ_G	0.18 nm	
Bin size in lamellar thickness distribution	m	108.4 bins/nm	
Maximum lamellar thickness	$l_{c,\mathrm{max}}$	9.23 nm	

deviation assumed to be $\sigma_G = 0.18$ nm. The initial average lamellar thickness of the powder corresponds to an initial peak melting temperature of $T_{m,0} = 177$ °C. The distribution is discretized by $m_{\text{bins/nm}} = 108.4$ bins/nm, from $l_c = 0$ to a maximum of six molecular unit cells in a single crystal $l_{c,\text{max}} = 6l_a = 9.23$ nm, using a molecular unit cell thickness of $l_a = 1.54$ nm [121]. This results in a total of $N_{\text{bins}} = 1000$ bins, where initially $\sim$230 bins (see Figure 3.9). The initial space-filling is set to one for numerical purposes, and the input parameters used for the initial- and boundary conditions are listed in Table 3.5.

3.3 Experimental

Experiments are performed to determine the effect of crystallization temperature on the microstructure and mechanical properties of PA12. For this purpose, mechanical testing and X-ray analysis results are combined, and corresponding procedures are described in this section.

3.3.1 Sample preparation and materials

The study uses a laser sintering grade of PA12 (type: PA2200, supplier: EOS GmbH). The PA12 powder is molten and pressed into 0.5 mm thick samples for mechanical testing and X-ray analysis. This is done with a Fontijne Holland (TP 400) hot press in a 200x200x0.5 mm mold with a constant pressure of 100 kN at 210 °C for 3 minutes. A PTFE sheet of 0.5 mm thick and a steel plate of 3 mm thick are positioned between the powder and the hot press. After pressing, crystallization at a controlled temperature is performed by transporting the mold to a cold press for 15 hours at either 60 or 160 °C. The PA12 plates are then stored and conditioned in a vacuum oven at 80 °C for 24 to 48 hours. ISO dogbone-shaped tensile specimens are punched from these plates and again held in the vacuum oven. Also, two virgin PA12 powder samples are manually compressed to 0.5 mm thick powder samples for the X-ray analysis of virgin powder.

3.3.2 Mechanical testing

Mechanical testing is performed within three days after punching the tensile specimen. A ZwickRoell Z010 testing machine with a 1 kN load cell performs uniaxial tensile tests. Tensile tests are performed at least twice per condition, with a range of strain rates from 10^{-2} up to 10^{-4} 1/s and testing temperatures of either 23 or 60 °C. After extraction from the oven, a tensile sample is conditioned for 15 minutes within the clamps of the tensile machine. A pre-load of 0.1 MPa is applied before testing.

To describe the yield kinetics of PA12, the modified Ree-Eyring equation is used [17, 88]. The modified Ree-Eyring equation consists of two distinct yield stress contributions relating to the two different deformation processes occurring in PA12: intra-lamellar (I) and inter-lamellar (II) deformation. Therefore, the yield stress follows from [88]:

$$\sigma_y = \sum_{i=I,II} \frac{k_b T}{V_i^*} \sinh^{-1}\left(\frac{\dot{\varepsilon}}{\dot{\varepsilon}_{0,i}} \exp\left(\frac{\Delta U_i}{RT}\right)\right), \qquad (3.25)$$

with $k_b = 1.38 \cdot 10^{-23}$ m²kg/(s²K) the Bolzmann constant, V_i^* the activation volume of deformation process i, ΔU_i the activation energy of deformation process i, T the temperature

and $\dot{\varepsilon}$ the applied strain rate. For each of the rate constants, $\dot{\varepsilon}_{0,i}$, in this equation, an empirical relation can be derived based on the lamellar thickness. For iPP [83, 84], and PA6 [85, 86] a logarithmic relation was proposed:

$$\log_{10}(\dot{\varepsilon}_{0,i}(l_c)) = c_i \frac{l_c}{l_{c,0}} + d_i, \quad \text{for } i = I, II \tag{3.26}$$

wherein, $\dot{\varepsilon}_{0,I}(l_c)$ is related to the intra-lamellar deformation process and $\dot{\varepsilon}_{0,II}(l_c)$ to the inter-lamellar deformation process, and $l_{c,0}$ is the minimum lamellar thickness.

3.3.3 X-ray analysis

X-ray experiments are carried out at the University of Twente. The following set of experiments are performed to study ex-situ lamellae structure formation:

- 2D WAXD patterns are recorded with a Eiger2R_500K detector. The detector has a pixel size of 75 x 75 µm^2 and is approximately 67 mm from the sample. The acquisition time is 300 s.

- 2D SAXS patterns are also recorded with a Eiger2R_500K detector with a pixel size of 75 x 75 µm^2. A sample-to-director distance of approximately 497 mm is used. The acquisition time is 3600 s.

The wavelength in all experiments is $\lambda = 1.54$ Å. The size of the spot of the beam is approximately 0.5 mm.

3.4 Numerical methods

The governing equations, including the energy balance and crystallization and melting equations, with the appropriate boundary conditions and initial conditions, are solved using an in-house developed software package based on the finite element method [127]. A mesh is generated using the meshing routine in the TFEM software package [127]. For the 2D geometry, the domain is discretized using triangular P_1 elements for the temperature and crystallization. The heat balance and crystallization equations are solved using a direct solver [128]. To describe the discontinuity induced by the condition stating that the crystallization can only be solved if the temperature has reached the onset of melting $T > T_{m,\text{onset}}$, the integration points for the crystallization consist of vertices of an element only. In this way, the crystallization equations are solved node-for-node and fully decoupled.

3.4.1 Time discretization

The rectangular part is formed by first depositing ten warming layers. To reduce computation times, this is done instantly in one step. Subsequently, the part is printed layer-by-layer. This starts with a recoating cycle by modeling the instant addition of a layer and waiting for $t_{\text{addLayer}} = 5$ s using a time step of $\Delta t = 0.01$ s. Subsequently, $t_{\text{wait}} = 10$ s is waited before the part is scanned. The scanning takes $t_{\text{scan,tot}} = l_x/v = 0.1$ s and is defined as the required time to move with the laser over the entire length of a layer (with a scan velocity v). The time step is reduced to $\Delta t = 500$ µs for accurate temperature and space-filling calculations during scanning. After scanning the last layer of the product, again, $t_{\text{wait}} = 10$ s has waited

before a new layer is applied on top of the scanned layer, and the time step is increased back to $\Delta t = 0.01$ s. A total of 6 cooling layers are applied after the last scan layer to mimic actual cooling conditions in SLS. After the total of 26 layers is deposited, the part is cooled for 2000 seconds using a time step of $\Delta t_{\text{cool}} = 0.5$ s.

The numerical procedure for every time step is discussed step by step. First, the rectangular geometry is generated from an image by storing the field η_{image}. Initially, the temperature field is set to the desired bed temperature T_0, a porosity of φ_0 is assumed, and the total space-filling is set to $\xi_0 = 1$. From this, the initial thermo-physical properties (ρ_0, $c_{p,0}$ and K_0) and optical properties ($\mathcal{T}_0$ and α_0) are calculated. The space-filling is divided into bins following the Gaussian initial lamellar distribution. From this, the initial average lamellar thickness, $\bar{l}_{c,0}$, and initial melting temperatures, $T_{m,0}$ and $T_{m,\text{onset},0}$, are derived. The initial derivative of the degree of space-filling $\partial \xi / \partial t|_0$ is zero.

In the following time steps, first, the temperature T^n at t^n is computed from the temperature T^{n-1} at the previous time step t^{n-1} using a first-order time-stepping procedure. Herein, the previously determined thermo-physical and optical properties ρ^{n-1}, c_p^{n-1}, K^{n-1} and α^{n-1}, and the change is space-filling $(\partial \xi / \partial t)^{n-1}$ are used as input for solving the energy balance in Equation (3.1). Note that the position of the laser beam at time t^n is used, which is determined from $x_b^n = x_b^{n-1} + v \Delta t$. The boundary condition for convection and radiation heat loss is implemented using [15]:

$$-K \nabla T \cdot \boldsymbol{n} = h(T - T_{\text{amb}}) + \sigma_B \epsilon (T^2 + T_{\text{amb}}^2)(T + T_{\text{amb}})(T - T_{\text{amb}}). \qquad (3.27)$$

Subsequently, the previous onset of melting temperature T_s^{n-1} is compared with the current temperature T^n to evaluate if melting has occurred $T > T_{m,\text{onset}}$. This information is stored in the vector b_{melt}, where 0 is still in powder form, and 1 indicates that the powder has previously been molten. The current viscosity η^n and surface tension γ^n are found from the current temperature T^n and previous space-filling ξ^{n-1}. In case $b_{\text{melt}} > 0$, the coalescence angle θ^n and porosity φ^n are calculated using a first-order time derivative. The thermo-physical and optical properties at the current time step, ρ^n, c_p^n, K^n and α^n, are derived from T^n.

Finally, the crystallization and melting equations are solved to find the current space-filling ξ^n. For this, several steps are required, starting with rewriting the Nakamura model for crystallization in Equation 3.14 in differential form as shown by Patel and Spruiell [112]. A similar derivation is used to write a differential form of the space-filling reduction following melting in Equation 3.20. Each time step, the resulting space-filling changes follow from a combination of crystallization $(\partial \xi_{\text{crys}} / \partial t)^n$ and melting $(\partial \xi_{\text{melt}} / \partial t)^n$, which are solved from the previous total space-filling ξ^{n-1} using:

$$
\begin{aligned}
\left(\frac{\partial \xi_{\text{crys}}}{\partial t} \right)^n &= n_a K_{\text{crys}}^n (1 - \xi^{n-1})[-\ln(1 - \xi^{n-1})]^{\frac{n_a-1}{n_a}} \\
\left(\frac{\partial \xi_{\text{melt}}}{\partial t} \right)^n &= -n_a K_{\text{melt}}^n \xi^{n-1}[-\ln(\xi^{n-1})]^{\frac{n_a-1}{n_a}} .
\end{aligned}
\qquad (3.28)
$$

As described in Section 3.2.4, a lamellar thickness distribution is utilized, where each bin i contains a space-filling ξ_i and lamellar thickness $l_{c,i}$. The current melting rate K_{melt}^n is a function of the lamellar thickness, which implies that the previous equations should be solved per bin (i.e., using ξ_i and $l_{c,i}$). However, solving the space-filling changes per bin is computationally expensive. Thus, the space-filling evolution is solved for each time step using only

the total space-filling ξ and the average lamellar thickness $\bar{l}_c$. The total space-filling is found from the distribution using $\xi = \sum_{i=1}^{N_{\text{bins}}} \xi_i$, with the number of bins $N_{\text{bins}} = l_{c,\text{max}} m_{\text{bins/nm}}$. Subsequently, the average lamellar thickness is derived using $\bar{l}_c = \frac{1}{\xi} \sum_{i=1}^{N_{\text{bins}}} \xi_i l_{c,i}$.

The powder is assumed to be completely molten if the total space-filling has dropped below a critical value of $\xi \leq 10^{-15}$. In this case, the distribution is completely emptied, and the total space-filling and the average lamellar thickness are set to zero ($\xi = 0$ and $\bar{l}_c = 0$). However, numerical issues arise when solving Equation (3.28) for $\xi^{\text{n}-1} = 0$ (and also for $\xi^{\text{n}-1} = 1$). Hence, in this equation, the total space-filling is limited to a minimum value of $\xi^{\text{n}-1} = \epsilon$ and a maximum value of $\xi^{\text{n}-1} = 1 - \epsilon$, with $\epsilon = 10^{-12}$.

The current crystallization rate $K_{\text{crys}}^{\text{n}}$ is calculated at T^{n} using Equation (3.15) and (3.16). The current melting rate $K_{\text{melt}}^{\text{n}}$ is derived from the previous peak melting temperature $T_m^{\text{n}-1}$ and the current temperature T^{n}. The peak melting temperature is calculated from the average lamellar thickness $\bar{l}_c$ as given by:

$$T_m^{\text{n}-1} = T_m^{\text{eq}} \left[1 - \frac{2\sigma_e}{\Delta h_f \bar{l}_c^{\text{n}-1}} \right]. \tag{3.29}$$

To prevent numerical issues in the case of complete melting, where $\bar{l}_c^{\text{n}-1} = 0$, the average lamellar thickness is replaced by the current lamellar thickness $l_c(T^{\text{n}})$, using $T_c = T^{\text{n}}$ in Equation (3.19). The current melting rate $K_{\text{melt}}^{\text{n}}$ then follows from substitution of $T_m^{\text{n}-1}$ and T^{n} in Equation (3.21) and (3.22).

The space-filling distribution is updated to derive the total space-filling from the changes in space-filling. In the case of crystallization, T^{n} determines the lamellar thickness that is currently formed, using $T_c = T^{\text{n}}$ in Equation (3.19). This determines which of the lamellar thickness bins the space-filling ξ_i can increase. Besides, it is assumed that the smallest lamellar structures melt first. Therefore, the absolute change in space-filling due to melting is subtracted from the lowest nonzero entry in the lamellar thickness distribution. If the absolute change is larger than the space-filling in the bin, the remaining absolute space-filling is subtracted from the next bin. This is repeated until the absolute space-filling is subtracted or until the distribution is completely emptied. This procedure of crystallization and melting, related to the lamellar distribution, is shown in Figure 3.10 for the particular case of crystal perfection. First, space-filling is added to the lamellar thickness bin related to crystallization.

(a) A distribution with $\xi = 1.0$ **(b)** Crystallization to $\xi = 1.1$ **(c)** Melting to $\xi = 1.05$ **(d)** Correction to $\xi = 1.0$
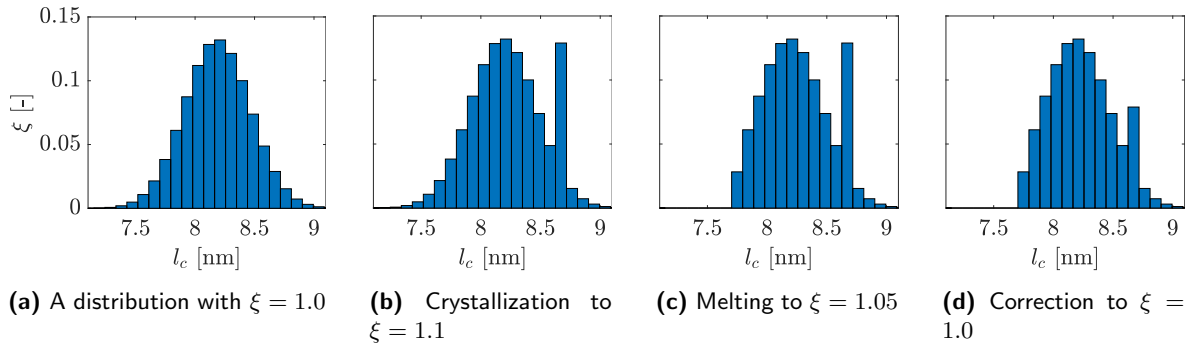
Figure 3.10: Procedure of updating the lamellar thickness distribution in a) due to the growth of lamellar structures by crystallization in b) and the melting of lamellar structures in c). If the final space-filling is larger than one after melting, the crystallized fraction is corrected in d) so that $\xi = 1.0$.

This results numerically in a (temporary) space-filling larger than one. Subsequently, a space-filling fraction is molten, reducing the total space-filling. In the case that after melting $\xi > 1$, a correction is performed on the bin in which lamellar are grown due to crystallization. This is because, physically, the space-filling cannot exceed one. The current average lamellar thickness $\bar{l}_c^{\mathrm{n}}$ and the total space filling ξ^n are derived from the updated lamellar thickness distribution.

3.4.2 Spatial discretization and shrinkage

The shrinkage effect due to a porosity reduction in SLS is studied only in use case one. Herewith, the accuracy of a product is to be evaluated. Figure 3.11 shows a schematic representation of the layer shrinking due to laser irradiation. The initial mesh consists of triangular elements positioned on a meshed grid to align the nodes from top to bottom.
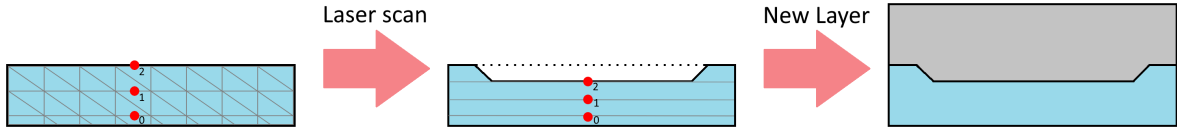
Figure 3.11: Illustration of porosity-induced shrinkage and the resulting down-shift of a layer. Deposition of a new layer fills the gap, and hence, the thickness of the new layer increases locally.

After a laser scan, the porosity reduces in case of melting, and the layer height reduces according to Equation (3.12), assuming shrinkage only occurs vertically in the negative y-direction. Due to nonisothermal heating, the porosity on each node might differ. Therefore, the shrinkage is evaluated on the difference between node j and the one below it $j-1$, such that:

$$\Delta H_j^{\mathrm{n}} = -(y_j^{\mathrm{n}-1} - y_{j-1}^{\mathrm{n}-1})\frac{\varphi_j^{\mathrm{n}-1} - \varphi_j^{\mathrm{n}}}{1 - \varphi_j^{\mathrm{n}}}, \tag{3.30}$$

with ΔH_j^{n} the current difference between the original position of node j and the position after porosity-induced shrinkage, y_j the vertical position the node and y_{j-1} the vertical position of the node below it. The vertical positions of the nodes at the bottom boundaries are y_0, and these cannot shift downwards (i.e., $\Delta H_0 = 0$). The shrinkage procedure starts with the nodes on the left side of the domain. For this vertical node-set, the new vertical position is calculated according to the following:

$$y_j^{\mathrm{n}} = y_{j-1}^{\mathrm{n}} + \sum_{j=1}^{j} \Delta H_j(t) \quad \text{for } j = 1, 2, ..., N_y, \tag{3.31}$$

with N_y the number of nodes in the vertical node-set. This equation considers the down-shift of the nodes below it by summation over the positional change of the nodes below it. This equation is used repeatedly for subsequent vertical node sets from the left boundary to the right boundary of the domain. Figure 3.11 shows that the newly deposited layer fills the gap due to shrinkage. In use case two, the effect of shrinkage is not considered, as this would complicate the interpretation of the crystallization and melting kinetics.

3.5   Results

The results of the developed model for use cases one and two are presented in this section. Starting with case one, the effect of porosity-induced shrinkage is studied for a rectangular part. Subsequently, the effects of crystallization and melting on the SLS process are simulated, and resulting lamellar thickness and yield stress predictions are shown. Finally, the part's geometry is adjusted to the TU/e logo and is simulated to study the complex interplay between geometry, temperature, crystallization, and melting in SLS.

3.5.1   Case one: Shrinkage and porosity

In Figure 3.12, the impact of volume reduction due to the sintering of powders is shown for the porosity-induced shrinkage. A laser with a power of 5.5 W/mm is moved over the scan lines of the rectangular geometry with a velocity of 0.5 m/s. As the part melts and the porosity decreases, the molten parts sag into the bed, which causes the edges to curl. This effect is simulated for initial porosity ranging from 0.15 to 0.75. The left corner of the rectangular part shows the impact of edge curling.

Edge curling is not seen for the smallest initial porosity of $\varphi = 0.15$ since the volume changes due to melting are limited. However, as the initial porosity increases, the layer thickness reduces following Equation (3.12). Therefore, the sagging is more significant, and the resulting parts will have upstanding edges after cooling. For the largest initial porosity $\varphi_0 = 0.75$, the layer thickness increases from bottom to top due to the increasing gap size caused by the shrinkage of underlying layers (see Figure 3.11). This necessitates the addition of more powder to the part as the thickness of each layer decreases over time. Additionally, the part is not fully molten, and the final porosity is around 0.4, which can be explained by the decrease in transmittance and absorption at large initial porosity.

Interestingly, for the standard value of initial porosity, taken as $\varphi_0 = 0.55$, the sagging, temperature history, and change in transmittance during fusion result in a nonconstant spacing between the layers.
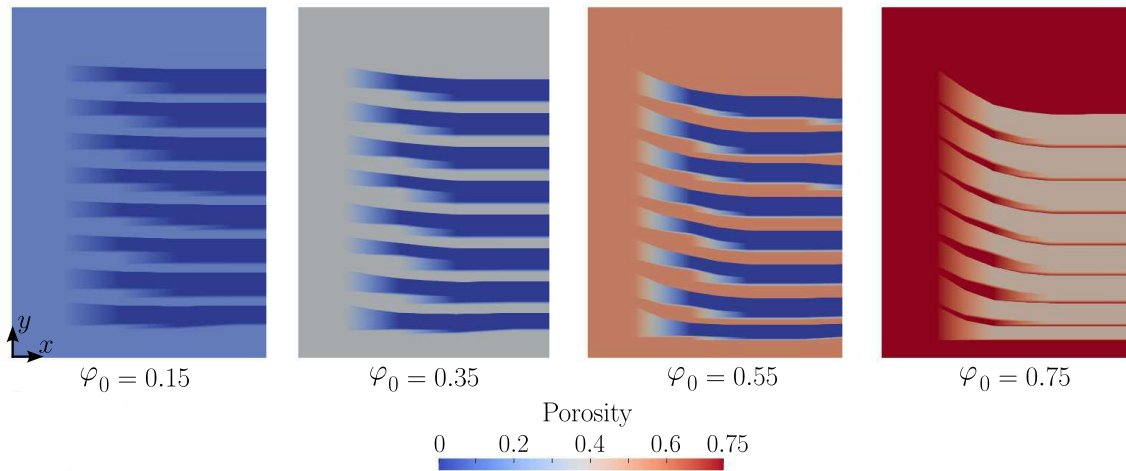

Figure 3.12: Curling of the edge for different values of initial porosity: 0.15, 0.35, 0.55, and 0.75. A power of $P_0 = 5.5$ W/mm is applied for each layer, with an initial layer thickness of $l_{y,0} = 150$ µm.
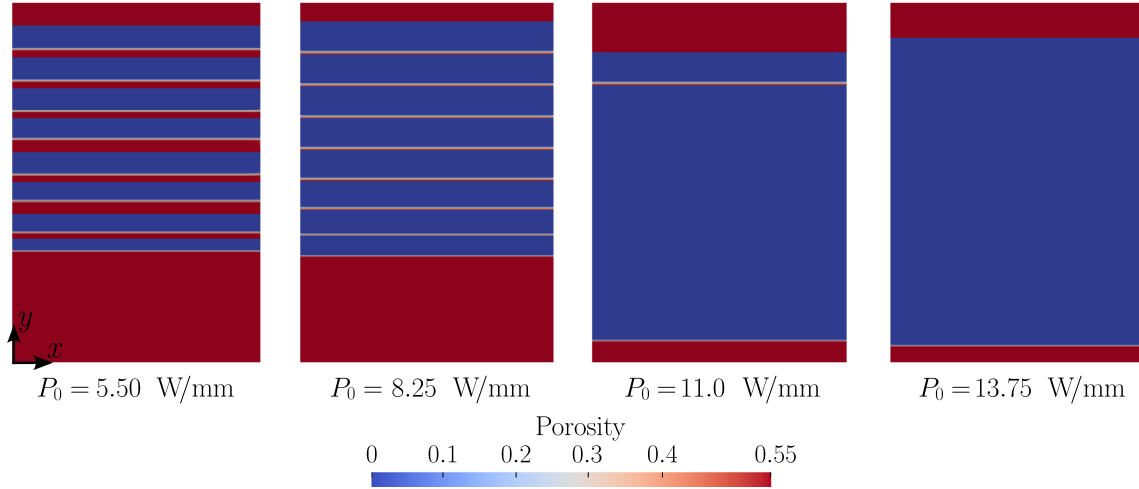
Figure 3.13: Porosity distributions at the center of the sample for laser powers of $P_0 = 5.50$, 8.25, 11.00, and 13.75 W/mm. The unmolten powder is given in red and has an initial porosity of $\varphi_0 = 0.55$.

The laser power can be raised to improve the bond between layers and decrease their spacing. Figure 3.13 illustrates the impact of laser power on porosity values for a standard powder ($\varphi = 0.55$). Laser powers of 5.5, 8.25, 11.0, and 13.75 W/mm are used, and the resulting porosity values at the middle of the rectangular part are measured. As the laser power is increased to 8.25 W/mm, the inter-layer spacing decreases due to the increase in the penetration depth of the laser. However, the thickness of the part is increased slightly as the laser sinters the surrounding powder below the part. This effect is more pronounced for higher laser powers (11.0 and 13.75 W/mm), where almost complete melting occurred, resulting in a drastic increase in the size of the part.

These figures demonstrate how the quality of a part is affected by its initial porosity and the power of the laser used. When it comes to mechanical properties, using high laser powers and low initial porosities will result in parts with low porosity and no inter-layer spacing. However, this approach sacrifices accuracy as the size of the part increases with higher laser power. Therefore, it can be argued that reducing initial porosity through compaction is better to minimize the laser power required to produce parts without inter-layer spacing and improve accuracy.

3.5.2   Case two: Crystallization, melting and yield stress predictions

Figure 3.14a shows the resulting yield stresses from tensile experiments. The modified Eyring equation uses only one process instead of two to describe the measured yield kinetics. The shift with crystallization temperature is assumed to depend solely on the difference in lamellar thickness between these samples. WAXD and SAXS measurements are used to find the corresponding lamellar thickness of the PA12 samples. The results of these procedures are discussed in detail in Appendix 3.A.2. Additionally, the measured lamellar thicknesses agree with theoretical predictions in Equation (3.6) and reference values from the literature, as shown in Figure 3.6. Combining these measurements of l_c with the empirical relation for the rate constant $\dot{\varepsilon}_0$ in Equation (3.26) results in the rate constant prediction shown in Figure 3.14b. The parameters corresponding to these yield kinetics are listed in Table 3.6 and used

(a) Tensile measurements

(b) Rate constant prediction
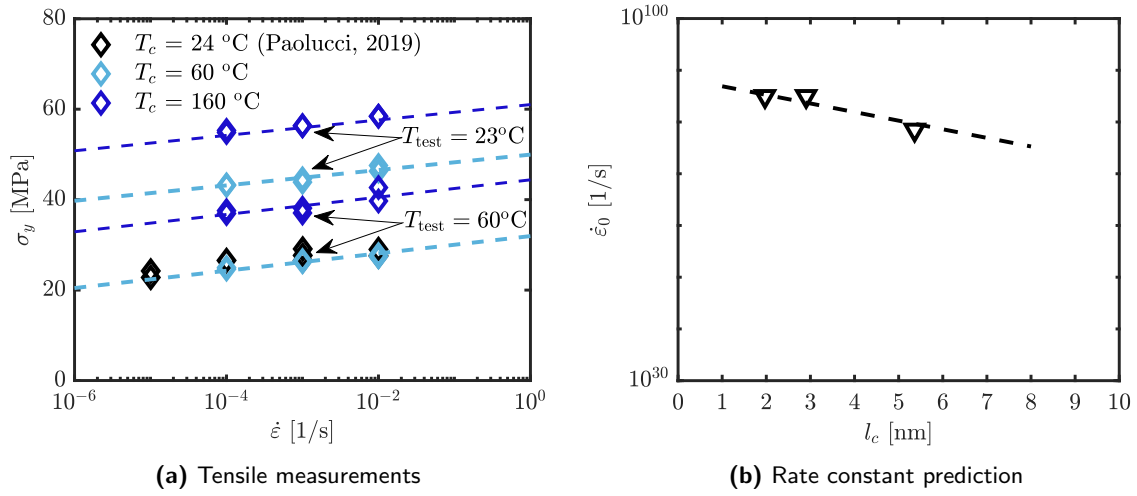
Figure 3.14: Yield kinetics for PA12 studied by tensile experiments as compared to data from Paolucci et al. [16]. Dashed lines indicate model predictions, and markers indicate experimental data of samples processed at different crystallization temperatures.

Table 3.6: Parameters used to describe the yield kinetics of PA12.

Parameter	Symbol	Value
Activation volume intra-lamellar deformation	V_I^*	5.52 nm^3
Activation energy intra-lamellar deformation	ΔU_I	6.46·10^5 J/mol
Minimum lamellar thickness	$l_{c,0}$	1.0 nm
Slope empirical intra-lamellar relation	c_I	-1.66
Reference value empirical intra-lamellar relation	d_I	88.57

in the simulations of use case two. The properties of SLS printed parts are directly coupled to the processing parameters (energy-to-melt ratio in Chapter 2). However, the structural evolution within these parts is complex to study, as the combined thermal history, layer-by-layer method, relaxation times in the polymer, coalescence, and crystallization and melting complicate the analysis. However, these effects can be modeled separately in simulations, allowing in situ visualization of the different processes.

Temperature history and crystallization kinetics in SLS

To investigate how processing affects structural development in PA12, the effect of temperature on the crystallization and melting kinetics is shown for typical SLS temperature profiles in Figure 3.15. Instead of solving the coupled temperature and crystallization equations with 2D FEM simulations, the lamellar thickness and space-filling contributions are solved first from zero-dimensional temperature profiles in 3.15a. The first temperature profile mimics a point in a SLS simulation and corresponds to a typical high-power SLS temperature profile (red line, with the maximum peak temperature). The other temperature profiles are found by scaling the high-power temperature profile T_{hP} using $T = (T_{hP} - T_0)/c + T_0$, with $c = [1.0 \ 1.375 \ 1.75 \ 2.125 \ 2.5]$. In this way, the peak temperatures are lowered (see peaks at $t < 250$ s), and the cooling rates are increased (see slopes at $t > 250$ s) systematically.

(a) Temperature

(b) Average lamellar thickness

(c) Total space-filling

(d) Melting space-filling change   **(e)** Crystallization space-filling change   **(f)** Combined space-filling change
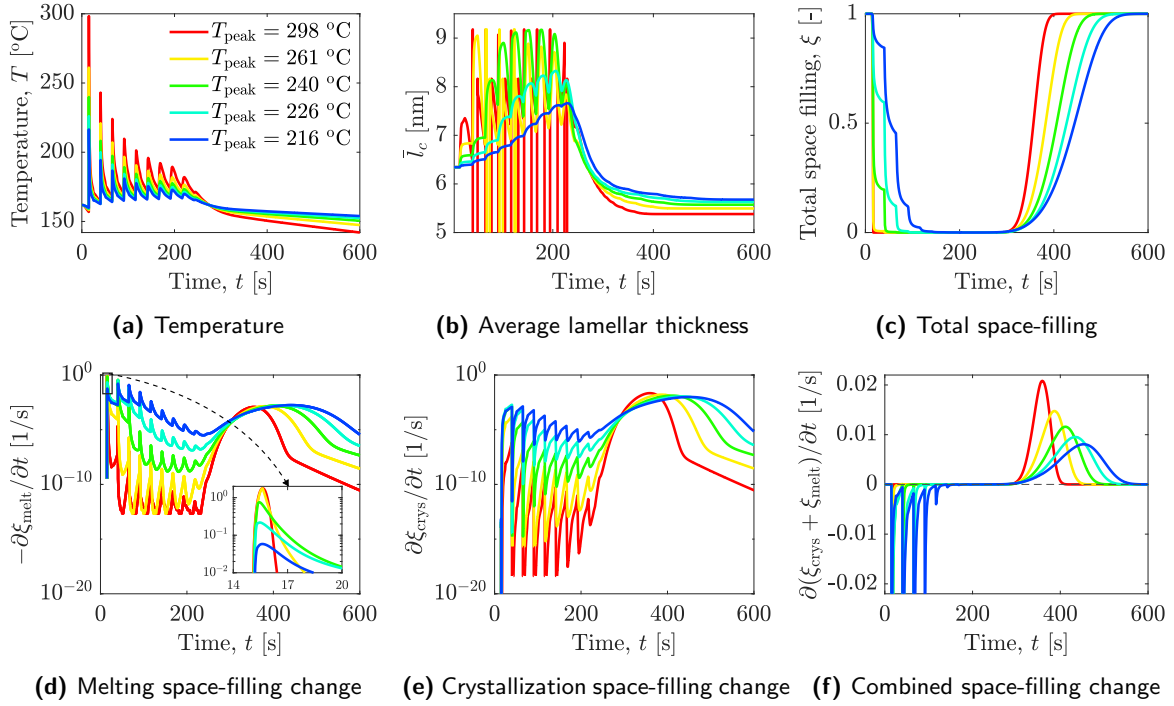
Figure 3.15: Evolution of temperature and structural properties for typical SLS temperature profiles. The temperature profile in the high-power simulation (dark red line) and corresponding (decoupled) structure evolution are found at the center point of layer 7. In a), other temperature profiles are presented that are derived by scaling the high-power temperature profile T_{hP} with $T = (T_{hP} - T_0)/c + T_0$, and $c = [1.0 \ 1.375 \ 1.75 \ 2.125 \ 2.5]$. The resulting profiles study the effects of reducing the peak temperatures at $t < 250$ s and increasing the cooling rate at $t > 250$ s. In b) the average lamellar thickness, in c) the total space-filling, in d) the space-filling change due to melting, in e) the space-filling change due to crystallization, and in f) the combined space-filling change (positive crystallization and negative melting) are given.

In Figure 3.15b, the average lamellar thickness of the powder is depicted, which is initially 6.34 nm for the PA12 powder. At $t = 15$ s, the laser energy is absorbed, which results in a sharp temperature increase. Using Equation (3.21), the melting rate based on the maximum temperature achieved is calculated. The smallest lamellar structures are melted first, increasing the average lamellar thickness. As a result, the total space-filling decreases (see Figure 3.15c). The total space-filling reduction depends on the peak temperature reached, where the temperatures of 261 and 298 °C result in (nearly) complete melting. In both cases, a small fraction of <0.1% of space-filling is left, and therefore, the average lamellar thickness does not jump to zero immediately after the first temperature peak.

After the first and highest temperature peak, the temperature drops to 162-168 °C. The melting kinetics are slowed for the highest peak temperature as the lamellar thickness increases to > 7 nm. Therefore, crystallization can start at these temperatures, reducing the average lamellar thickness to < 7 nm. This effect of lamellar thinning is substantial here because the total space-filling is very low, and a slight change in space-filling induces a relatively large change in the average lamellar thickness. This reduction in average lamellar thickness is not

visible for the smaller peak temperature profiles, as the temperature is higher and the average lamellar thickness is smaller.

After a second layer is deposited, the laser passes the powder for a second time, but the extra layer reduces the maximum temperature increase. Nevertheless, the temperature increase is sufficient to melt the powder in the second layer further. After this heating step, the powder is either fully molten ($\xi = 0$ and $\bar{l}_c = 0$) or partly molten. In the latter case, the average lamellar thickness increases, and the total space-filling reduces further. Both cases allow for crystallization as the temperature drops after the second irradiation. The layer addition and laser irradiation procedure is repeated until the final layer is deposited at $t \approx 250$ s.

After the final layer is deposited, the temperature reduces gradually. The crystallization kinetics are faster for increasing cooling rates, resulting in smaller crystals and faster space-filling growth rates. The final average lamellar thickness is smallest, $\bar{l}_c = 5.4$ nm, for the highest temperature profile ($T_{\mathrm{peak}} = 298$ °C) and largest, $\bar{l}_c = 5.7$ nm, for the lowest temperature profile ($T_{\mathrm{peak}} = 216$ °C). From Figure 3.14, it follows that at a strain rate of 10^{-4} 1/s and room temperature, this results in an intrinsic yield stress difference of about 1 MPa.

Simulations of the rectangular geometry

A simple rectangular geometry is used in the following results, and sagging due to porosity-induced shrinkage is neglected. Powers of 5 W/mm to 40 W/mm are applied, and degradation is assumed to be nonexistent, as this is not the scope of this study. Water uptake is detrimental to the final mechanical properties [16] and will not be studied here. So, the yield stresses presented in the following analysis are indicative and solely result from (micro-)structural evolution in SLS 3D printing.

Figure 3.16 depicts the space-filling evolution within the part over time. Laser powers of 30 W/mm is used. Initially, the powder has a space-filling of one, which can only change if the temperature is increased above the onset of melting. While printing, melting reduces the space-filling at the scan paths of the laser. The laser penetration of the first layer is larger for increasing laser powers. The sides and bottom of the rectangular part cool first as the surrounding material has a relatively low temperature. At these lowered temperatures, the polymer melt crystallizes ($K_{\mathrm{crys}} > K_{\mathrm{melt}}$), and the space-filling increases while printing. The part is almost fully molten at the last scanning layer, while the polymer has been repeatedly molten and crystallized. Subsequently, after the previous recoating layer, the part has partly cooled down from the bottom to the top. Herein, it is visible that the laser power drastically affects the temperature history, resulting in a different structure development within the parts. Finally, the parts are fully crystallized after cooling, resulting in a space-filling of $\xi = 1$.

The average lamellar thickness under particular tensile testing conditions determines the yield stress of a part. For a strain rate of 10^{-4} 1/s and testing temperature of 23 °C, the yield stress distribution over the part's geometry due to the manufacturing process is shown in Figure 3.17. Using the lamellar thickness at the end of cooling, the yield stress is calculated using Equation (3.25) and (3.26). A higher laser power used during manufacturing leads to a greater spread in yield stresses. For a laser power of 40 W/mm, yield stress values are lower at the top of the part than at the center and bottom. This is because, for the 40 W/mm simulation, most of the top part is still molten when the powder bed cools down. In contrast, the rest of the part has been mostly crystallized (see Figure 3.16). The top part crystallizes at a lower temperature, which results in a greater fraction of space-filling corresponding to lower lamellar thicknesses, eventually leading to a lower value for the yield stress.
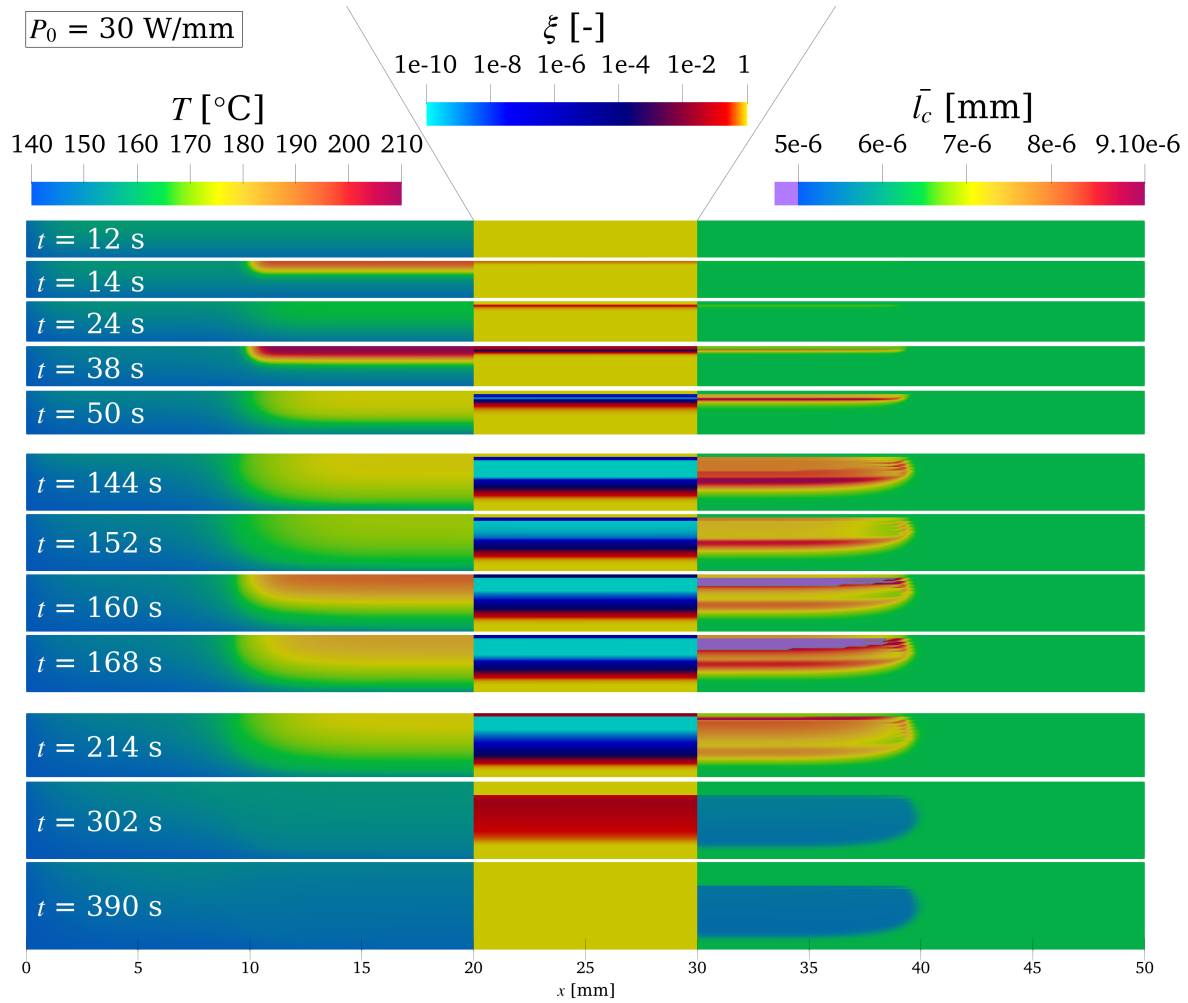
Figure 3.16: Temperature T, space-filling ξ, and average lamellar thickness $\bar{l}_c$ evolution over time t for a power of $P_0 = 30$ W/mm. The time evolution is subdivided into three parts, where the top part is the scanning and crystallization of the 11th and 12th layers. The middle part shows the crystallization and (full) melting of the scanned and subsequent layers. The bottom part shows the cooling and corresponding crystallization.

For a laser power of 10 and 20 W/mm, lines with lower yield stress values can be observed inside the generated geometry. This is because of the remelting of crystallized material when subsequent layers are heated. These lines do not occur for higher laser power values since enough heat is supplied during the build process so that the material does not crystallize while printing subsequent layers.

It has been reported that Young's modulus of polyethylenes correlates linearly with the yield stress [82], and similar behavior is observed for polyamides [129]. Therefore, assuming that the same relation holds for PA12, the distribution of Young's modulus is expected to be similar to the yield stress distribution shown in Figure 3.16. These simulation results demonstrate the importance of considering material properties in relation to process conditions, thermal history, and crystallization and melting when processing polymeric materials with SLS 3D printing.
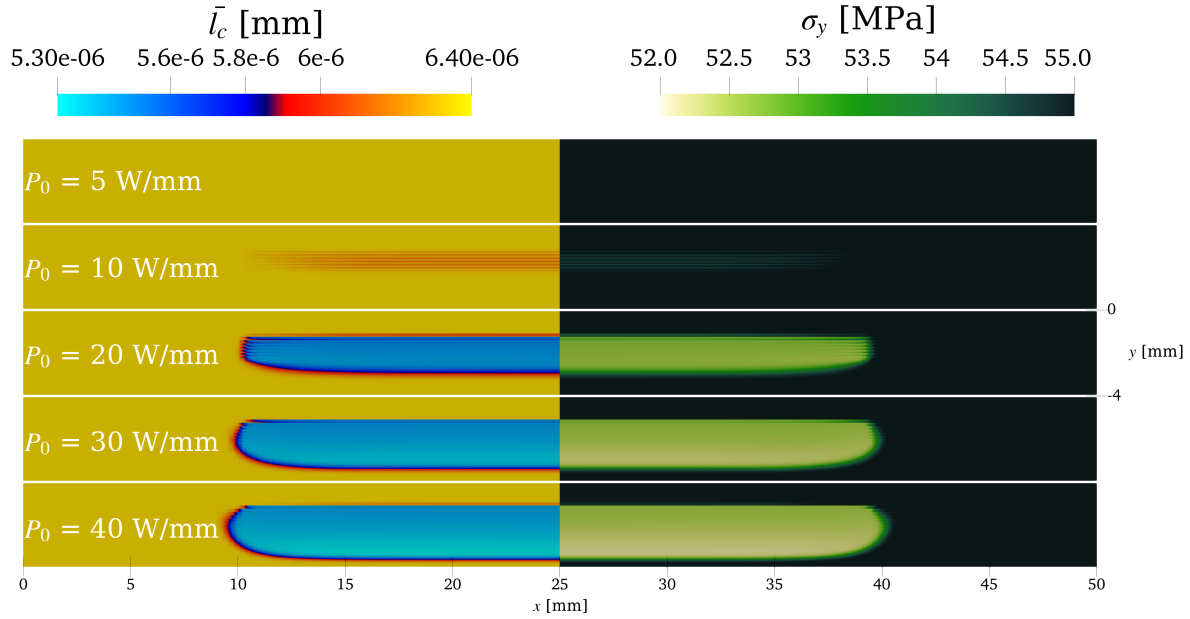
Figure 3.17: Yield stress distribution of the rectangular print for powers of 5, 10, 20, 30, and 40 W/mm after cooling. At low powers, the lamellar thickness equals the powder's thickness of 6.34 nm, as no melting has occurred. At increasing powers, melting effectively lowers the lamellar thicknesses, resulting in a lower intrinsic yield stress than the powder.

Simulations of the TU/e logo

A more complex geometry, the TU/e logo, is simulated as shown in Figure 3.18. Herein, the temperature and structure evolution during printing and cooling are visualized. Initially, at $t = 0$ s, the bed temperature is 161 °C, and the average lamellar thickness equals 6.34 nm.
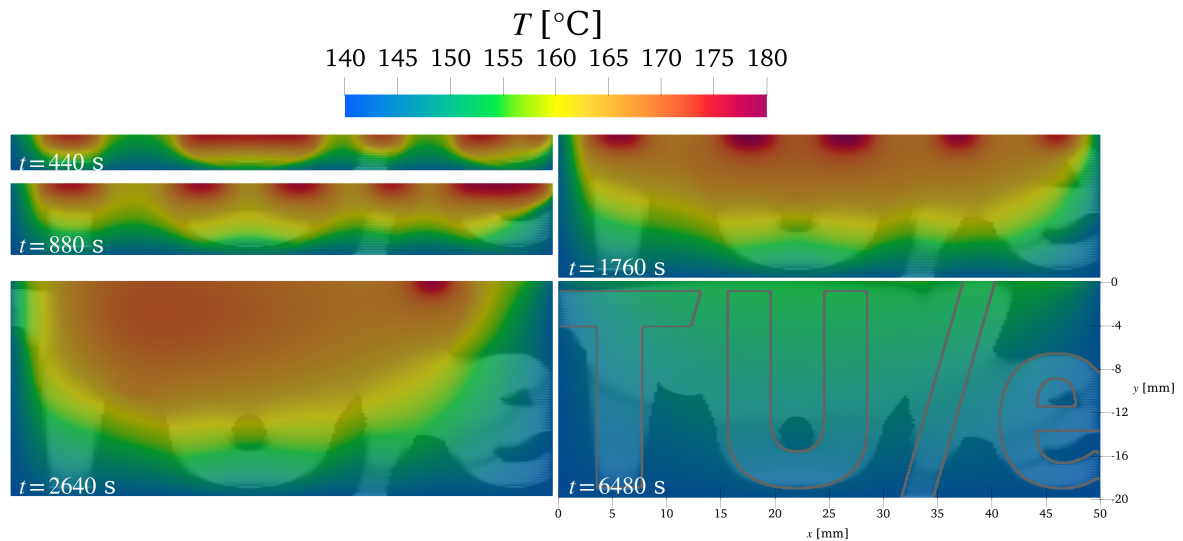
Figure 3.18: Temperature evolution and structure formation (in white) for simulating the printing of the TU/e logo (grey outlines) at a laser power of $P_0 = 20$ W/mm.

For visualization, structure development is indicated in white and consists of lamellar structures smaller than the initial average lamellar thickness. During building, at 440 seconds, the laser scans explicitly the TU/e logo, as indicated by the increase in temperature to about 180 °C. As a result of subsequent scanning, the initial temperature of the bed starts to increase. After 880 seconds, the temperature of the surrounding powder has risen to 165 °C. At a time of $t = 1760$ s, it is visible that the surrounding powder has reached the onset of the melting temperature ($T > 170$ °C). Therefore, an area of melt is formed that distorts the creation of the TU/e geometry. After 2640 seconds, the last printing layer was scanned, and the cooling started. After the final cooling step, at $t = 6480$, a structure has been generated that is sintered at undesired areas of the powder bed. The cause of this discrepancy could originate from an excess of energy input (i.e., power) or because the time between layers is too short for the top of the powder bed to cool down.

To study both causes, the power and the time between layers is varied. In Figure 3.19, the structure development after cooling is visualized for laser powers of 5, 10, 15, and 20 W/mm. At a laser power of 5 W/mm, the melting temperature of the powder is not reached initially. However, the input of the laser energy eventually increases bed temperature. After

Figure 3.19: Effect of laser power on structure development in SLS printing of a TU/e logo. After cooling, the average lamellar thickness and yield stress distribution resulting from printing the TU/e logo with laser powers of 5, 10, 15, and 20 W/mm are given.

more than 100 layers, the bed temperature has reached a temperature just below the onset of melting, and the small energy input of 5 W/mm is sufficient to melt the top part of the TU/e logo. Increasing the laser power to 10, 15, and 20 W/mm results in melting the TU/e logo's bottom part and the surrounding powder. The powder between the "T" and "U" of the logo already melts at powers of 10 W/mm, indicating that solely decreasing the power is insufficient. For the largest input power of 20 W/mm, the difference in yield stress throughout the part is about 1-2 MPa. Features of the objects closest to the walls, with a larger thermal conductivity, undergo relatively rapid cooling compared to the internal object features. Therefore, smaller lamellar structures grow, leading to a smaller average lamellar thickness and a lower yield stress.

These results indicate that the development of structures throughout the part should be controlled by both cooling and energy input. For the inter-layer times in this simulation, simply varying the laser power does not result in an accurate part. Optimally, variable power along the scan path would be required to limit the temperature increase of surrounding powers while supplying sufficient energy for melting.

The inter-layer time (ILT) consists of the time for powder recoating when no laser radiation is turned on, t_{addLayer}, and the time in the scanning phase, which is needed until a particular volume element experiences laser exposition due to part scanning in a specified manner, t_{wait}. The ILT determines the cooling time of the powder after scanning. In Figure 3.19, the layer addition time is set to $t_{\text{addLayer}} = 5$ seconds. After that, $t_{\text{wait}} = 10$ seconds is waited to mimic the scanning until the part experienced its first laser exposition.

In Figure 3.20, the structure formation after printing the TU/e geometry is simulated for layer addition times of 5, 15, 25, and 50 seconds at a laser power of 20 W/mm. Herein, the average lamellar thickness distribution is given after cooling. The scanning times of this 50x20 mm geometry increase linearly with ILT such that $t_{\text{scan}} = [2660, 3990, 5320, 14630]$ s for the increasing layer addition times. Increasing the ILT improves the accuracy as the undesired
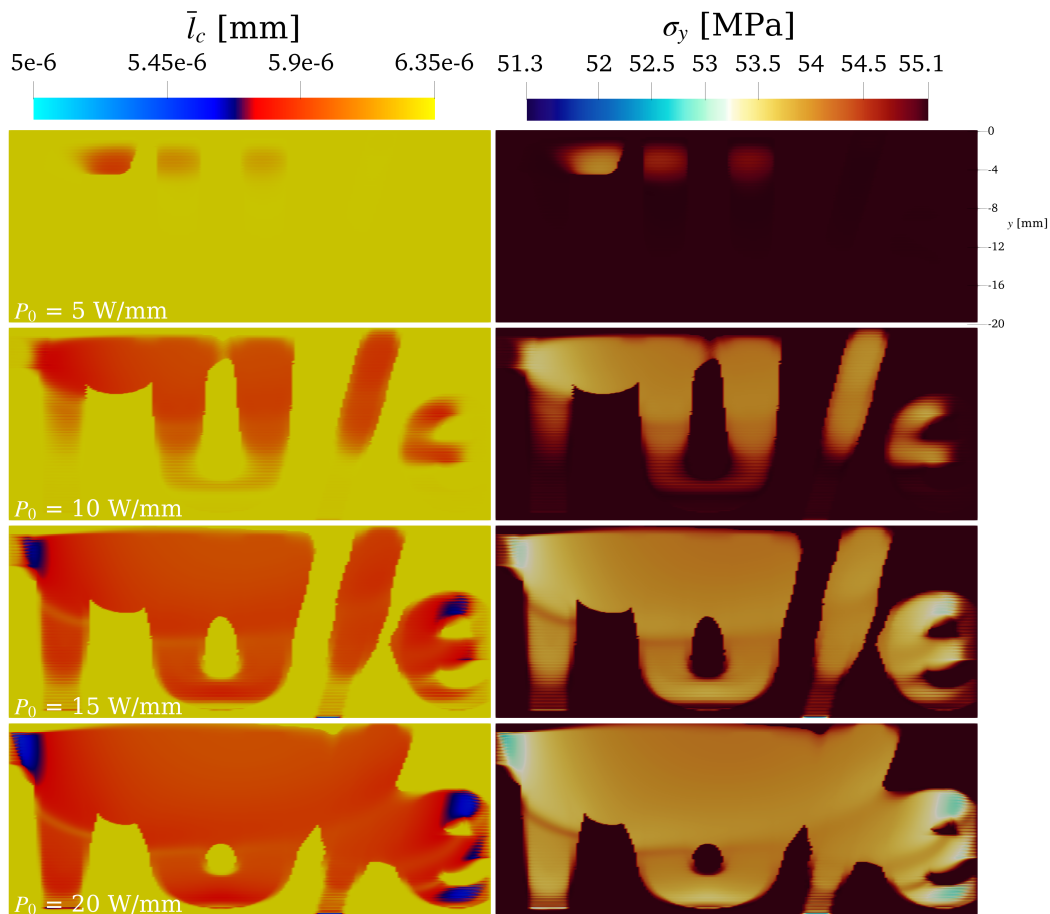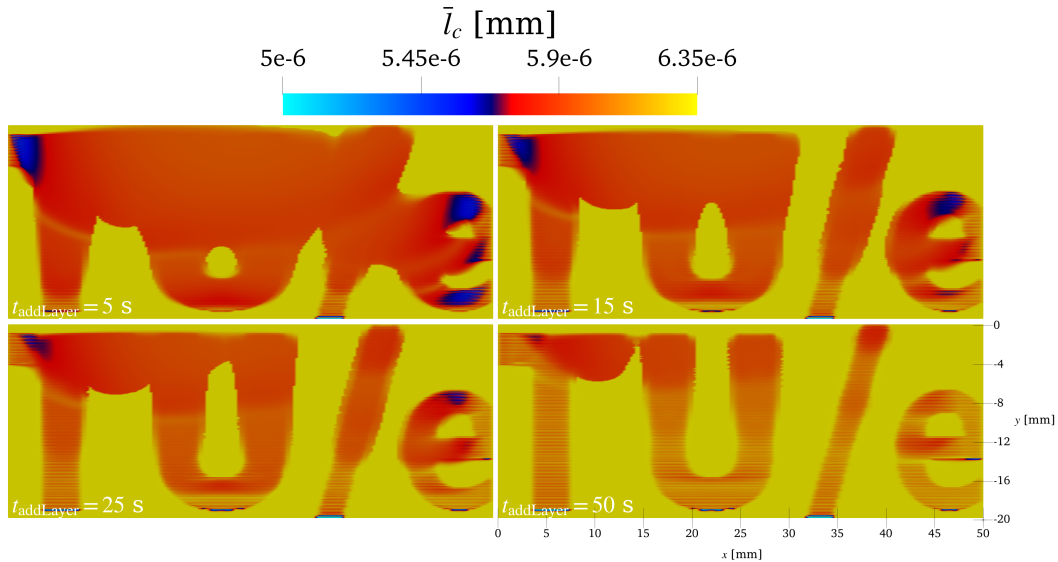

Figure 3.20: Effect of layer addition time on structure development in SLS printing of a TU/e logo. After cooling, the average lamellar thickness resulting from printing the TU/e logo with a laser power of $P_0 = 20$ W/mm is given.

melting of surrounding powder decreases but comes at the cost of longer printing time. At the longest ILT, these 20 W/mm simulations show inter-layer structural differences that indicate partial melting. Increasing energy input by power or bed temperature increase or scan velocity reduction will result in a more homogeneous structure with improved mechanical properties. Therefore, the numerical toolbox should be extended for optimization to minimize printing time and maximize mechanical properties and accuracy. In this optimization, a variable energy input along the scan path and a variable ILT should be implemented, as this could vastly improve the SLS printing quality and speed of complex part geometries.

The simulations show that internal structure formation can be modeled for the SLS printing process. Improvements regarding accuracy, printing times, and mechanical properties can only be made if the combination of part geometry, processing conditions, material properties, and process control are considered. In future studies, the numerical toolbox can be used to systematically address these fields and develop optimization schemes to improve the quality of SLS printed parts.

3.6   Conclusions

This paper proposes a numerical model to investigate how initial porosity, crystallization, and melting affect the accuracy and mechanical properties of products produced using selective laser sintering (SLS). The model is an extension of a previously developed numerical model for SLS [15], and the paper provides a detailed overview of the material properties of polyamide 12 (PA12) used in the simulations. It discusses the relationship between the lamellar thickness and the yield kinetics via the rate constants and the modified Ree-Eyring Equation. The effectiveness of the model is demonstrated through two case studies.

The first case study found that initial porosity significantly affects the shrinkage behavior of PA12 powder and the accuracy of parts produced with SLS. Higher initial porosity leads to more shrinkage and lower accuracy. In the second case study, the yield kinetics of a simple 2D product made out of PA12 is used to quantify the effect of microstructural changes on the yield stress characteristics of PA12 parts. The simulation results show that the processing conditions significantly affect the average lamellar thickness, resulting in a yield stress distribution inside PA12 parts produced with SLS. Therefore, it is essential to carefully control the initial porosity, crystallization and melting, laser power, and scanning speed to make SLS products with optimal mechanical properties and accuracy.

The numerical model developed in this research is a valuable tool for predicting how different processing parameters affect the final product in SLS. The simulation toolbox is suitable for optimizing processing conditions and improving SLS-produced products' accuracy and mechanical properties, as demonstrated by the results from simulating a TU/e logo. Future research can focus on expanding the model to study the combined effects of variable laser power along the scan path and inter-layer times on product quality and printing times. Additionally, experimental validation of the model can be conducted to enhance accuracy and mechanical properties predictions. It is recommended that the melting model be improved by incorporating larger and different melting rates. DSC and FDSC curves of PA12 melted at various heating rates are available in the work of Laumer et al. [124]. Heating rates of $5 \cdot 10^4$ K/min, typical in SLS, can suppress the melting temperature to 150 °C [124]. This results in transitions from meso, γ, and α' crystal phases. It is suggested to model these crystal phases separately as, for example, proposed by Paolucci et al. [16].

3.A   Additional information

3.A.1   Crystallization kinetics fitting procedure

The rate constant parameters K_0 and K_G are fitted using DSC data of PA2200 crystallization from Neugebauer et al. [109]. From the lamellar thickness model fit in Figure 3.6, it follows that $T_m^{\text{eq}} = 500$ K. It is assumed that $n_a = 2.82$ as in the work of Neugebauer et al. [109]. Figure 3.21a shows the resulting fit of the crystallization half-time. Herein, $K_0 = 4.09 \cdot 10^{11}$ s and $K_G = 7.09 \cdot 10^5$ K^2 is found to best describe the data in Figure 3.21b, using $U^* = 6270$ J/mol. These fitting results predict the isothermal and nonisothermal crystallization kinetics in Figure 3.5. Herein, the prediction of isothermal crystallization agrees with the measurements. However, the prediction of nonisothermal crystallization kinetics at larger cooling rates is visibly off. This indicates that at large undercooling ($T_c < 158$ °C), the crystallization rate, modeled by K_{crys}, is larger than the actual crystallization rate.

(a) Initial porosity

(b) Laser Power
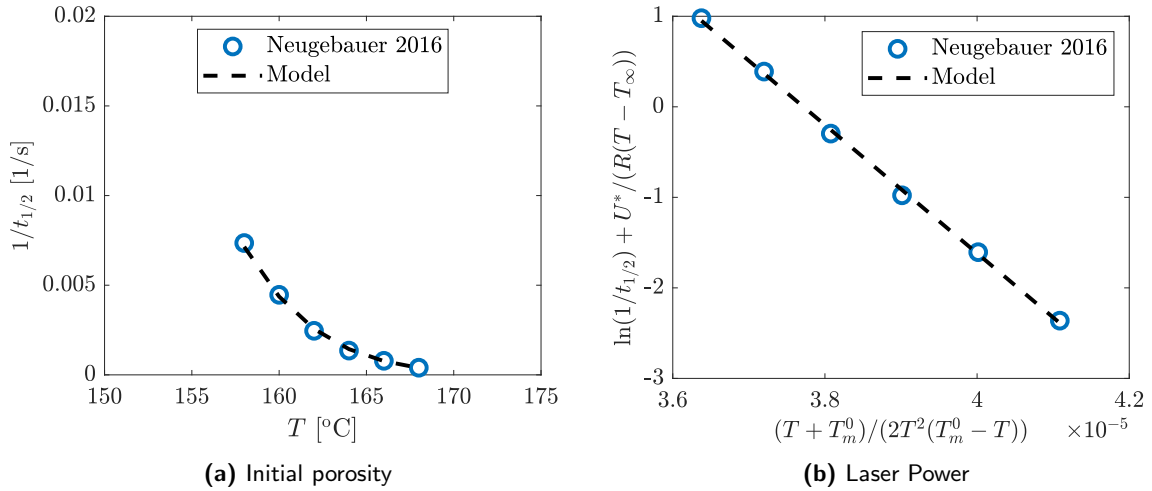
Figure 3.21: Fitting of isothermal DSC curve data of PA2200 from Neugebauer et al. [109] to determine the rate constant parameters K_0 and K_G for $n_a = 2.82$ and $T_m^{\text{eq}} = 500$ K.

3.A.2   X-ray analysis results

Wide-angle X-ray diffraction (WAXD) results are shown in Figure 3.22 and 3.23. WAXD results of quenched PA12 samples from Li et al. [130] is used for the amorphous halo (dashed lines). A background correction is performed so that I is the background-corrected intensity. This results in a crystallinity of $\chi = 0.54\text{-}0.55$ for PA2200 virgin powder, and $\chi = 0.25$ and 0.35 for PA2200 samples isothermally crystallized at $T_c = 60$ and 160 °C, respectively.

Small-angle X-ray scattering (SAXS) results are given in Figure 3.24. Again, a background correction is performed so that I is the background-corrected intensity. The long period is derived from the intensity maxima for the isothermally crystallized samples crystallized at $T_c = 60$ and 160 °C. The maxima are positioned at $q_{\text{max}} = 0.54$ and 0.41 1/nm, respectively. The maxima of the scaled intensity Iq^2 is used for the powder, resulting in $q_{\text{max}} = 0.54$ 1/nm. Therefore, the long period is derived as $L_p = 2\pi/q_{\text{max}} = 11.58$ nm for PA2200 virgin powder, and $L_p = 11.61$ and 15.32 nm for PA2200 samples isothermally crystallized at $T_c = 60$ and
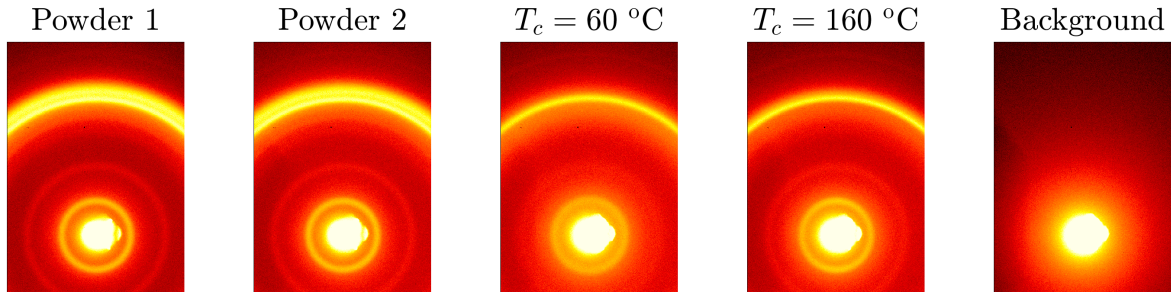
Figure 3.22: 2D WAXD scans for PA2200 in powder form (2x) and crystallized at $T_c = 60$ and 160 °C.
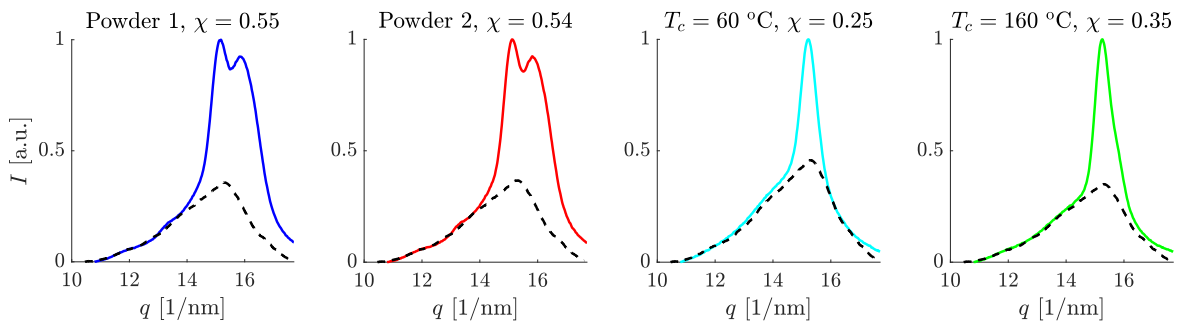
Figure 3.23: WAXD results for PA2200 samples in virgin powder form (2x) and crystallized at $T_c = 60$ and 160 °C. The dashed lines indicate the amorphous halo [130].

160 °C, respectively. Using the crystallinity values from the WAXD results, the lamellar thickness are $l_c = L_p \chi = 6.25\text{-}6.36$ nm for PA2200 virgin powder, and $l_c = 2.90$ and 5.36 nm for PA2200 samples isothermally crystallized at $T_c = 60$ and 160 °C, respectively.

(a) Intensity I

(b) Scaled intensity Iq^2
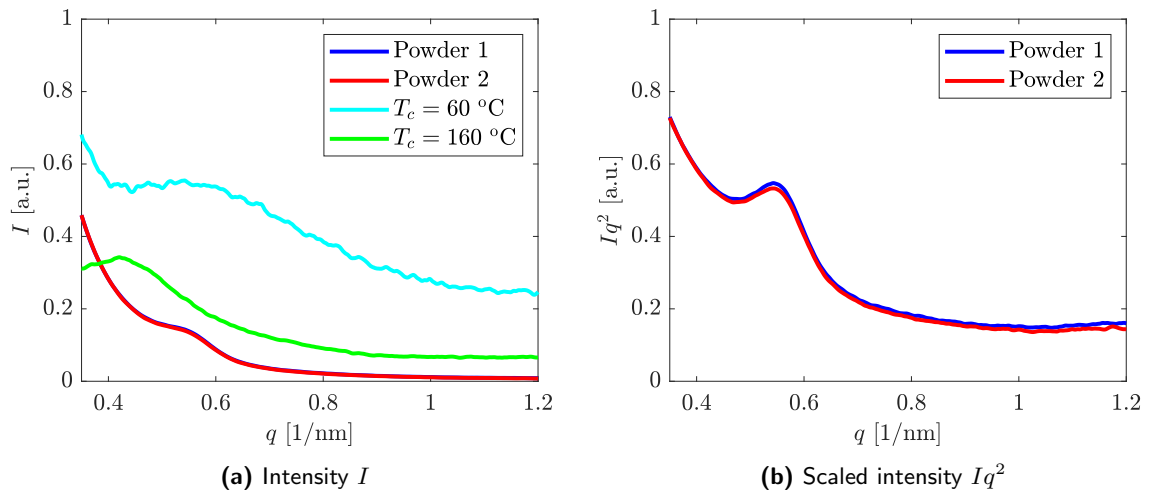
Figure 3.24: SAXS results for PA2200 in powder form (2x) and crystallized at $T_c = 60$ and 160 °C.

Chapter 4

Selective Acoustic Sintering: a Framework to Study Focused Ultrasound 3D Printing

Abstract

This study presents a mathematical model for assessing the practicality of a novel 3D printing process known as selective acoustic sintering (SAS). SAS utilizes focused ultrasound transducers to fuse powder particles within a dense powder volume, enabling rapid printing and close-to-solid part densities via sintering. The framework highlights the critical processes that occur in the SAS 3D printer. It demonstrates that the temperature increase near the printer's center is affected by energy input, energy gain from geometrical focusing, and energy loss due to attenuation. Additionally, the framework establishes relationships between printer dimensions, acoustic and thermal material properties, and transducer properties on local temperature increase and focal spot diameter. By analyzing a diverse dataset of printable materials, the study concludes that optimization enables printing with various materials, including metals, polymers, and ceramics, opening up new possibilities for the 3D printing industry.

4.1 Introduction

Additive manufacturing processes are widely used to produce models, prototypes, tools, and even end products cost-effectively and efficiently. Chemical and physical processes are used to create these products directly from computer-generated models, using shapeless (liquids, powders, etc.) or shape-neutral (e.g., strip-shaped or wire-shaped) starting materials. Standard ISO/ASTM52900 has defined seven categories of additive manufacturing (AM) processes: binder jetting, directed energy deposition, material extrusion, material jetting, powder bed fusion, sheet lamination, and vat photopolymerisation [2]. A common constraint among these

---

3D printing processes is that they can only add material and form it on the surface of the previous layer. This limitation occurs because of how energy or material is applied during printing. In fused deposition modeling (FDM), a melted filament is deposited layer by layer until the part is completed. The nozzle head cannot move through an extruded layer using FDM printing [131]. Similarly, selective laser sintering (SLS), stereolithography (SLA), and other additive processes that use light-emitting energy sources to form products can mainly not penetrate several surface layers of the parts [131]. Even in cases they can penetrate, like UV light through a translucent material, they may adversely affect the layers it passes through. This leads to inherently limited printing speeds in conventional 3D printing techniques [132]. Therefore, it is necessary to develop 3D printing processes that can penetrate deep into a target location with minimal adverse effects on surrounding material, thus eliminating the constraint of unidirectional layer-by-layer printing.

High-intensity focused ultrasound (HIFU) is an emerging medical technology that has shown promising results in treating various disorders. This technology concentrates ultrasound waves from outside the body onto a single target, generating intense vibration, pressure, and heat. It has been successfully used in medical applications for occupational therapy, physical therapy, cancer treatment by ablation of tissue, breaking up of kidney stones by lithotripsy, cataract treatment by phacoemulsification, and body contouring cosmetic operations [133]. In tissue ablation, HIFU can reach temperature increases of at least 60 °C at target locations without harming surrounding tissue [134]. Therefore, HIFU could be suitable for eliminating the layer-by-layer printing strategy.

Ultrasound energy is used in only a few 3D printing manufacturing processes. Ultrasonic Additive Manufacturing (UAM) is a 3D printing process that welds thin sheets of multi-material metals together using ultrasound. [135–137]. Another 3D fabrication process, introduced by Melde et al. [44], involves trapping particles with acoustic holograms. Due to acoustic radiation forces, the particles assemble from a suspension along the high-pressure lines in the acoustic hologram and are then fixed (crosslinked) in a UV-triggered reaction. This method shows promise for bio-fabrication since conventional methods are generally slow and apply mechanical or chemical stress on biological cells [45]. Recently, Habibi et al. [138] developed a 3D printer prototype that uses HIFU to activate ultrasound-activated sonochemical reactions. Structures are developed by acoustic cavitation produced directly by focused ultrasound, creating sonochemical reactions in highly localized cavitation regions. With this Direct Sound Printing (DSP) method, heat-curing polymers with free radical polymerization processes, such as heat-curing thermosets, which cannot be printed directly by photo or heat energy sources in AM processes, can be printed directly.

A novel 3D printing method, denoted as selective acoustic sintering (SAS), is studied for the first time in this research. SAS involves selectively fusing or sintering powder-based materials using a HIFU source. By applying concentrated ultrasound energy at the focal point, the temperature of the powder in the focal region is increased. An array of acoustic emitters can be used as a coordinated phased array emitter capable of beam steering and focusing. Scanning throughout the volume lets the material be heated in an omnidirectional scan path. As a result, the powder material is liquefied at the predetermined scan paths, just like in powder bed fusion 3D printing. Solidified parts are created by cooling, and the nonliquefied surrounding powder can be removed to extract these parts from the powder volume.

The SAS 3D printing technique has been the subject of several patents, including the one by G. Moagăr-Poladian, who was the first to explain how to use HIFU for selective acoustic

sintering [139–143]. These patents suggest that SAS technology has several advantages over traditional powder-based 3D printing techniques. The volumetric scanning method used in SAS eliminates the need for layer-by-layer deposition. This means the 3D printing process is faster, and the requirement for powders to be spreadable is removed. As a result, it is possible to compress the build volume before or during the building process, leading to improved part density and mechanical properties. Support structures are unnecessary as the object is embedded in the pressed powder. Furthermore, filler materials in gas, liquid, or solid form can be added without a spreading step. Advanced phased array systems can generate a plurality of predefined focal spots or holograms, which allows for the simultaneous irradiation of multiple sections of a 3D part. This results in the possibility of homogenizing temperatures throughout the part. The frequency of the ultrasound sources is tunable, allowing for use with a large group of materials without changing the working system. In addition, frequency adjustment can tune the focal spot size to achieve small spot sizes. The use of frequency-dependent transducers enables in-situ visualization of the 3D printed parts, allowing real-time monitoring and characterization of the acoustic 3D environment inside the build volume. Despite the many possible advantages of the SAS printing process, there is currently no model to study the feasibility of using HIFU for volumetric powder-based 3D printing.

The objective of this research is to establish a theoretical framework that can ascertain the feasibility and applicability of using the SAS method for different materials, including polymers, ceramics, and metals. This paper builds upon recently filed patents by the authors [144, 145] and fits in with our fundamental approach to understanding the process and material properties in 3D printing processes [15, 146–148].

The ability of powder particles to fuse depends on the maximum achievable temperature in the focal spot, which determines the feasibility of using the SAS printing technique. In Section 4.2, an analytical model has been developed to predict the temperature increase at a focal spot for multiple HIFU sources positioned on a spherically shaped build volume. The acoustic intensity at the focal spot is calculated by combining linear wave propagation theory for focused ultrasound emitters as derived by O'Neil [149] with Beer-Lambert's attenuation theory. To calculate the temperature increase for a moving focal spot using this intensity, a new method is presented to simplify the temperature increase equations derived by Goldenberg [150]. From this simplification and nonlinear wave propagation limits [151–153], limiting values for scanning speed and transducer power are derived. Subsequently, in Section 4.3, a flow chart is presented to study the feasibility of using the SAS method. The flow chart helps to evaluate the suitability of a specific material, printer size, and resolution. This suitability is determined by comparing the maximum temperature increase to the required temperature increase for melting. Next, the applicability of using SAS for different materials is studied in Section 4.4. A dataset comprising the thermal and acoustic properties of 458 solids is generated. The performance of these materials within given printer dimensions is assessed by optimizing the temperature increase equations and evaluating the resulting temperature increase, resolution, scan velocity, and power consumption. Hereof, promising materials are highlighted, and the applicability of the SAS technique is demonstrated. Finally, Section 4.4.5 presents a discussion regarding this work's findings and future perspectives. While the analytical derivations in this work may not result in a qualitative description of heating in SAS, the equations are a powerful means to quantify the physical relations and predict the feasibility of using focused ultrasound as an energy source for volumetric 3D printing.

4.2   The basics of SAS

4.2.1   Definitions

To develop a framework for studying SAS methods, parameters related to transducer and printer dimensions and shapes must be defined. Therefore, Figure 4.1a shows the definitions used for a focused circular transducer and spherically shaped SAS printer. Transducers emit an acoustic wave with a center frequency f. The wave travels through the medium of the build volume with a speed of sound c_0, so that the wavenumber and wavelength are given by $k = 2\pi/\lambda$ and $\lambda = c_0/f$. In dimensionless form, the transducer radius a is expressed as $\xi = F/a$, where F represents the focal distance. As the wave travels along the axial axis x in Figure 4.1a, the pressure increases due to focussing. This leads to a drastic increase in energy locally in the focal spot, as intensity is proportional to the square of pressure ($I \sim p^2$) [149]. Conversion of energy into heat increases temperature in the focal region, selectively fusing powder particles.

The SAS 3D printer is conceptualized as a spherical device that combines various transducers on the sphere with radius $R = F$, as shown in Figure 4.1b. Each transducer can hold multiple elements, enabling beam steering and focusing by phase-dependent superposition of multiple radiated waves. A spherical printer configuration is selected to minimize the path length of an ultrasound wave to the focal spot. By combining many transducers, the focal spot becomes even more localized, resulting in a spherically symmetric focal volume with a similar size as the lateral beam width D_{spot}. The analysis presented in this work for a spher-

(a) Bowl-shaped focused ultrasound transducer, and the axial pressure field and temperature increase

(b) Conceptual spherical SAS 3D printer that prints the TU/e logo within the build volume
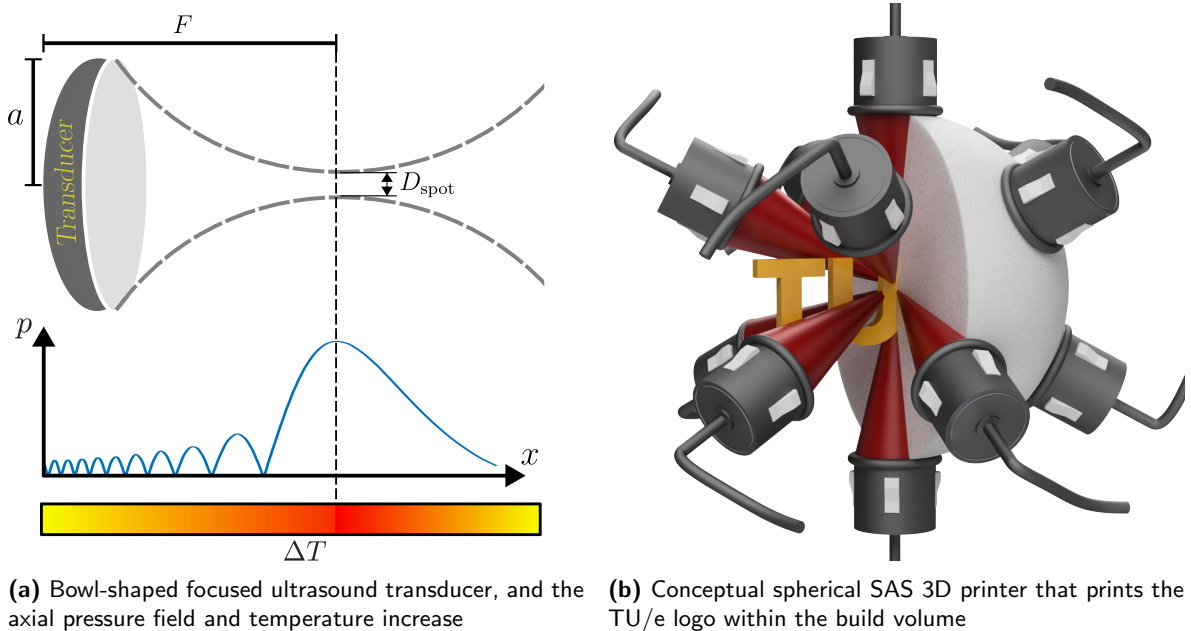
Figure 4.1: Definitions used for a focused circular transducer and the spherical SAS 3D printer. In (a), the image shows the essential parameters for a bowl-shaped ultrasound transducer. These parameters include the radius of the transducer radius a, the focal distance F, and the lateral beam width D_{spot}. In (b), multiple transducers combine to selectively fuse particles within a spherical build volume. The resulting spot is spherical and has a diameter equal to the lateral spot size D_{spot}. Each transducer can consist of multiple elements to create omnidirectional scan paths within the build volume.

ically shaped build volume can be extended to other shapes, such as cylindrical, rectangular, or multi-faced volumes.

For linear wave evolution equations, assuming Fresnel's near-field approximation $F < a^2/\lambda$, the intensity at a radial distance r_F from the focal axis at the focal spot $x = F$ of a focused bowl-shaped transducer has been derived in the work of Gohari [154]. In this study, the following definition is used: $I(F, r_F) = I_{SP} \, \text{jinc}^2(r_F/(\lambda\xi))$, where I_{SP} is the spatial peak intensity at the focal spot, and $\text{jinc}(X) = 2/(\pi X) \, J_1(\pi X)$. Here, $J_1(z)$ is the first-order Bessel function of the first kind. Within the Fresnel zone, the intensity-based focal diameter at -6 dB (lateral beam width) follows from $D_{spot} = 1.03\lambda\xi/2$. In the case of the spherically shaped 3D printer, this spot size is the diameter of the focal volume. Resolution is defined as the reciprocal of the spot size $\text{Res} = 1/D_{spot}$, so that:

$$\text{Res} = \frac{2f}{c_0\xi}. \tag{4.1}$$

Assuming that the focal spot cannot be smaller than the wavelength for a single transducer, the dimensionless element radius is $\xi \geq 2$.

4.2.2   Intensity gains and losses

For calculating the temperature increase due to acoustic irradiation, the acoustic intensity in the focal volume must be determined using the definitions for a spherically shaped SAS 3D printer mentioned above. Because of the geometrical focusing of the acoustic waves, the intensity amplitude increases over the axial distance. At the focal spot, the intensity is maximum. For the focused bowl-shaped transducer in Figure 4.1a, the focal spot intensity gain (with respect to the surface intensity I_0) is given by [149]:

$$G_I = (kh)^2 = \left(\frac{fS}{c_0F}\right)^2, \tag{4.2}$$

where $h = S/(2\pi F)$ is the depth of the transducer and $S = 2F^2\mathcal{F}(\xi)/\xi$, with $\mathcal{F}(\xi) = \pi\left(\xi - \sqrt{\xi^2 - 1}\right)$ is the surface area of the bowl-shaped transducer [149, 155]. In this derivation, several assumptions are made. The depth of the transducer and wavelength must be small compared to the radius a, and the focal distance must be large with respect to the radius a. The wavelength should be smaller than the depth h to obtain a strong focusing effect, resulting in $\lambda \ll h \ll a \ll 2F$ [149]. More specifically, the pressure focal gain has to be at least $(kh)_{min} = 35$ [149]. From this, a minimum frequency follows as $f_{kh,min} = (kh)_{min}c_0/(\mathcal{F}(\xi)F)$ and a material-independent minimum resolution $\text{Res}(f_{kh,min}) = 2(kh)_{min}/(\xi\mathcal{F}(\xi)F)$. For $\xi = 2$, this results in $\text{Res}(f_{kh,min}) = 41.6/F$, and thus the spot size must be at least 41.6 times smaller than the focus distance (i.e. the radius of the sphere), $\chi = F/D_{spot} \geq 41.6$.

Acoustic waves lose energy as they move through a medium, resulting in a decrease in pressure amplitude and intensity. This phenomenon is known as attenuation. The reduction in acoustic intensity due to attenuation follows an exponential function with distance, as described by Vary [156]. For homogeneous materials, the loss at the focal spot can be calculated using [157]:

$$\eta_\alpha = \exp(-\alpha(f)F), \tag{4.3}$$

where $\alpha(f)$ is the frequency-dependent intensity-based attenuation. Ultrasonic attenuation in engineering solids is mainly governed by two energy loss mechanisms, scattering, and absorption, which occur in the frequency ranges of interest. Extrinsic losses such as diffusion,

Rayleigh, and stochastic (phase) scattering are caused by external factors, while intrinsic losses such as absorption from dislocation damping, anelastic hysteresis, relaxation, and thermoelastic effects are specific to individual grains like crystallites [156]. The total attenuation coefficient is the sum of coefficients from each mechanism contributing to one or more loss mechanisms. A more comprehensive form of the total attenuation coefficient, which encompasses all of the loss mechanisms mentioned earlier, is given by [158]:

$$\alpha = a_0 + a_1 f + a_2 f^2 + a_3 f^3 + a_4 f^4, \tag{4.4}$$

where a_i are positive material attenuation coefficients, and the frequency is given in Hz. In special cases, attenuation with a noninteger frequency exponent can be empirically defined by a power-law relation (see, e.g., [159]):

$$\rangle \alpha \langle = \alpha_y f^y. \tag{4.5}$$

Here, $\rangle \alpha \langle$ denotes that α is empirically defined on a limited frequency range $f_1 < f < f_2$. Herein, α_y is the power-law attenuation coefficient (in Np/Hz^y), and y is the power-law exponent of the frequency.

By combining the gain in intensity due to focusing with the loss in intensity caused by attenuation, the spatial peak intensity at the focal spot is approximated by:

$$I_{\text{SP}} = I_0 G_I \eta_\alpha = \frac{P_0 f^2}{c_0^2 \exp{(\alpha F)}} \frac{2\mathcal{F}(\xi)}{\xi}, \tag{4.6}$$

where $I_0 = P_0/S$, with P_0 being the total power at the surface of the transducer. To clarify, the total power denoted by P_0 is the power necessary to operate all the transducers together. The attenuation and geometrical focusing effect on the intensity is depicted in Figure 4.2. Two continuous harmonic acoustic pressure waves are used with different frequencies, $f = 1$
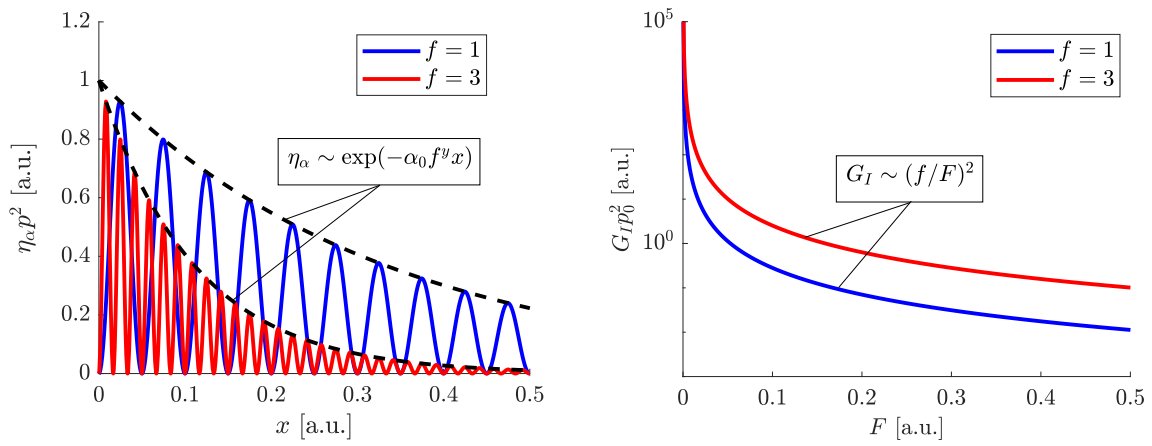
(a) The intensity scales with $p^2\eta_\alpha$, as attenuation decreases its amplitude over distance

(b) The intensity scales with $p_0^2 G_I$, as focussing increases its amplitude

Figure 4.2: The amplitude of a focused acoustic wave, given by I_{SP}, is determined by the product of attenuation loss η_a and focusing gain G_I. The effect of travel distance x, focal distance F and frequency f on these two processes is shown in accordance with Equation (4.2) and (4.3).

and $f = 3$ in arbitrary units (a.u.). Figure 4.2a illustrates the effect of attenuation, which causes the intensity to decrease exponentially with wave travel distance x, while Figure 4.2b shows how geometrical focusing results in an intensity decrease with focal distance F following a quadratic decrease. In addition, attenuation causes the spatial peak intensity to drop with increasing frequency. Conversely, the intensity increases with frequency due to the decrease in spot size with increasing frequency, resulting from geometrical focusing. Therefore, an optimum frequency value for spatial peak intensity in the focal spot can be found.

4.2.3   Transient acoustic heating

From the intensity equations, the temperature increase in the focal spot can be derived. The coupling between acoustic energy and volumetric heat generation is defined by a volumetric heat source, which is determined by the absorption of acoustic energy in the material. The heat source is given by $Q(r) = \alpha_{\mathrm{abs}} \langle I(r) \rangle$, where $Q(r)$ is the volumetric heat source, α_{abs} is the absorption coefficient in units of reciprocal meters, and $\langle I(r) \rangle$ is the time-averaged acoustic intensity field. For continuous waveforms, the time-averaged acoustic intensity equals the spatial acoustic intensity, $\langle I(r) \rangle_{\mathrm{CW}} = I(r)$.

An analytical solution proposed by Goldenberg [150] can be used to calculate the temperature increase in an infinite medium when the initial temperature is zero. The solution assumes a constant heat rate denoted by Q, in a spherical region from 0 to a distance of a_s, for $t > 0$, with $a_s = 0.618 D_{\mathrm{spot}}$. To use this solution, the intensity field due to focusing is simplified to a uniform spherical spot with a radius of a_s. Within the spherical spot, Q depends on the absorption coefficient (α_{abs}) and the incident intensity (I_{SP}). Specifically, the heat rate is given by $Q = \alpha_{abs} I_{SP}$ if $0 \leq r \leq a_s$, and $Q = 0$ if $r > a_s$. Appendix 4.A discusses this spherical source approximation. A transient analytical solution for the stationary temperature increase of the form $\Delta T_s(r,t) = A_s \mathcal{G}(r^*, t^*)$ follows from this, with $A_s = Q a_s^2 / (2K)$ the stationary temperature increase amplitude, and the normalized radius and time are given by $r^* = r/a_s$ and $t^* = t\kappa/a_s^2$, respectively [150]. Herein, the thermal diffusivity is given by $\kappa = K/(\rho_0 c_p)$, where K is the thermal conductivity and $\rho_0 c_p$ is the volumetric specific heat. The dimensionless function $\mathcal{G}(r^*, t^*)$ is given in Appendix 4.A. This dimensionless function converges at small times to $\lim_{t^* \to 0} \mathcal{G}(r^*, t^*) = 2t^*$ within the focal region $0 < r^* < 1$. In homogeneous solids where $\alpha \approx \alpha_{abs}$, this results in the simplified expression for stationary temperature increase:

$$\Delta T_s(t) = \frac{\alpha I_{\mathrm{SP}} t}{\rho_0 c_p}, \tag{4.7}$$

for $t^* \ll 1$ and $0 < r^* < 1$. In this simplified version of the transient heat equation, the error is less than ten percent compared to the full version when $t^* < 0.1$ (see Appendix 4.A for details).

4.2.4   Heating with a moving acoustic intensity spot

The acoustic intensity source is scanned throughout the volume instead of heating a stationary focal spot. This is modeled in a way that a spherical spot moves over a line with a constant velocity of v_{scan}, as shown in Figure 4.3a. The cylindrical coordinate system (x_c, r_c) is introduced, with x_c as the scan direction and r_c as the cylindrical radius. By scanning the spot through fixed points $\mathcal{P}_i(x_0, r_c)$, which are positioned on the cylindrical radius between $0 \leq r_c \leq D_{\mathrm{spot}}/2$, the heating time for each of these points can be evaluated. The heating
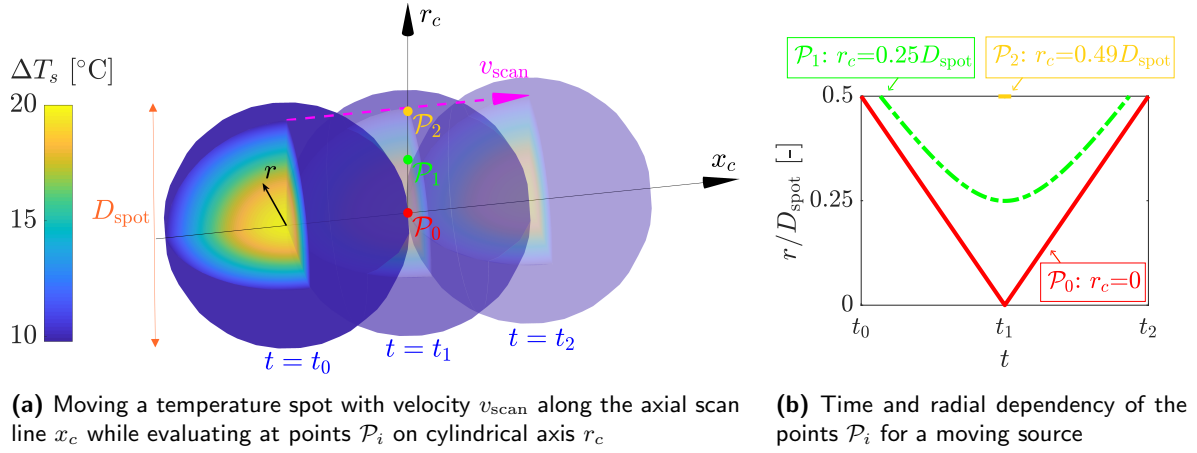
(a) Moving a temperature spot with velocity v_{scan} along the axial scan line x_c while evaluating at points $\mathcal{P}_i$ on cylindrical axis r_c

(b) Time and radial dependency of the points $\mathcal{P}_i$ for a moving source

Figure 4.3: The diagram illustrates how the temperature increase of a moving spot (ΔT) can be determined by using the stationary temperature increase (ΔT_s). It shows the movement of the spot through different points $\mathcal{P}_i$ over time. It is important to note that the contact duration between the spot and each point ($\Delta t_{\text{spot}}(r_c)$) differs. Furthermore, the spherical radius (r) perceived by a point varies depending on its cylindrical position (r_c). To calculate the temperature increase of a moving spot, the contact duration and average radius are used to find $\Delta T(r_c) = \Delta T_s(\langle r \rangle, \Delta t_{\text{spot}})$.

time, Δt_{spot}, is then a function of the cylindrical radius of these points, the spot size, and the scan velocity v_{scan}, according to the following equation: $\Delta t_{\text{spot}} = \sqrt{D_{\text{spot}}^2 - (2r_c)^2}/v_{\text{scan}}$. As r_c increases from $\mathcal{P}_0$ to $\mathcal{P}_2$, the time that the spherical spot is in contact with the point decreases. This is shown in Figure 4.3b by the length of the lines. The maximum temperature increase is found at $r_c = 0$, where $\Delta t_{\text{spot,max}} = D_{\text{spot}}/v_{\text{scan}}$.

While scanning, the temperature increase rate in the focal region is not constant. This is due to the radial dependence in the stationary temperature increase equation. However, this radial dependence drops out in the simplified temperature equation in Equation (4.7). By defining a time-averaged spherical radius $\langle r \rangle$, it follows that the minimum averaged spherical radius resulting in the maximum temperature increase is given by $\langle r \rangle_{\text{min}} = D_{\text{spot}}/4$. Appendix 4.A gives more details on the time-averaged spherical radius. Since, on average, the spherical radius is smaller than a_s, the simplified temperature increase in Equation (4.7) can be used to approximate the temperature increase of a moving acoustic focal spot if $t^* \ll 1$. Therefore, the spatial peak temperature increase, ΔT_{SP}, for a moving acoustic focal spot then follows from:

$$\Delta T_{\text{SP}} = \underbrace{\frac{P_0}{\rho_0 c_p v_{\text{scan}}}}_{\text{I}} \underbrace{A(f, c_0, \alpha, F)}_{\text{II}} \underbrace{\mathcal{F}(\xi)}_{\text{III}}, \tag{4.8}$$

where

$$A(f, c_0, \alpha, F) = \frac{f\alpha}{c_0 \exp{(\alpha F)}}. \tag{4.9}$$

The equation above is made up of three terms. I is an energy term with a unit of $1/\text{m}^2$. It contains the line energy input $E_l = P_0/v_{\text{scan}}$ and the volumetric specific heat. As per the Dulong-Petit law, $\rho_0 c_p \approx 3 \text{ MJ}/(\text{m}^3\text{K})$ for all solids [160]. Since the volumetric specific heat for solids in practice varies only slightly from about 1 to 5 $\text{MJ}/(\text{m}^3\text{K})$ [161, 162], this constant value is used in this paper. II is a frequency- and material-dependent function A

in Equation (4.9), which relates to intensity gains and losses described in Section 4.2.2. III is a dimensionless transducer size-dependent function $\mathcal{F}(\xi)$. For $\xi = 2$, corresponding to 12 transducers closely packed on a sphere, $\mathcal{F}(2) \approx 0.84$. It is assumed that Equation (4.8) also applies to a transducer consisting of many smaller elements. With such a phased array configuration, scanning an ultrasound beam throughout the volume is possible if ξ is small and the transducer radii are large. When ξ is large, the transducer configuration can be regarded as a phased array since many small transducers are positioned on the sphere. This study focuses on material dependency, and a constant $\xi = 2$ is chosen to minimize the spot size.

4.2.5   Maximum temperature increase

The geometrical focusing and attenuation have an opposite frequency dependency. This frequency dependency of the temperature increase of a moving spot is found in Equation (4.9). Therefore, an optimum frequency exists for the temperature increase of a moving spot, as shown in Figure 4.4a. The optimum frequency for heating at a constant power and scan velocity, f_{opt}, is found for the power-law type of attenuation in Equation (4.5) as $f_{\mathrm{opt}} = [(1/y + 1)/(F\alpha_y)]^{1/y}$, with $0.5 \leq y \leq 4$ for solids. At this optimal frequency, the attenuation is given by $\alpha(f_{\mathrm{opt}}) = (1/y + 1)/F$. This shows that to achieve optimal printing results in SAS, it is essential to consider the relationship between the acoustic material parameters and the printer dimensions. This is because the ideal attenuation coefficient of a material is inversely proportional to the focal distance and printer size. Therefore, finding the optimal printing parameters requires understanding the coupling between the printer dimensions and the acoustic material properties.

The SAS 3D printer allows for manual power and scan velocity adjustment to find the best print settings, resulting in the highest temperature increase at the focal spot. However, the temperature increase relation in Equation (4.8) only applies within a specific range of input powers and scan velocities. Therefore, to compare SAS printing for different materials using this relation, it is necessary to identify the maximum allowable power and minimum allowable scan velocity that provide maximum temperature increase.

To derive Equation (4.7), a linear temperature increase ($t^* \ll 1$) has been assumed wherein the heating process is faster than thermal diffusion. To meet this criterion, a minimum scan velocity is defined as:

$$v_{\mathrm{scan,min}} = \frac{K}{\rho_0 c_p} \frac{2f}{t^*_{\max} 0.618^2 c_0 \xi}, \tag{4.10}$$

with $t^*_{\max} = 0.1$ the upper limit for a linear temperature increase. It is also assumed that nonlinear wave propagation is negligible, which means there is a maximum allowable total power for linear wave propagation. To determine this, the nonlinear parameter $N = F/x_s$ is introduced from the axially symmetric Khokhlov-Zabolotskaya-Kuznetzov (KZK) equation [151–153]. This equation uses a parabolic approximation of diffraction effects and includes nonlinear wave propagation, where x_s corresponds to the shock formation distance for an initially harmonic plane wave. The nonlinear parameter is derived using the material property for nonlinearity (i.e., the coefficient of nonlinearity) $\beta = 1 + \frac{B}{2A}$ and is given by $N = 2\beta p_0 \pi f F/(c_0^3 \rho_0)$. Here, $p_0 = \sqrt{2\rho_0 c_p P_0/S}$ is the power-equivalent average pressure over the surface of the transducer [155, 163]. nonlinear effects can be ignored for nonlinear parameters much smaller than one. The linear wave equations result in less than 10 % error if $N < 0.1$ even for large linear focal gains $kh < 100$, as shown in the work of Bessonova

(a) Constant power and velocity

(b) Maximum power and minimum velocity
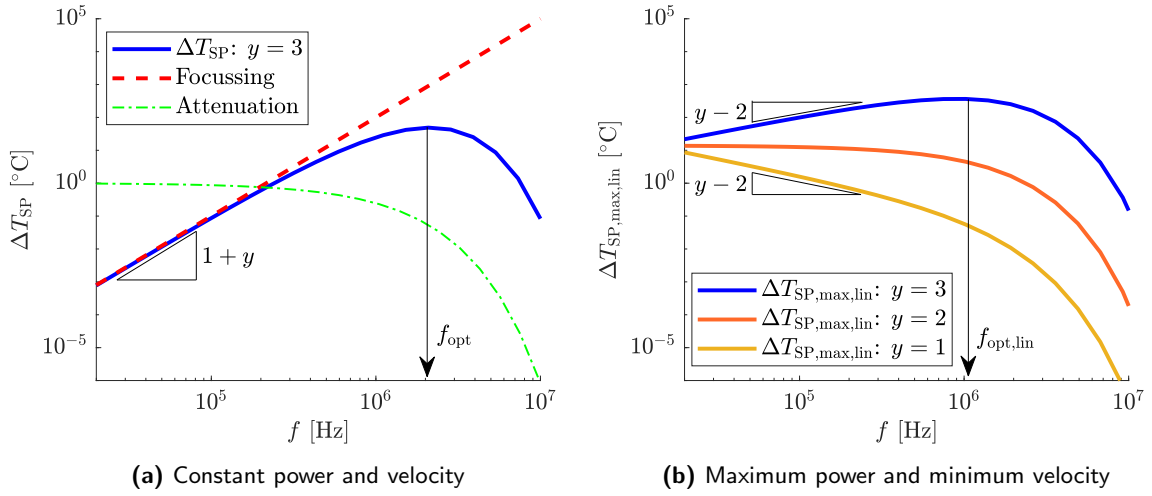
Figure 4.4: The graphs show the relationship between the frequency and spatial peak temperature increase in SAS. In (a), the temperature increase at a constant power and scan velocity is shown for materials with an attenuation power-law coefficient of $y = 3$. In this case, it can be observed that there is an optimal frequency at f_{opt}. On the other hand, in (b), the temperature increase is shown at maximum power and minimum scan velocity. Here, it is notable that there is only an optimum frequency ($f_{\mathrm{opt,lin}}$) found for materials with $y > 2$.

et al. [153]. Therefore, the maximum total power at the surface for linear wave propagation is given by:

$$P_{0,\mathrm{max,lin}} = \frac{N_{\mathrm{max}}^2 \rho_0 c_0{}^5}{4\beta^2 f^2 \pi^2} \frac{\mathcal{F}(\xi)}{\xi}, \tag{4.11}$$

where $N_{\mathrm{max}} = 0.1$. The nonlinear coefficient β depends on the speed of sound, density, and temperature of a material. Measurements have shown that it ranges from $\beta \approx 1$ for relatively large speed of sound values (i.e., metals) to $\beta \lesssim 10$ for low speed of sound values (i.e., polymers) [164, 165]. Measurement techniques for nonlinear coefficients in solids have limitations and lead to uncertainties, as discussed by Panfilova et al. [166]. Therefore, this work uses the limiting nonlinear coefficient of $\beta = 10$ throughout the analysis.

By substitution of the minimum scan velocity and the maximum total power in Equation (4.8), the maximum achievable temperature increase in the linear regime can be derived as:

$$\Delta T_{\mathrm{SP,max,lin}} = \mathcal{C}_{\mathrm{max}} \, B(K, \rho_0, \beta) \, A_{\mathrm{max}}(f, c_0, \alpha, F) \, \mathcal{F}(\xi)^2, \tag{4.12}$$

with

$$\mathcal{C}_{\mathrm{max}} = \frac{0.618^2 N_{\mathrm{max}}^2 t_{\mathrm{max}}^*}{8\pi^2}, \tag{4.13}$$

$$B(K, \rho_0, \beta) = \frac{\rho_0}{K\beta^2}, \tag{4.14}$$

$$A_{\mathrm{max}}(f, c_0, \alpha, F) = \frac{c_0^5 \alpha}{f^2 \exp(\alpha F)}, \tag{4.15}$$

a constant, a thermal-acoustic term, and a frequency-dependent term, respectively. The term A_{max}, dependent on frequency, contains a denominator with a squared frequency term because the total power increases to its maximum as the frequency decreases. Therefore, for

materials with power-law coefficients of two or less ($y \leq 2$), it is best to minimize the frequency to achieve maximum temperature increase, as illustrated in Figure 4.4b. For $y \leq 2$, the optimal attenuation coefficient is $\alpha = 1/F$ at constant frequency. On the other hand, for materials with power-law coefficients greater than two ($y > 2$), it has been found that the optimal frequency for maximum temperature increase in the linear regime is given by $f_{\text{opt,lin}} = [(1 - 2/y)/(F\alpha_y)]^{1/y}$. At this optimal frequency, the attenuation coefficient is given by $\alpha(f_{\text{opt,lin}}) = (1 - 2/y)/F$. This indicates, once again, that the optimal attenuation coefficient of a material is inversely proportional to the focal distance and, consequently, the size of the printer.

4.3   Feasibility of SAS

To evaluate the feasibility of using a specific material, printer size, and resolution for SAS printing, it is necessary to compare the maximum temperature increase to the required temperature increase for melting, represented as ΔT_{liq}. In case the material shows a significant temperature rise while scanning ($\Delta T_{\text{SP}} > \Delta T_{\text{liq}}$), it is feasible to print with SAS.

A flowchart has been created to test this feasibility criterion of the SAS 3D printing process, as illustrated in Figure 4.5. The flowchart starts with the user input, where the user selects the part, the resolution, and the material. The flowchart can be followed for this combination of inputs to determine if this combination results in a feasible print with the SAS printer. The size of the part and the desired resolution determine the required focal distance and maximum spot size, respectively.

To follow the diagram further, the user has to proceed from left to right: (A) thermal analysis, (B) acoustic analysis, and (C) transducer configuration analysis. In step (A), represented by the yellow box, the thermal analysis is done based on the material input. First, the melting temperature T_{liq} needs to be measured using calorimetry techniques. If a material cannot melt or return to its original state after melting, it is unsuitable for SAS. By selecting an initial temperature of the build volume T_0, the temperature increase required for melting is defined as $\Delta T_{\text{liq}} = T_{\text{liq}} - T_0$. The thermal diffusivity can be evaluated using thermal conductivity measurements, resulting in the volumetric heat capacity and the thermal conductivity used in the temperature increase equation (4.8).

The acoustic analysis is summarised in step (B) in blue in Figure 4.5. All user input parameters are required for this analysis. The measurements of the acoustic material properties are crucial, as they determine the best frequency for printing with the input conditions and the resulting peak temperature increase and resolution. The following procedure can be followed to perform the acoustic analysis:

1. To determine the spot size, it is necessary to know the speed of sound of the material. Assuming the media is nondispersive, the speed of sound is independent of the frequency. Therefore, the first step is to measure the speed of sound at a constant frequency, typically in orders of megahertz (at T_0). These acoustic measurements can be performed using pulsed-echo or through-transmission characterization techniques. The minimum frequency required to acquire the input spot size is given by the formula $f_{\text{spot,min}} = c_0\xi/(2D_{\text{spot,in}})$, which is dependent on the dimensionless transducer radius (ξ). Initially, a value of $\xi = 2$ is assumed to minimize this frequency, with transducer configuration to be discussed later. Based on the assumption presented in Equation (4.2), the minimum frequency for the measurement can be determined

from $f_{\text{meas,min}} = \max(f_{kh,\text{min}}, f_{\text{spot,min}})$. The maximum frequency of the measurement $f_{\text{meas,max}}$ has to be larger than the minimum frequency. A typical practice is to set it one order of magnitude higher [158]. The frequency range for acoustical property measurements is between $f_{\text{meas,min}}$ and $f_{\text{meas,max}}$ at temperature T_0. Measuring the speed of sound, attenuation, and nonlinear coefficient within this frequency range is necessary. Note that these measurements for powder-based materials are nontrivial, as powders are nonhomogeneous media with intrinsically increased attenuation due to the scattering of ultrasound waves. Therefore, the effects of porosity and filler materials are crucial for material selection in SAS 3D printing.

2. To identify the best frequency f_{best} that maximizes the temperature increase at the focal spot, the acoustic properties must be substituted in A_{max} into Equation (4.15). An optimum frequency is found if A_{max} has a maximum within the measured frequency range. If the slope of this function is positive at the maximum measuring frequency, the acoustic property measurement should be repeated by expanding the frequency range. On the other hand, if the slope is not positive at the maximum frequency, the minimum measured frequency is chosen as the best frequency for maximizing the temperature increase.

3. The material-term at the best frequency $A_{\text{max}}(f_{\text{best}})$, the thermal- and acoustic properties and $\mathcal{F}(2) = 0.84$ are then used to estimate the maximum temperature increase in Equation (4.12). If $\Delta T_{\text{SP,max,lin}} > \Delta T_{\text{liq}}$, printing with SAS is theoretically feasible for the given input parameters for a system with a dimensionless transducer radius of $\xi = 2$.

In step (C), shown in pink in Figure 4.5, the analysis of transducer configuration is provided. While it is theoretically possible to print, the system has some practical limits. First, it is assumed that $\xi = 2$ can be used. However, this results in problems with fabricating the transducers for high frequencies and large focal distances, as fragile piezoelectric elements are required. If this condition is not met, the analysis has to be repeated with a different value for ξ. Additionally, if ξ and the number of transducers M are large, the spot size no longer follows the relation in Equation (4.1). In such cases, the transducers are essentially elements positioned in a phased array at the entire sphere surface. The distance between the transducers, rather than the size, is dominant in determining the spot size. These transducer configurations are to be studied to find the proper relation for the resolution, including the number of transducers. A more in-depth analysis of the transducer configuration on the spot size and intensity amplitude may be performed using numerical simulations, where interference effects can be studied.

The last step is to evaluate the maximum total power and minimum scan velocity. Theoretically, power consumption in the order of megawatts is possible. However, practically, this is undesired. So, the total power must be reduced and set to a constant value. By changing the limit in power, the complete analysis has to be repeated because scalings with frequency change if a constant power is used, as explained in Section 4.2.4. On the other hand, for lower power consumption, the total power could be increased beyond the maximum linear limit, as nonlinear effects can be beneficial for maximizing the temperature increase at the focal spot. This process will be discussed later.

When the assumptions are valid, and the conditions are met, the final spatial peak temperature increase in Equation (4.8) follows from combining the results of (A), (B), and (C).
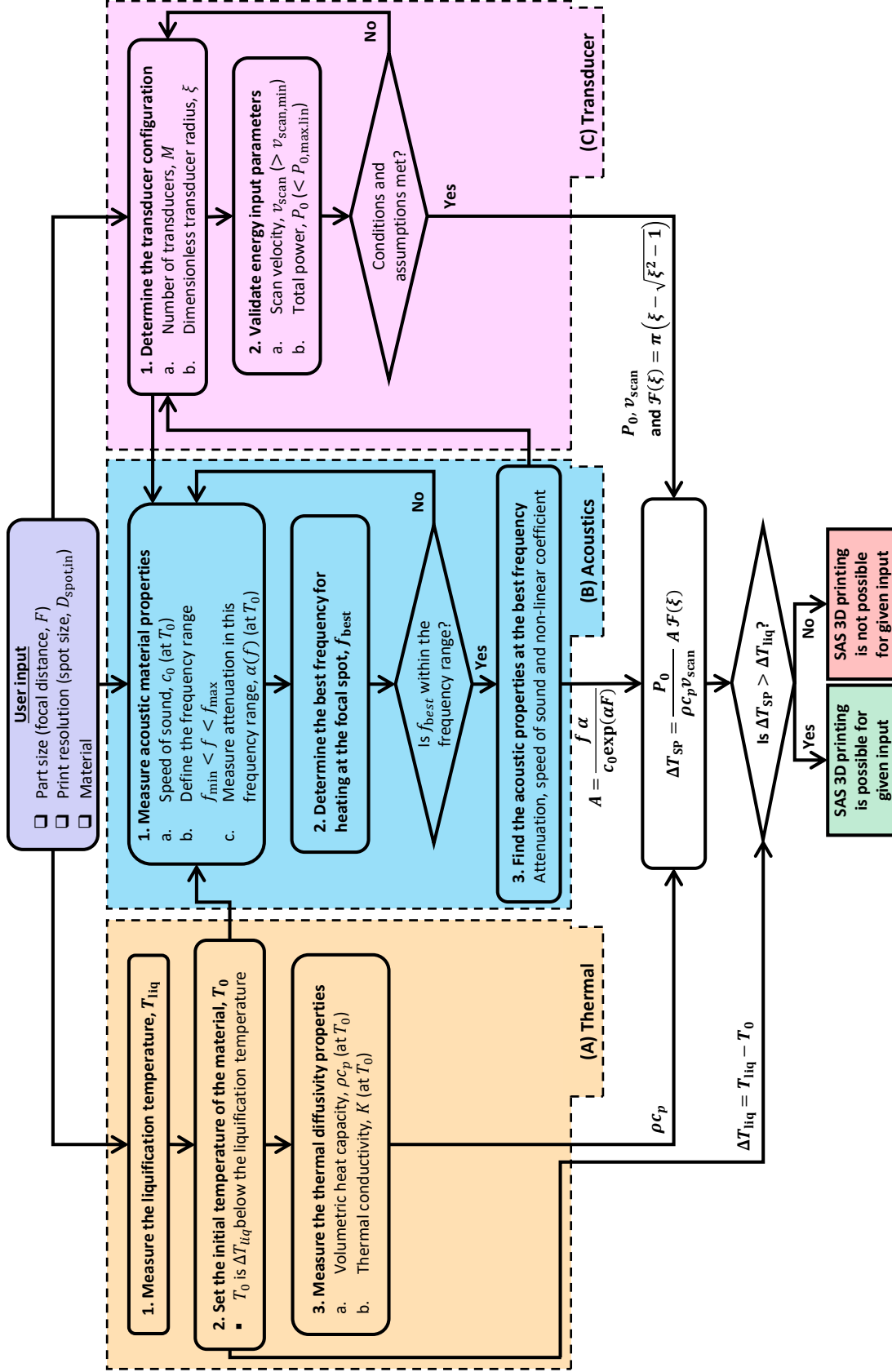
Figure 4.5: This flowchart outlines a step-by-step process for validating the feasibility of printing with a spherical SAS 3D printer. The user input, which includes the part size, resolution, and material, is analyzed by measuring and evaluating thermal, acoustic, and transducer properties. These properties are then combined to calculate the temperature increase using Eq. (4.8). Printing is feasible if the calculated temperature increase is sufficient to liquefy the material.

The printing feasibility is evaluated solely based on the melting temperature, $\Delta T_{SP} > \Delta T_{liq}$. Hence, eventually, if the spatial peak temperature increase in the focal spot is larger than the required temperature increase for melting, SAS 3D printing is possible for the user input values. If the determined temperature increase is far beyond the melting temperature, the line energy input $E_l = P_0/v_{scan}$ can be decreased, or the spot size can be reduced by increasing the frequency.

4.4 Applicability of SAS

To evaluate the performance of a material within given printer dimensions, it is essential to consider both the resolution and temperature increase. A material performs better when both the resolution (calculated using Equation (4.1)) and temperature increase (computed using Equation (4.12)) are maximized. It is worth noting that the frequency-dependency of these equations indicates that the resolution is maximized when the frequency is increased. However, there is a nonlinear relationship between the temperature increase and frequency. This section aims to determine the applicability of different materials in the SAS printer. To achieve this, optimal performance must be evaluated with regard to temperature increase. Therefore, the maximum total power and minimum scan velocity are necessary to estimate the theoretical maximum temperature increase. So, Equation (4.12) is used in the following analysis.

4.4.1 Material selection

Considering compacted powder-based materials in the analysis is essential because the SAS 3D printer uses powder-based materials to sinter. However, acoustic literature data for compacted powder-based materials is lacking. Nonetheless, some statements can be made about the impact of using powders. The difference in acoustic impedance between powder particles and the pore material leads to frequency-dependent scattering, drastically limiting energy transmission. Hence, noncompacted powders with large porosities of 40-50% limit the printer size and are nonoptimal in that sense. To reduce this scattering, compaction can decrease porosity, or a filler material with a better impedance match can be used. Liquids have smaller attenuation, speed of sound, and specific volumetric heat than solids, making them good candidates as filler materials in SAS. A liquid filler could also be initially a solid filler at room temperature that is molten at the initial temperature ($T_L < T_0$). The scattering power-law coefficient can vary depending on the diameter of the powder relative to the wavelength. Rayleigh scattering with a power-law scattering coefficient of $y_{scatter} = 4$ is dominant for powder diameters smaller than the wavelength. This scattering regime is expected in SAS, where the spot size is approximately the same as the wavelength of the transducer, and the powder diameter has to be smaller than the spot size.

To improve the transmittance of ultrasound energy, the build volume is expected to consist of a dense matrix of compacted powder with a small fraction of filler material. The material properties of such systems are close to the solid matrix properties. Therefore, a pre-selection of materials can be done by evaluating solid materials. For solid materials, thermal and acoustic material properties are measured in several literature sources [158, 159, 162, 167–175]. A dataset comprising thermal and acoustic properties of 458 solids at room temperature has been compiled from these measurements. The complete dataset is available as supplementary content online. A selection of promising materials (Table 4.1) is used to study applicability

Table 4.1: This table lists acoustic and thermal materials properties for promising materials in SAS 3D printing. Volumetric specific heat and nonlinearity parameters are assumed to be $\rho_0 c_p = 3$ MJ/(m^{3}K) and $\beta = 10$, respectively, and $a_0 = 0$ and $a_3 = 0$ for the selected materials.

Name	ρ_0	c_0	a_1	a_2	a_4	α_y (y)	K	T_{liq}
	[kg/m^3]	[m/s]	[1/(Hz^{1}m)]	[1/(Hz^{2}m)]	[1/(Hz^{4}m)]	[1/(Hz^{y}m)] ([-])	[W/(Km)]	[°C]
Pyrex glass	2230	5520	2.42E-6	0	0	0	1.1	1250
Iron (ductile)	7150	4650	0	5.46E-12	0	0	32	1538
Steel SS302	7920	5870	4.28E-6	0	0	0	16	1430
Aluminum 6061	2700	6350	3.32E-6	0	0	0	167	635
Inconel 718	8190	5790	3.62E-6	0	5.11E-28	0	10	1300
PEI	1280	2430	2.22E-5	0	0	0	0.22	320
HDPE	953	2432	0	0	0	9.10E-8 (1.39)	0.4	130
PCL	1145	2300	2.32E-5	0	0	0	0.3	60
PEEK	1252	2586	0	0	0	2.15E-3 (0.70)	0.25	340
PPS	1359	2496	0	0	0	2.99E-4 (0.77)	0.35	280
Inconel 738(T)	8110	5730	0	0	2.88E-26	0	10	1300

in 3D printing. In the following study, a distinction will be made between the materials with nearly linear power-law exponents of $y \leq 2$ and the ones with highly nonlinear power-law exponents $2 < y \leq 4$, as they require different optimization in terms of frequency (see Figure 4.4b). The effect of focal distance and material properties on the temperature increase will be discussed.

4.4.2 Material performance of nearly linear attenuating materials

Figure 4.6a shows the maximum linear temperature increase as a function of resolution for these promising materials with nearly linear attenuation exponents $y \leq 2$. Herein, the materials are compared at the best frequency for maximizing temperature increase. For $y \leq 2$, this means that the maximum temperature increase and resolution are determined by using the minimum frequency $f_{kh,\min}$ as the best frequency, resulting in:

$$\text{Res}(f_{\text{best}}) \sim \frac{1}{F} \qquad \text{for } y \leq 2, \qquad (4.16)$$

$$\Delta T_{\text{SP,max,lin}}(f_{\text{best}}) \sim \frac{\rho_0}{\beta^2 K} \frac{\alpha_y F^{2-y} c_0^{3+y} C_{\mathcal{F}}^{y-2}}{\exp\left(\alpha_y F^{1-y} c_0^y C_{\mathcal{F}}^y\right)} \qquad \text{for } y \leq 2, \qquad (4.17)$$

with the constant $C_{\mathcal{F}} = kh_{\min}/\mathcal{F} \approx 41.6$ for $\xi = 2$. It becomes apparent from the first equation that resolution is inversely proportional to focal distance and does not depend on any of the material properties. Hence, to determine which material performs best for $y \leq 2$, the maximum temperature increase is the only important function.

The performance of a material depends on the focal distance, as shown in Figure 4.6a. From Equation (4.17) it follows that the temperature increase scales with the focal distances according to $\Delta T_{\text{max,lin}}(f_{\text{best}}) \sim F^{2-y} \exp\left(-\tau F^{1-y}\right)$, with $\tau = \alpha_y c_0^y C_{\mathcal{F}}^y$. This relation shows that the attenuation power-law coefficient changes the curves' shape in Figure 4.6a. For materials with $y < 1$ (e.g. PEEK), an optimal focal distance exists and can be found from $F_{\text{opt}} = (\tau(1-y)/(2-y))^{1/(y-1)}$. For PEEK, this optimum is approximately $F_{\text{opt}} \approx 0.1$ m, which indicates that PEEK performs best at this specific printer size. However, for materials with $1 \leq y \leq 2$, the temperature increase grows for increasing focal distance, independent of
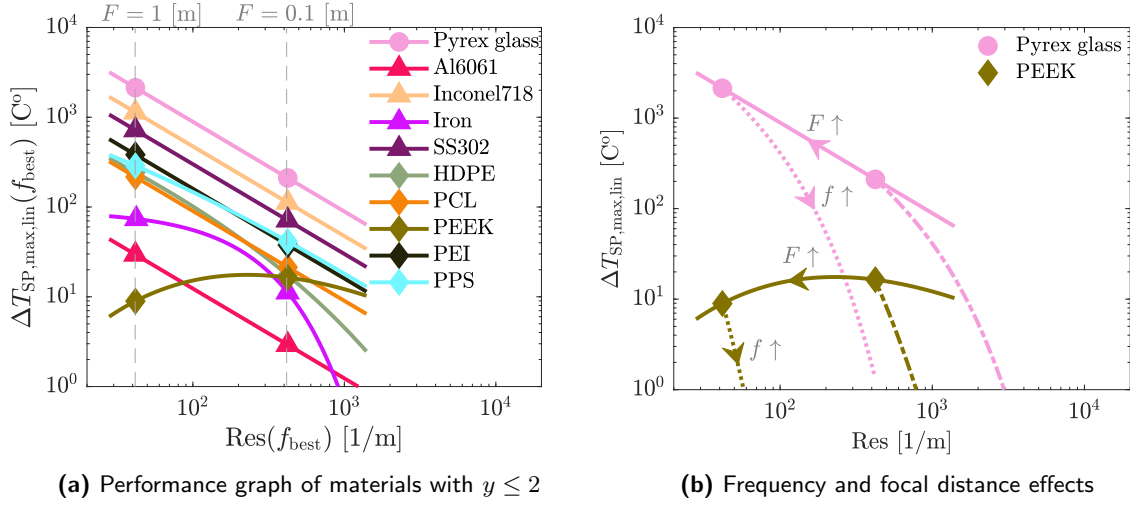
(a) Performance graph of materials with $y \leq 2$ **(b)** Frequency and focal distance effects

Figure 4.6: The graph shows the maximum temperature increase as a function of resolution for materials with a power-law coefficient $y \leq 2$. In (a), the maximum temperature increase is evaluated at the best frequency $f_{kh,\min}$, as the power-law coefficient $y \leq 2$ for these materials. Thus, the resolution is $\mathrm{Res} = 41.6/F$. Therefore, the lines in this graph can be used to determine the performance of a material for a given focal distance. The markers indicate $F = 1$ and 0.1 m from left to right. In part b), the maximum temperature increase is evaluated at these focal distances ($F = 1$ or 0.1 m) for increasing frequency. The dashed lines, starting from the best frequency indicated by the markers, show the temperature decrease following a frequency increase of one order of magnitude. The resolution increases linearly with the frequency increase according to Equation (4.1). Therefore, improving the resolution by increasing the frequency is inefficient, leading to a drastic drop in the maximum temperature increase.

the other material properties. Hence, no optimal focal distance exists, and these materials perform best at large printers. This seems counter-intuitive, but it is due to the decrease in minimum frequency $f_{kh,\min}$ with increasing focal distance. Lowering the frequency reduces the minimum scan velocity and increases the maximum allowable power.

Figure 4.6a shows that various materials can achieve a maximum temperature increase of over 100 °C. This analysis is based on a single-line scan and assumes a temperature increase in the linear regime. However, this can be extended to overlapping scans or a nonlinear regime, where higher temperature increases are possible. As a result, different material classes, such as metals, polymers, and ceramics, can be used in the SAS printing process. Ceramic glasses, such as Pyrex glass or Soda-lime glass, are particularly noteworthy as they can achieve theoretical temperature increases of over 1000 °C in the linear regime. In addition, Inconel718 is an exciting material for aerospace industries. Several polymers, including polyphenylene sulfide (PPS), high-density polyethylene (HDPE), polyethyleneimine (PEI), and Polycaprolactone (PCL), are also suitable for specific configurations of the SAS 3D printer. Note that the feasibility of printing with any of these materials depends primarily on their acoustic frequency dependency with respect to the focal distance. If the temperature increases beyond the melting temperature, it is possible to decrease the spot size by increasing the frequency.

Figure 4.6b shows the effect of increasing frequency on the maximum temperature and resolution for Pyrex glass and PEEK. The dashed lines, starting from the best frequency at $F = 1$ and 0.1 m as indicated by the markers, demonstrate the temperature reduction after a frequency increase of one order of magnitude. The resolution increases linearly with the

frequency increase, as shown by Equation (4.1). However, while increasing the frequency can improve resolution, it results in a significant drop of three orders of magnitude in terms of the maximum temperature increase. Therefore, improving the resolution by increasing the frequency is inefficient for materials with $y \leq 2$. This implies that materials with $y \leq 2$ have a resolution limit of about $1/50$ times the focal distance ($\chi \approx 41.6$).

Regarding material properties, it follows from Equation (4.17) that materials with relatively low thermal conductivity K and nonlinear coefficient β in combination with large density ρ perform best in terms of temperature increase. Metals have a far-from-ideal thermal conductivity, which is about 10 to 1000 times larger than polymers and glass ceramics, and hence, larger minimum scan velocities are required, decreasing the maximum temperature increase. The speed of sound c_0, power-law attenuation coefficient α_y, and power-law exponent y relate to the maximum temperature more complexly, depending on the focal distance. In an attempt to explain the effectiveness of these properties, a minimum and maximum range for a combination of these parameters is derived from Table 4.1 resulting in $10^{-7} < \alpha_y^{1/y} < 10^{-4}$, and $2000 < c_0 < 7000$. The resulting $A_{\max}(f_{\text{best}}$ for $y \leq 2$ for $F = 0.1$ and 1 [m] are given in Figure 4.7. In this figure, the color map indicates the material-dependent temperature increase factor $A_{\max}$, evaluated at the best frequency $f_{kh,\min}$. This map shows that the tem-

(a) Material property dependency of $A_{\max}$ for $F = 1$ [m] and $y \leq 2$

(b) Material property dependency of $A_{\max}$ for $F = 0.1$ [m] and $y \leq 2$

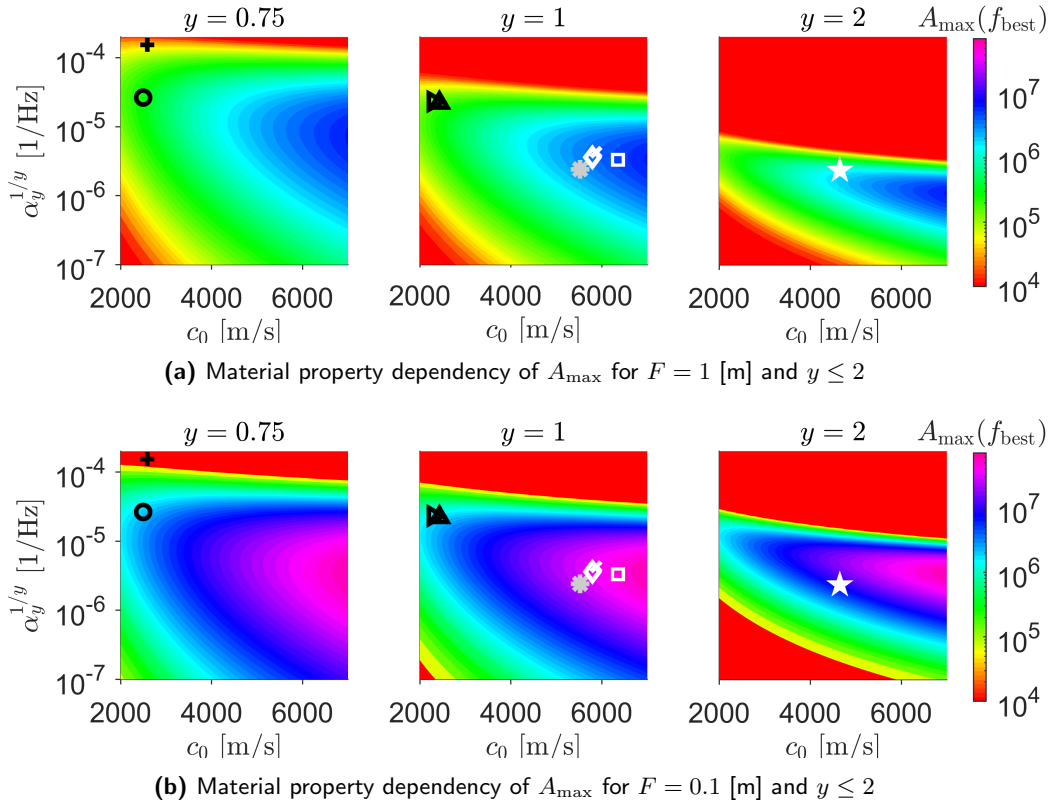**Figure 4.7:** Effect of acoustic material properties on material performance with $y \leq 2$ in SAS 3D printing. A large value of $A_{\max}$ results in an enhanced temperature increase in the focal region. The markers indicate acoustic data from the literature, where black markers indicate the polymers $0.7 \leq y \leq 1$, the grey marker is the ceramic Pyrex glass $y = 1$, and the white markers are metals $1 \leq y \leq 2$.

perature increase is maximized at the large speed of sound values and that an optimum of $\alpha_y^{1/y}$ exists. The location of this optimum in the maps depends on the focal distance F, speed of sound c, and the power-law exponent y. The figure also includes the material properties from the selected materials in Table 4.1 as markers. Black markers indicate the polymers $0.7 \leq y \leq 1$, the grey marker is the ceramic Pyrex glass $y = 1$, and the white markers are metals $1 \leq y \leq 2$. For the selected metals and ceramic glass, the attenuation coefficient is close to optimal for the corresponding speed of sound at the given focal distances. However, the attenuation coefficient for the polymers is 10 to 100 times as large as the optimum. The polymer's relatively low speed of sound results in a factor ten reduction in temperature increase compared to the selected metals and ceramic glass. This brings us to the following conclusions about the selected materials with $y \leq 2$:

- Acoustic material properties of metals and ceramic glasses are in terms of attenuation coefficient ideal for printers with a size of 0.1 to 1 m. They gain from their large speed of sound in combination with the relatively small attenuation coefficient. A large density of these materials is also beneficial. However, metals have a relatively large thermal conductivity compared to other material classes. Hence, the temperature increase is mainly limited by the thermal conductivity. A material property optimization could be performed by changing from a solid to a filled powder-based description of the material, as powders inhibit a lower thermal conductivity but suffer from increased attenuation and decreased speed of sound.

- Acoustic material properties of polymers are worse regarding attenuation coefficient, as the large attenuation value is unsuitable for the 0.1 to 1 m build volumes. Besides, the speed of sound and density are relatively small. However, polymers have a relatively low thermal conductivity, allowing for slow printing speeds and sufficient temperature increase for melting. Moving to powder-based polymers would require limiting scattering as much as possible by compaction and filler material while regulating the already excessive attenuation coefficient. This regulation depends on the desired part size, as smaller parts require increasingly larger attenuation coefficients.

4.4.3   Material performance of highly nonlinear attenuating materials

The temperature increase relations change for materials with highly nonlinear power-law attenuation with $y > 2$. This nonlinear attenuation is found throughout all material classes, especially at frequencies above 5-10 MHz, resulting from random scattering centers such as grain-boundary and distributed second-phase particles [158, 176]. Such materials have an optimum frequency $f_{\mathrm{opt,lin}}$, according to Equation (4.15). To find the effect of the focal distance and material properties on the performance of these materials, the resolution and the maximum temperature increase at the best frequency $f_{\mathrm{best}} = f_{\mathrm{opt,lin}}$ can be derived as:

$$\mathrm{Res}(f_{\mathrm{best}}) \sim \frac{(1 - 2/y)^{1/y}}{c_0 (F \alpha_y)^{1/y}} \qquad \text{for } y > 2, \qquad (4.18)$$

$$\Delta T_{\mathrm{SP,max,lin}}(f_{\mathrm{best}}) \sim \frac{\rho_0}{\beta^2 K} \frac{\alpha_y^{2/y} F^{2/y - 1} c_0^5}{(1 - 2/y)^{1/y} \exp{(1 - 2/y)}} \qquad \text{for } y > 2. \qquad (4.19)$$

Herein, the resolution is inversely proportional to the acoustic material properties c_0 and $\alpha_y^{1/y}$, while the temperature increase is proportional with c_0^5 and $\alpha_y^{2/y}$. As the scaling of

these material properties with resolution and temperature increase are inverted, no optimal attenuation coefficient or speed of sound exists in terms of performance. However, increasing the speed of sound and attenuation coefficient are effective strategies to enhance the maximum temperature increase for these materials. Like materials with $y \leq 2$, the material performance increases for a relatively large density and nonlinearity coefficient in combination with low thermal conductivity.

Figure 4.8a illustrates how the temperature increase varies with focal distance for $y > 2$. The graph compares the maximum temperature increase at the optimum frequency $f_{\mathrm{opt,lin}}$ with the minimum frequency $f_{kh,\mathrm{min}}$ for Inconel738(T) $y = 4$. For small printers ($F < 5$ cm), the optimum frequency is lower than the minimum frequency, and as a result, the lines overlap. This is because the minimum frequency is the best possible frequency in this range. However, at larger focal distances, an optimum frequency for heating can be found for Inconel738(T), and the lines start to deviate. Compared to the temperature increase at minimal frequency, the slope of the temperature increase with respect to focal distance decreases from 2 to 1/2. Hence, materials with power-law exponents of $y > 2$ with an optimal frequency are more efficient for increasing focal distance than materials with no optimal frequency $y \leq 2$.

In Figure 4.8b, the effect of focal distance on resolution is visualized for Inconel 738(T) with $y = 4$. The same argument is used to show that the resolution improves with the minimum frequency case. At focal distances of $F = 1$ m, the resolution improves by one order of magnitude compared to materials with $y \leq 2$ due to the change in slope. Therefore, materials with $y > 2$ are promising because they can enhance resolution and temperature increase at large focal distances.

(a) Temperature increase and focal distance for $y = 4$ (b) Resolution and focal distance for $y = 4$
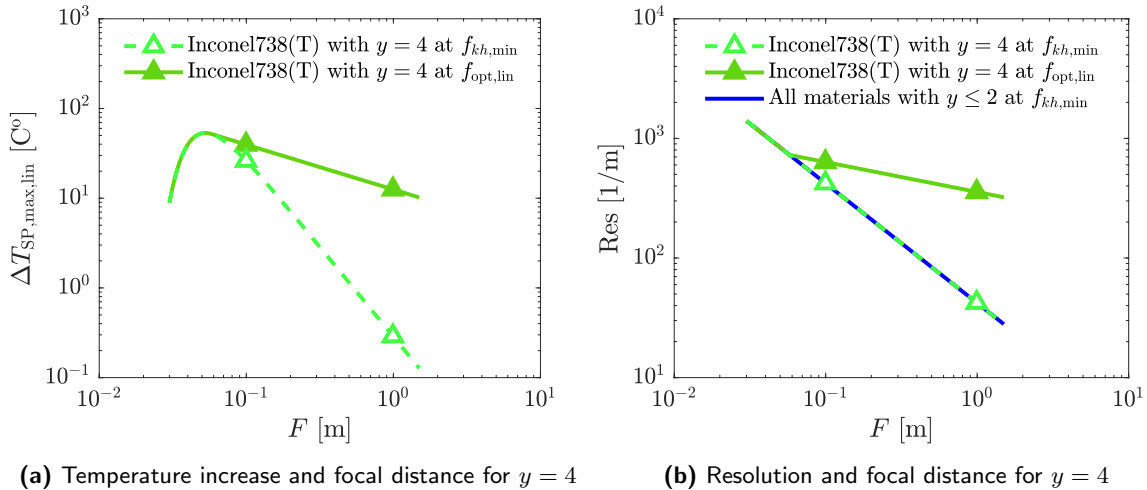
Figure 4.8: This figure evaluates the performance of a material with a power-law coefficient of $y = 4$ by plotting the temperature increase in (a) and the resolution in (b) as a function of the focal distance. The maximum temperature increase at the best frequency $f_{\mathrm{best}=f_{\mathrm{opt,lin}}}$, is given by the solid line, and the maximum temperature increase at the minimum frequency $f_{kh,\mathrm{min}}$ by the dashed line. The $y = 4$ materials perform better at large focal distances where the slopes of the lines deviate increasingly.

4.4.4 Power consumption and scan velocity

In the previous sections, the performance of materials was discussed in terms of their maximum temperature increase and resolution. The current section discusses the power and scan velocity required to achieve these temperature increases and resolutions. Figure 4.9 shows the maximum total power and minimum scan velocity for materials with $y \leq 2$ and $y = 4$. The minimum scan velocity and total maximum power consumption can be determined using Equation (4.10) and (4.11), respectively.

Figure 4.9a depicts the power and velocity requirements with $y \leq 2$. The markers indicate the required power and scan velocity at $f_{\text{best}} = f_{kh,\text{min}}$ for $F = 1$ and 0.1 m (from left to right). It can be observed that power consumption at $F = 1$ m is two orders of magnitude larger than at $F = 0.1$ m, while the minimum scan velocity is one order of magnitude lower. For Pyrex glass and Inconel718, a significant amount of power of more than 0.2 MW is needed to reach the maximum temperature increase. Large printers cannot print these materials at the minimum frequency. Increasing the frequency by one order of magnitude (as shown by the dashed lines) is equivalent to decreasing the printer by one order in focal length, which leads to a drop of two orders of magnitude in power consumption. However, as shown in Figure 4.6b, this frequency increase results in 3 orders of magnitude drop in temperature at $F = 1$ m. Reducing one order of magnitude in focal distance lowers power consumption, and temperature increases by one order of magnitude. Hence, changes in focal distance are more effective in reducing power consumption while maintaining a sufficient temperature increase. The minimum scan velocity also increases in Figure 4.9a and scales linearly with frequency and $1/F$ for materials with $y \leq 2$. Additionally, scan velocities can be limited to < 1 mm/s for well-insulating materials like PEEK. This limited scan velocity shows the need to consider

(a) Power and velocity for $y \leq 2$

(b) Power and velocity for $y = 4$
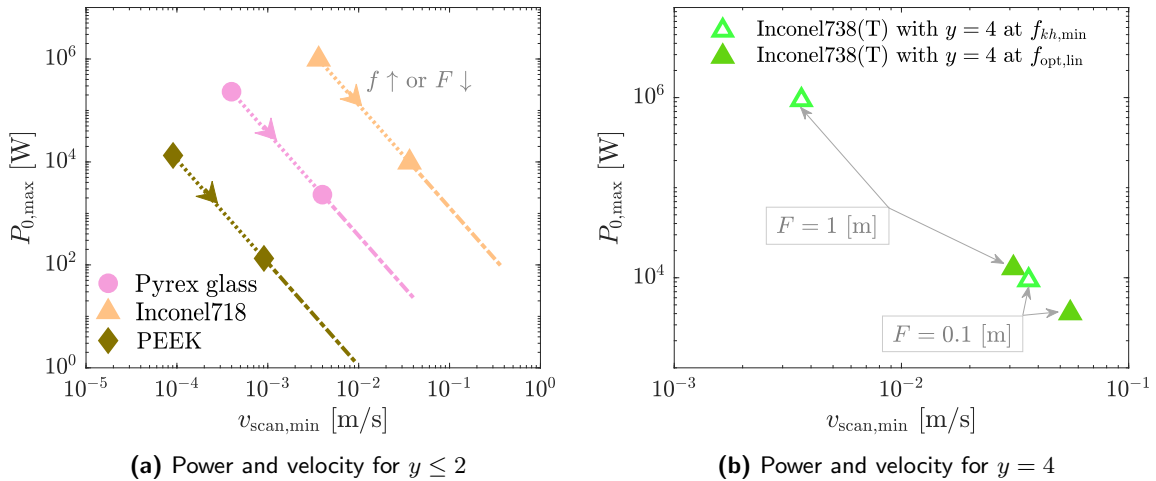
Figure 4.9: The graphs display how different materials and focal lengths affect the relationship between the maximum total power and minimum scan velocity. In (a), the markers at the top-left to the bottom-right indicate a focal distance of $F = 1$ and $F = 0.1$ m for each material with $y \leq 2$. Increasing the frequency or decreasing the focal distance results in a larger scan velocity and lower maximum power consumption. In (b), Inconel738(T) with $y = 4$ is shown at the optimal frequency and minimum frequency $f_{kh,\text{min}}$. For $F = 1$ m at the optimal frequency, the required power consumption is almost two orders of magnitude smaller, and the scan velocity is about one order of magnitude larger than at the minimum frequency.

multi-focal scanning or holographic 3D printing with the SAS technique. Especially since, in powders, porosity reduces thermal conductivity, hence the minimal scan velocity.

Figure 4.9b shows the power consumption and minimum scan velocity for attenuation exponents of $y = 4$. The filled and open markers indicate the power and scan velocity for Inconel738(T) at optimum and minimum frequencies, respectively. The open markers can be compared with Inconel718 in Figure 4.9a, as they are almost identical in maximum total power and minimum scan velocity at $f_{kh,\min}$. For $F = 1$ m at the optimal frequency, the required power consumption of Inconel738(T) is almost two orders smaller than that of Inconel718. Additionally, the scan velocity is about one order of magnitude larger. Therefore, materials with power-law coefficients of $y = 4$ can effectively reduce power consumption at increased scan velocity. The difference between Inconel718 and Inconel738(T) is due to their microstructure. The microstructure of Inconel738(T) causes Rayleigh scattering, which dominates the measured frequency range. Therefore, the intrinsic absorption contribution with $y = 1$ is minimal compared to scattering with $y = 4$, as listed in Table 4.1. Consequently, the material exhibits nonlinear attenuation with a power-law coefficient of $y = 4$ at higher frequencies. So, when dealing with large focal distances, it is essential to consider two key factors - power consumption and scan velocity. These factors can potentially limit the SAS process. Based on the analysis, it is concluded that increasing the frequency beyond the minimum frequency to release these limits only proves effective for materials with an optimal frequency ($y > 2$).

4.4.5   Future perspectives

Complex material behavior and its coupling to part size and processing conditions have been demonstrated using linear wave equations. The presented results indicate the printability and applicability of the SAS methods. Some additions to the model are required to move to a more qualitative description of compacted and filled powder-based materials.

Firstly, the linearity assumption of the wave equations could be replaced by nonlinear wave equations to account for higher harmonics. Bessonova et al. [153] have shown that at small nonlinear parameters, the positive peak pressure can be more than 10% larger compared to the amplitude of harmonic waves. This nonlinearity leads to a nonsinusoidal wave shape that introduces higher harmonic components in the frequency spectrum. According to the frequency-dependent attenuation relations, an increase in frequency results in increased attenuation, which enhances the temperature increase near the focal spot. Therefore, the temperature increase at the focal spot in the linear regime can be regarded as a minimum limit. Using the same reasoning, it can be inferred that for powers above the linear limit, the temperature can significantly increase in the focal region [153]. However, the pressure in the focal spot eventually saturates, making it inefficient to increase the power further. Also, a limit in power may exist for polymers as they tend to degrade at high energies due to temperature increase [177]. Ultrasound-induced degradation of solid polymers undergoing melting while irradiating is a complex and poorly understood phenomenon and, therefore, not included in the analysis. Expanding the model to nonlinear wave equations through analytical models or numerical simulations is required. Additionally, experiments should be performed to find improved models for maximum power and measure compacted powders' nonlinearity coefficient.

Figures 4.8 and 4.9b show that this biquadratic frequency scaling benefits resolution, power consumption, and scan velocity. Furthermore, the thermal properties of the powder-based

material change with filler fraction [178]. Since filler materials can be gas, liquid, relatively small solid particles, or combinations of these materials, studying their impact is essential. Material optimization is required to include different powder and filler properties, particle size, and porosity in the SAS system analysis.

Setting the initial temperature of the build volume is a critical step in the 3D printing process. Data on the acoustic and thermal properties of materials is required to determine the optimal starting temperature. The temperature needed to liquefy metals and ceramics can be over a thousand degrees. Therefore, using an initial temperature close to the melting temperature would be convenient to minimize the energy input required. However, this requires knowledge of the temperature dependence of thermal and acoustic material properties, which depends on the powder properties and pore material, making the optimization analysis more complex. Another challenge to consider, connected to the initial temperature optimization, is cooling the print volume, especially as the printer size increases. As the distance to cooling increases and the ratio of cooling surface to material volume decreases drastically, the cooling to the surroundings can become ineffective. This is particularly true for well-insulated materials such as powders. Therefore, advanced print and scan strategies are required to tackle this cooling challenge. Addressing these issues in subsequent studies is essential for improving the SAS 3D printing process.

4.5   Conclusions

The novel 3D printing technique, Selective Acoustic Sintering (SAS), introduced in this work, shows great potential in improving part quality and print time reduction. It involves using focused ultrasound transducers to fuse powder particles. Unlike other powder-based 3D printing methods, this technology uses ultrasound to create volumetric scan paths or holographic shapes, which results in reduced printing times and high-density products. This study proposes a mathematical framework to determine the feasibility of this method, which directs future research and development of selective acoustic sintering.

The framework highlights the crucial processes in a spherical-shaped 3D printer, including energy input, energy gain from geometrical focusing, and energy loss due to attenuation. It further establishes relationships between printer dimensions, acoustic and thermal material properties, and transducer properties on temperature increase and focal spot diameter. These relationships can optimize printing and determine the appropriate process parameters for different materials and applications.

The analysis of a diverse dataset of printable materials shows that selective acoustic sintering has potential for various applications, including printing metals, ceramics, and polymers. Promising materials for this technique include ceramic glasses such as Pyrex glass, nonferrous metals like Inconel, semi-crystalline polymers including PPS, HDPE, and PEEK, as well as amorphous polymers like PEI. Future work involves transitioning from solid to compacted and filled powder-based materials.

The proposed framework provides a comprehensive and systematic approach to evaluate the feasibility of selective acoustic sintering as a 3D printing method for a specific material. It offers insights into the essential physical processes involved, provides a foundation to optimize printing conditions, and offers a valuable tool for researchers and engineers to advance the development of this technology for a variety of applications.

4.A   Additional information

Source approximation

In Section 4.2, the radial dependency of the intensity is discussed for a focused ultrasound transducer. The intensity follows a jinc^2 distribution over the radius. An approximation of this type of distribution can be obtained using a Gaussian source, which is given by the following equation:

$$I_\sigma(r_F, F) = I_{\text{SP}} \exp\left(-\left(\frac{r}{\sigma}\right)^2\right), \tag{4.20}$$

where σ is approximately equal to $0.618 D_{\text{spot}}$ [179]. To obtain an analytical solution, it is assumed that the spot is a sphere with a radius of a_s. The equation for the intensity then becomes:

$$I_s(r) = \begin{cases} I_{\text{SP}} & \text{if } 0 \leq r \leq a_s, \\ 0 & \text{if } a_s < r \leq R. \end{cases} \tag{4.21}$$

The radius a_s is derived so that the resulting maximum temperature increase at a steady state for a uniform source equals a Gaussian source. If $R \gg \sigma$, the spherical radius can be simplified to $a_s \approx \sigma \approx 0.618 D_{\text{spot}}$. The steady-state expressions are provided in Appendix 4.A. Figure 4.10 illustrates the difference between the intensity sources.
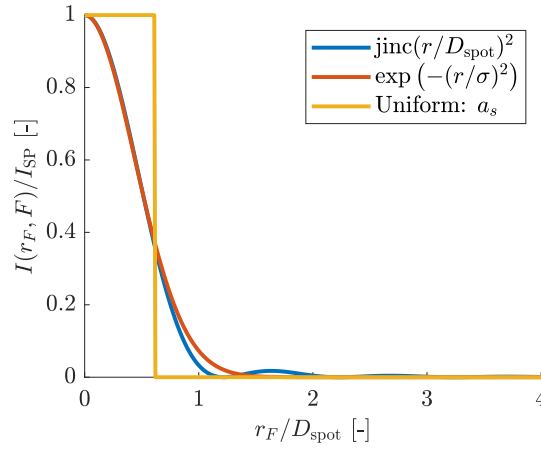
Figure 4.10: Comparison of the jinc^2, Gaussian and Uniform (spherical) intensity sources.

Steady state temperature relations

To calculate the temperature increase in the focal spot, the linear bio-heat transfer equation without perfusion [180] needs to be solved. The one-dimensional heat balance in spherical coordinates, with a constant thermal conductivity of K and a volumetric heat source of Q, is defined as:

$$\frac{1}{\kappa}\frac{\partial T}{\partial t} = \frac{1}{r^2}\frac{\partial}{\partial r}\left(r^2\frac{\partial T}{\partial r}\right) + \frac{Q(r)}{K}, \tag{4.22}$$

where T is the temperature and $\kappa = \frac{K}{\rho_0 c_p}$ the thermal diffusivity. If a spherical volume with a radius of R and $T(R) = 0$ is present, an analytical solution can be obtained for the Gaussian

source in Eq. (4.20) at a steady state. The steady-state solution is given by:

$$
T_\sigma(r,\infty) = \begin{cases} A_\sigma \frac{\sqrt{\pi}}{2}\left(\frac{2}{\sqrt{\pi}} - \frac{\sigma}{R}\mathrm{erf}\left(\frac{R}{\sigma}\right)\right) & \text{if } r = 0, \\ A_\sigma \frac{\sqrt{\pi}}{2}\left(\frac{\sigma}{r}\mathrm{erf}\left(\frac{r}{\sigma}\right) - \frac{\sigma}{R}\mathrm{erf}\left(\frac{R}{\sigma}\right)\right) & \text{if } 0 < r \leq R. \end{cases}
\tag{4.23}
$$

Following the study by Goldenberg [150], the analytical solution for a uniform source in Equation (4.21) is given by the following equation at steady-state:

$$
T_s(r,\infty) = \begin{cases} A_s\left(1 - \frac{r^2}{3a_s^2}\right) & \text{if } 0 \leq r \leq a_s, \\ A_s\frac{2\,a_s}{3\,r} & \text{if } a_s < r \leq R. \end{cases}
\tag{4.24}
$$

Here, $A_s = \alpha I_{\mathrm{SP}}a_s^2/(2K)$ and $A_\sigma = \alpha I_{\mathrm{SP}}\sigma^2/(2K)$. Wu and Du [181] derived similar expressions for the temperature increase in focused Gaussian beams in steady-state conditions.

Transient dimensionless temperature relation

The temperature increase of a spherical heat source with a radius of $r^* = r/a_s$, located at the center of an infinite sphere, varies over time ($t^* = t\kappa/a_s^2$) according to the transient temperature equation derived by Goldenberg [150]. In this work, the equation is rewritten as follows:

$$
\Delta T_s(r,t) = A_s\mathcal{G}(r^*,t^*),
\tag{4.25}
$$

(a) Time dependence of $\mathcal{G}$ **(b)** Error of using the simplified expression $2t^*$
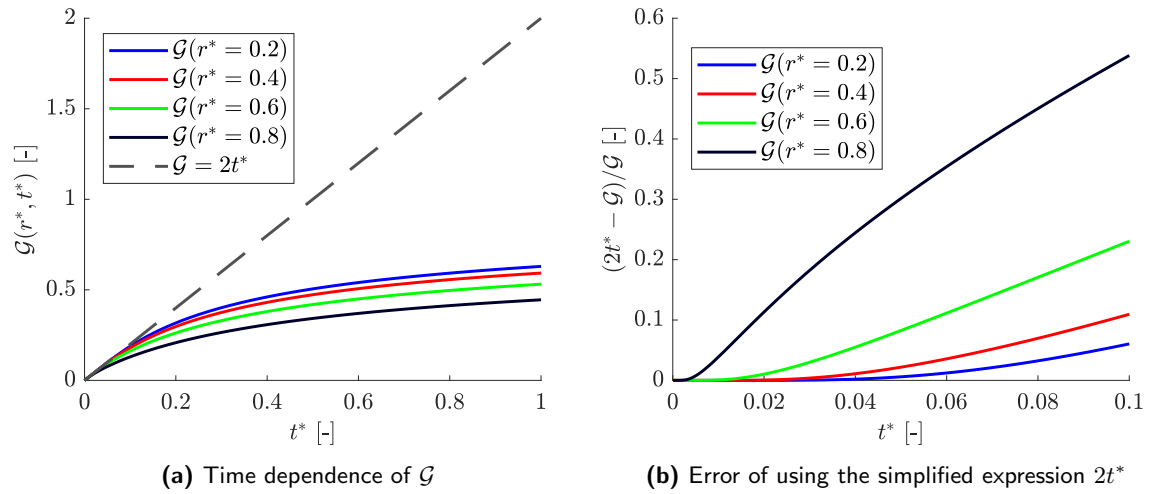
Figure 4.11: Dimensionless heating function $\mathcal{G}$ as a function of the dimensionless time for $r^* = [0.2\,0.4\,0.6\,0.8]$ and the error of using the simplified zero-limit function $\lim_{t^*\to 0}\mathcal{G} = 2t^*$.

where $\mathcal{G}(r^*, t^*)$ represents a function that can be defined as:

$$\mathcal{G} = \begin{cases} \dfrac{\operatorname{erf}\left(\sqrt{\frac{1}{4t^*}}\right)(2\,t^* - 1) - \sqrt{\frac{4t^*}{\pi}}\,e^{-\frac{1}{4\,t^*}} + 1}{} & \text{if } r^* = 0, \\[2ex] \begin{aligned} 2\,t^* - \dfrac{1}{r^*}\Bigg\{ &\left(\operatorname{erf}\left(\tfrac{r^*-1}{2\sqrt{t^*}}\right) + 1\right)\left(r^*\,t^* - \tfrac{3r^*}{2} - \tfrac{r^{*3}}{6} + r^{*2} + \tfrac{2}{3}\right) + \\ &\left(\operatorname{erf}\left(\tfrac{r^*+1}{2\sqrt{t^*}}\right) - 1\right)\left(\tfrac{r^*}{2} - r^*\,t^* - \tfrac{r^{*3}}{6} + \tfrac{1}{3}\right) + \dfrac{4\,t^{*3/2}\,e^{-\frac{(r^*-1)^2}{4\,t^*}}}{3\sqrt{\pi}} - \\ &\dfrac{4\,t^{*3/2}\,e^{-\frac{(r^*+1)^2}{4\,t^*}}}{3\sqrt{\pi}} + \dfrac{\sqrt{t^*}\,e^{-\frac{(r^*-1)^2}{4\,t^*}}\left(\tfrac{r^{*2}}{3} + \tfrac{r^*}{3} - \tfrac{2}{3}\right)}{\sqrt{\pi}} + \\ &\dfrac{\sqrt{t^*}\,e^{-\frac{(r^*+1)^2}{4\,t^*}}\left(-\tfrac{r^{*2}}{3} + \tfrac{r^*}{3} + \tfrac{2}{3}\right)}{\sqrt{\pi}} \Bigg\} \end{aligned} & \text{if } 0 < r^* < 1, \\[2ex] \begin{aligned} &t^* - \operatorname{erfc}\left(\tfrac{1}{\sqrt{t^*}}\right)\left(t^* - \tfrac{2}{3}\right) - \dfrac{4\,t^{*3/2}}{3\sqrt{\pi}} - \dfrac{2\sqrt{t^*}\,e^{-\frac{1}{t^*}}}{3\sqrt{\pi}} + \dfrac{4\,t^{*3/2}\,e^{-\frac{1}{t^*}}}{3\sqrt{\pi}} \\ &-\dfrac{1}{r^*}\Bigg\{ \left(\operatorname{erf}\left(\tfrac{r^*-1}{2\sqrt{t^*}}\right) - 1\right)\left(\tfrac{r^{*2}}{2} - r^* + t^* + \tfrac{1}{2}\right) + \\ &\left(\operatorname{erf}\left(\tfrac{r^*+1}{2\sqrt{t^*}}\right) - 1\right)\left(\tfrac{r^*}{2} - r^*\,t^* - \tfrac{r^{*3}}{6} + \tfrac{1}{3}\right) + \\ &(r^* - 1)\left(\left(\operatorname{erf}\left(\tfrac{r^*-1}{2\sqrt{t^*}}\right) - 1\right)\left(\tfrac{r^{*2}}{6} - \tfrac{r^*}{3} + t^* + \tfrac{1}{6}\right)\right) + \\ &(r^* - 1)\left(\dfrac{\sqrt{t^*}\,e^{-\frac{(r^*-1)^2}{4\,t^*}}(r^*-1)}{3\sqrt{\pi}} + \dfrac{4\,t^{*3/2}\,e^{-\frac{(r^*-1)^2}{4\,t^*}}}{3\sqrt{\pi}\,(r^*-1)}\right) - \\ &\dfrac{4\,t^{*3/2}\,e^{-\frac{(r^*+1)^2}{4\,t^*}}}{3\sqrt{\pi}} + \dfrac{\sqrt{t^*}\,e^{-\frac{(r^*+1)^2}{4\,t^*}}\left(-\tfrac{r^{*2}}{3} + \tfrac{r^*}{3} + \tfrac{2}{3}\right)}{\sqrt{\pi}} + \\ &\dfrac{\sqrt{t^*}\,e^{-\frac{(r^*-1)^2}{4\,t^*}}(r^*-1)}{\sqrt{\pi}} \Bigg\} \end{aligned} & \begin{aligned}&\text{if } r^* = 1, \\[1ex] &\text{if } r^* > 1.\end{aligned} \end{cases} \tag{4.26}$$

For the range of $0 < r^* < 1$, which is relevant for the temperature increase equations in this paper, Figure 4.11a shows $\mathcal{G}(r^*, t^*)$ as a function of dimensionless time t^*. The figure includes four dimensionless radii, including $r^* = D_{\text{spot}}/4/a_s \approx 0.40$, used in the moving source analysis. Additionally, Figure 4.11b shows the error with respect to the simplified equation $\lim_{t^* \to 0} \mathcal{G} = 2t^*$. This proves the validity of using the simplified equation for small radii $r^* \leq 0.40$, as the error is below 10%.

Time-averaged radius

As the source moves across the scan line, the spherical radius at a point located at a radial distance of r_c from this scan line changes. This change in radius can be calculated as follows:

$$r(t, r_c) = \sqrt{B^2 + r_c^2}, \tag{4.27}$$

with

$$B = \sqrt{\left(\frac{D_{\text{spot}}}{2}\right)^2 - r_c^2} - v_{\text{scan}}t. \tag{4.28}$$
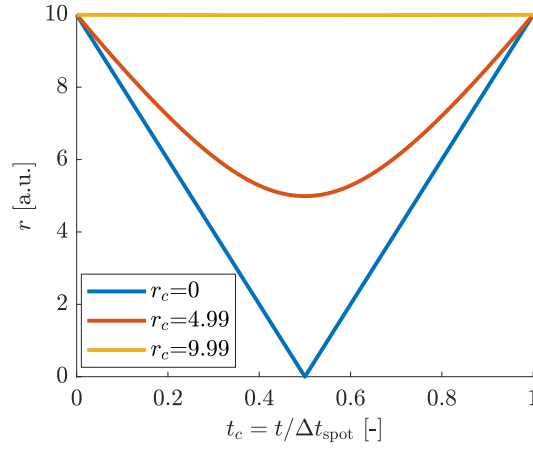
Figure 4.12: Time dependence of the spherical radius r at different radial positions r_c on the scan axis. The time axis is the dimensionless ratio of the time and the scan time.

The equation $\Delta t_{\text{spot}} = \sqrt{D_{\text{spot}}^2 - (2r_c)^2}/v_{\text{scan}}$ can be used to calculate the scan time Δt_{spot} required for the spherical spot to move through a point $\mathcal{P}_i$. Figure 4.12 illustrates the results of this equation for $D_{\text{spot}} = 20$ and $v = 0.1$ with respect to the scaled time $t_c = t/\Delta t_{\text{spot}}$. As shown in Figure 4.3b, when the radial distance is far away from the spot (where $r_c = 9.99$), the point $\mathcal{P}_2$ is only partially in contact with the spherical spot, while at $\mathcal{P}_0$ (where $r_c = 0$), the point is always in contact with the spherical spot. Using the scaled time and substituting it in the equation, the time-averaged spherical radius can be found by numerically integrating over $r(t_c, r_c)$, as given by:

$$\langle r \rangle = \int_0^1 r(t_c, r_c) \, \mathrm{d}t_c. \tag{4.29}$$

Three different approximation methods have been utilized to match the numeric average radius. These methods include linear, quadratic, and (second-order) polynomial approximations of the time-averaged radius. The linear, quadratic, and polynomial equations for the approximations are as follows:

$$\langle r \rangle \approx \begin{cases} \frac{1}{2}r_c + \frac{D_{\text{spot}}}{4} & \text{Linear} \\ \frac{1}{D_{\text{spot}}}r_c^2 + \frac{D_{\text{spot}}}{4} & \text{Quadratic} \\ \frac{5}{9D_{\text{spot}}}r_c^2 + \frac{2}{9}r_c + \frac{D_{\text{spot}}}{4} & \text{Polynomial} \end{cases}. \tag{4.30}$$

Figure 4.13a presents the results of the time-averaged spherical radius, indicating that all three approximations are reasonable to good. The accuracy of the approximation can be evaluated by examining Figure 4.13b, which demonstrates that the polynomial equation has the smallest error, less than 2%.

(a) Time

(b) Scaled time t_c
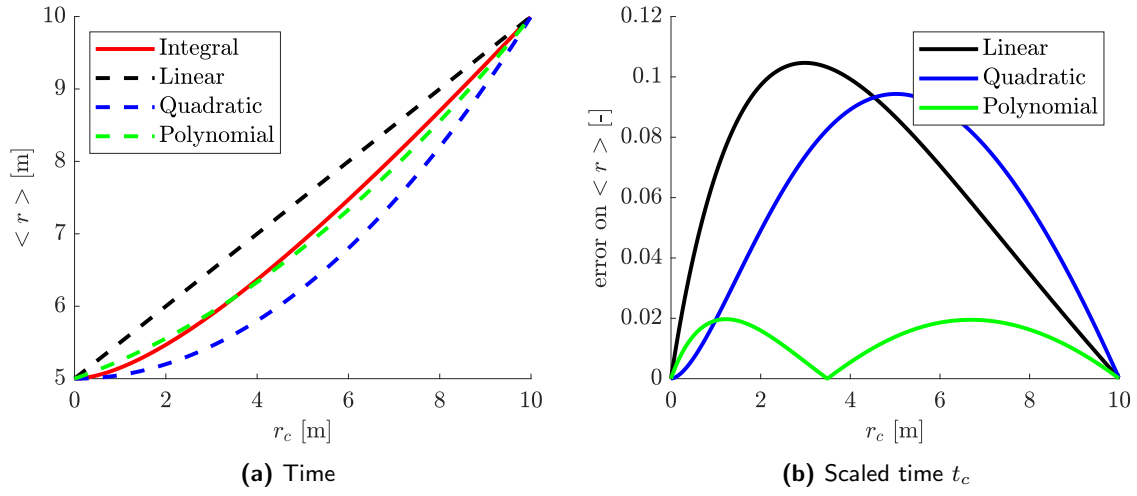
Figure 4.13: Time-averaged spherical radius as a function of the radial position r_c on the scan axis.

The temperature increase at the spot due to a moving source is found by substitution of the time-averaged radius and scan time in Eq. (4.25), given by:

$$\Delta T(r_c) = \Delta T_s(\langle r \rangle, \Delta t_{\text{spot}}). \tag{4.31}$$

This substitution results in a complex analytical function for the temperature increase. The spacial peak temperature increase is defined as $\Delta T_{\text{SP}} = \Delta T(0)$, for which $\Delta t_{\text{spot}} = D_{\text{spot}}/v_{\text{scan}}$ and $\langle r \rangle = D_{\text{spot}}/4$. By assuming that the scan time is much shorter than the diffusion time (i.e., $t^* \ll 1$), the spatial peak temperature is found by simplifying Eq. (4.31).

Chapter 5

Selective Acoustic Sintering: Numerical Analysis of Printer Configurations

Abstract

The field of additive manufacturing has made significant progress, but ultrasonic technology for sintering purposes is still in its early stages. This study explores Selective Acoustic Sintering (SAS), highlighting the crucial role of high-intensity focused ultrasound (HIFU) in sintering powder-based materials. Our research highlights a pivotal gap in the existing mathematical models, which fail to consider the effects of off-center focal spot positioning on the sintering process. Therefore, numerical simulations are utilized to study the effects of off-center volumetric scanning in SAS, and a time-reversal method is introduced to maintain spot size accuracy. Additionally, this paper revisits the core principles of phased array configurations, exploring their practical implications in enhancing SAS printer designs. Through numerical analysis, we underscore the potential of optimizing focal spot accuracy, which is paramount in boosting efficiency and broadening the applicability of SAS in future manufacturing processes.

5.1   Introduction

Recent developments in acoustic 3D printing have shown that high-intensity focused ultrasound (HIFU) can be used to sinter powder-based materials in the selective acoustic sintering (SAS) 3D printing method [182]. This work emphasizes the benefits of using ultrasound as an energy source in 3D printing, wherein, most importantly, phased arrays allow for a volumetric scanning approach. Nevertheless, the presented mathematical framework does not account for the effects of off-center focusing of the focal spot, and hence, this requires more investigation.

In 1801, Thomas Young introduced the concept of phasing. He experimented with wave interference utilizing two light sources and found that light waves are reinforced when they crossed in phase and canceled out when they crossed out of phase (see Figure 5.1a) [183]. Because of this initial finding, phasing became a method for controlling time wavefronts from multiple sources to bend, steer, and focus the energy, as shown in Figure 5.1b. Early

conventional ultrasonic testing used single or dual-element probes limited to gathering data in a fixed area of focus. A phased array was introduced into ultrasonics to overcome those limitations by applying time delays to multiple elements to focus and steer the sound beam at designated areas within the material. The first ultrasound phased array systems were developed in the 1960s and were mainly used in medical applications like brain imaging [184]. When the phased array was introduced in industrial settings in the 1980s, it allowed users to collect information and visualize data in applications conventional ultrasonic testing could not adequately accomplish, including weld inspection, bond testing, thickness mapping, and in-service crack detection [185]. Ultrasonic brain imaging was one of the earliest applications of phased arrays inside the human body [184]. In the last decades, the transition into the digital world and the rapid development of inexpensive embedded microprocessors enabled more rapid growth of the next generation of phased array equipment [185]. This also enabled the development of medical treatments inside the body with ultrasound, like live cancer treatment, solid tumor ablation [40] or improving blood-brain tumor barrier permeability [186]. An example of a multi-element hemispherical-shaped phased array used for noninvasive brain therapy applications is shown in Figure 5.1c. This setup resembles half the spherically-shaped SAS 3D printer as presented in previous work [182].

(a) Two-point source interference pattern, e.g., throwing two stones in a pond [185]

(b) Linear phased-array focusing and steering by electronic delay patterns [187]

(c) Hemispherical transducer with ∼1000 elements used to scan inside the brain [186]
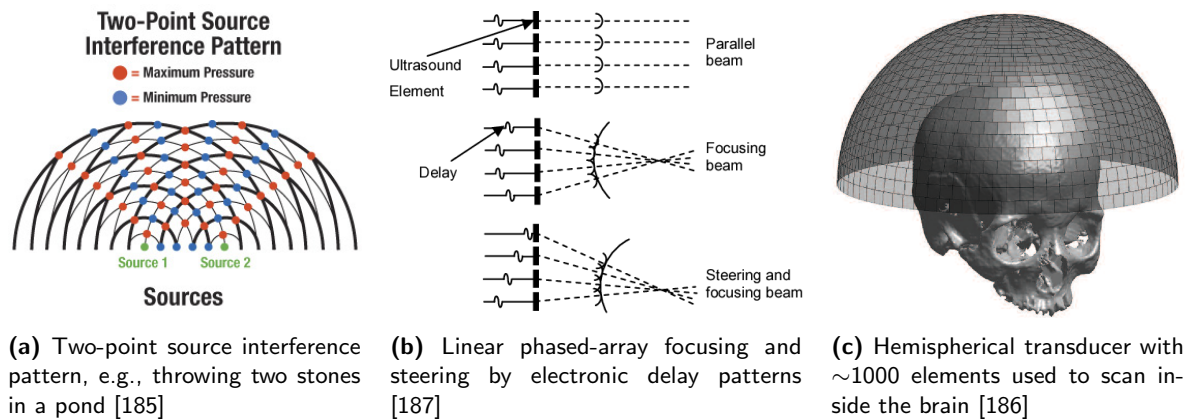
Figure 5.1: The principles and applications of phasing and phased-array configurations.

The hemispherical shape is incorporated to maximize the penetration area on the skull surface, thus minimizing undesired heating [188]. The design of such a spherical phased-array configuration depends, amongst others, on the required focal dimensions, the investigated material(s), and the desired local temperature increase. Simulations have proven useful in predicting these ultrasound-assisted temperature increases inside the body.

In the work of Chaplin et al. [189], a hemispherical phased-array setup is accurately modeled via nonhomogeneous 3D acoustic simulations. These simulations optimized transducer geometry concerning focus size, grating lobes, and directivity. Clement et al. [188] numerically showed that increasing the number of elements would increase the power delivered to the focus, thus reducing the increase in temperature at the bone surface. Decreasing the element size increases the range for electronic beam steering [188]. Besides, simulations by Pernot et al. [190] indicate that the magnitude of grating lobes increases when the focus is electronically moved off-axis, and an aperiodic distribution of elements can reduce this effect. Multi-frequency arrays offer variable transmit focal sizes under a fixed aperture and detect

different spectral content on receive for imaging purposes [191]. For applications in tactile displays, Gavrilov [192] shows by simulations that randomization of element locations on the spherical surface is useful in creating multiple-focus ultrasonic fields. The multi-point focal capabilities of such systems were later also demonstrated in the thermal ablation of pork meat [193].

A useful toolbox for simulating ultrasound wave propagation is k-Wave [194, 195]. k-Wave is an open-source MATLAB toolbox designed for the time-domain simulation of propagating acoustic waves in 1D, 2D, or 3D. The toolbox uses advanced numerical models that account for linear and nonlinear wave propagation, an arbitrary distribution of heterogeneous material parameters, and power law acoustic absorption [194, 195].

This work aims to study the effect of off-center focusing by using multiple ultrasound elements in SAS 3D printer and create a numerical framework to design and evaluate the performance of such a 3D printer. The k-Wave simulational toolbox is used to modify the printer configuration to a shape different from the proposed spherical build volume and to change the shape and positions of the elements.

This chapter is built up as follows: first, in Section 5.2, a problem description is given, followed by a detailed description of the numerical method of the pseudospectral framework in Section 5.3. Herein, the methods for solving the wave equations and the energy balance with thermal-acoustic coupling are presented. Finally, the simulation results are given in Section 5.4.

5.2   Problem description

In this chapter, we limit ourselves to two SAS 3D printer build volume shapes: a spherical build volume or a cubical build volume. These problems are schematically depicted in Figure 5.2 and 5.3. The elements are grouped per transducer.

For example, in the two-dimensional representation of the sphere in Figure 5.2a, $N = 6$ transducers with $N_{el} = 4$ elements are shown. The element size h_{el} and spacing h_s are equal for each transducer. The elements are positioned at a radius R_{sp} from the center of the sphere, and the desired focal position is indicated by the vector $\bar{\boldsymbol{F}}$. The simulation domain is defined as Ω, and the length of the domain is L_Ω. This domain is a square box around the build volume and is extended by a perfectly matching layer (PML) of length L_{PML}, which will be discussed later. The conversion of the 2D circular geometry to a 3D build volume is shown in Figure 5.2b. In the presented example, the number of transducers is 12, and each transducer has 817 elements.

Figure 5.3a shows the two-dimensional representation of the cubical volume. Each transducer can be moved over its surface to move the focal spot through the volume. This allows for a reduction of the total number of elements required. In this figure, the length of the square is given by L_{sq}. On the square, similar transducers are poisoned; however, the number of active elements depends on the position of the transducer relative to the focal position. By definition, $N_{el,1}$ and $N_{el,2}$ are the number of active transducer elements of transducer sets 1 and 2. The subscript numbers 1 or 2 indicate that the transducer is closest to the focus location and furthest away from the focus location, respectively. The number of active elements is larger for transducers furthest away from the focal point $N_{el,2} < N_{el,1}$. Inactive elements are not drawn in the schematics, and the transducer size equals $h = h_{el}N_{el,1} + h_s(N_{el,1} - 1)$.

Figure 5.3b shows the entire three-dimensional geometry of the cubical build volume. Herein, elements are placed in a matrix and have a squared shape. Again, the inactive elements are not illustrated.

5.2.1   Governing equations

The medium is treated as a sound-absorbing media in which the absorption follows a frequency power law of the form:

$$\alpha_p = \alpha_\omega \omega^y, \tag{5.1}$$

where α_p is the pressure-based absorption coefficient in units of $1/\mathrm{m}$, α_ω is the power law pre-factor in $\mathrm{Np/(m(rad/s)}^y)$, y is the power law exponent, $\omega = 2\pi f$ the radial frequency with f the frequency. Absorption of this form is commonly seen in polymers, metals, and ceramics [158, 170].

When acoustic absorption and heterogeneities in the material parameters are included, the wave propagation is solved by the following system of coupled first-order partial differential equations:

$$\frac{\partial \mathbf{u}}{\partial t} = -\frac{1}{\rho_0}\nabla p + \boldsymbol{S}_F, \qquad\qquad (\text{ momentum conservation }) \tag{5.2}$$

$$\frac{\partial \rho}{\partial t} = -\rho_0 \nabla \cdot \mathbf{u} - \mathbf{u}\cdot\nabla\rho_0 + S_M, \qquad (\text{ mass conservation }) \tag{5.3}$$

$$p = c_0^2\left(\rho + \mathbf{d}\cdot\nabla\rho_0 - \mathrm{L}\rho\right). \qquad (\text{ pressure-density relation }) \tag{5.4}$$

Here, $\boldsymbol{u}$ is the acoustic particle velocity, p is the acoustic pressure, ρ is the acoustic density, ρ_0 is ambient (or equilibrium) density, c_0 is the isentropic sound speed, $\boldsymbol{d}$ the acoustic particle
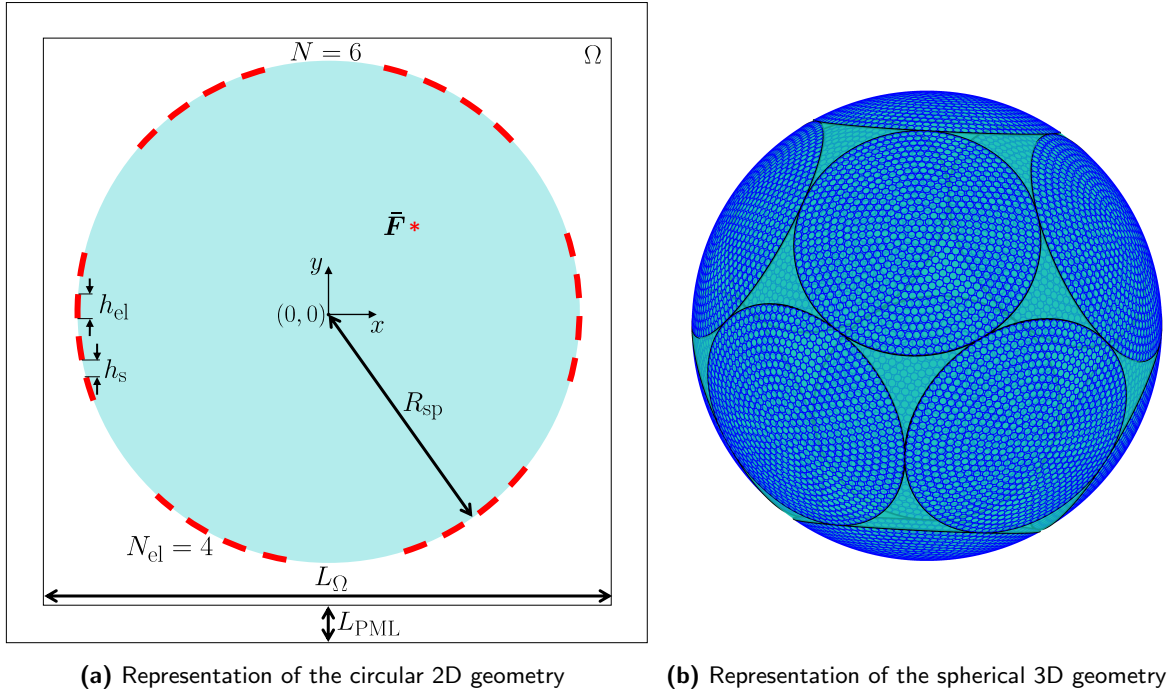

(a) Representation of the circular 2D geometry   **(b)** Representation of the spherical 3D geometry

Figure 5.2: Problem description of the circular and spherical geometry.

(a) Representation of the square 2D geometry   (b) Representation of the cubical 3D geometry
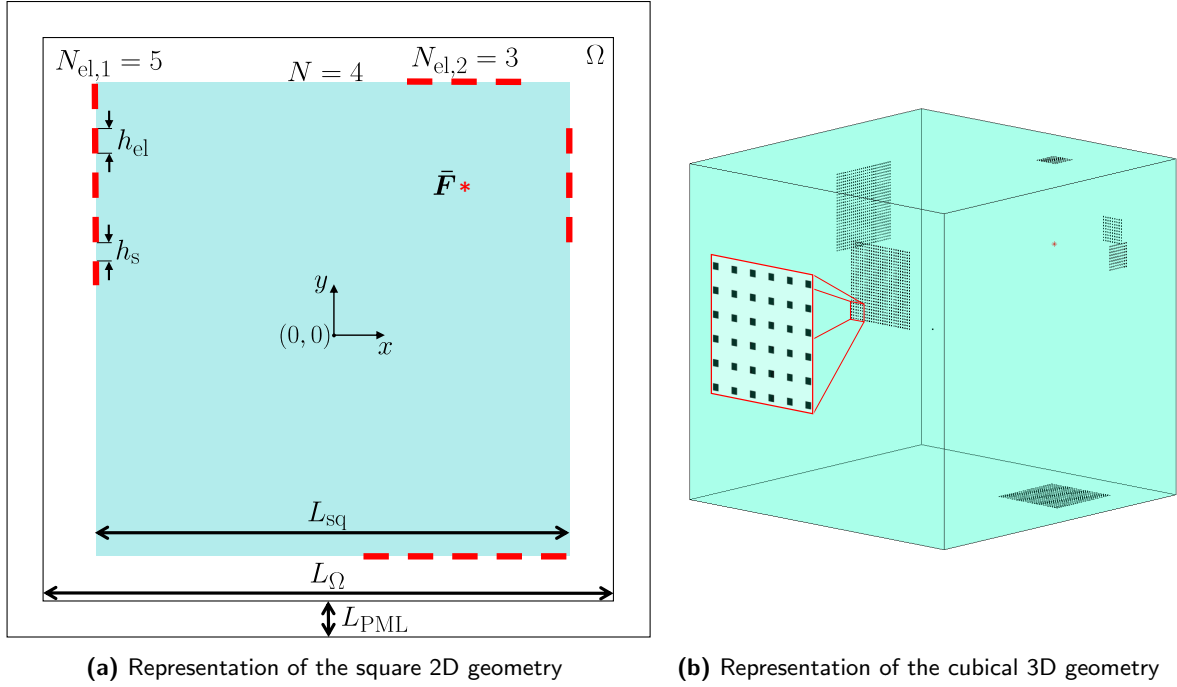
Figure 5.3: Problem description of the square and cubical geometry.

displacement, $\boldsymbol{S}_F$ a force source term and represents the input of body forces per unit mass in units of N/kg and S_M a mass source term and represents the time rate of the input of mass per unit volume in units of kg/(m³s). These equations show that the spatial gradient of the applied force and the time rate of change of the mass injection rate (volumetric acceleration) give rise to sound. Within k-Wave, force, and mass sources are applied as velocity and pressure, respectively.

The operator, L in the pressure-density relation, is a linear integrodifferential operator that accounts for acoustic absorption and dispersion that follows a frequency power law as in Equation (5.1). Acoustic absorption must physically be accompanied by dispersion (dependence of the sound speed on frequency) to obey causality [196]. The operator used in k-Wave has two terms, both dependent on a fractional Laplacian, and is given by: [197, 198]

$$\mathrm{L} = \tau \frac{\partial}{\partial t} \left(-\nabla^2\right)^{\frac{y}{2}-1} + \eta \left(-\nabla^2\right)^{\frac{y+1}{2}-1}. \tag{5.5}$$

Here, τ and η are absorption and dispersion proportionality coefficient $\tau = -2\alpha_\omega c_0^{y-1}$, and $\eta = 2\alpha_\omega c_0^y \tan(\pi y/2)$, respectively. The two terms in L separately account for power law absorption and dispersion for $0 < y < 3$ and $y \neq 1$ under particular smallness conditions [198, 199]. For very high absorption and frequency values, the loss operator's behavior deviates from a power law due to second-order effects [199, 200]. If the three coupled equations are combined, they give a generalized form of the Westervelt equation [201] (assuming the nonlinear coefficient $A/B = 0$).

To calculate the temperature resulting from the acoustic focal energy, the energy balance

is solved:

$$\rho c_p \frac{DT}{Dt} = \nabla \cdot (\boldsymbol{K} \nabla T) + S_H, \tag{5.6}$$

where ρ is the density, c_p the heat capacity at constant pressure, T the temperature and $\boldsymbol{K}$ the thermal conductivity tensor. The thermal source term S_H corresponds to the injection of heat per unit volume per unit time, for example, due to energy absorption from a modulated laser beam. In the case of ultrasonic heating, the heating intensity can be calculated from the absorbance according to:

$$S_h = \alpha I_{\text{avg}} = \frac{\alpha |p|^2}{\rho c_0}, \tag{5.7}$$

with I_{avg} the average sound intensity, $\alpha = 2\alpha_p$ the intensity-based attenuation coefficient and $|p|$ the magnitude of the complex pressure.

5.3   Numerical method

Here, we are interested in the time domain solution of the wave equation for broadband acoustic waves in nonhomogeneous media (attenuation). The drawback with classical finite difference and finite element approaches for solving this type of problem is that at least ten grid points per acoustic wavelength are generally required to achieve a proper level of accuracy. This often results in computational grids that are too big to solve using regular computers. To reduce the memory and number of time steps required for accurate simulations, k-Wave solves the coupled acoustic equations described in the previous sections using the k-space pseudospectral method (or k-space method) [194].

5.3.1   k-space method

This method combines spectral calculation of spatial derivatives (in this case, the Fourier collocation method) with a temporal propagator expressed in the spatial frequency domain or k-space. The Fourier collocation spectral method estimates spatial gradients (globally) by fitting a Fourier series to all of the data [194]. There are two significant advantages to using the Fourier series. First, the amplitudes of the Fourier components can be calculated efficiently using the fast Fourier transform (FFT). Second, the basis functions are sinusoidal, so only two grid points (or nodes) per wavelength are theoretically required, rather than the six to ten required in other methods.

While the Fourier collocation spectral method improves efficiency in the spatial domain, conventional finite difference schemes are still needed to calculate the gradients in the time domain. It has been shown that an exact pseudospectral scheme for solving the acoustic equations expressed as coupled first-order partial differential equations can be obtained by replacing Δt in a first-order accurate forward difference with $\Delta t \, \text{sinc} \, (c_0 k \Delta t / 2)$ [202, 203]. The operator κ is known as the k-space operator given by:

$$\kappa = \text{sinc}(c_{\text{ref}} k \Delta t / 2), \tag{5.8}$$

where c_{ref} is a scalar reference sound speed. For large-scale acoustic simulations where the waves propagate over distances of hundreds or thousands of wavelengths, this seemingly small correction becomes critically important. Without this term, the finite difference approximation of the temporal derivative introduces phase errors, which accumulate as the simulation

runs. When nonlinearity, heterogeneous material parameters, or acoustic absorption are included in the governing equations, the temporal discretization using the k-space operator is no longer exact. However, if these perturbations are minor, including this operator can still significantly reduce the unwanted numerical dispersion [195, 202].

5.3.2   Discrete k-space Equations

As well as using the k-space operator, additional accuracy and stability are obtained by computing odd-order derivatives using staggered spatial and temporal grids [204]. For the Fourier collocation spectral method, spatial shifts are obtained using the shift property of the Fourier transform, where $\mathcal{F}_x\{f(x + \Delta x)\} = e^{ik_x \Delta x}\mathcal{F}_x\{f(x)\}$.

Starting with the linear case, the mass and momentum conservation equations in Equation (5.2-5.4) written in discrete form using the k-space pseudospectral method become:

$$\frac{\partial}{\partial \xi}p^n = \mathcal{F}^{-1}\left\{ik_\xi \kappa e^{ik_\xi \Delta\xi/2}\mathcal{F}\{p^n\}\right\}, \tag{5.9}$$

$$u_\xi^{n+\frac{1}{2}} = u_\xi^{n-\frac{1}{2}} - \frac{\Delta t}{\rho_0}\frac{\partial}{\partial \xi}p^n + \Delta t \mathrm{S}_{\mathrm{F}\xi}^{\mathrm{n}}, \tag{5.10}$$

$$\frac{\partial}{\partial \xi}u_\xi^{n+\frac{1}{2}} = \mathcal{F}^{-1}\left\{ik_\xi \kappa e^{-ik_\xi \Delta\xi/2}\mathcal{F}\left\{u_\xi^{n+\frac{1}{2}}\right\}\right\}, \tag{5.11}$$

$$\rho_\xi^{n+1} = \rho_\xi^n - \Delta t\rho_0\frac{\partial}{\partial \xi}u_\xi^{n+\frac{1}{2}} + \Delta t\mathrm{S}_{\mathrm{M}\xi}^{\mathrm{n}+\frac{1}{2}}. \tag{5.12}$$

Equations (5.9) and (5.11) are spatial gradient calculations based on the Fourier collocation spectral method, while (5.10) and (5.12) are update steps based on a k-space corrected first-order accurate forward difference. These equations are repeated for each Cartesian direction in $\mathbb{R}^N$ where $\xi = x, y, z$ in $\mathbb{R}^3$ ($N = 3$ is the number of spatial dimensions). Here, $\mathcal{F}$ and $\mathcal{F}^{-1}$ denote the forward and inverse spatial Fourier transform, i is the imaginary unit, k_ξ represents the wavenumbers in the ξ direction, $\Delta\xi$ is the grid spacing in the ξ direction, Δt is the time step, and κ is the k-space operator defined in Equation (5.8). The discrete wavenumbers are defined according to

$$k_\xi = \begin{cases} \left[-\frac{N_\xi}{2}, -\frac{N_\xi}{2} + 1, \dots, \frac{N_\xi}{2} - 1\right]\frac{2\pi}{\Delta\xi N_\xi} & \text{if } N_\xi \text{ is even} \\[2ex] \left[-\frac{(N_\xi - 1)}{2}, -\frac{(N_\xi - 1)}{2} + 1, \dots, \frac{(N_\xi - 1)}{2}\right]\frac{2\pi}{\Delta\xi N_\xi} & \text{if } N_\xi \text{ is odd,} \end{cases} \tag{5.13}$$

where N_ξ is the number of grid points in the ξ-direction. The acoustic density (physically a scalar quantity) is artificially divided into Cartesian components to apply an anisotropic perfectly matched layer to be applied. The exponential terms $e^{\pm ik_\xi \Delta\xi/2}2$ within Equations (5.9) and (5.11) are spatial shift operators that translate the result of the gradient calculations by half the grid point spacing in the ξ-direction. This allows particle velocity components to be evaluated on a staggered grid. An illustration of the staggered grid scheme is shown in Figure 5.4. Note, the density ρ_0 in Equation (5.10) is understood to be the ambient density defined at the staggered grid points. The corresponding pressure-density relation is given by:

$$p^{n+1} = c_0^2\left(\rho^{n+1} - \mathrm{L}_\mathrm{d}\right), \tag{5.14}$$
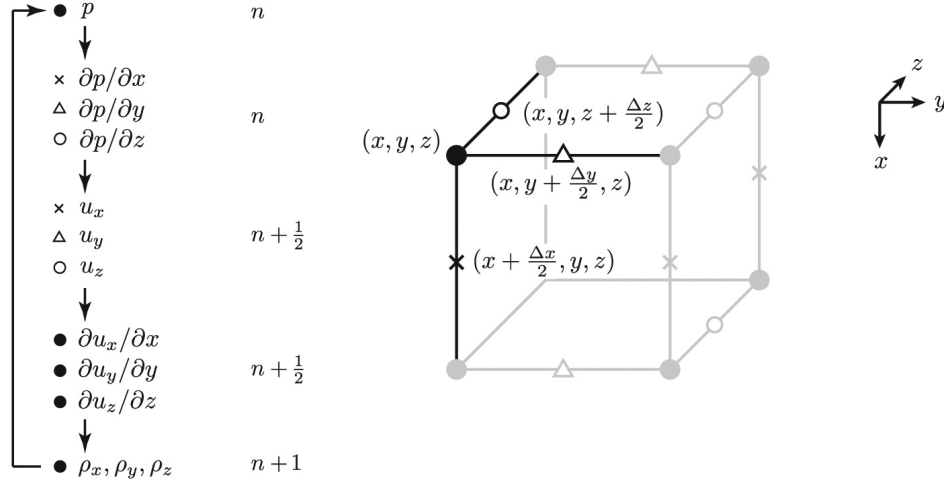
Figure 5.4: Schematic showing the computational steps in solving the coupled first-order equations using a staggered spatial and temporal grid in 3D. Here $\partial p/\partial x$ and u_x are evaluated at grid points staggered in the x-direction (crosses), $\partial p/\partial y$ and u_y evaluated at grid points staggered in the y-direction (triangles), and $\partial p/\partial z$ and u_z evaluated at grid points staggered in the z-direction (open circles). The remaining variables are evaluated on the regular grid (dots). The time staggering is denoted using n, $n+\frac{1}{2}$ and $n+1$ [205].

with the total acoustic density $\rho^{n+1} = \sum_\xi \rho_\varepsilon^{n+1}$. Here, L_d is the discrete form of the power law absorption term L, which is given in Equation (5.5). In all the equations above, the superscripts n and $n+1$ denote the function values at current and next time points and $n-\frac{1}{2}$ and $n+\frac{1}{2}$ at the time staggered points. This time-staggering arises because the update steps, Equations (5.10) and (5.12), are interleaved with the gradient calculations, (5.9) and (5.11).

To avoid needing to calculate the time derivative of the acoustic density explicitly (which would require storing a copy of at least ρ^n and ρ^{n-1} in memory), the temporal derivative of the acoustic density is replaced using the linearized mass conservation equation $\partial\rho/\partial t = -\rho_0 \nabla \cdot \boldsymbol{u}$, which gives:

$$L_d = -\tau \mathcal{F}^{-1} \left\{ k^{y-2} \mathcal{F} \left\{ \rho_0 \sum_\xi \frac{\partial}{\partial \xi} u_\xi^{n+\frac{1}{2}} \right\} \right\} + \eta \mathcal{F}^{-1} \left\{ k^{y-1} \mathcal{F} \left\{ \rho^{n+1} \right\} \right\}. \qquad (5.15)$$

The notations here indicate that the acoustic density and particle velocity numerical values are temporally offset by $\Delta t/2$. This introduces an additional phase offset between the acoustic density and the pressure, which causes a small error in the modeled values of absorption and dispersion. This error vanishes when the time step is reduced.

5.3.3 Discretization of acoustic source terms

The acoustic source terms defined in Equations (5.10) and (5.12) represent the input of body forces per unit mass and the time rate of input of mass per unit volume. However, within k-Wave, the source terms defined by the user are given in units of acoustic pressure and velocity. These terms are used because the available measurements of acoustic sources are typically either measurements of acoustic pressure or particle velocity. Consequently, the user inputs are scaled by k-Wave to be in the correct units before adding them to the discrete

equations. The Cartesian components of the force source term S_{F_ξ} are calculated from the user input $u_{\xi,\text{in}}$ by converting from units of velocity (m/s) to units of acceleration (m/s^2). The components of the mass source term S_{M_ξ} are calculated from the user input p_{in} by converting from units of pressure to units of density and then from units of density to the time rate of density. The final source scaling factors used in k-Wave are:

$$S_{F_\xi} = u_{\xi,\text{in}} \frac{2c_0}{\Delta \xi}, \tag{5.16}$$

$$S_{M_\xi} = \frac{p_{\text{in}}}{c_0^2 N} \frac{2c_0}{\Delta \xi}. \tag{5.17}$$

One disadvantage of the staggered grid scheme used in k-Wave is that user inputs and outputs must also follow this scheme. This means inputs and outputs for the particle velocity is defined on staggered grid points, while inputs and outputs for the pressure are defined on regular grid points. This is further complicated by the staggered time scheme, as the outputs for both pressure and velocity are offset by $\Delta t/2$ relative to the inputs. However, it is possible to compensate for these offsets with a little care. The effect of the staggered grid scheme on the inputs and outputs is summarized in Table 5.1.

Table 5.1: Effect of the staggered grid scheme on the input and output pressure and particle velocity values in 3D.

Parameter	Position	Time
x -direction velocity input	$x + \Delta x/2, y, z$	t
x -direction velocity output	$x + \Delta x/2, y, z$	$t + \Delta t/2$
y -direction velocity input	$x, y + \Delta y/2, z$	t
y -direction velocity output	$x, y + \Delta y/2, z$	$t + \Delta t/2$
z -direction velocity input	$x, y, z + \Delta z/2$	t
z -direction velocity output	$x, y, z + \Delta z/2$	$t + \Delta t/2$
pressure input	x, y, z	$t + \Delta t/2$
pressure output	x, y, z	$t + \Delta t$

5.3.4   Perfectly matched layer

In Fourier pseudospectral and k-space numerical models, using the FFT to calculate spatial gradients implies that the wave field is periodic. This causes waves leaving one side of the domain to reappear on the opposite side. The wave wrapping caused by the FFT can be largely eliminated using a perfectly matched layer (PML) [206, 207]. This thin absorbing layer encloses the computational domain and is governed by a nonphysical set of equations that cause anisotropic absorption. In pseudospectral models, such a layer must meet two requirements: (1) the layer must provide sufficient absorption so the outgoing waves are significantly attenuated, and (2) the layer must not reflect any waves into the medium.

k-Wave uses Berenger's original split-field formulation of the PML [206, 208]. This requires the acoustic density or pressure to be artificially divided into Cartesian components, where $\rho = \rho_x + \rho_y + \rho_z$. The absorption is then defined so that only wave field components traveling within the PML and normal to the boundary are absorbed. Using the homogeneous linear

case to illustrate, the first-order coupled equations, including the PML, become:

$$\frac{\partial u_\xi}{\partial t} = -\frac{1}{\rho_0}\frac{\partial p}{\partial \xi} - \alpha_\xi u_\xi, \qquad \text{(momentum conservation)} \qquad (5.18)$$

$$\frac{\partial \rho_\xi}{\partial t} = -\rho_0\frac{\partial u_\xi}{\partial \xi} - \alpha_\xi \rho_\xi, \qquad \text{(mass conservation)} \qquad (5.19)$$

$$p = c_0^2 \sum_\xi \rho_\xi. \qquad \text{(pressure-density relation)} \qquad (5.20)$$

$$(5.21)$$

Here, $\boldsymbol{\alpha} = \{\alpha_x, \alpha_y, \alpha_z\}$ is the anisotropic absorption in Nepers per second. All three components are zero outside the PML, and inside the PML, they are zero everywhere except within a PML layer perpendicular to their associated direction. The fact that the absorption coefficient is anisotropic in this way, and the same absorption coefficient acts on both the density and particle velocity, which is sufficient for no reflections from the edge of the PML. Following Yuan et al. [209] Equations (5.18) and (5.19) are transformed and discretized using a first-order accurate forward difference scheme so that the discrete equations given in Equation (5.10) and (5.12) including a PML can then be written as:

$$u_\xi^{n+\frac{1}{2}} = e^{-\alpha_\xi \Delta t/2}\left(e^{-\alpha_\xi \Delta t/2}u_\xi^{n-\frac{1}{2}} - \frac{\Delta t}{\rho_0}\frac{\partial}{\partial \xi}p^n\right), \qquad (5.22)$$

$$\rho_\xi^{n+1} = e^{-\alpha_\xi \Delta t/2}\left(e^{-\alpha_\xi \Delta t/2}\rho_\xi^n - \Delta t\rho_0\frac{\partial}{\partial \xi}u_\xi^{n+\frac{1}{2}}\right). \qquad (5.23)$$

This is the form of the PML equations implemented in k-Wave. α_ξ is chosen as a function of the position in the PML layer. Because on the one hand, a large value of α_ξ will impose a large gradient across the PML boundary, which will cause a reflection. On the other hand, a small value of $\alpha_x i$ implies that the decay within the PML will be slow, and hence, a very thick PML will be required. The following function is used in k-Wave to make the decay smoother at the boundary edges: [202]

$$\alpha_\xi = \alpha_{\max}\left(\frac{\xi - \xi_0}{\xi_{\max} - \xi_0}\right)^m, \qquad (5.24)$$

where ξ_0 is the coordinate at the start of the PML and $\xi_{\max}$ is the coordinate at the end. A value of $m = 4$ is used to give a balance between minimizing the amplitude of the wrapped wave and minimizing the amplitude of the reflected wave [202]. Using a staggered spatial grid significantly improves the performance of the PML. The PML absorption coefficient α_ξ used in the equations above is defined in units of Nepers s^{-1}. Within k-Wave, the absorption parameter α_{PML} is instead defined in normalized units of Nepers per grid point, where $\alpha_{\mathrm{PML}} = (\Delta\xi/c_0)\alpha_\xi$. The corresponding PML thickness L_{PML} is also defined in units of grid points.

5.3.5   Stabilization, grid spacing, and time step

The numerical model used in k-Wave is stable when [195]

$$|\sin\left(c_{\mathrm{ref}}k\Delta t/2\right)| \leq \frac{c_{\mathrm{ref}}}{c_0}. \qquad (5.25)$$

A number that is used to impose this stability is the one-dimensional Courant-Friedrichs Lewy (CFL) number, which is defined as the ratio of the distance a wave can travel in one time step to the grid spacing:

$$\text{CFL} \equiv c_0 \Delta t / \Delta x. \tag{5.26}$$

The required time step for a given grid spacing Δx thus follows from:

$$\Delta t = \frac{\text{CFL} \Delta x}{c_{\max}}, \tag{5.27}$$

with $c_{\max}$ the maximum speed of sound of the media. A CFL value of 0.3 typically balances accuracy and computational speed for weakly heterogeneous media [195, 202]. The grid size is derived from the user's input points per wave (PPW), following:

$$\Delta x = \frac{c_{\min}}{\text{PPW} f}, \tag{5.28}$$

with $c_{\min}$, the minimum speed of sound. Three points per wave are at least required for stable simulations.

5.3.6   Off-grid source formulations

Initial conditions are set by using an input source. Time-varying pressure sources are implemented after the update steps by adding the source terms to the relevant field values at the desired grid points within the domain. The desired grid points are the locations of the elements, and a continuous sinusoidal pressure source is applied. Instead of directly applying the pressure source to the desired grid points, an off-grid source formulation is utilized [210]. On-grid sources will often be subject to staircasing effects, resulting in errors. Upsampling by increasing the spacing of the off-source integration points relative to the grid spacing is required to eliminate these effects. The upsampling ratio UpRate is therefore defined, which is given by [210]:

$$\text{UpRate} = \frac{M_{\text{grid}}}{M_{\text{integration}}}, \tag{5.29}$$

with $M_{\text{grid}} = A_{\text{source}}/(\Delta x)^2$ the number of grid points of the source given by the ratio of area of the source A_{source} and the grid spacing Δx, and $M_{\text{integration}}$ the number of integration points of the off-grid source. In principle, the definitions for the off-grid sources require evaluating all grid points to yield an exact expression. However, it can be computationally beneficial to restrict the discretized source to grid points near the support of the true source. Therefore, a truncation threshold BLItol is used to reduce the computational expenses [210].

5.3.7   Off-center focusing

The existing modeling framework of a SAS spherical 3D printer, given in previous work [182], is derived for a spot moving close to the center of a sphere. It is not generally applicable to spots that move further away from the sphere's center. In those cases, the travel distance of the waves from each ultrasound transducer differs.

Therefore, simulations are utilized to systematically study the performance of the spherical SAS 3D printer for off-center focal spots. The principle of phased arrays is used to find the correct timing of the ultrasound elements. Herein, the delay between the transmission of

ultrasound elements, $\Delta t_{\text{delay},j}$, is determined by the distance of each element location, $\boldsymbol{r_j}$, to the focal spot location, $\boldsymbol{F}$, according to:

$$\Delta t_{\text{delay},j} = \frac{\lfloor d_j f_0 / c_0 \rfloor}{f_0} - \frac{d_j}{c_0}, \tag{5.30}$$

with the distance of each element, d_j, given by:

$$d_j = ||\boldsymbol{r_j} - \boldsymbol{F}||. \tag{5.31}$$

Herein, the modulo operation by the division of $1/f_0$ is used to scale the delays.

Attenuation is a function of distance, for which the pressure scales exponentially according to Beer-Lambert's law $p = p_0 \exp{-\alpha_p d}$, with α_p the pressure-based attenuation coefficient and d the travel distance. The pressure amplitude decreases with distance for a point source according to $p \sim 1/d$. This implies that in the case of nonconstant element-focal point distances, a correction of the source pressure amplitudes must be applied to get equal contributions of each element to the focal spot pressure. This correction is called the apodization of the source element. Theoretically, for a collection of point sources, the apodization weighting of each source w_j is determined by:

$$w_j = \frac{\min\{d_1 \exp(\alpha_p d_1), \dots, d_j \exp(\alpha_p d_j)\}}{d_j \exp(\alpha_p d_j)}. \tag{5.32}$$

The source pressure amplitude of each element is then corrected by $p_{0,j} = p_0 w_j$. The presented delays and corrections are valid in the case of homogeneous media. Also, the pressure amplitude correction assumes that the elements are point sources, meaning that the sound source is much smaller than the wavelength of sound it emits. These assumptions are not always accurate, as a coupling media between the elements might be desired, and relatively large bowl-shaped elements can be used during printing.

Therefore, a time-reversed simulation method is proposed. This method positions a point source at the desired focal position (see Figure 5.5). The ultrasound elements are modeled as sensors (red dots in Figure 5.5a), which record the pressure magnitude over time. In time, each element records a waveform originating from the point source, and the time of flight and pressure amplitude are extracted from the first peak of this waveform (see Figure 5.5b). Utilizing time reversal, the delays between the elements, shown in Figure 5.5c and apodization weighting can be calculated from the time of flight $\text{TOF}_{\text{point},j}$ and the inverse of the pressure amplitude $p_{\text{point},j}$, according to:

$$\Delta t_{\text{delay},j} = \frac{\lfloor \text{TOF}_{\text{point},j} f_0 \rfloor}{f_0} - \text{TOF}_{\text{point},j}, \tag{5.33}$$

$$w_j = \frac{\min\{p_{\text{point},1}, \dots, p_{\text{point},j}\}}{p_{\text{point},j}}. \tag{5.34}$$

This method assumes the superposition of pressure fields and a single frequency, which is valid for the proposed linear wave equations, including attenuation (not for nonlinear wave equations).
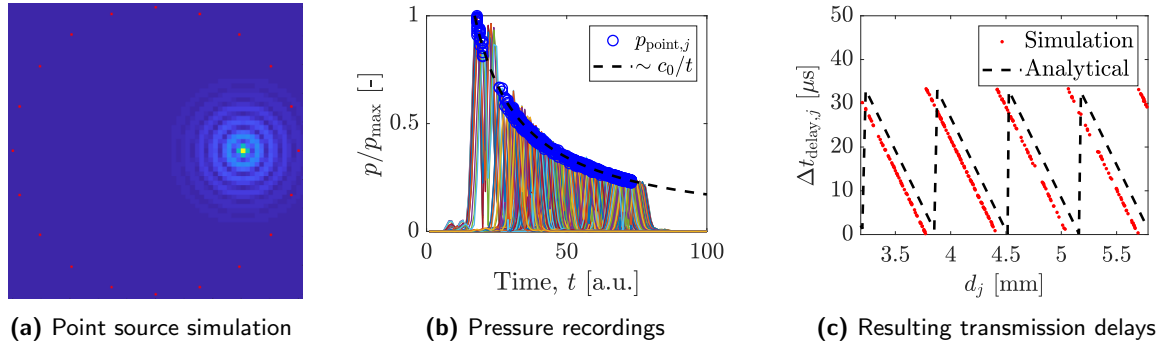
(a) Point source simulation   **(b)** Pressure recordings   **(c)** Resulting transmission delays

Figure 5.5: Time reversal method starting from a point source simulation to determine the pressure weightings and transmission delays. Elements are used as sensors to capture the maximum pressure in time (see b). Element delays are found from the recording times of the maximum pressures (see c).

5.3.8 Simulation protocol

The size of the grid elements in 3D simulations must be relatively large to avoid memory issues [211]. This leads to a coarse mesh and coarse pressure or intensity field solutions. Using the CFL < 0.2 and PPW > 3, the simulations are (in principle) accurate on these course meshes [211]. An interpolation of the complex pressure field on the course grid is performed to extract more detailed features smaller than the grid element size in these simulations, like the focal spot shapes and the peak focal pressure. An extract representation of the pressure field near the focal spot is found by interpolating the Fourier transform of the complex pressure magnitude. This interpolation is only performed in a smaller box with length L_{box} around the focal spot to reduce computational costs and the resulting matrix sizes of the pressure field. Using the interpolated intensity field, the heating near the focal spot is simulated by solving the energy balance in Equation (5.6).

Configuration   Pressure/Intensity field   Fourier interpolation   Temperature field
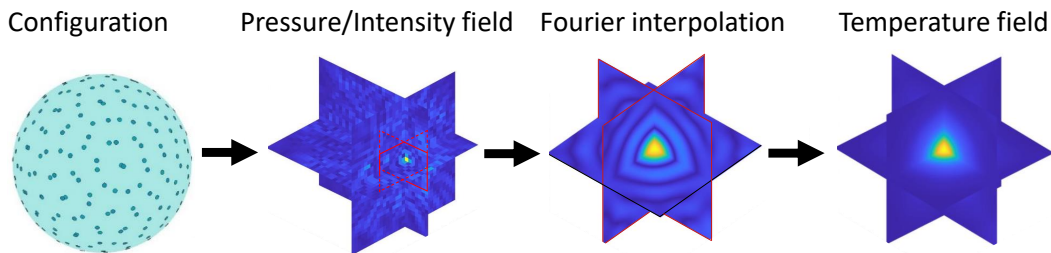
Figure 5.6: Simulational protocol to go from a coarse grid with a certain element configuration to a fine grid to perform the temperature simulations close to the focal point.

5.4 Results and discussion

A spherical build volume shape is examined to study the effects of transducer configuration on SAS printing. The effects of element size and focal distance on pressure amplitude and resolution are discussed using the above-described numerical methods.

5.4.1   Validation

Validation simulations of the presented methods in 3D (and axisymmetric 2D) are given in Figure 5.7. In these simulations, a bowl-shaped transducer with a diameter of $D = 30$ mm and a focal distance of $F = 30$ mm is modeled (see Figure 5.7a). The frequency of the transducer is $f = 1$ MHz, the initial pressure $p_0 = 1$ MHz, and the medium has a density of $\rho = 1000$ kg/m^3, speed of sound of $c_0 = 1500$, and attenuation of $\alpha_p = 0$. The grid spacing and time step are $\Delta\xi = 300$ µm and $\Delta t = 40$ ns, respectively, following from cfl $= 0.2$ and ppw $= 5$. The transducer is modeled by the off-grid source definition, with BLITol $= 0.05$ and UpRate $= 100$. An analytical solution for focused ultrasound sources, shown by Treeby et al. [211], is utilized to validate the 3D simulation results in 5.7a. Excellent agreement is found between the pressure amplitude over distance in the simulations and the analytical solution. In addition, two analytical approximations are derived by O'Neil [149], which are used in the modeling framework of the SAS 3D printer [182]. For the first and simplest approximation, it is assumed that the linear pressure focal gain, G_p, equals the wave number times the depth of a bowl-shaped transducer (i.e., $G_{p1} = kh$). O'Neil [149] shows that this approximation is valid for $kh > 34$. The presented simulation has a linear focal gain of $kh \approx 16$, and hence, also a second analytical approximation is shown defined as $G_{p2} = kh + 12/(kh)$ [149]. Both approximations give a reasonable approximation of the maximum focal pressure.

(a) 3D simulation of a focused transducer (xy-plane)   **(b)** Comparison with analytical solutions
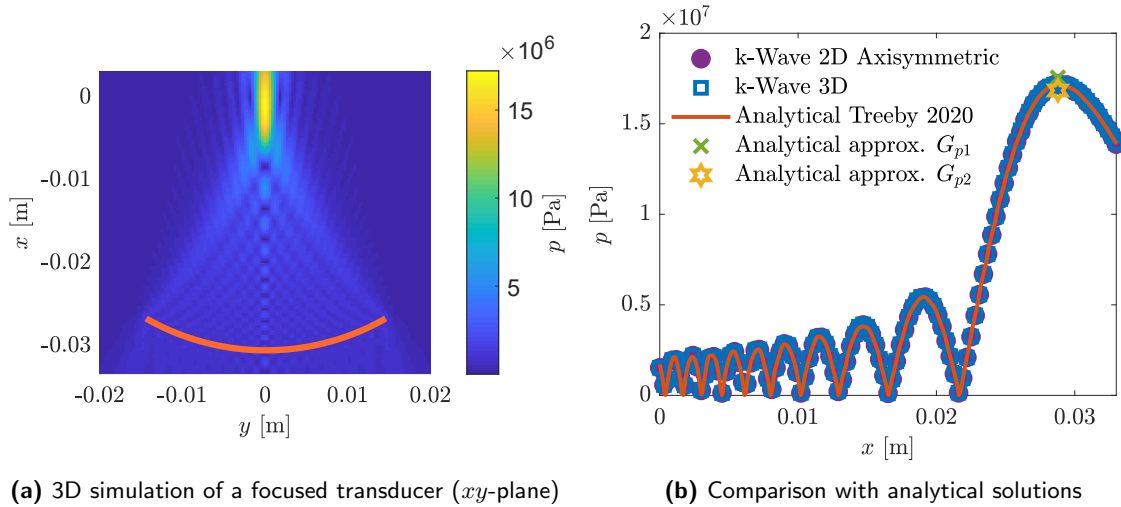
Figure 5.7: Validation of the 3D simulations by comparison with an axisymmetric 2D simulation and analytical solutions [149, 211].

These results show the validity of the presented k-Wave simulations in three dimensions. For more details on grid size, mesh size, and time step effects on simulation accuracy, memory use, and computational costs, see [211].

5.4.2   Off-center focusing and the effects of focal distance and element size

The effectiveness of the proposed methodology for off-center focusing is shown by first simulating three-dimensional wave propagation in a spherical SAS 3D printer with elements smaller than the wavelength. The transducer fully covers the sphere and contains $N_{el} = 642$

Figure 5.8: Effect of focal location on the focal spot.
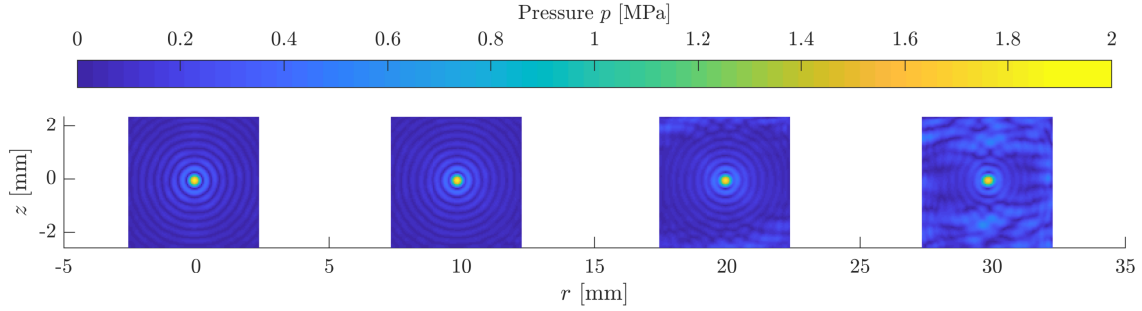
elements of $h_{el} = 500$ µm, positioned in a geodesic pattern on the sphere's surface (see Figure 5.6). The frequency of the sources is $f = 3$ MHz, and a homogeneous media with a density of $\rho = 930$ kg/m^3, speed of sound of $c_0 = 1936$ m/s and attenuation of $\alpha_p = 21.7$ 1/m is used ($\alpha_0 = 0.7328$ dB/(cm MHz^y) and $y = 0.8607$). The wavelength is $\lambda = 645$ µm ($h_{el} < \lambda$), implying that Equation (5.32) is applicable. Simulations of an 80 mm spherical volume ($R_{sp} = 40$ mm) are performed for focal distances of $F_x = 0$, 10, 20, and 30 mm. For a CFL $= 0.5$ and PPW $= 3$, the grid spacing and time step are $\Delta x = 215$ µm and $\Delta t = 55.6$ ns, respectively.

Figure 5.8 shows a 2D view of the resulting interpolated pressure fields of the four simulations with different focal distances. Each pressure field represents a $L_{box} = 5$ mm box of the single simulation, interpolated at an interpolated grid spacing of $\Delta x_{interp} = 50$ µm. For a sphere, the focal position in the Cartesian coordinate system can be described by a radial vector e_r. Hence, the r-axis replaces the x-axis in the figure.

The pressure-based spot size is defined as the pressure peak's full-width half-maximum (FWHM at -6 dB). From left to right, a focal spot size of 370 to 440 µm is found. Additionally, the pressure at the focal spots is similar. Surprisingly, combining multiple elements makes focal spot sizes smaller than the wavelength. The SAS mathematical framework in van Berlo et al. [182] assumes that focal spots are limited to the wavelength. Hence, the restriction in terms of resolution presented in this work can be released, and the theoretical minimum focal spot size should be revisited. The focal spot definition should also include the case of many elements with $\xi = F/h_{el} >> 2$. This case has not yet been mathematically studied but is now shown to be promising through numerical analysis.

Therefore, the effect of element size on the off-center focusing capabilities is studied next. Similar simulations at a focal distance of $F = 30$ mm are performed to study this effect with element sizes ranging from 250 to 3125 µm. The resulting pressure fields for $h_{el} = 300$, 1000 and 3125 µm are given in Figure 5.9. For the smallest element size of 300 µm, smaller than the wavelength, the pressure fields are similar to Figure 5.8 with 500 µm. Below the wavelength, the spot size is inversely proportional to the element size: $D_{spot} \sim 1/h_{el}$. However, increasing the element size above the wavelength distorts the wave field near the focal spot. The wavefronts irradiated by the larger bowl-shaped elements are directed towards the sphere's center. Increasing the element size reduces the fraction of the waves directed away from the center. This effect increases if the element size is increased. Therefore, a distorted focal shape is seen for the largest element size of 3125 mu.
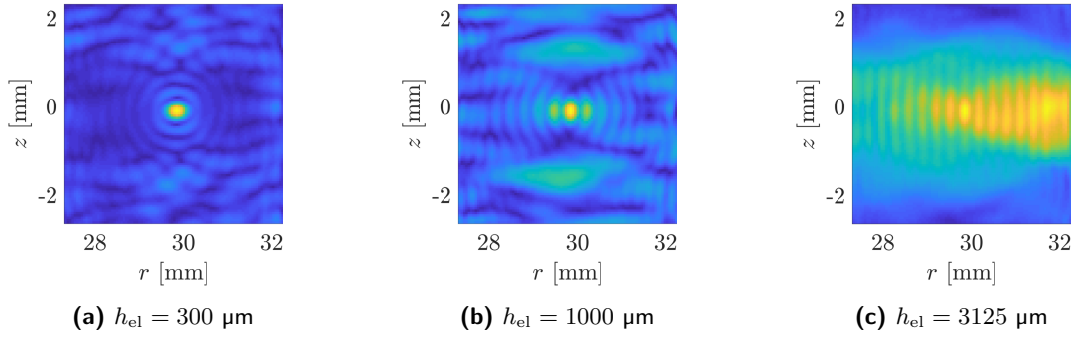
(a) $h_{\mathrm{el}} = 300$ µm   **(b)** $h_{\mathrm{el}} = 1000$ µm   **(c)** $h_{\mathrm{el}} = 3125$ µm

Figure 5.9: Effect of element size on the focal spot.

5.4.3   Off-center focusing in heterogeneous media

Moving from a homogeneous spherical volume to a multi-layered heterogeneous media can improve transmission efficiency. Each medium would represent a shell around the powder core as depicted in Figure 5.10a for two media. For a heterogeneous media, the emitted waves of each element, j, travel a distance, d_{ij}, through each media, i. At the boundaries of each media, the ultrasound waves are reflected and transmitted, and attenuation causes energy loss over distance. The outer shell is designed to have a small attenuation to improve acoustic transmission compared to the powder (core) volume. This is useful, as the focal spot shape is not preserved close to the elements. Sound speed and density are also chosen, similar to the material of the core, to minimize reflections.

In Figure 5.10a, the focal spot is positioned at a distance $F = r$ from the sphere's center. The radius of the core-shell is R_1, and the outer radius of the second media R_2 equals the sphere radius in this case. The red squared markers indicate elements positioned on the sphere, and the orange lines connect these elements to the focal position, indicating the total distance $d_j = \sum_{i=1}^{N} d_{ij}$, with N the number of media and d_{ij} the distance a wave travels through each media i. The angle between the sphere's center and the element is defined as θ. The radii and distance are dimensionalized by defining the core's radius as the characteristic radius, such that $X^* = X/R_1$, with X the radius or distance.

It has been shown that the elements can be modeled as point sources if the element size is smaller than the wavelength. Additionally, sufficient elements are required to maintain the focal spot shape. For a point source, the intensity at the focal spot in a lossless media is inversely proportional to the square of the distance. Besides, in two lossy heterogeneous shells with similar speed of sound and density, the intensity at the focal spot, I, can be approximated by summation over the many elements on a sphere, such that:

$$I \sim \left(\sum_{j=1}^{M} \frac{1}{d_j} \prod_{i=1}^{N} \exp\left(-\alpha_i d_{ij}\right) \right)^2 \tag{5.35}$$

with M the number of elements, N the number of media, and $\alpha = 2\alpha_p$. Also, $d_{1,j}$ is the distance from the focal spot to the interface between media 1 and 2 (on the axis normal to an element), $d_{2,j}$ is the distance from the point source to the interface between media 1 and 2, and $d_j = d_{1,j} + d_{2,j}$ is the distance from the point source to the focal spot at r (see Figure 5.10a).

(a) Spherical heterogeneous media of two shells

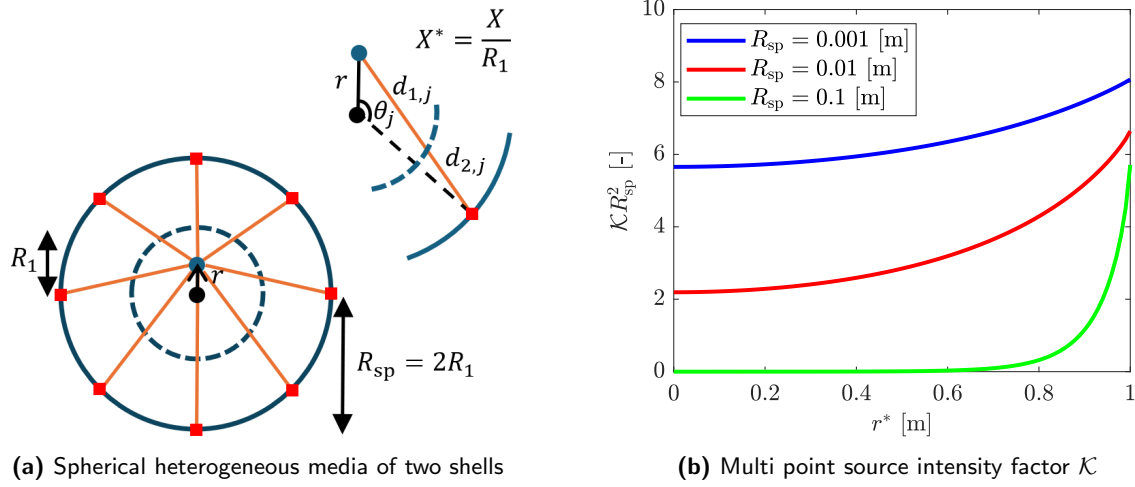(b) Multi point source intensity factor $\mathcal{K}$

Figure 5.10: Off-center focusing in heterogeneous media. Definitions for a sphere with two shells are given in a). The red squared markers are elements positioned on the surface of the sphere. Orange lines indicate the distance d to the focal spot at a radius r from the sphere's center. In b), the intensity factor $\mathcal{K}$ is shown for different printer radii R_{sp}. The $\mathcal{K}$ value measures how much energy is transmitted from multiple point sources to a focal spot. This value increases by moving the focal spot away from the sphere's center (i.e., increasing r^*).

Assuming that many point sources are positioned on this sphere, the summation over the elements can be treated as a single integral over the angle θ. The right-hand-sight in Equation (5.35), is defined as the intensity factor $\mathcal{K}$, which follows from:

$$\mathcal{K} = \int_0^{2\pi} \left(\frac{1}{R_1 d^*(\theta)} \right)^2 \exp\left(-\alpha_1 R_1 d_1^*(\theta)\right) \exp\left(-\alpha_2 R_1 d_2^*(\theta)\right) \mathrm{d}\theta, \qquad (5.36)$$

assuming many elements. Here, d, d_1, and d_2 are continuous functions of the angle θ and solely depend on the geometry. The resulting set of equations is solved by numerical integration over θ, as explained in detail in Appendix 5.A.1.

The resulting intensity factors for a multi-point source, scaled by the focal distance squared, are given in Figure 5.10b. This shows that the further away the spot is from the center, the more energy is deposited at the spot. This results from a decrease in the average distance through media 1 for increasingly off-centered focal spots. In terms of printing, this is beneficial since moving away from the center of the sphere requires less power of the elements. Therefore, apodization between point sources can always be applied in these heterogeneous systems to correct spot-shape inaccuracies. This solves the issue of spot size and shape deviations from a spherically shaped spot and reduces the required power by adding the low-attenuation coupling shell. Figure 5.10b shows that it depends on the printer radius R_{sp} how much energy is transmitted towards the focal location.

5.4.4 Cubical build volume

One of the benefits of using the SAS technique is the freedom to place the transducers and elements. The configuration of elements is adjustable to the shape and dimensions of a part. One of the possible build volume shapes that could be useful is a cubical shape (see Figure

5.3b). Contrarily to a spherical build volume, the cubical shape requires moving sources (two directions) over the faces of the cube to scan within most of the volume. These surfaces are flat instead of curved, so these movements are relatively simple in terms of control. The benefit of using moving sources is that fewer elements are required effectively, as they can be positioned as close as possible to the focal spot, reducing the path length.

Simulation results for a $L = 80$ mm cubical SAS 3D printer, with six square-shaped transducers containing $N_{el} = 729$ elements of $h_{el} = 400$ µm, positioned at an element distance of $h_s = 300$ µm are shown in Figure 5.11. The simulations show the off-center focusing at a focal position of $\bar{F} = [20,\ 20,\ 20]$ mm for a center frequency of 4 MHz ($\lambda = 484$ µm). For a CFL $= 0.5$ and PPW $= 3$, the grid spacing and time step are $\Delta x = 161$ µand $\Delta t = 41.7$ ns, respectively.

The resulting pressure field represents this cubical configuration's main focal beam shape and grating lobes. Grating lobes result from the element size, element spacing, and finite size of the transducers and are, in this case, in magnitude at least four times smaller than the maximum focal pressure. A nearly cubical focal spot is generated by limiting the number of active elements of the transducers closest to the focal position, as illustrated in Figure 5.11b. Although the shape of the focal spot is cubical, the pressure field at the focal contains several peaks (see Figure 5.11c). These peaks result from an upper limit on element pitch (and size) that follows from the logical extension of the Nyquist sampling theory to the spatial domain. Herein, the "half wavelength rule" [212] states that the pitch of the elements should be at most half the wavelength, which is not the case in the simulation. Reducing the element size and spacing below 200 µm should reduce the spot size and remove the peaks at the focal spot.

(a) Off-center focusing in a square **(b)** Cubical focal spot shape **(c)** Focal spot size and lobes
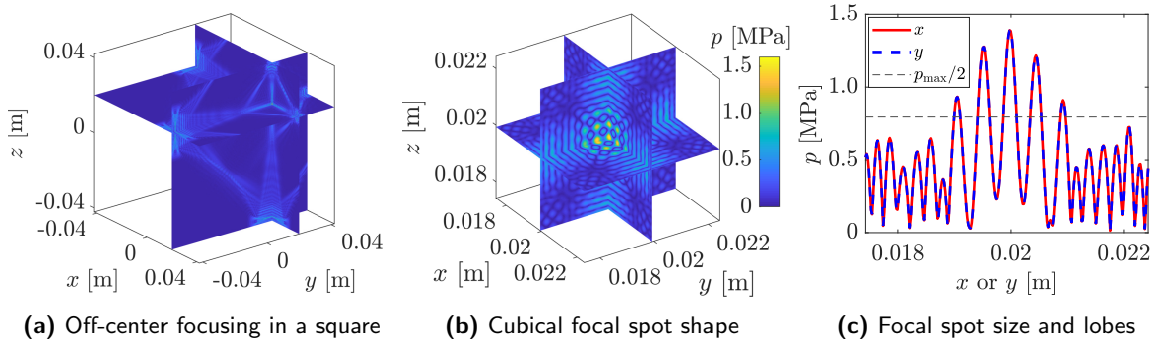
Figure 5.11: Cubical build volume with six moving transducers. The number of active elements is related to the distance of the transducer to the focal spot.

A cylindrical build volume shape is an intermediate shape that could combine the benefits of a spherical and cubical build volume. It benefits from a short distance to the focal location in the radial direction and only one moving ring of the transducer in the axial direction [144]. The benefit of this shape is that in terms of control, the transducers only need to move in one plane, requiring only one movement (up and down). Additionally, this geometry is particularly of interest for continuous manufacturing. In terms of simulations, the domain size is also small, as only the region near the element rings needs to be modeled. Studying the cylindrical geometry in future work is advised.

5.4.5   Acoustic-thermal simulations

The temperature increase of the focal spot is found by acoustic-thermal coupling in the energy balance in Equation (5.6). The energy balance is solved in three dimensions from the interpolated intensity field ($|p|^2$) near the focal region ($\Delta x_{\text{interp}} = 20$ µm). The resulting temperature increases after 1 second of ultrasonic heating for both spherical and cubical geometries are given in Figure 5.12.

Both geometries contain in total approximately 2500 (active) elements of 400 µm, and the spacing of the rectangular elements is 300 µm. Center frequencies are 4 MHz, and the length of both systems is 80 mm, with $R_{\text{sp}} = 40$ mm. The focal position is set at $\bar{\boldsymbol{F}} = [20\ 20\ 20]$ mm in both cases. The material resembles a compacted PA12 powder, for which a density, speed of sound, and attenuation of $\rho = 930$ kg/m^3, $c_0 = 1936$ m/s, and $\alpha_p = 27.8$ 1/m are assumed. The focal spot pressure amplitude of the wave simulations is set to 10 MPa for both configurations. The initial temperature is 178 °C, and the time step of the thermal simulations is 0.01 s. The thermal conductivity and specific heat are $K = 0.11$ W/(K m) and $c_p = 1700$ J/(kg K).

(a) Temperature field of spherical configuration

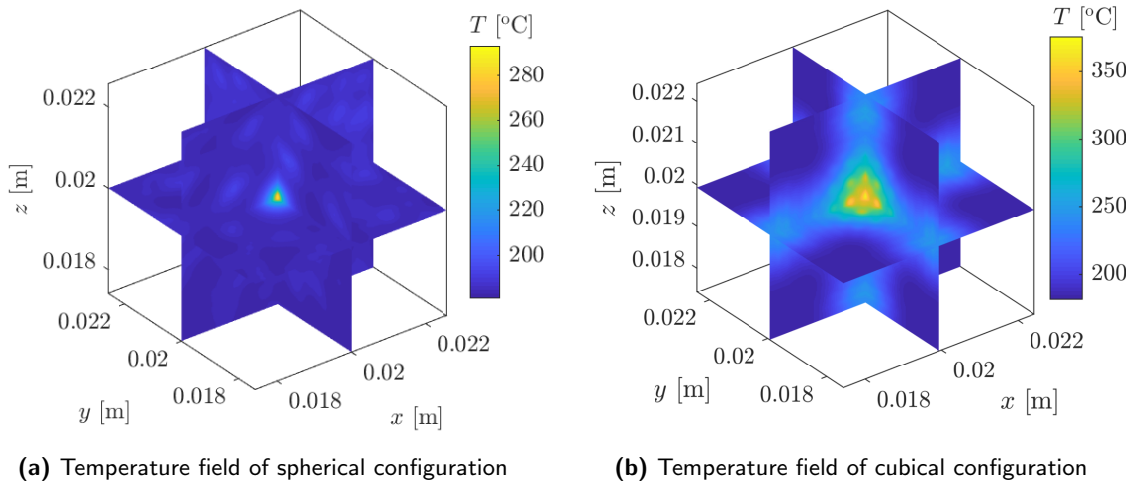(b) Temperature field of cubical configuration

Figure 5.12: Temperature increases near the focal region in a spherical and cubical SAS 3D printer configuration.

Figure 5.12a shows the spherical configuration's temperature field near the focal spot. The temperature magnitude at the focal spot scales with the pressure magnitude squared. The thermal diffusion time is large ($\sim \rho c_p/K$) compared to the heating time; the temperature-based spot size is smaller than the pressure-based spot size.

The temperature field of the cubical configuration is shown in Figure 5.12b. Herein, the temperature increase exceeds 350 °C in the focal region. The focal spot size is larger than the spherical configuration due to side lobes near the focal point, resulting in a high maximum temperature. Additionally, the surrounding temperature increases more compared to the spherical configuration. This means that the presented cubical configuration is less effective in focusing ultrasound and, thus, less effective in heating the focal spot without affecting the surrounding material.

5.5   Conclusions

In this study, we explored the innovative 3D printing technique of Selective Acoustic Sintering (SAS) through a comprehensive numerical analysis focused on optimizing printer configurations. The pivotal role of high-intensity focused ultrasound (HIFU) in the sintering of powder-based materials is thoroughly examined, revealing the significant potential of ultrasound technology in enhancing the efficiency and applicability of additive manufacturing processes.

A significant contribution of this work to the field of SAS 3D printing is the development of a means to accurately study and quantify the temperature increase at off-center focal positions. This advancement is crucial, as it addresses one of the key challenges in SAS—maintaining consistent sintering quality across the entire print bed. By enabling precise control and prediction of temperature distributions, even in off-center positions, we have laid the groundwork for more reliable and efficient sintering processes.

Using numerical simulations, we have demonstrated the feasibility of off-center volumetric scanning in SAS, introducing a time-reversal method that ensures spot size accuracy. Systematically varying the focal position and element size resulted in two important findings:

- Spot sizes smaller than the wavelength can be achieved by positioning many elements on the build volume.

- Element sizes below the wavelength are required to benefit from these enhanced focal spot effects

Besides, in heterogeneous media with a coupling media to enhance ultrasound transmission, the method of SAS 3D printing is more effective. The presented apodization methods also apply to these heterogeneous media, opening new design possibilities in SAS. Finally, the effectiveness of the numerical tool is shown by altering the design of the build volume to a cubical-shaped printer. The interference patterns and temperature increase at the focal spot are demonstrated, which allows for complex model-based designs of SAS 3D printing.

In conclusion, this research provides valuable insights into optimizing SAS printer configurations, marking a significant step forward in additive manufacturing. By harnessing the power of HIFU and advancing the capabilities of phased array technology, we can unlock new possibilities in SAS manufacturing that were previously unexplored. We continue to explore and refine this technology to meet the industry's evolving demands.

5.A   Additional information

5.A.1   Intensity factor derivations

The functions of $d(\theta)$, $d_1(\theta)$ and $d_2(\theta)$ are found from the following set of equations, which follow from geometrical analysis of the dimensionless distances and radii:

$$(d_1^* + d_2^*)^2 = r^{*2} - 4 \cos(\theta) \, r^* + 4 \tag{5.37}$$

$$\cos(\theta_1) = \frac{-d_1^{*2} + r^{*2} + 1}{2 \, r^*} \tag{5.38}$$

$$d_2^{*2} - \frac{2 \, d_2^* \left((d_1^* + d_2^*)^2 - r^{*2} + 4 \right)}{4 \, d_1^* + 4 \, d_2^*} + 1 = 2 - 2 \cos(\theta_2) \tag{5.39}$$

$$\theta = \theta_1 + \theta_2 \tag{5.40}$$

with θ_1 and θ_2. The resulting dimensionless distances and the relative angles as a function of angle θ are given in Figure 5.13 for $R_{\mathrm{sp}} = 0.01$ m.

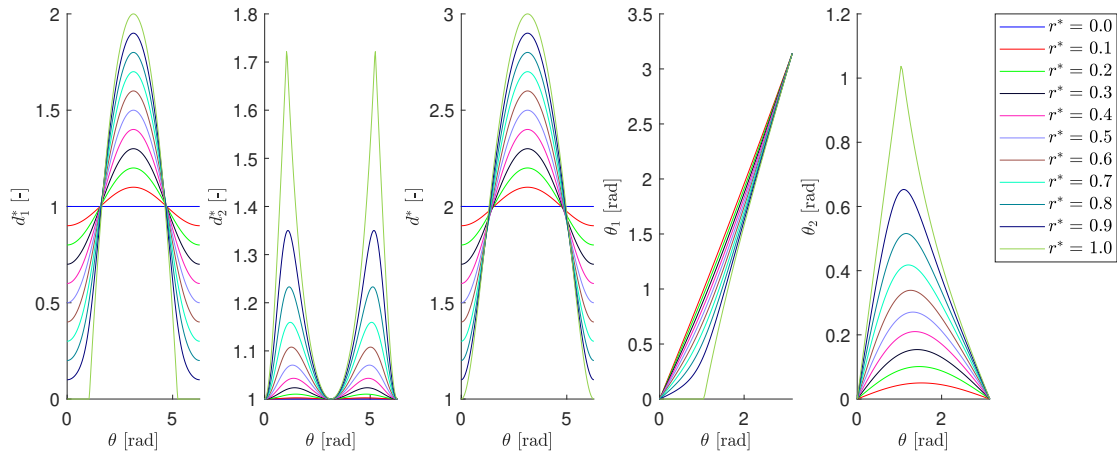**Figure 5.13:** The θ dependency of the distances and angles for different focal locations indicated by r^*.

These results are used to numerically solve the intensity factor in Equation (5.36).

Chapter 6

Selective Acoustic Sintering: Acoustic Characterization of Powder Compacts

Abstract

This chapter discusses the acoustic characterization of powder compacts for selective acoustic sintering (SAS) using ultrasound (US) techniques. The SAS process requires using powder-based materials that can be sintered with acoustic energy. However, there is limited literature available on the US characterization of powders. Most studies focus on the US characterization of solids. This chapter explores pulse-echo and through-transmission US techniques to measure the speed of sound, reflection coefficient, and acoustic attenuation of powder compacts. The chapter also highlights the challenges of US characterization in nonhomogeneous media and the potential sources of error that can affect measurements. Furthermore, the chapter presents a model-based design of a US characterization method and a fully operational setup for characterizing unfilled and filled powder compacts. Overall, this chapter provides valuable insights into the US characterization of powder compacts, which are crucial for developing new powder-sintering processes such as SAS.

6.1   Introduction

Many literature studies present ultrasound (US) characterization results on solids rather than powders and lack a fundamental validation of their US characterization setup. From the limited available literature, the work of Hentschel and Page [213] discusses the relation between the speed of sound and porosity in compacted powders. The resulting drop in modulus and density with increasing pore fraction drastically decreases the speed of sound of these compacts. Similar trends with porosity are reported by Amado-Becker et al. [214] for laser-sintered PA12 particles. This shows that tuning porosity can be an effective way to adjust the acoustic properties of powder-like materials.

Among the acquisition methods used in ultrasonic tests, pulse-echo (PE) [215–221] and through-transmission (TT) [222–227] are the most common. The basis of these ultrasonic analyses is the relationship between the measurable ultrasonic properties (speed of sound, reflectance, and attenuation) and the material and (micro)structural properties of the sample

(e.g., composition, structure, physical state) [228]. In PE and TT, dimensional measurements, time of flight, and signal amplitude allow the speed of sound, reflection coefficient, and acoustic attenuation of the medium to be determined [229–231].

The ultrasonic systems may or may not be immersed in a water bath. For a sample in an aqueous medium, the reflection coefficient is influenced only by the properties of water and that of the sample. In contrast, in contact ultrasound, a coupling is usually used to ensure the transmission of signals to the sample surface. A combined pulse-echo and through-transmission method for contact ultrasound has recently been proposed by Dourado et al. [232]. Herein, measurements were performed simultaneously with the two receiving transducers. The method's usefulness for determining a combined reflection coefficient and improvements in the estimates of acoustic attenuation in low-loss samples has been shown, and numerical simulations were used to validate the proposed method.

Towsyfyan et al. [233] discussed the challenges of the ultrasonic inspection of aerospace composites. They reported that the traditional approach of immersing the transducer and pieces in a water tank provides the best results. Therefore, in a follow-up of an immersed through-transmission (TT) setup developed by our colleagues at Eindhoven University of Technology [234], this work focuses on the development of an immersed setup combing through-transmission and pulsed-echo (TT/PE).

Similarly to Dourado et al. [232], this study aims to explore the impact of ultrasound probe frequency, coupling media, and material properties on the accuracy of the measurements using numerical simulations. The resulting model-based design of an ultrasound characterization method will be translated into a fully operational setup with known errors and limitations. The setup will be combined with existing techniques to characterize unfilled and filled powder compacts.

Recently, our work on acoustic 3D printing, selective acoustic sintering (SAS), has provided a need for the characterization of powder-based materials applicable for powder-sintering [182]. Ultrasonic propagation in homogeneous materials is well-known. However, this phenomenon in nonhomogeneous media, mainly for US characterization applications, has challenged researchers [228]. Therefore, new measurement methods are constantly being developed. Although powder media are inhomogeneous, loosely to fully compacted powders can be treated as homogeneous media in standard US characterization techniques because wave speeds are insensitive to density variations, and linear elasticity applies as ultrasound induces small displacements [213].

As with any measurement technique, it is essential in ultrasound (US) characterization measurements to thoroughly understand its underlying physical principles and potential sources of errors adversely affecting measurements. Several physical phenomena result in promotional energy losses in this process: spherical divergence, dispersion, diffraction, attenuation by absorption and scattering, and losses at the interfaces [235–238].

An ultrasonic system typically comprises generation equipment, transducers, receiving equipment, cables, and connectors. Therefore, in addition to the propagation losses within a material or system, ultrasonic transmission, and reception systems play complementary roles in energy loss [228]. Sources of errors mainly arise in wave propagation data, that is, most variant, in situations where the measured absorption is either very low or very high [239]. This has important implications for the design of characterization setup in which it is necessary to optimize the sample thickness, the operating frequency range, filtering and averaging schemes to control the signal-to-noise ratio (SNR), and the design of electronic systems that are crucial

to overall performance [239]. Besides, parallel alignment of the transducer and receiver faces is crucial to prevent signal distortions and avoid low pass envelope on the received signal [240].

As scattering contributions in particle-filled systems result in significant energy losses, the TT/PE setup design will mainly focus on accurately measuring high-attenuation materials. The effect of powder compaction and filler type will be studied to find the dependency of acoustic material properties on the porosity. These results can be used in the design of a selective acoustic sintering 3D printer, as described in our previous work [182].

The main objective of this work is to develop a reliable and accurate characterization method for powder-based materials, which can be used in a practical setting for various applications. Section 6.2 describes the experimental techniques used in this study, including through-transmission and pulse-echo measurements. In Section 6.4, the experimental results are presented, including the impact of ultrasound probe frequency, coupling media, and material properties on the accuracy of the measurements. Subsequently, in Section 6.4, the results of the model-based design analysis are presented, and US measurement results are shown for filled and unfilled powder compacts. Finally, Section 6.5 summarises the main conclusions.

6.2   Materials and experimental methods

Acoustic measurements of the speed of sound, impedance, and attenuation of liquid, solid, and powder-like materials were conducted using a through-transmission (TT) or a combination of through-transmission and pulse-echo (TT/PE) measurements. In Figure 6.1, the reverberation paths of the combined through-transmission and pulse-echo technique are given for a sample between two coupling media. Herein, the transducer sends a pulsed source signal S through a sample enclosed by two couplant media. The compliant media are required for powder compacts, as the setup is immersed in a water bath. These couplants are used as sample holders in the TT setup [234]. In the case of the through-transmission setup (TT), the transmitted signals Q are recorded on the receiver side. Following the reverberation paths, it can be seen that reflections at the water-couplant, sample-couplant, and receiver-water interfaces result in many reverberation paths that lead to multiple received signals. In the case of the combined through-transmission setup and pulsed-echo (TT/PE) measurements, the echo signals E are also recorded. Again, multiple interfaces contribute to the formation of multiple echoes.

Measurements of the speed of sound, impedance, and attenuation of the sample are performed by processing the transmitted and echo signals. The speed of sound of the sample is derived from the time between the source signal S and the received signal Q_1. This time difference is defined as the time-of-flight TOF. The speed of sound of the sample can be determined from:

$$c_3 = d_3 \left(\text{TOF}_{Q_1} - \sum_{i=1, i \neq 3}^{5} \frac{d_i}{c_i} \right)^{-1}, \qquad (6.1)$$

with TOF_{Q_1} the time-of-flight of the received signal Q_1, which is found by cross-correlation of the source signal S with the received signal Q_1. Cross-correlation is proven to be an accurate TOF estimation technique as it uses all the information in the signals [241] and performs well at low signal-to-noise ratios [242]. For this to work, the reflected or multipath signal at the receiver has to be separated in time by more than the width of the correlation peak [243, 244].
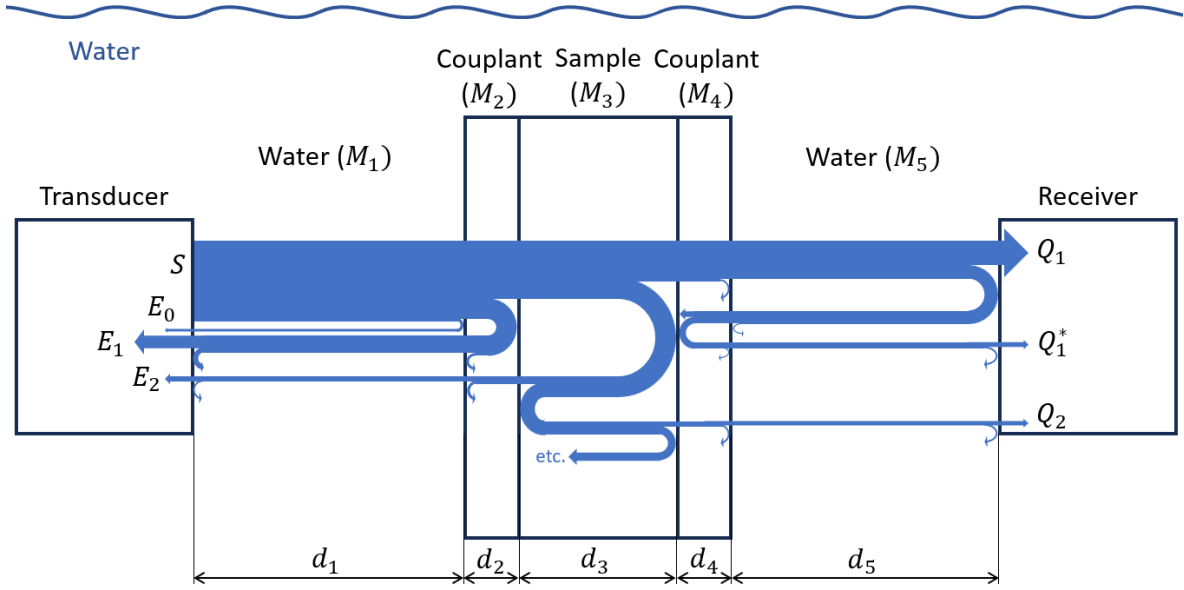
Figure 6.1: Reverberation paths of the combination of pulse-echo and through-transmission measurements.

To ensure this separation, the receiver is positioned so that $(d_4/c_4 + d_5/c_5) > \Delta t_{\text{pulse}}/2$. Here, Δt_{pulse} is the time of the source pulse S, and this condition implies that the signal originating from the reflection from the receiver surface Q_1^* does not overlap with the received signal Q_1.

In the case of the through-transmission (TT) method, the reflection coefficient is estimated from the density and speed of sound of the water and couplant. The magnitude of the reflection coefficient $|\mathcal{R}|$ of two-layered media M_i and M_j is found from the impedance mismatch between the layers:

$$|\mathcal{R}_{ij}| = \frac{|Z_i - Z_j|}{(Z_i + Z_j)} \quad \text{for } i \neq j. \tag{6.2}$$

In the case of a couplant, the magnitude of the reflection coefficient of three layered media M_1, M_2, and M_3 has to be used [245]:

$$|\mathcal{R}_{123}| = \left(1 - \frac{4}{2 + \left(\frac{Z_3}{Z_1} + \frac{Z_1}{Z_3} \right) \cos(k_2 d_2)^2 + \left(\frac{Z_2^2}{Z_1 Z_3} + \frac{Z_1 Z_3}{Z_2^2} \right) \sin(k_2 d_2)^2} \right)^{1/2}, \tag{6.3}$$

with $k_2 = 2\pi f/c_2$. This relation depends on the frequency, sound speed, and thickness of the couplant media M_2. It can be shown that the three-layered relation reduces to Equation (6.2) if media one and two have the same impedance. For a large width of media two and high frequencies, the reflection can be split into the reflection on interface 12 and interface 23. Assuming that the couplant media two has such a small thickness that $Z_2 \sin(k_2 L) \ll 1$ and $\cos(k_2 L) \approx 1$, the reflection coefficient reduces to a two-layered media $|\mathcal{R}_{13}|$, as given in Equation (6.2).

These reflection equations are valid, assuming viscoelastic effects are negligible. In Appendix 6.A.1, a derivation of two viscoelastic media is given to estimate the impact of the attenuation coefficient on the magnitude of reflection. It follows that for samples with significant

attenuation ($\alpha_2 > 10$ dB/cm) and a speed of sound close to that of water ($750 < c_2 < 2250$ m/s), the proposed magnitude of the reflection equations should be replaced by a frequency- and attenuation-dependent reflection coefficient. However, the attenuation is unknown in the TT measurement. Therefore, only samples with small attenuation coefficients can be measured with a TT setup. Besides, powders are heterogeneous, and assuming an effective impedance might not be valid.

The TT/PE technique measures the reflected signal to overcome these issues. Using the source signal S and the reflected signal E_1, the magnitude of the reflection coefficient is found as follows:

$$|\mathcal{R}_{13}| = \frac{S}{E_1} \exp\left(2(\alpha_1 d_1 + \alpha_2 d_2)\right), \tag{6.4}$$

with α_1 and α_2 the attenuation coefficients of water and coupling media, respectively. An impedance match between water and couplant is assumed.

In both cases, TT and TT/PE, the attenuation of the sample is found from the transmitted signal by correcting for the reflected fraction of the signal and the attenuated fraction from the other media. The attenuation of the sample follows from:

$$\alpha_3 = \frac{1}{d_3}\left(\ln\left(\frac{S\mathcal{T}_{\text{tot}}}{Q_1}\right) - \sum_{i=1, i\neq 3}^{5} \alpha_i d_i\right), \tag{6.5}$$

with $\mathcal{T}_{\text{tot}} = \prod_{j=2}^{5} \mathcal{T}_{j-1,j}$ the total transmission coefficient. Assuming an impedance match between water and the couplant, and that media $M_1 = M_5$ and $M_2 = M_4$, the total transmission coefficient is reduced to $\mathcal{T}_{\text{tot}} = \mathcal{T}_{13}^2 = 1 - |\mathcal{R}_{13}|^2$, using the reflection coefficient in Equation (6.4). To convert the attenuation from Np to dB/cm, the relation 1 Np = $20/\ln(10)/100$ dB/cm is used. This method of measuring the absorption coefficient permits correction for the losses during multiple reflections of ultrasonic pulses in the sample, thereby considerably improving the measurement accuracy. Possible types of error that remain are, e.g., improper alignment of the sample, inaccurate determination of the pulse amplitudes, diffraction effects, and the influence of the side walls of the sample [246]. The latter two are only important in low-attenuation samples [246].

6.2.1 Ultrasound characterization setups

In this work, two types of setups are used: the through-transmission setup (TT) and the combined through-transmission and pulsed-echo setup (TT/PE).

TT set-up

The TT set-up of Panfilova et al. [234] measures the speed of sound and attenuation of liquids and low-attenuation solids. Herein, the characterization setup is submerged in degassed water, as shown in Figure 6.2 [234]. The sides of the water tank are lined with foam to avoid possible reflections. The source, receiver, and cuvette are mounted on a rail system to provide their alignment. A gelatin cuvette is used as a couplant media and sample holder. The utilized transducers are single-element focused circular transducers with a diameter of 25 mm and a focal distance of 64 mm. The center of the sample is positioned in the focal region of the transducer. A planar receiver is fixed in a holder at a distance of 85 mm from the cuvette. The source signal passes through a sequence of water (49 mm), gelatine (10 mm), sample (10 mm), gelatine (10 mm), and water (85 mm) before it reaches the receiver.
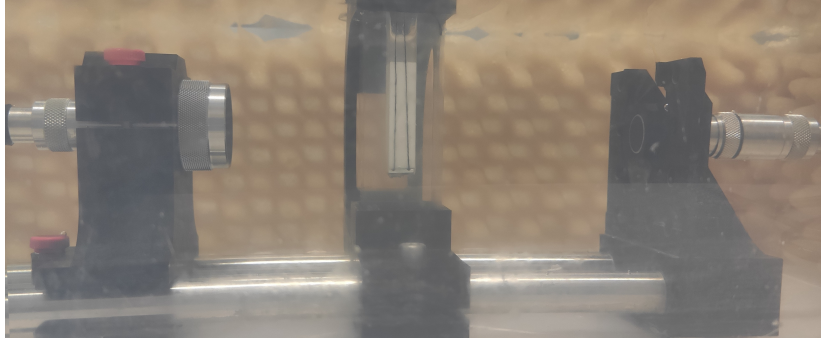
Figure 6.2: through-transmission (TT) setup for measuring the speed of sound and attenuation of liquids and low-attenuation solids [234].

Transducers of type V302-SU-F, V304-SU-F, and V380-SU-F (Olympus) are excited at their center frequencies of 1.0, 2.25, and 3.5 MHz, respectively. Herewith, sinusoidal tune bursts with a rectangular window are transmitted with 20 cycles. The silence between the pulses is set to 250 μs to prevent interference of any possible reflection of the preceding pulse with the following pulse. A total of 92–95 pulses are transmitted at every acquisition. The transmitted signal is received by different unfocused transducers, depending on the transmitted frequencies. A plane piston V306 transducer (Olympus), centered at 2.25 MHz, was used as the receiver for measurements at 1.0 and 2.25 MHz, and a plane piston V309 (Olympus), centered at 5 MHz, was used for 3.5 MHz.

Labview (National Instruments Corp.) is used to control the ultrasound acquisition. A 33220A arbitrary wave generator (Agilent Technologies), controlled by dedicated Labview software, generates the driving signals and transmits them to a 50-dB 2100L RF Power amplifier (Acquitek) connected to the transducer. The source and received signals are displayed on a TDS2014 oscilloscope (Tektronix) and sampled with a NI-5122 (National Instruments Corp.) acquisition board at a frequency of 25 MHz, connected back to the desktop, where the data was stored for analysis. For each acquisition, an average Fourier amplitude spectrum was calculated based on 92 acquisitions using the fast Fourier transform function in Matlab. A Hanning window was used in all cases to reduce spectral leakage.

Before the measurement, the setup is submerged in a degassed water bath and left for half an hour, allowing the gelatin cuvette, initially stored in a fridge, to acclimatize to the water temperature. After that, the water temperature is measured with a thermocouple. A 20 ± 1 °C temperature is measured for all presented TT results in this work. The measurement procedure starts with a reference measurement using water. For this, the cuvette is filled with water, and the transmitted signal Q_0 is measured to determine the source signal S. Subsequently, the water was removed, and a liquid or solid sample was inserted. The solid samples were manufactured to fit inside the cuvette. However, 0.1-1 ml of water (or oil) must be added to form a thin layer between the cuvette and the sample to ensure perfect coupling between the cuvette and the solid samples. Also, air bubbles in this liquid layer must be removed with a stirrer to prevent undesired reflections. As the speed of sound and density of water and the gelatin cuvette are close, it is assumed that the reflection of water (M_1) with the gelatin cuvette (M_2) is negligible. Hence, the reflection coefficient of the sample with water $|\mathcal{R}_{13}|$ is calculated using Equation (6.2) and substituted in Equation (6.5) to find the attenuation coefficient.

TT/PE set-up

A TT/PE set-up is designed to measure the reflection, speed of sound, and attenuation of low- and high-attenuation solids and powder compacts. Details about the design will be discussed in the following sections. The TT/PE setup consists of a high-intensity focused ultrasound (HIFU) transducer, an aluminum sample holder, a disk-shaped sample, and a planar receiver, as shown in Figure 6.3. The source signal passes through a sequence of water (25 mm), sample (6 mm), and water (19 mm) before it reaches the receiver. This setup allows for a 0.5 mm thick elastic couplant (Aqualene, Olympus NDT) at the sample's front and back to shield it from the water.
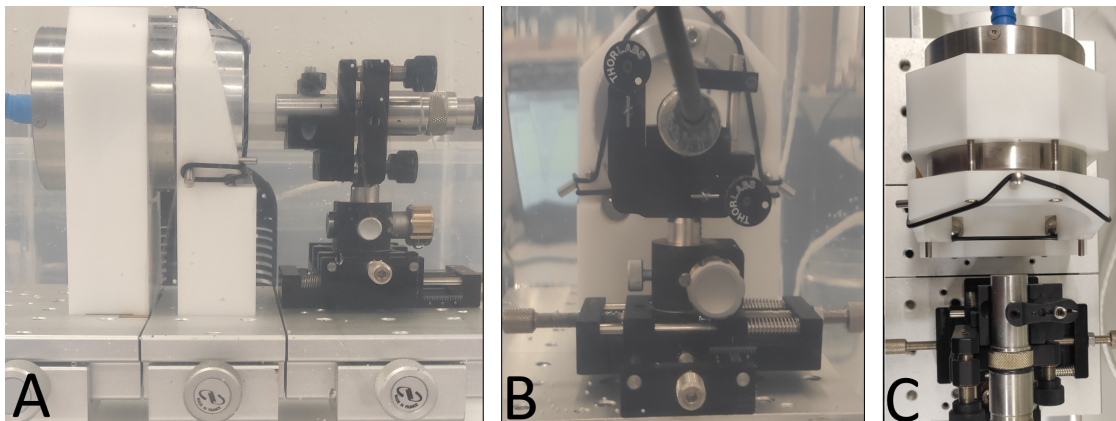

Figure 6.3: Combined through-transmission and pulsed-echo (TT/PE) setup for measuring the reflection, speed of sound, and attenuation of low- and high-attenuation solids and powder compacts. In A), the side view of the setup is shown, wherein from left to right, a HIFU transducer sample holder and planar receiver are seen. In B), a front view is given, and in C), a top view is given.

A single-element PA1864 HIFU transducer (Precision Acoustics) is excited at 2.65 MHz. Herewith, sinusoidal tune bursts are transmitted with a length of 5 cycles and width of 4.5 µs. The silence period between the pulses is set to 10 ms. The diameter of the transducer is 60 mm, the focal distance is 50 mm, and the depth of the piezoelectric element is 10 mm. The HIFU transducer is also a receiver for the reflected/echo signals. The connection between the function generator and the transducer is switched off after the pulse has been transmitted to avoid interference of the send signal with the reflected signal. The front of the sample is positioned at half the focal distance. In this way, the transducer is located at the focal point of the reflected signal, maximizing the echo amplitude. The sample is held in place by a changeable aluminium sample holder. A rubber loop ring (86x2 mm) fixes the sample holder to the set-up. The plane piston V306 transducer (Olympus) is the receiver, centered at 2.25 MHz. It is positioned at the focal point of the transducer to maximize the received signal. A customized compact 5 DOF positioning system consisting of an XYZ stage (Misumi) and a kinetic mirror mount (Thorlabs) is designed for this.

A Matlab GUI is designed to control the ultrasound acquisition. An RSDG2042X arbitrary wave generator (RS PRO) generates the driving signals. It transmits 10 Vpp sinusoidal tone bursts via an SP2T RF Switch F2912 (Renesas Electronics, Evaluation Board, < 1 µs switching time) to the transducer. After 12 µs, a 5V trigger signal is sent to the switching board to open the transducer-oscilloscope connection to receive the echo signal. The source and received signals are displayed on an MSO5104 oscilloscope (Tektronix) using 128 averages, and

each channel is sampled with a frequency of 25 MHz. Pre-amplifiers (Tekbox TBHDR1) and high-pass electrical filters (Thorlabs EF509, 1.8 MHz) are positioned between the transducer-oscilloscope and receiver-oscilloscope connections. The oscilloscope is connected to a laptop that stores the data for analysis.

Before the measurement, the setup is submerged in a degassed water bath and left for half an hour. The samples are loaded after that and are only for 5 minutes in the water bath to limit the water diffusion for nonshielded samples. An aquarium heater (JULIAQUA CS-60, 25 W) controls the water temperature at 25 °C. Two reference measurements must be performed before the sample measurements. Firstly, no sample is used to measure the received signal in pure water. Subsequently, an iso-standard steel C1018 sample is used to relate the measured echo signal to a known reflection coefficient. The sound speed is found from the time-of-flight measurement utilizing Equation (6.1). The reflection coefficient of the sample is measured from the echo signal E_1 using Equation (6.4). The attenuation in Equation (6.5) is derived from this reflection coefficient and the received signal Q_1.

Positioning errors or delays in the setup might affect the time of flight of the reference measurement. Hence, a time correction must be used. The time corresponding to the maximum amplitude of the reference water measurement, $t_{Q_1,\text{ref}}$, is compared to the time of the maximum of the send signal, $t_{S,\text{ref}}$, to find the time of flight of the reference measurement, $\text{TOF}_{Q_1,\text{ref}}$. A time correction can be defined by comparing the time-of-flight of the reference to the actual time-of-flight in water $\text{TOF}_w = c_w/\sum_{i=1}^{5} d_i$, with $c_w(T)$ the temperature-dependent speed of sound of distilled water [247]. This yields $\Delta t_{\text{corr}} = \text{TOF}_{Q_1,\text{ref}} - \text{TOF}_w$. Other samples' received time-of-flight values are corrected by this time correction. Then Equation (6.1) is used to derive the samples' sound speed from the measurement.

To find the reflection coefficient of a sample, a loss of energy at the transducer surface for both sending the pulse and receiving the echo has to be corrected. Therefore, a reference reflection coefficient $|R_{13}|_{\text{ref}}$ is determined from the measured impedance of the steel sample and water using Equation (6.2). The reference echo signal $E_{1,\text{ref}}$ is determined from the maximum amplitude of the reflected signal from the steel surface. Therefore, a corrected source signal can be determined by rewriting Equation (6.4) such that $S_{\text{corr,E}} = |R_{13}|_{\text{ref}} E_{1,\text{ref}} \exp(-2(\alpha_1 d_1))$. The corrected source signal is substituted in Equation (6.4)) to determine other samples' reflection coefficients.

The attenuation coefficient is then found from Equation (6.5) by combining the reflection coefficient and received signal amplitude from the measurements. The received signal amplitude is also corrected for energy loss at the transducer and receiver surfaces. As water attenuation α_w is known [248], a corrected source signal is determined from the received signal of the water reference measurement. The corrected source signal for the received signal is given by $S_{\text{corr,Q}} = Q_{1,\text{ref}} \exp\left(\alpha_w \sum_{i=1}^{5} d_i\right)/(1 - |\mathcal{R}|_{13}^2)$. Substitution of this corrected source signal in Equation (6.5) results in actual sample attenuation.

6.2.2 Sample preparation

Due to sample shape and thickness differences, samples are prepared differently for the TT and TT/PE setups. For the TT setup, rectangular blocks are created measuring 10x16x60 mm. This is achieved by cold pressing virgin PA12 powder (PA2200, EOS) at room temperature using a custom-made steel mold and stem in a hydraulic press. The weight is varied for the samples consisting of PA12 powder, resulting in sample densities up to 923 kg/m^3 ($\rho_{\text{solid,PA12}} = 1030$ kg/m^3). Alternatively, solid PA12, PBT (Arnite AM1210(P), DSM),

PMMA, and HDPE blocks are machined from sheet material in a mill. PA12 and PBT sheets are made in-house by hot pressing powder. PA12 is pressed at 210 °C to a thickness of ∼12 mm, and PBT is pressed at 250°C to a thickness of ∼12 mm. Both materials are slowly cooled to ambient temperature. The PMMA and HDPE are machined directly from stock material. These blocks are placed inside a gelatine cuvette of 30x36x116 mm with a hole of 10x16x90 mm. The gelatine is prepared by dissolving 12 sheets in 100 ml of water, corresponding to a concentration of 13 g of gelatin per 100 ml. Cuvettes are cast in a 3D-printed mold and placed in a fridge for 5 hours to solidify. Castor oil (Volatile, 100% pure) and rice bran oil (Alpha One) are tested in identical cuvettes.

For the TT/PE setup, round disk shapes with a diameter of 45 mm and a thickness of 6 mm are used. Disks are prepared by cold pressing virgin PA12 powder (PA2200, EOS) using a custom-made stainless steel mold. The mold is loaded with PA powder ranging from 5.777 to 8.737 grams, resulting in effective densities ranging from 583 to 836 kg/m^3. After placing the stem of the mold, it is placed in a manual hydraulic press, and slowly, the sample is compressed up to 50 MPa. The sample height of 6 mm is a fixed dimension in the mold, allowing for samples with different effective densities. After preparation, samples are weighed (Sartorius A 210 P), and outside dimensions are measured using a digital caliper and digital micrometer (Mitutoyo). Besides, solid PA12, PBT, and PMMA disks are machined from sheet material on a lathe. PA12 and PBT sheets are made in-house by hot-pressing powders using settings similar to those used for the TT setup. PA12 powder and PBT powder are pressed to a ∼12 mm thickness at 210 °C and 250 °C, respectively. Both materials are slowly cooled to ambient temperature. The PMMA is machined directly from a 10 mm stock sheet.

6.3   Numerical methods

A model-based approach designs the combined through-transmission and pulsed-echo (TT/PE) characterization setup. In this approach, numerical simulations of a sample between two coupling media are performed with the k-Wave software package in Matlab [194]. The goal of performing these simulations is to study the effect of sample and couplant properties on the measurement accuracy in terms of speed of sound and attenuation coefficient.

Figure 6.4a shows the two-dimensional simulation domain for these simulations. Herein, the front of the sample and the receiver are positioned at 25 and 50 mm from the curved transducer, respectively. The transducer has a focal distance of 50 mm, and the planar receiver has a width of 14 mm, similar to the ones in Figure 6.3. Details about the numerical method used for solving the wave-equation in k-Wave are presented in Chapter 5.

The 5-cycle sinusoidal pulse, generated by the HIFU transducer, is used as input for the simulations. This is a band-limited signal measured with the planar receiver of the TT/PE setup. Interpolation of this pulse is required to allow for a simulation time step of $\Delta t = 1.3477$ ns, which is smaller than the sampled time step $\Delta t_s = 40$ ns following from a $f_s = 25$ MHz sampling frequency. Therefore, a bandlimited interpolation method is implemented with a sinc kernel [249], as given in Figure 6.4b. Subsequently, the signal is filtered using the Kaiser windowing method, with a cutoff at 12.4 MHz [198]. To accommodate for an accurate description of the echoes in the thin layers of couplant media, ppw = 14 and cfl = 0.05 are used, resulting in a grid spacing of $\Delta x = 39.946$ µm. The transducer, coupling media, sample, and receiver positions are slightly shifted at multiples of $2\Delta x$ to always be exactly on the grid.

The echo and transmit signals are recorded using the transducer and receiver as sensors.

The received signals are derived by summating the pressure amplitude at the grid points of the sensor. The magnitude of the reflected signal and the transmitted signal are used to compare the measured speed of sound and attenuation coefficient with the input speed of sound and attenuation coefficient. Similar to the experiments, reference measurements for reflection and transmission are performed, which validate the working principle of the TT/PE setup.
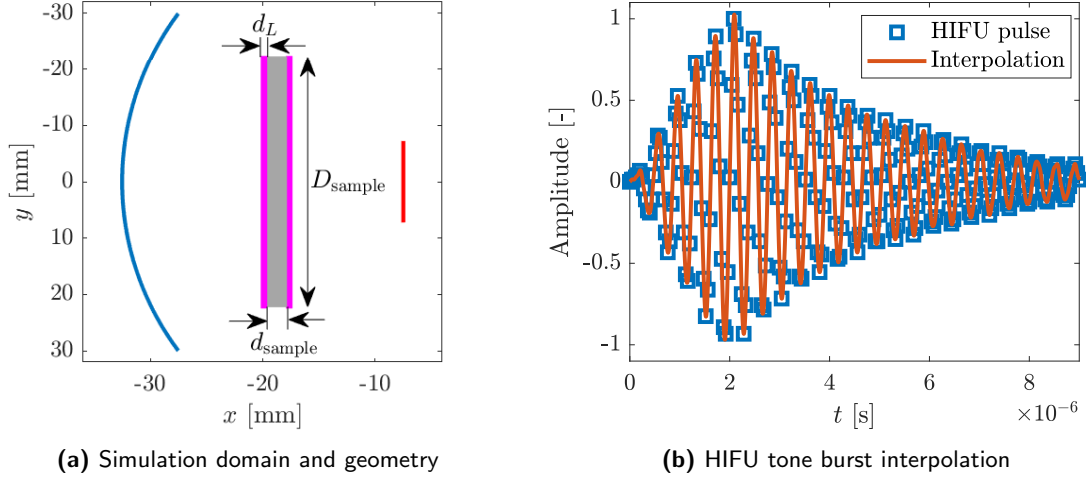

(a) Simulation domain and geometry

(b) HIFU tone burst interpolation

Figure 6.4: Simulation domain and geometry, and the HIFU tone burst used in the numerical simulations. In a) the curved line represents the HIFU source, and the straight red line represents the receiver. The sample in grey is positioned between two coupling media in pink. In b), the interpolated pulse is shown upto $t = 2\Delta t_{\text{pulse}} = 9$ ms.

6.4   Results and discussion

The transmission of ultrasound energy by a material in SAS determines the focal size and printability of that material [182]. Therefore, tuning reflection coefficients and attenuation of the print volume material is crucial. Hence, a need is provided to measure the acoustic properties of powder-based materials. This section presents the results of ultrasound characterization methods based on the through-transmission (TT) and combined through-transmission pulsed-echo (TT/PE) techniques. Firstly, the TT/PE design results are given based on the numerical simulations. These simulations estimate the accuracy of the TT/PE method for highly attenuated materials like powders. Subsequently, ultrasound measurements on liquids and solids are performed to show the validity of the characterization methods. Finally, the experimental results of compacted and filled powders are discussed to find the effect of porosity on the reflection coefficient, speed of sound, and attenuation.

6.4.1   TT/PE design based on numerical simulations

Two reference measurements are performed to calibrate the simulations. Firstly, a wave in pure water is simulated, where the receiver is placed at the focus location of the transducer. An analytical solution exists for this case and was used in Chapter 5 to validate the k-Wave simulations. The speed of sound and attenuation in the degassed water are listed in Table 6.1. The simulated time-of-flight is determined by correlating the source and received signal using

a cross-correlation function. The simulated amplitude difference is determined by dividing the maximum absolute value of the source signal by the received signal. It is assumed that these corrections result from the amplitude increase of focusing of the transducer and phase differences due to diffraction and attenuation inside the material. The transducer is also used as a sensor to capture the reflected signal from the sample. A steel (C1080) sample with a 25 mm thickness is used to calibrate this. The steel C1018 is ideal for referencing echo signals due to the large impedance mismatch between water and the steel and relatively low attenuation coefficient, limiting viscoelastic effects on the reflection coefficient (see Table 6.1). The samples used in the characterization are the so-called polymer and powder samples, for which the properties are estimated from PA12 and a PA12 powder, presented later on.

Table 6.1: Material properties of sample media used in the numerical simulations.

Sample name	ρ [kg/m^3]	c_0 [m/s]	α [dB/cm] (2.65 MHz)	Reference
Water	998	1482	0.0153	[247, 248, 250]
Steel C1018	7800	5917	0.147	[251]
Polymer	1018	2315	7.80	
Powder	500	1500	30	

From the geometry of the sample in Figure 6.4a, three adjustable parameters can be defined: the sample diameter D_{sample}, the sample thickness d_{sample} and the couplant thickness d_L. Herein, both couplants at the front and back of the sample are of the same material and thickness.

Sample diameter

The sample diameter is the first parameter that is studied. In the design of a TT/PE setup, the sample diameter to sample thickness ratio is essential. The sample's integrity may be compromised for large ratios, especially for powdery samples. The reflection coefficient is calculated from the echo signal in the simulation to show the effect of sample thickness on acoustic properties. The simulation results of the reflection coefficient are shown in Figure 6.5a. Here, convergence to $|\mathcal{R}| = 0.2325$ is shown, which starts at a sample thickness of 45 mm. Parts of the focused acoustic waves do not reflect on the sample surface at smaller sample diameters. Therefore, a sample thickness of 45 mm is used in the numerical-based design.

Couplant thickness and material

If sample materials prone to water absorption (e.g., powders) are used, the sample must be shielded from the water. This implies that the couplant cannot contain water; hence, a gelatin cuvette cannot be used. Four solid couplant materials are simulated: PVC, Glass, PS, and Aqualene, with the acoustic properties of these couplant materials given in Table 6.2. The resulting reflection coefficients as a function of couplant thickness are depicted in Figure 6.5b.

The couplant thickness affects the powder sample's reflection coefficient. Following the three-layered reflection coefficient theory in Equation (6.3), the solid lines predict the effect of sample thickness and material. From this theory, it follows that at a quarter wavelength $d_L = \lambda/4$, the reflection coefficient reduces to the reflection between the water and the powder (i.e., $|\mathcal{R}_{13}| \approx 0.23$). It can be seen that for relatively small couplant thicknesses (d_L/λ), the simulations follow the three-layer reflection theory. However, as sample thickness increases,

(a) Sample diameter
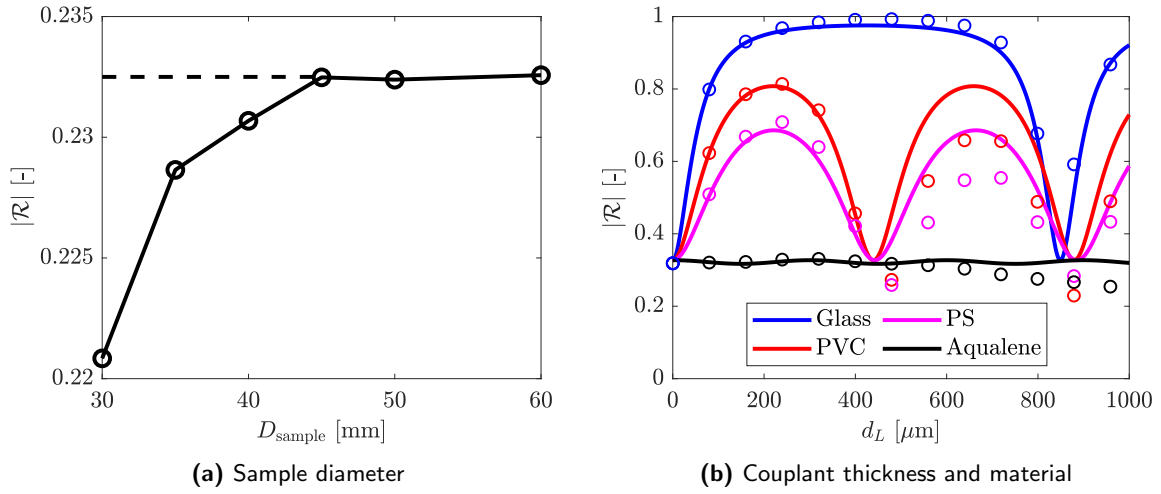
(b) Couplant thickness and material

Figure 6.5: The effect of sample diameter, couplant material, and couplant thickness on the measured reflection coefficient. In a) convergence is found for samples with 45 mm. In b), simulation results of different couplant materials and thicknesses (markers) are compared with the multi-layer theoretical predictions (solid lines).

the effect of multi-scattering in the couplant film causes the simulation results to deviate from the lines.

The couplant material also profoundly affects the reflection coefficient and the wavelength of the couplant material. For Glass, the speed of sound is largest, introducing the largest impedance mismatch and wavelength. Therefore, the reflection coefficient is relatively large, and the quarter wavelength is found for larger couplant thicknesses than the other couplant materials. Using a couplant material with a significant impedance mismatch is undesired, as a slight deviation in couplant thickness can drastically increase the reflection coefficient. Besides, if the driving frequency of the source is slightly changed, this also leads to a drastic increase in the reflection coefficient. Hence, reflected signals of a broadband signal would mainly depend on the frequency, and possibly, the relatively small amplitude of the echo of the driving frequency cannot be captured. The results of the Aqualene couplant are promising, as reflection coefficients are low. This is due to the impedance match with the water. The comparison with the three-layer reflection theory shows good agreement with the simulations for couplant thicknesses below 600 µm. Therefore, the following model-based design uses an Aqualene couplant with a thickness of 500 µm. The same conclusions are derived for the polymer sample in Appendix 6.A.1.

Table 6.2: Material properties of coupling media used in the numerical simulations.

Couplant name	ρ [kg/m^3]	c_0 [m/s]	α [dB/cm] (2.65 MHz)	Reference
PVC	1386	2330	6.07	[252, 253]
Glass	2100	4500	0.0133*	[250, 254]
PS	1040	2346	1.72	[255, 256]
Aqualene	920	1590	1.59	[257]

* About 2 Np/m at 10 MHz [250] and approximately 0.0133 dB/cm at 2.65 MHz.

The effect of the couplant thickness and material is also studied in terms of the accuracy of the resulting speed of sound and attenuation measurements. Therefore, the error in the speed of sound and attenuation measurements for the different layers using the powder sample material are given in Figure 6.6. The speed of sound error is larger for materials with an increasingly larger wavelength. This is attributed to the coupling layers' phase shift upon reflection and transmission. These phase-shift errors increase with wavelength and are more profound for the PVC coupling media. A phase correction, based on the complex reflection and attenuation coefficients, is introduced in the work of Tsuji et al. [159] to find the correct speed of sound. However, the Aqualene sample is used in this work, wherein phase shifts are negligible. Besides, due to impedance mismatches, the angle of incidence can change. This results in a slight shift in the location of the focus spot behind the sample. This effect is much smaller than the phase shift effects for samples with larger wavelengths. Regarding error propagation, reflection measurement errors at a more significant reflection coefficient result in a larger error on the attenuation as $\alpha_2 \sim (1 - |\mathcal{R}|^2)$. Thus, it can be seen that at the quarter wavelengths of the materials, where the reflection coefficient is smallest, the error on the attenuation is also close to zero. Therefore, again, the Aqualene sample performs best over the entire range of couplant thicknesses.
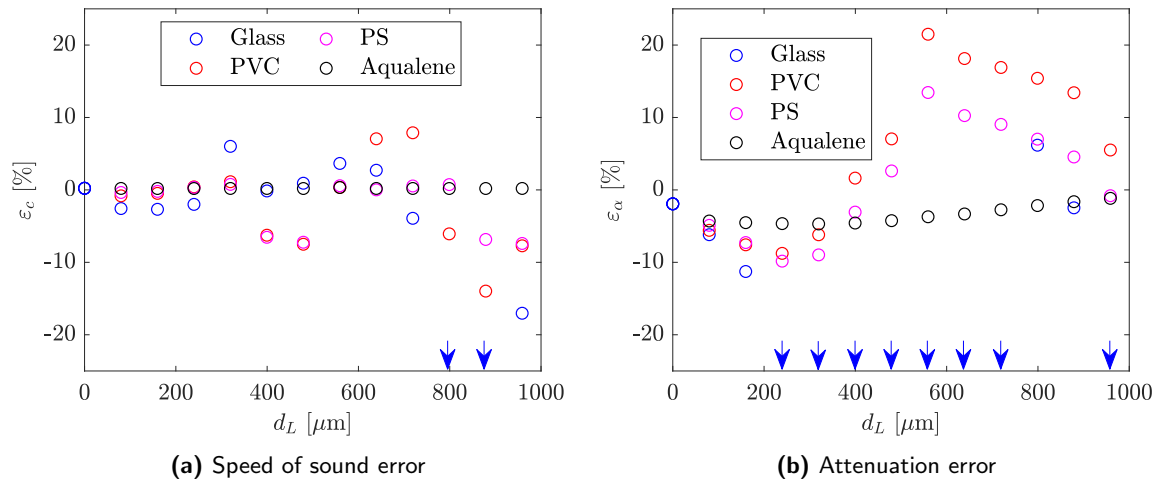

(a) Speed of sound error   **(b)** Attenuation error

Figure 6.6: Effect of sheet thickness on the error on the speed of sound and attenuation for different sheet material using a 4 mm powder Sample. The blue arrows indicate the thicknesses where the error of the glass sample exceeds -25 %.

6.4.2   Sample thickness and material

The last parameter that can be optimized is the sample thickness. This is done by studying the reflection coefficient and the interplay between transmission and multi-reflections. Three powder samples with a speed of sound of 1500, 2250, and 3000 m/s are simulated, respectively. Regarding the reflection coefficient, the simulation results converge towards a constant value for layer thicknesses larger than 3 mm (see Figure 6.7a). For smaller sample thicknesses, the second reflection from the back of the sample interferes with the first echo signal, yielding larger reflection coefficients. For materials with a larger speed of sound, the wavelength is increased, and the minimum sample thickness also increases.

Transmission is large for a relatively thin sample material as the attenuation distance is short. However, if the pulse length is larger than the layer thickness, the first and second transmitted signals are superimposed. In this case, the received amplitude is larger, resulting in a negative error on the attenuation $\varepsilon_\alpha < 0$. On the other hand, if the sample material is relatively thick, the transmitted signal amplitude is reduced. The relative error on the attenuation increases with the reflection coefficient for decreasing signal amplitude. Therefore, for the sample with a speed of sound of $c_0 = 3000$ m/s with the largest speed of sound, the error on the attenuation increases at a sample thickness of 7 and 8 mm. Hence, an optimal sample thickness of 6 mm is found, which results in attenuation errors of $|\varepsilon_\alpha| < 7\%$ for the investigated speed of sounds.
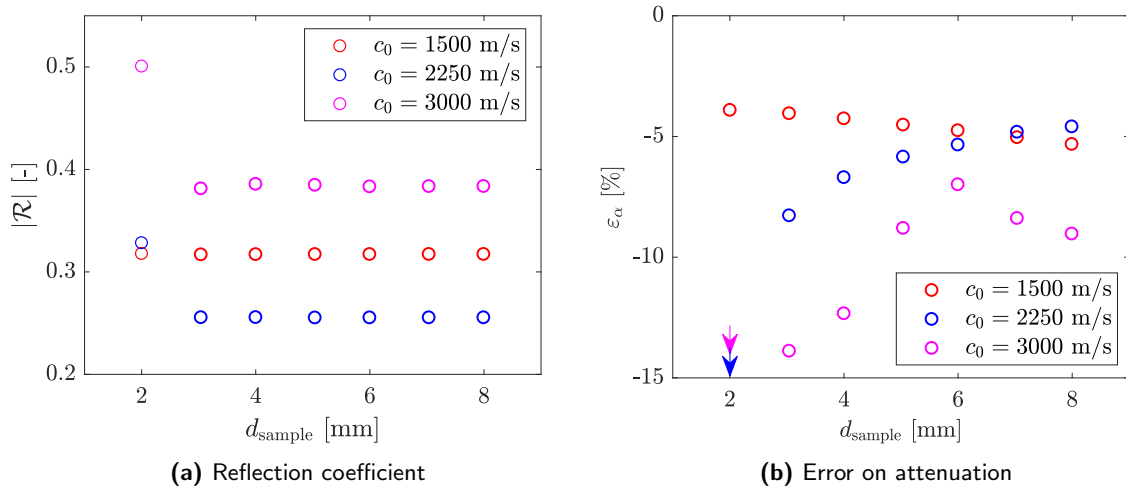

(a) Reflection coefficient   **(b)** Error on attenuation

Figure 6.7: Effect of sample thickness on the reflection coefficient and the error on attenuation for a 500 μm Aqualeen sheet. The arrows indicate the thicknesses where the attenuation error exceeds -15 %.

Parameter space and resulting errors

The values of attenuation, speed of sound, and density are changed to measure the error in the speed of sound and attenuation. The results of these simulations are shown in Figure 6.8. According to the results, the entire range of material properties can be measured within a reasonable error on the speed of sound, as the predicted errors are lower than 10% (indicated in green). However, when the attenuation is large (100 dB/cm), the phase shifts caused by attenuation result in inaccurate predictions of the speed of sound. These phase-shift errors increase with wavelength and are only present for the largest speed of sound values.

The material properties are much more critical in the attenuation coefficient measurements. Small attenuation values result ($\alpha \leq 1$) in the largest errors. In these cases, transmission is only limited by the reflection at the interfaces of the sample material. Hence, minor errors in the reflection coefficient, due to, for example, phase shifts, can drastically affect the measured attenuation coefficient. Reflection is the smallest for the speed of sound values of 1500 m/s; hence, the errors are reduced. At significant attenuation (100 dB/cm), the error in the attenuation measurement increases as the relative error on the attenuation increases with the reflection coefficient for decreasing signal amplitude.
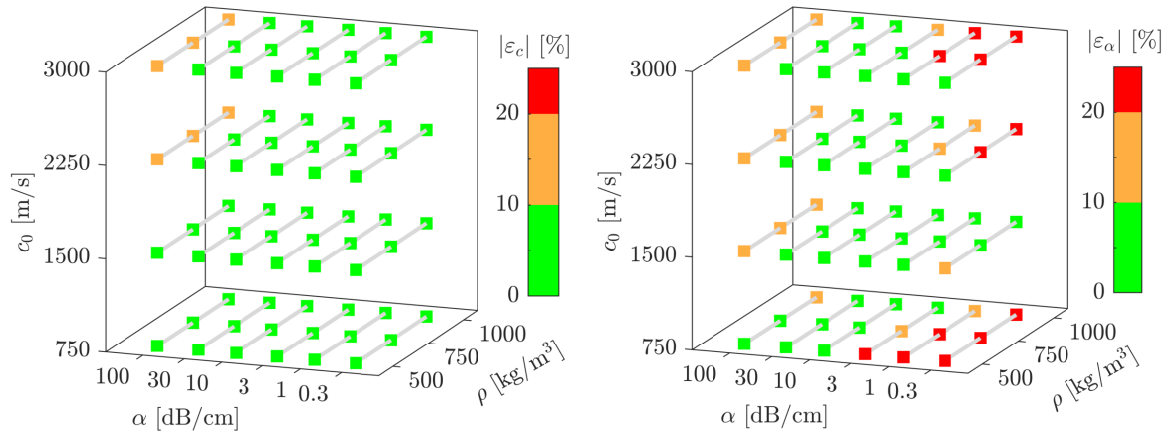
(a) Error on the simulated speed of sound measurement   **(b)** Error on the simulated attenuation measurement

Figure 6.8: Parameter space simulations for determination of the measurement errors in the TT/PE setup. The varied parameters are the sample's attenuation, density, and speed of sound. The absolute error of the speed of sound (a) and attenuation (b) measurements are given. If the markers are red, the simulated speed of sound or attenuation measurement is at least 20% off compared to the set/actual material property.

6.4.3   Validation of measurement techniques

For validation of the ultrasound characterization setups, reference speed of sound and attenuation values from the literature are compared with measurement results using the setups. For the designed TT/PE setup, results of reflected and received signals for validation are given in Figure 6.9. Two reference measurements of well-characterized materials steel C1018 and water are performed to determine the reference echo signal $E_{1,\mathrm{ref}}$ and the reference transmitted

(a) Echo/reflection signals   **(b)** Transmission/received signals

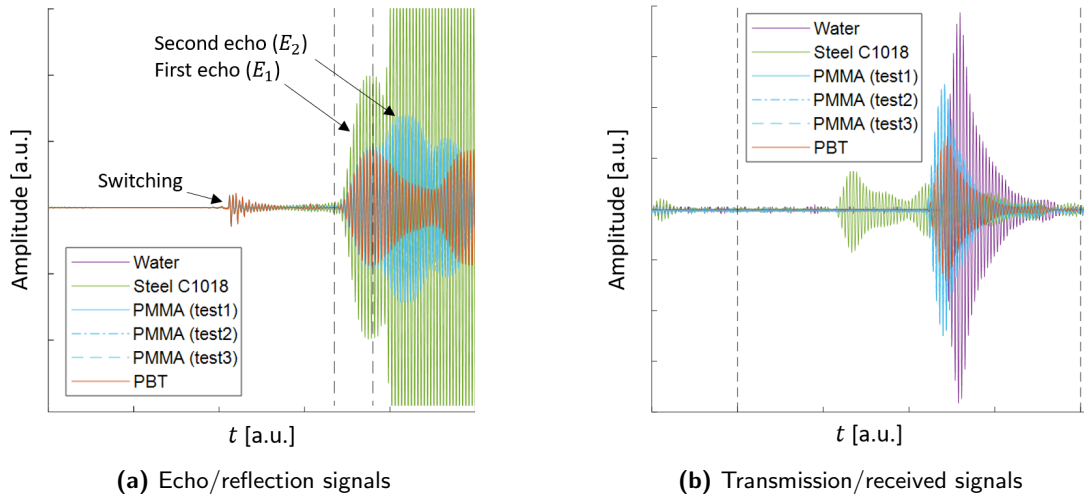**Figure 6.9:** The recorded wave amplitudes with the TT/PE setup are presented in two parts: a) showing the echo/reflection signals and b) displaying the transmission/received signals. To determine the speed of sound and attenuation of PMMA (tested three times) and PBT, two reference measurements of water and steel C1018 are used. Vertical dashed lines indicate the maximum amplitude data extraction regions.

signal $Q_{1,\text{ref}}$, respectively. In the following measurements, no coupling media are used. The first echo signal of the steel sample in Figure 6.9a is analyzed by extracting the maximum amplitude of the signal (in Vpp) within the extraction region between the vertically dashed lines. This maximum corresponds to the amplitude at the center frequency of 2.65 MHz. An extraction range is required because the second echo E_2 amplitude is larger than the first. Note that the second echo is clipped to improve the accuracy of the first echo measurement. The echo extraction region $\text{TOF}_{E_1} < t < \text{TOF}_{E_1} + \Delta t_{\text{pulse}}$ is found from the time of flight of the echo signal $\text{TOF}_{E_1} \approx 2d_1/c_1 \approx 33$ µs, and the pulse width $\Delta t_{\text{pulse}} = 4.5$ µs. Also, the first echo signal overlaps with the second echo signal. Therefore, frequency-dependent signal amplitudes calculated with an FFT analysis cannot be used, as this would result in superimposed magnitudes.

The first received signal of the water reference measurement, Q_1, is determined by analyzing the signal shown in Figure 6.9b. The time-of-flight and the maximum amplitude of the signal (in Vpp) are measured within the time range marked by the dashed lines. The left dashed line represents the switching trigger at 20 µs, and the right dashed line indicates the TOF of a sample with a speed of sound of 250 m/s. The latter is not a limit, but sample sound speeds lower than 250 m/s are not expected. For the reference steel C1018 sample, a speed of sound of $c_0 = 5762$ m/s is measured, which is only 3% lower than the reported speed of sound in Table 6.1. The slight difference in the density ($\rho = 7838$ kg/m^3) and measurement errors account for the minor mismatch in the speed of sound values.

(a) Speed of sound
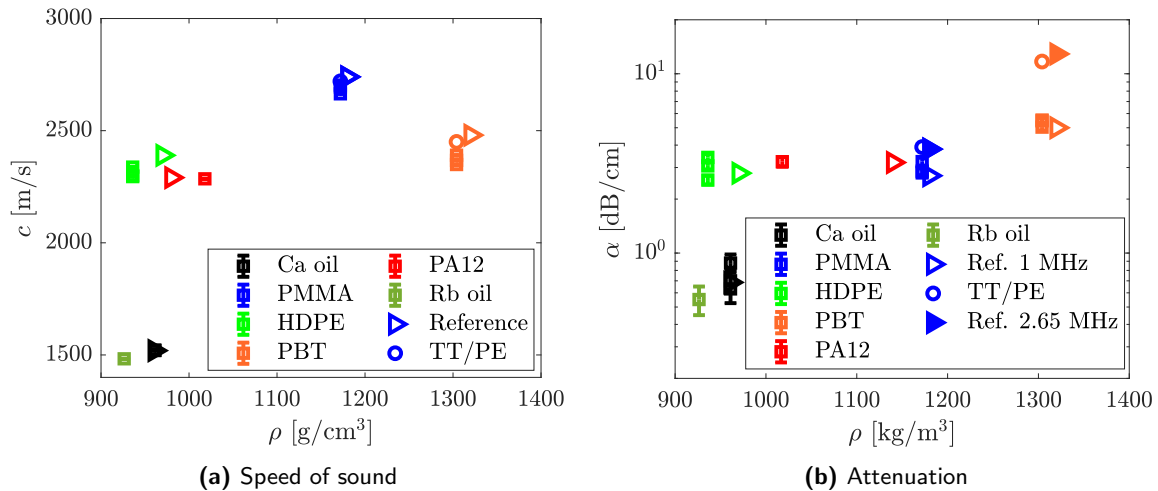
(b) Attenuation

Figure 6.10: Comparison of the speed of sound and attenuation of multiple materials (fluid and solids) measured with the TT setup (squares with error bars) and TT/PE setup (circles) compared with reference values of [170] at 1 MHz (triangles, unfilled) and (triangles, filled). The error bars in the TT measurements indicate the error due to noise for three distinct measurements. Noise in the TT/PE measurements is negligible for the presented materials.

The speed of sound and attenuation measurements of the PBT and PMMA samples in Figure 6.9 are compared to reference data from the literature (at 2.65 MHz) in Figure 6.10. A good agreement with the literature is shown, and the PMMA samples are reproducible. The TT characterization technique has been validated elsewhere [234]. For completeness, the results of the TT measurements on several polymers are compared to reference values

in the literature (at 1 MHz) in Figure 6.10. The reference data of the speed of sound and attenuation of the polymers are extracted from acoustic measurements of Bloomfield [170] at 1 MHz and 2.65 MHz. The speed of sound of laser-sintered Nylon 12 (PA12) is found in the work of Amado-Becker et al. [214]. No attenuation data of PA12 is available; therefore, the attenuation is compared to Nylon 6.6 (PA6.6) [170]. Good agreement is found between the speed of sound of nearly solid-density sintered PA12 and the PA12 solid sample used in this study. Besides, the attenuation values of PA6.6 and PA12 are in good agreement. Additionally, two oils are acoustically characterized. For Castor oil (Ca oil), reference values of Reis [258] are shown, which show perfect agreement. No literature data on rice bran oil (Rb oil) is available. However, this material is interesting due to its temperature stability, slightly lower sound speed (closer to water), and attenuation than castor oil, rendering it a possible replacement for water and castor oil in high-temperature ultrasound applications.

6.4.4   Characterization of low-attenuation powder compacts

The transmission of ultrasound energy by a material in SAS determines the focal size and printability of that material [182]. Therefore, tuning reflection coefficients and attenuation of the print volume material is beneficial. One of the possible routes is to adjust the bulk density of the powder-based materials in SAS using compaction. However, only powders with small attenuation coefficients can be measured with the TT setup due to limited signal-to-noise ratios. Besides, the heterogeneous powder systems with rough surfaces reflect sound differently than homogeneous materials. Hence, the theoretical reflection coefficient required in this technique is not accurate. Nevertheless, assuming the reflection theory is valid for
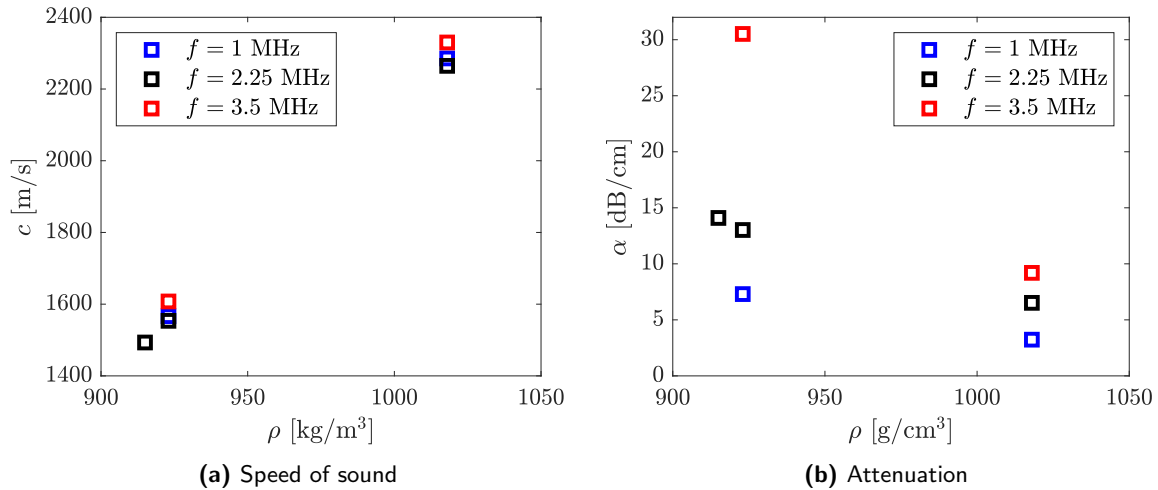
Figure 6.11: Speed of sound and attenuation measurements of compressed PA12 powder samples (two lowest densities) and a fully solid PA12 sample (highest density). These measurements are performed with the TT setup.

bulk densities close to solid densities, the TT method is used to study the attenuation in low-porous powder compacts. Figure 6.11 shows the speed of sound and attenuation results for low-attenuation PA12 powder compacts. In these measurements, two samples are produced by powder compaction with densities of $\rho = 915$ and $\rho = 923$ kg/m^3. These are compared

with a nearly-solid PA12 sample extracted from a hot-pressed plate. The measurements are performed at three frequencies for the solid and highest-density compacted sample. From the speed of sound measurements in Figure 6.11a, the effect of density and frequency on the speed of sound is depicted. As the effective density of the material increases, the sound velocity is raised, too. Additionally, only a slight increase in the speed of sound with frequency is depicted, which is within the error of the measurements. Hence, the speed of sound is nearly frequency-independent.

The attenuation coefficients of the samples are decreased with increasing density (see Figure 6.11b). Additionally, an increase in attenuation with frequency is found. They fit the data of solid PA12 for the three frequencies, resulting in an attenuation coefficient of $\alpha_y = 3.232$ dB/MHz^{y}cm, with the power law constant $y = 0.82$ (see Appendix 6.A.4). A power-law constant of just below one is commonly seen for polymers [159]. The same fitting can be performed for the sample with a 923 kg/m^3 density, as shown in Appendix 6.A.4. However, the attenuation coefficient measured at a frequency of 3.5 MHz should be used cautiously, as the wave shape is distorted due to possible nonlinear wave propagation and a low signal-to-noise ratio (see Appendix 6.A.4). The slope of the two data points at 1 and 2.25 MHz, respectively, is similar to the solid PA12 sample, $y \approx 0.82$. However, the attenuation change from 2.25 to 3.5 MHz has a slope much larger than $y = 1$, indicating a possible shift in a Mie scattering or Reighlay scattering regime with $2 \leq y \leq 4$, depending on the pore size.

6.4.5   Characterization of high-attenuation powder compacts

To move to powder compacts with lower density, the TT/PE setup has been designed. The porosity φ is defined as $\varphi = (\rho_{\text{solid}} - \rho)/(\rho_{\text{solid}} - \rho_{\text{pore}})$, with ρ_{solid} the density of the solid material and ρ_{pore} the density of the pore material. In Figure 6.12, the speed of sound and reflection coefficient measurements are given as a function of porosity. The circular error bars indicate the results of the TT/PE measurements. The speed of sound is lowered as the porosity of the compacts increases (see Figure 6.12a). The measurements with the TT setup align with the findings of the TT/PE setup. As a guide through the eye, the speed of sound has been fitted by the empirical relation $c_{\text{fit}} = a_c \rho_{\text{disk}}^{b_c} + c_{\text{air}}$, which might be related to percolation theory as described in our previous works on mechanical testing of SLS-printed PA12 tensile specimen [182]. For porosities above 0.4, the speed of sound measurements could not be performed, as attenuation is too large for measuring a received signal.

The fitted speed of sound is used to find the expected reflection coefficient, using the impedance mismatch between the water and the sample with $Z_{\text{eff}} = c_{\text{fit}}\rho_{\text{disk}}$. Comparing the measured reflection coefficients to the fitted expected reflection coefficients in Figure 6.12b shows that there is an offset. The measurements reveal that the reflection coefficient of the porous compacts is larger than the expected reflection coefficient. This offset originates from the impedance prediction using an effective density, assuming a homogeneous material. However, inhomogeneities in the powder compacts, such as surface roughness and pores, induce scattering, leading to an increased reflection coefficient. This finding illustrates the importance of measuring the reflection signal of porous samples in the TT/PE setup.

The results of the attenuation of the TT/PE measurements are indicated by the circular error bars in Figure 6.13. The reflection coefficient around $\varphi_0.1$ is smaller than 0.1, resulting in an error on the attenuation of less than 1%. For this reason, the TT setup measurements at 2.25 MHz are included in Figure 6.13 and show excellent agreement with the trend of the TT/PE measurements. The attenuation of air is about 11 dB/cm, indicated by a porosity

(a) Speed of sound

(b) Reflection coefficient

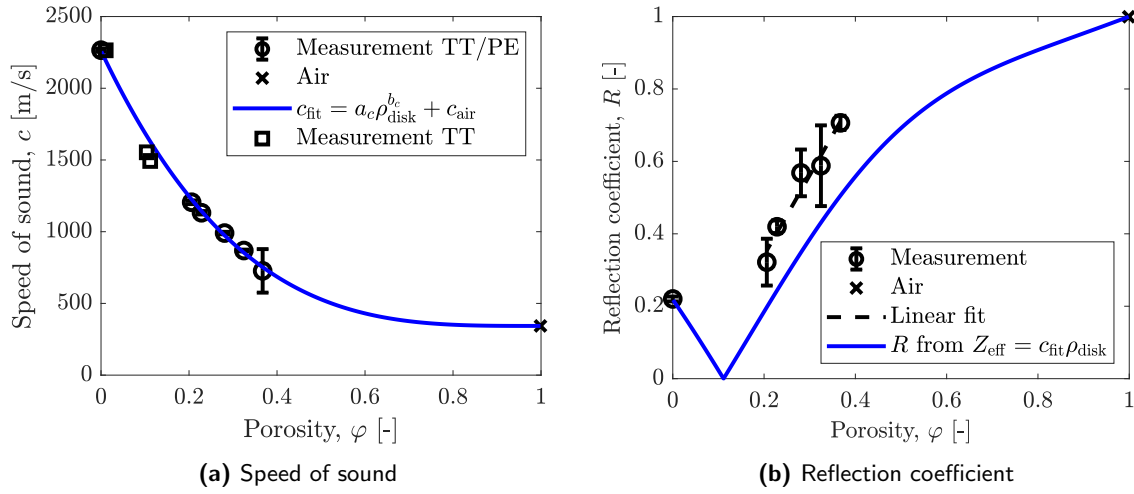**Figure 6.12:** Speed of sound and reflection coefficient measurement results of compressed PA12 samples and a solid PA12 sample. These measurements are performed using the TT/PE setup. The crossed markers indicate the speed of sound and reflection coefficient of air ($\varphi = 1$).

value of one. As the powder compacts' attenuation is larger compared to air, this means that scattering is dominant. Therefore, the multi-scatting theory introduced by Epstein, Cahart, Allegra, and Hawley (ECAH) is also used to find the attenuation at low particle concentrations [259–261]. This theory is implemented as described in the works of Alam et al. [262] and Tsuji et al. [263]. The theoretical attenuation from multi-scatting is then solved by:

$$\alpha = \alpha_{\text{air}} - \frac{3\phi}{k^2 R^3} \sum_{n=0}^{n_{\max}} (2n + 1) \text{Re}(A_n), \tag{6.6}$$

where solid volume fractions $\phi = 1 - \varphi$ ranges from 0 to 0.2, A_n is the complex scattering
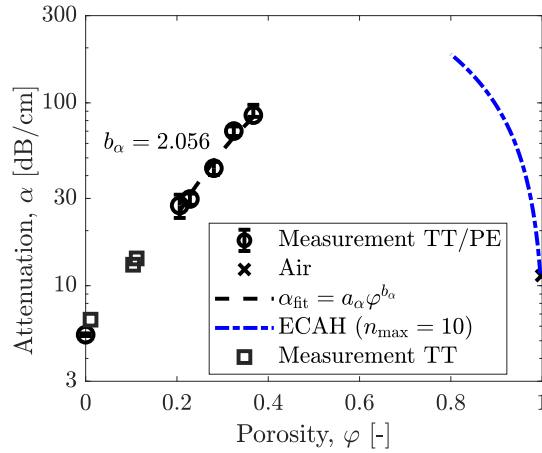

Figure 6.13: Results for attenuation of compressed PA12 samples using the TT/PE setup. The TT setup measurement of low-attenuating solids, the attenuation of air, and the multi-scatting theory predictions (ECAH) are included.

amplitudes. Besides, n is the mode number using $n_{max} = (a_{max} + 4a_{max}^{1/3} + 2) \approx 10$ modes [264], with $a_{max} = \max(kR)$ the maximum ratio of particle radius R to wave length. The resulting theoretical attenuation prediction in Figure 6.13 shows that the attenuation rapidly increases when the porosity decreases from 1 to 0.8. This theory is only valid for small solid fractions assuming ($\varphi > 0.8$), as it assumes that the attenuation of many spheres is additional. The resulting attenuation should be regarded as a trend line, as ECAH theory is derived from assuming incompressibility (fluids); hence, extensions are required to incorporate the compressibility of air. Further advancements in multi-scattering models, particularly for air-solid, fluid-solid, and solid-solid systems, are required to model the particle-based systems in this work accurately.

Without compaction, $\varphi \approx 0.5$, the attenuation is >100 dB/cm. Regarding printer size in SAS, this indicates that only parts smaller than ~1 mm could be printed [182], as otherwise, all energy would be attenuated in the first centimeter. These small printer sizes are unusable as the powder size is approximately 50 µm. This shows that powder compaction is crucial in the SAS 3D printing method.

6.4.6   Characterization of filled powder compacts

Next to compaction, adding filler material can also be beneficial for ultrasound energy transmission, as this would decrease the scattering. Additionally, in SAS, filler materials can have other applications, such as components for post-treatment or tuning the thermal-physical properties. Therefore, the effect of filler material has been investigated by introducing a liquid filler, Rb Oil, and a solid filler, Paraffin wax. First, the paraffin wax results are shown in Figure 6.14.

A pure paraffin sample has a speed of sound close to 2000 m/s, which is significantly larger than the speed of sound of air. Besides, the paraffin sample density is 884 kg/m3. Thus, scattering is expected to decrease as a good impedance match between the paraffin and
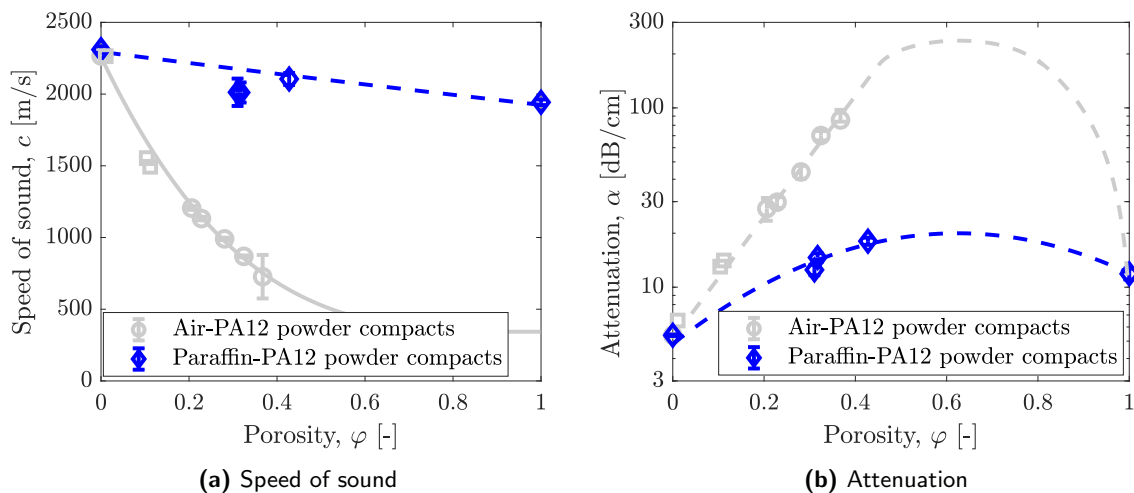

(a) Speed of sound

(b) Attenuation

Figure 6.14: Results for speed of sound and attenuation of PA12-Paraffin compacts using the TT/PE setup. The measurements are compared to the Air-PA12 powder compacts (in grey), and the dashed lines are a guide through the eye.

PA12 particles is found. This is also clearly visible from the data points, as the attenuation of Paraffin-PA12 compacts is 2 to 5 times smaller than the air-PA12 compacts. So, adding a filler material is an excellent option to tune the attenuation and speed of sound of a powder-based material. Analytical solutions are derived by Ying and Truell [265] for scattering models of solid-solid systems. However, these are not presented here, as they are only valid for low particle concentrations.

In terms of the SAS applicability of a paraffin-PA12 sample, an experiment has been performed to test if the fusion of particles is still possible. In this experiment, the Snowwhite SLS 3D printer is used at different powers to fuse the PA12 particles on the surface of the paraffin-PA12 compacted disk. A square geometry of 5x5 mm is irradiated, with a hatch spacing of 0.1 mm, powers between 3-5 W, and scan velocities between 70-235 mm/s. The irradiated regions on the compacted disk are yellowish, as shown in Figure 6.15. Fusion of PA12 particles is found for all power-velocity ratios that result in a measured temperature above the melting temperature of PA12 ($P/v_{\text{scan}} > 22$ Ws/m). This shows that adding a paraffin filler material can reduce the scattering contribution to attenuation while maintaining the sinterability of the PA12 particles.

Figure 6.15: Sintering of PA12 particles at the surface of PA12-paraffin compacted disks for different powder-velocity ratios using the Sharebot SnowWhite SLS 3D printer. The numbers indicate the power-velocity ratio in Ws/m used to produce 5x5 mm squares with a hatch spacing of 0.1 mm.

Lastly, the ultrasound characterization results for Rb oil as filler material for PA12 powder are discussed. Rb oil is stable at temperatures above the melting point of PA12. Therefore, filling PA12 particles in the SAS 3D printer would be a suitable liquid. However, the speed of sound and attenuation results for Rb oil as a filler are not shown. Surprisingly, the attenuation is much higher than anticipated by the scattering contribution. The attenuation is at least 100 dB/cm; as such, a small fraction of the source signal penetrated the material that was not recordable by the receiver. Hence, the attenuation is larger as unfilled PA12 powder, which does not make sense from a scattering point of view. However, this result might be attributed to the low density of the samples. The sample density is about 10-15% lower than the Rb oil density. This is unclear but could be attributed to the sudden volume expansion of about 10 % after releasing the compact from the mould. This expansion is much larger than the Paraffin wax samples, which could be an effect of liquid pressure from liquid between the cylinder and the mold. The particles are hypothesized to expand elastically after release, which could cause air to diffuse into the sample. If air penetrates the sample, the presence of gas bubbles

in the Rb Oil can dramatically influence its ultrasonic properties by the phenomenon known as resonant scattering [266], which arises from the large difference in compressibility between a gas and a liquid. The frequency at which resonance occurs f_r depends on the physical properties of the component phases and air bubble radius r_b. A bubble radius of $r_b \approx 1\ \mu\text{m}$ would match a resonance frequency of 2.65 MHz. This bubble radius is feasible in the pores of the compacted disks and might explain the increased attention. Further research is required to explain this density decrease and increased attenuation.

6.5   Conclusions

This study focused on developing and validating methods for accurate acoustical characterization of powder-based materials. The impact of ultrasound probe frequency, coupling media, and material properties on the accuracy of the measurements was explored through numerical simulations. The study resulted in a model-based design of an ultrasound characterization method and a fully operational setup with known errors and limitations. This setup combined existing techniques to characterize unfilled and filled powder compacts. The effect of powder compaction and filler type on the acoustic material properties was studied to find the dependency of these properties on the porosity.

The results show that using ultrasound to characterize materials with varying physical properties is feasible. The developed ultrasound characterization method can accurately measure the speed of sound, impedance, and attenuation of the materials. The experiments demonstrated that the coupling media used in the setup significantly impacts the accuracy of the measurements, especially for powder-based materials. Additionally, the study found that the degree of compaction and the type of filler used in the powder compacts affect the acoustic properties of the materials. Powder compaction reduces the air fraction and, therefore, the internal scattering of ultrasound waves, such that the speed of sound increases and attenuation decreases. Besides, adding a paraffin wax filler to the PA12 powder compacts can further reduce the attenuation coefficient while maintaining sinterability.

Overall, these findings have implications for selecting selective acoustic sintering 3D printers, as the results can be used to optimize the printing process for specific materials and applications. The reduction in porosity and type of filler material are crucial parameters in the SAS process to design printers with efficient ultrasound transmittance while generating sufficient heat for melting the powder.

6.A   Additional information

6.A.1   Reflection coefficient - viscous versus viscoelastic

Using the Kelvin-Voigt model, the complex reflection coefficient for viscoelastic materials is defined as:

$$R_{\text{VE}} = \frac{(F_{12} - F_{21}) + \omega\,(Z_2 - Z_1)\,\text{i}}{(F_{12} + F_{21}) + \omega\,(Z_2 + Z_1)\,\text{i}}, \tag{6.7}$$

with $Z_i = \rho_i c_i$ and $F_{ij} = c_i \alpha_i Z_j$ for $i, j = [1, 2]$ and $i \neq j$. Then, the magnitude of the complex reflection coefficient is derived as follows:

$$|R_{\text{VE}}| = \frac{\sqrt{\left(F_{12}{}^2 - F_{21}{}^2 + \omega^2\left(Z_2^2 - Z_1^2\right)\right)^2 + 4\,\omega^2\left(F_{12}\,Z_1 - F_{21}\,Z_2\right)^2}}{\omega^2\left(Z_2 + Z_1\right)^2 + \left(F_{12} + F_{21}\right)^2}. \tag{6.8}$$

By assuming that the attenuation of medium 1 is much smaller than the attenuation of medium 2, it follows that:

$$|R_{\text{VE}}|_{\alpha_1 << \alpha_2} = \frac{\sqrt{\omega^4 \left(Z_2^2 - Z_1^2\right)^2 + 2\,\omega^2 F_{21}^2 \left(Z_2 + Z_1\right)^2 + F_{21}^4}}{\omega^2 \left(Z_2 + Z_1\right)^2 + F_{21}^2}. \tag{6.9}$$

Assuming attenuation of the second medium is also negligible, the reflection coefficient is reduced to the viscous reflection coefficient:

$$|R| = \frac{\left|Z_2^2 - Z_1^2\right|}{(Z_2 + Z_1)^2} = \frac{|Z_2 - Z_1|}{(Z_2 + Z_1)}, \tag{6.10}$$

which is the equation used to calculate the magnitude of the reflection coefficient in the TT setup. In Figure 6.16, a comparison is made between the viscous magnitude of reflection coefficient $|R|$ and the viscoelastic magnitude of reflection coefficient $|R_{VE}|$ at a frequency of 2 MHz. Herein, the speed of sound of media one is assumed to be 1500 m/s, and its attenuation is zero. The attenuation coefficient of media two ranges from 0.1 to 100 dB/cm, and it is found that the magnitude of the reflection coefficient increases with increasing attenuation. In Figure 6.16c, the error of using $|R|$ as compared to $|R_{VE}|$ is visualized. Herein, the red line indicates a 10% error. This figure shows that for viscoelastic materials with a speed of sound close to that of water, the error of using $|R|$ is large. At significant attenuation $\alpha > 10$ dB/cm, the relative error also increases at larger wave velocities due to the more viscoelastic nature of the material.
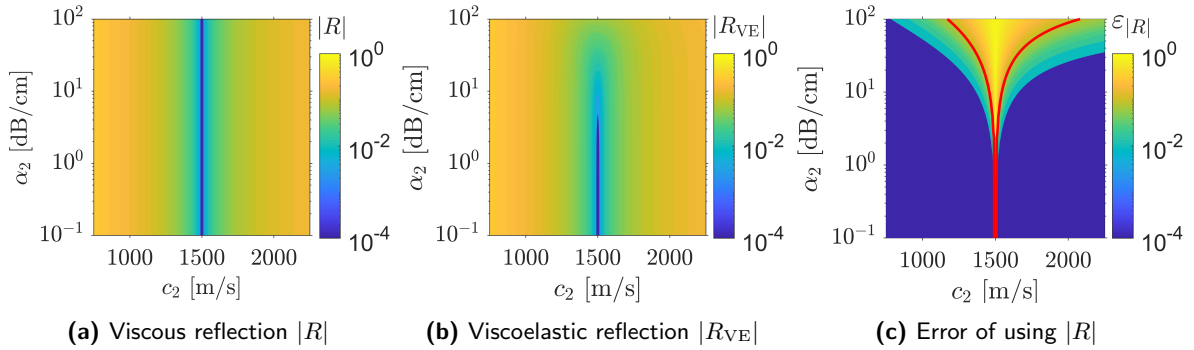

(a) Viscous reflection $|R|$ **(b)** Viscoelastic reflection $|R_{\text{VE}}|$ **(c)** Error of using $|R|$

Figure 6.16: A comparison between the viscous $|R|$ and viscoelastic $|R_{\text{VE}}|$ magnitude of reflection coefficients and the relative error $\varepsilon_{|R|}$ of using the viscous reflection coefficient for $f = 2$ MHz, $c_1 = 1500$ m/s, and $\alpha_1 = 0$ dB/cm. In c), the red line indicates an error of 10%.

6.A.2   HIFU probe characterization

A fully automated scanning system (UMS4 Precision Acoustics) designed for mapping acoustic fields is used to find the characteristics of the HIFU transducer. The HIFU probe is immersed in water, and a needle hydrophone (Onda) is automatically positioned in 3 degrees of freedom, using step sizes of 10 mu (see Figure 6.17). The resulting three-dimensional acoustic field is shown in Figure 6.18. Herein, the peak pressures $p(c)$ are derived from the deconvolution of the 5-cycled received signal. The focal region is positioned at approximately 50 mm from the sources, as specified by the manufacturer. The resulting pressure maps are compared with
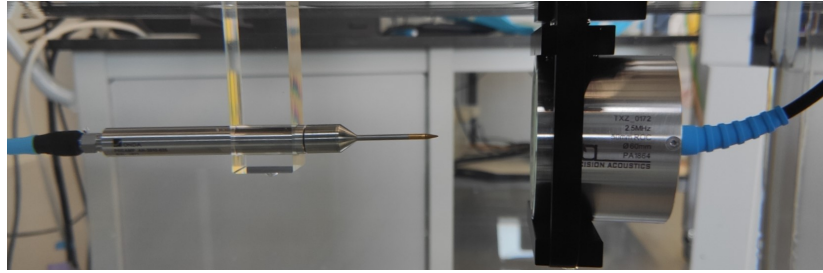
Figure 6.17: UMS4 scan tank that is used to characterize the HIFU transducer with a movable needle hydrophone.
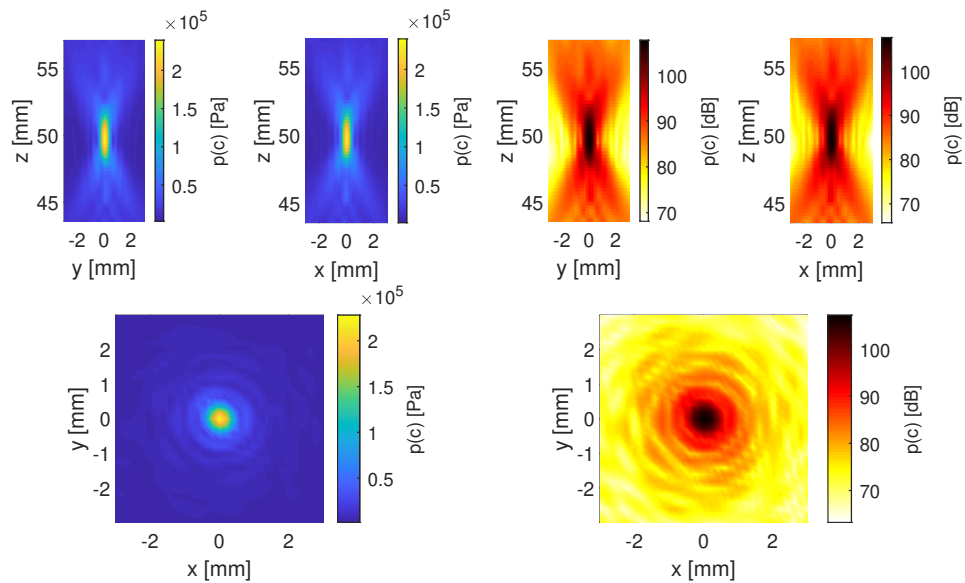
Figure 6.18: Acoustic field map of the HIFU probe.

the simulated pressure fields to verify that the numerical simulations are comparable to the actual pressure fields of the HIFU probe. Figure 6.19 shows the results at the focal region. The top figure is the pressure map of the experiment, and the bottom figure is the pressure map of the simulations. Excellent agreement between simulations and experiments can be seen.

6.A.3   Reflection coefficient and couplant thickness

As described in Section 6.4.1, the couplant material and thickness drastically affect the reflection coefficient. Aqualene is best suited as a couplant material due to the impedance match with the water. To show that this is also true for different sample materials, the reflection coefficient of the polymer sample is shown in Figure 6.20. The comparison with the three-layer reflection theory indicates good agreement with the simulations for couplant thicknesses below 500 μm. Again, reflection coefficients are the smallest for the Aqualene couplant.
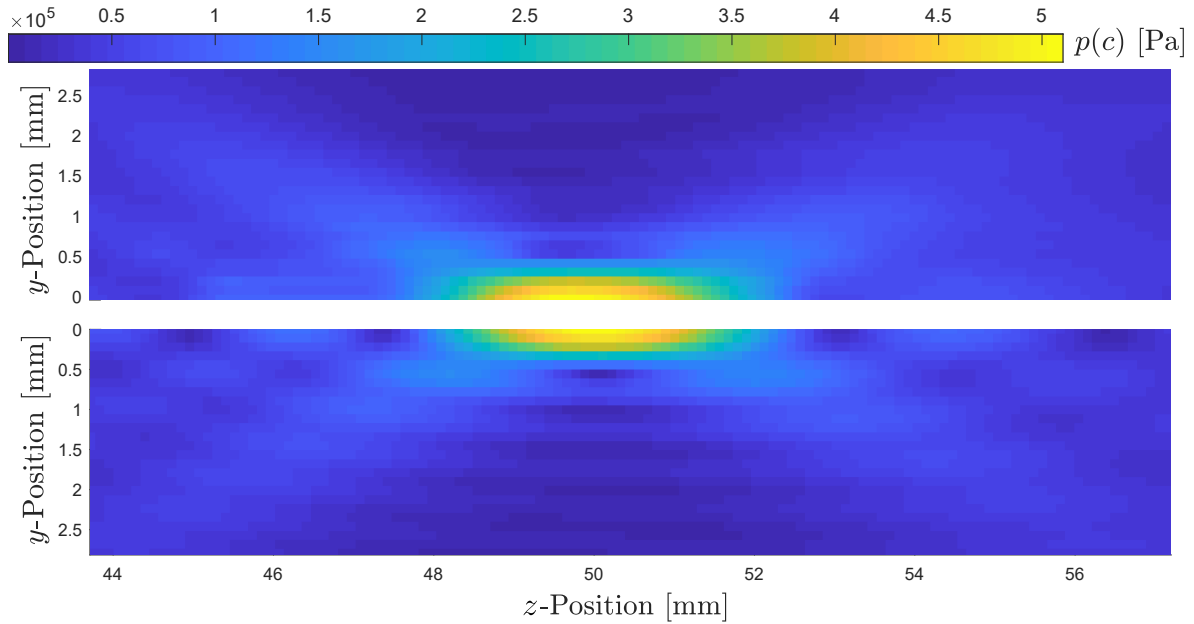
Figure 6.19: A comparison between the pressure map of the characterization measurements of the HIFU probe (top figure) and the pressure map resulting from the numerical simulations (bottom figure).
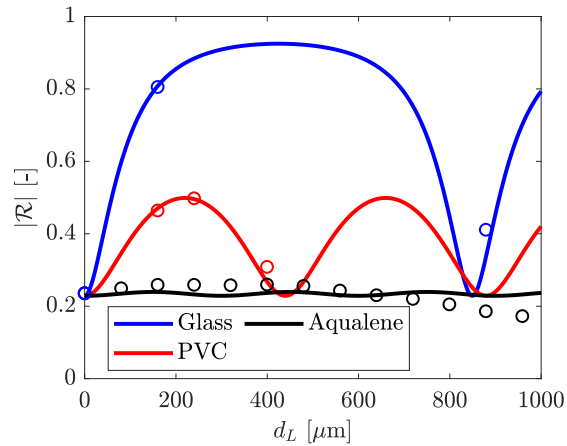
Figure 6.20: Reflection coefficient simulation results and the effect of couplant material and thickness for a polymer sample.

6.A.4   Attenuation and frequency-effects in PA12 solid and compact

Figure 6.21 shows the received signals using a 3.5 MHz transducer for a solid and compacted PA12 sample in the TT setup. The PA12 powder compact has a porosity of $\varphi = 0.1$. The signal for the powder compact sample should be used cautiously, as the signal changes shape for small densities and high attenuation and is close to the noise amplitude.

By rearranging the data in Figure 6.11b, the frequency dependency of the attenuation is derived as shown in Figure 6.22. Here, a power-law exponent of $y = 0.82$ describes the data of the solid PA12 sample. The powder compact shows a slope similar to the solid sample

(a) Solid PA12
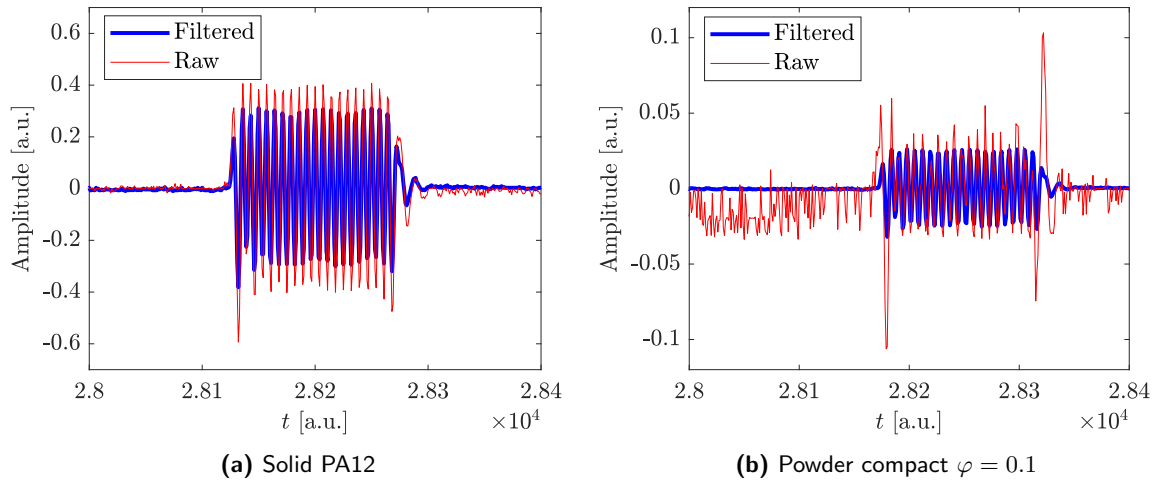
(b) Powder compact $\varphi = 0.1$

Figure 6.21: Received signals using a 3.5 MHz transducer in the TT setup for a solid PA12 sample and a PA12 powder compact with a porosity of $\varphi = 0.1$.

at lower frequencies. Meanwhile, at 3.5 MHz, the attenuation seems to increase drastically. This can indicate a transition to a scattering Mie or Rayleigh scattering regime $2 \leq y \leq 4$. However, data points are necessary to make this conclusive, and the signal of the compact at 3.5 MHz is challenging to access as it is close to the noise.
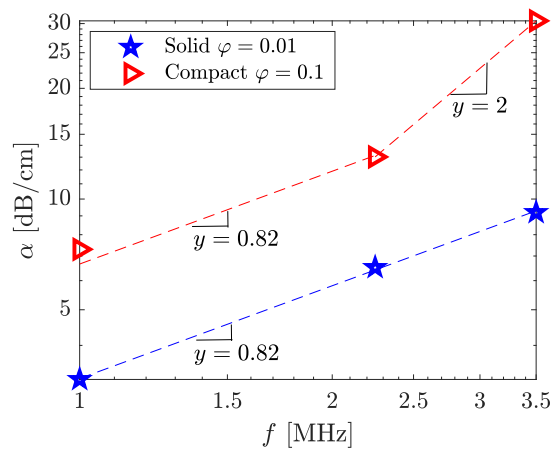
Figure 6.22: Attenuation as a function of frequencies for the solid and compressed PA12 sample.

Chapter 7

Conclusions and Recommendations

7.1 Conclusions

In this thesis, the complex interplay between process parameters and intrinsic material properties is assessed by introducing new concepts in selective laser sintering (SLS) 3D printing and by studying, for the first time, an ultrasound-based 3D printing technique called selective acoustic sintering (SAS).

The first part of the dissertation focuses on laser-assisted 3D printing. To determine the relevant process parameters in SLS and their coupling with final part properties, well-controlled SLS experimental strategies and improved numerical models of the SLS process are introduced. First, experimentally, the effects of laser power, scan speed, and bed temperature are systematically assessed by linking them to physical phenomena related to energy melt ratio and percolation theory. Subsequently, the numerical simulations show the effects of porosity-induced shrinkage and combined crystallization and melting kinetics of PA12.

The second part of the thesis aims to study the feasibility and applicability of ultrasound sources for producing high-performance materials. The potential of using SAS in powder bed fusion is discussed, wherein volumetric 3D printing (holograms), near-net part densities from compaction, and material diversity are the main benefits of this technique. A modeling framework theoretically describes the process of studying temperature increases resulting from focused ultrasound sources for different materials, resolutions, and printer dimensions. Next, the effects of changing transducer configurations are examined by numerical simulations. Finally, the properties of powder compacts that can be used in a SAS 3D printer are measured by ultrasound characterization setups. The main conclusions are:

Selective Laser Sintering

- Accurate temperature control, by adding an infrared camera to the SLS printer processes, is crucial to improving the part consistency and quality in a desktop SLS printer. The attenuation melt ratio (AMR) is an effective tool for constructing a printability map and predicting printing parameter combinations that can lead to improved mechanical properties of the prints. It is also revealed that percolation theory provides a useful method of predicting the mechanical properties of SLS-printed parts from the density of the part, resulting in a new process-material relationship for predicting the mechanical characteristics of SLS-printed parts. These findings highlight the importance of accurate temperature control and process-property relations in 3D printing and demon-

strate the potential for more efficient and accurate 3D printing processes. (*Chapter 2*)

- Numerical simulations are crucial in studying the structure development of particles and microstructure in SLS 3D printing. In a first case study, it was found that initial porosity significantly affects the shrinkage behavior of PA12 powder and affects the accuracy of parts produced with SLS. Higher initial porosity and high laser powers lead to severe shrinkage and edge curling, so compaction of the material is favorable to reduce the initial porosity and required power. In the second case study, the yield kinetics of a simple 2D product made out of PA12 was used to quantify the effect of microstructural changes on the yield stress characteristics of PA12 parts. The simulation results show that the processing conditions significantly affect the lamellar thickness, resulting in a yield stress distribution inside PA12 parts produced with SLS. Therefore, it is essential to carefully control the initial porosity, crystallization and melting, laser power, and scanning speed to make SLS products with optimal mechanical properties and accuracy. (*Chapter 3*)

Selective Acoustic Sintering

- A new 3D printing technique, Selective Acoustic Sintering (SAS), is introduced that fuses powder particles together using focused ultrasound transducers. This technology creates volumetric scan paths or holographic shapes, reducing printing times and producing fully dense products. A mathematical framework is proposed to determine the feasibility of this method, which optimizes the printing process and determines the appropriate process parameters for different materials and applications. The analysis of a diverse dataset of printable materials shows that selective acoustic sintering has potential for various applications, including printing metals, ceramics, and polymers. This framework provides a systematic approach and offers a valuable tool for researchers and engineers to advance the development of this technology for various applications. (*Chapter 4*)

- To further extend the modeling framework, numerical simulations are presented that model the coupling between acoustic wave propagation and acoustic thermal heating. With the numerical toolbox, the temperature increases at off-center focal positions are studied and quantified, and the feasibility of off-center volumetric scanning in SAS is shown. (*Chapter 5*)

- A model-based ultrasound characterization method for powder-based materials is realized, which accurately measures the speed of sound, impedance, and attenuation of the materials. The results showed that coupling media used in these setups can significantly impact the accuracy of the measurements, especially for powder-based materials. Additionally, the degree of compaction and the type of filler used in the powder compacts affect the acoustic properties of the materials. The findings have implications for the design of the selective acoustic sintering 3D printer, as mainly attenuation determines the acoustic energy transmitting and, thus, printer dimensions. Therefore, it is concluded that reducing the porosity of the powder by compaction or filling is necessary to reduce attenuation and enable sufficient heating inside the powder build volume in SAS 3D printers. The study supports the author's vision that material understanding is essential for designing efficient, high-quality 3D printing processes. (*Chapter 6*)

7.2   Recommendations

No research is ever complete, and there is always room for improvement, especially in a subject in its infancy, such as selective acoustic sintering. However, improvements are also desired for well-studied subjects like SLS. Many ideas about new research directions or how to improve results have been formed in studying these powder-based systems. The most relevant recommendations are discussed in this section. Some of these have been treated in this dissertation, but they will be readdressed for the sake of completeness.

7.2.1   Part predictions in SLS

In Chapter 2, single-layer hexagonal products were printed and tested using mechanical testing machines. The discussion mentioned that percolation theory can be used to predict the effect of porosity on the mechanical properties of these single-layer prints. However, the finite-size effects of the samples might affect the measured properties. Therefore, these finite-size effects should be studied by changing the width and thickness of the tensile bars for a range of sample densities.

Moving from single-layer to multi-layer parts would be the next step. However, this will complicate the analysis. This induces thermal history effects, and a tensile test would be an average measurement over all layers. Other techniques might be required to predict the mechanical properties resulting from processing. For example, the laminate theory can be used in cases with little layer adhesion. Besides, representative volume element (RVE) models and computer tomography (CT) information can be combined to model the microstructure of these SLS prints. In addition, digital image correlation can extract the true strain field of the tensile experiments. However, no standardized way of measuring these SLS products exists, and therefore, different mechanical tests are to be developed to quantify multi-layer SLS prints.

Despite its excellent predictability of the single-layer systems, we realize that the AMR relation is not suitable for a complete description of the SLS process. For example, it contains constant thermal and optical properties, while these temperature-dependent properties vary during printing. Besides, viscosity and other time scales (scan length versus scan velocity, diffusion times, etc.) are not considered. It is unclear which of these parameters should be regarded in a more elaborate prediction of the SLS process. The following options could be addressed in future research:

- A different polyamide powder is advised to study time effects in SLS. PA2200 powder might not be perfectly suitable for this, as post-condensation reactions affect the viscosity and sintering kinetics over time [29]. This could be circumvented by choosing a stabilized material like PA12 Orgasol. The relatively large viscosity of Orgasol slows down the sintering kinetics, which should be considered.

- Part geometry is crucial in selecting the processing parameters. For the hexagonal geometry, the edges show different maximum temperatures than the middle section. Therefore, a step-wise part with varying levels of scan length is advised to study the effects of scan length, hatch spacing, and scan velocity.

- Irradiation of single-layer parts starts from initially a constant bed temperature. In multi-layer parts, all subsequent layers are affected by the previously scanned layers,

changing the temperature field and bed temperature. Hereto, inter-layer time is an essential factor that should be regarded in multi-layer systems, as it affects the bed temperature and the diffusion of layers. Combining the knowledge obtained for single-layer parts, a controller could vary the laser power and scan velocity while printing depending on the actual temperature field of the bed. So, it is recommended that the SLS printer be upgraded to control the scan velocity and power along the scan path based on the temperature field measured by the IR camera.

- As pointed out in the work of Vande Ryse et al. [62], upgrading the AMR relations is possible by, for example, adding a temperature-dependent specific heat coefficient and including the packing factor. Besides, an overlap ratio is recommended, which defines the spot size ratio to the hatch spacing.

7.2.2 Modelling in SLS

Computational times are significant for the 2D FEM simulation presented in Chapter 3. Full 3D simulations on the product size level will be unfeasible for now and require parallelization or a mapping strategy to reduce computational costs. Other options are homogenization of parameters or multi-scale modeling. It is useful to study which microstructural variables are dominant to reduce the number of parameters in the FEM model. Combining micro-, meso- and macro descriptions of the SLS process is required to highlight the dominant material and process parameters (e.g., DEM simulations [267]).

The presented numerical model for SLS printing is based on existing theory, with known limitations, and a newly introduced melting kinetics theory. The presented melting kinetics model describes time- and temperature-dependent melting of melt-crystallized PA12. However, the powder is not melt-crystallized, as PA2200 particles are formed with a solution–precipitation process in ethanol at elevated temperature [29]. This results in a different polymorph system containing α' and γ crystal phases. Each phase's crystallization and melting kinetics should be included in the following version of the model. This would require a description using the Schneider rate's equations instead of the Nakamura model. Developing such a polymorph system model for PA12 is ongoing work in our group.

The melting kinetics of semi-crystalline polymers depend on the heating rate, where melting enthalpy and melting temperature shift with heating rate [123, 124]. Also, as shown by the SAXS measurements, the crystallinity is a function of the crystallization temperature. Both these effects are disregarded but could improve the melting description further.

A comparison between the model prediction and well-controlled experiments is advised. In the work of Laumer et al. [124], high-speed and flash DSC measurements of PA12 are presented, which show a significant effect of heating rates on melting temperature. Also, Lanzl et al. [268] designed a combined flash DSC and CO_2 laser setup that can mimic actual process and melting conditions in SLS. Both works could be used as a starting point for comparison of the SLS simulations.

7.2.3 Theoretical framework of the SAS 3D printer

Chapter 4 shows the theoretical feasibility of printing different types of materials with SAS. The proposed theoretical framework combines linear wave equations with the energy balance to predict the temperature increase at the focal position. The model assumes that the spot size is limited to the ultrasonic wavelength. However, numerical simulations have shown that

spot sizes below the wavelength are achievable for many element configurations. Besides, in the case of decreasing the element size, the spot size, according to Equation (4.1), would indefinitely increase. Therefore, only the case of $\xi = 2$ has been treated. The spot size formulation in Equation (4.1) should be altered for many small elements on a sphere. If the element size and spacing are below the wavelength, the elements can be considered point sources on a sphere, and this spot size can be derived from the superposition of these point sources.

Following the linear theory, the power consumption of a spherical SAS printer limits the current design to a radius of about 10 cm. However, nonlinear effects can dramatically change this limit because higher harmonics increase absorption at the focal spot. These nonlinear effects are advised to be implemented in the theoretical model by, for example, using the Khokhlov-Zabolotskaya-Kuznetzov (KZK) nonlinear wave equations [151–153].

7.2.4   Model-based design of the SAS Printer

The numerical model used to simulate the SAS print process for different printer configurations in Chapter 5 is developed to create a model-based design. However, the presented simulations lack proper material input as such assumptions in material properties were made. The tools are shown to perform a model-based design study, but it is recommended to perform the simulations with actual material properties as measured in Chapter 6.

The effect of positioning transducers and the size of elements were found to be especially important in the design. In practice, limiting the number of elements is convenient as this would require extensive calibration and high production costs. Options to limit the elements are changing the build chamber shape to a cylindrical geometry or optimization of the transducer and element configuration. A systematic approach is advised in both cases using the presented numerical toolbox.

Pressure and temperature fields are solved decoupled. However, the effect of temperature on the acoustic wave formation is important, as the material parameters are temperature-dependent. A coupled approach would be advised, similar to the numerical model of the SLS printing process. This also enables the simulation of the actual scanning of the focal spot throughout the volume.

7.2.5   Measurements of ultrasound properties

The nonlinear coefficients of the powder-based materials should be characterized to implement these nonlinear effects in the models. The proposed characterization setup (TT/PE) in Chapter 6 has not been used to measure these nonlinear coefficients. However, the trough-transmission characterization technique can be extended to measure the nonlinear coefficient as described in the work of Panfilova et al. [269]. Studying the feasibility of performing the nonlinear coefficient measurements by employing nonlinear simulations is advised, as the large attenuation values of powder can result in measurement errors in the nonlinear coefficients.

Another option is to perform experiments in a commercial setup used for particle size analysis, as these commercial devices can extract information about the scattering of the powder. An example of a possible device is the DT-100 Acoustic Spectrometer, with temperature control and thermal conductivity measurement options [270].

7.2.6   Cooling the build volume in SAS

One of the critical processes in SAS is cooling the build volume. This matter has not been addressed in detail in this dissertation. However, cooling large volumes with small surface-to-volume ratios is ineffective for well-insulting powder-based materials. Note that cooling rates depend on the printer's design, printing strategy, and material. Further investigation would require a theoretical study using the analytical expression for cooling in a spherical volume (see Carslaw and Jaeger [271], §9.4). Besides, numerical modeling of the cooling process, similar to the SLS simulations, can give insight into cooling times and structure development.

7.2.7   Outlook

The potential and findings of this dissertation have inspired me to further research the SAS 3D printing technique. The first crucial step is to develop a proof-of-principle demonstrator to validate the theoretical feasibility of this technique. The demonstrator will initially be built to sinter within a volume and can later be extended to holographic 3D printing. The future of SAS is seen in high-tech industries that demand high-quality specialty or niche products with complex shapes or nonprintable materials. Specifically, products made of technical glass or ceramic with near-net density will be targeted. Applications of SAS go beyond conventional 3D printing, as it could be used for melting behind or inside existing objects. For example, this technique could be used to improve weak spots in a material by local post-heat treatment or for the acoustic welding of surfaces at the back of an object. Although the development of the SAS 3D printing technique is in its early stages, I believe that SAS will become an enabling technology that can revolutionize the existing 3D printing market.

References

[1] S. C. Ligon, R. Liska, J. Stampfl, M. Gurr, and R. Mülhaupt. Polymers for 3D Printing and Customized Additive Manufacturing. *Chemical Reviews*, 117(15):10212–10290, 2017. 10.1021/ACS.CHEMREV.7B00074.

[2] International Organization for Standardization. Additive manufacturing - General principles - Fundamentals and vocabulary. *ISO/ASTM*, page 52900:2021(E), 2021.

[3] A. Jandyal, I. Chaturvedi, I. Wazir, A. Raina, and M. I. Ul Haq. 3D printing – A review of processes, materials and applications in industry 4.0. *Sustainable Operations and Computers*, 3:33–42, 2022. 10.1016/J.SUSOC.2021.09.004.

[4] S. Kumar. Laser Powder Bed Fusion. In *Additive Manufacturing Processes*, pages 41–63. Springer, Cham, 2020. 10.1007/978-3-030-45089-2_3.

[5] R. J. N. Joshua, S. A. Raj, M. T. Hameed Sultan, A. Łukaszewicz, J. Józwik, Z. Oksiuta, K. Dziedzic, A. Tofil, and F. S. Shahar. Powder Bed Fusion 3D Printing in Precision Manufacturing for Biomedical Applications: A Comprehensive Review. *Materials 2024, Vol. 17, Page 769*, 17(3):769, 2024. 10.3390/MA17030769.

[6] W. E. King, . A. T. Anderson, . R. M. Ferencz, . N. E. Hodge, . C. Kamath, S. A. Khairallah, . A. M. Rubenchik, A. T. Anderson, R. M. Ferencz, N. E. Hodge, C. Kamath, and A. M. Rubenchik. Laser powder bed fusion additive manufacturing of metals; physics, computational, and materials challenges. *Applied Physics Reviews*, 2(4):041304, 2015. 10.1063/1.4937809.

[7] Sharebot. Solutions for Additve Manufacturing: Sharebot 3D, 2023. `https://www.sharebot.us/`.

[8] P. Hejmady. *Selective laser sintering of polymer particles studied by in-situ visualization*. PhD thesis, Eindhoven University of Technology, Eindhoven, 2021.

[9] M. Baumers, C. Tuck, and R. Hague. Selective Heat Sintering Versus Laser Sintering: Comparison of Deposition Rate, Process Energy Consumption and Cost Performance. In *International Solid Freeform Fabrication Symposium*. University of Texas at Austin, 2015.

[10] N. Holt, A. Van Horn, M. Montazeri, and W. Zhou. Microheater array powder sintering: A novel additive manufacturing process. *Journal of Manufacturing Processes*, 31:536–551, 2018. 10.1016/J.JMAPRO.2017.12.009.

[11] R. Brown, C. Morgan, and C. Majewski. Not Just nylon... improving the range of materials for high speed sintering. In *Solid Freeform Fabrication Symposium*. Laboratory for Freeform Fabrication and University of Texas at Austin, 2018.

[12] E. Jerby, Y. Meir, A. Salzberg, E. Aharoni, A. Levy, J. P. Torralba, and B. Cavallini. Incremental metal-powder solidification by localized microwave-heating and its potential for additive manufacturing. *Additive Manufacturing*, 6:53–66, 2015. 10.1016/J.ADDMA.2015.03.002.

[13] P. Hejmady, L. C. A. Van Breemen, P. D. Anderson, and R. Cardinaels. Laser sintering of polymer particle pairs studied by in situ visualization. *Soft Matter*, 15(6):1373–1387, 2019. 10.1039/c8sm02081g.

[14] C. Balemans, P. Hejmady, R. Cardinaels, and P. D. Anderson. Towards unraveling the sintering process of two polystyrene particles by numerical simulations. *Korea Australia Rheology Journal*, 31(4):285–295, 2019. 10.1007/S13367-019-0028-Z/METRICS.

[15] C. Balemans, S. F. S. P. Looijmans, G. Grosso, M. A. Hulsen, and P. D. Anderson. Numerical analysis of the crystallization kinetics in SLS. *Additive Manufacturing*, 33:101126, 2020. 10.1016/J.ADDMA.2020.101126.

[16] F. Paolucci, L. E. Govaert, and G. W. M. Peters. In Situ WAXD and SAXS during Tensile Deformation Of Moulded and Sintered Polyamide 12. *Polymers*, 11(6):1001, 2019. 10.3390/polym11061001.

[17] F. Paolucci, G. W. M. Peters, and L. E. Govaert. Plasticity-controlled failure of sintered and molded polyamide 12: Influence of temperature and water absorption. *Journal of Applied Polymer Science*, 137 (14):48525, 2020. 10.1002/APP.48525.

[18] K. Wudy and D. Drummer. Aging effects of polyamide 12 in selective laser sintering: Molecular weight distribution and thermal properties. *Additive Manufacturing*, 25:1–9, 2019. 10.1016/J.ADDMA.2018.11.007.

[19] M. Schmid. *Laser Sintering with Plastics*. Carl Hanser Verlag, München, 2018. 10.3139/9781569906842.

[20] E. Schubert, I. Zerner, and G. Sepold. New possibilities for joining by using high power diode lasers. In *ICALEO*, pages G111–G120. AIP Publishing, 1998. 10.2351/1.5059189.

[21] N. K. Tolochko, T. Laoui, Y. V. Khlopkov, S. E. Mozzharov, V. I. Titov, and M. B. Ignatiev. Absorptance of powder materials suitable for laser sintering. *Rapid Prototyping Journal*, 6(3):155–160, 2000. 10.1108/13552540010337029.

[22] W. Schnabel. Degradation by High Energy Radiation. In *Polymer Degradation: Principles and Practical Applications*, chapter 14, pages 131–153. Hanser International, München, 1981.

[23] S. Lazare and P. Benet. Surface amorphization of Mylar(R) films with the excimer laser radiation above and below ablation threshold: Ellipsometric measurements. *Journal of Applied Physics*, 74(8):4953 – 4957, 1993. 10.1063/1.354333.

[24] P. Shumyatsky and R. R. Alfano. Terahertz sources. *J. Biomed. Opt.*, 16(3):033001, 2011. 10.1117/1.3554742.

[25] Edinburgh Instruments. Products - CO2 Lasers (9.1 μm - 10.9 μm), 2023. `https://www.edinst.com/us/products/co2-gas-lasers-9-1-%CE%BCm-10-9-%CE%BCm/`.

[26] Treffert. Laser Welding and Laser Marking of plastics, 2023. `https://treffert.eu/product-expertise/laserwelding-lasermarking-plastic/`.

[27] Laser Focus World. Terahertz Generation: Near-IR lasers may close the terahertz gap, 2008. `https://www.laserfocusworld.com/test-measurement/research/article/16555115/terahertz-generation-nearir-lasers-may-close-the-terahertz-gap`.

[28] EOS GmbH. Material Datasheet PA2200, 2019. `https://eos.materialdatacenter.com/eo/`.

[29] L. Verbelen, S. Dadbakhsh, M. Van Den Eynde, J. P. Kruth, B. Goderis, and P. Van Puyvelde. Characterization of polyamide powders for determination of laser sintering processability. *European Polymer Journal*, 75:163–174, 2016. 10.1016/j.eurpolymj.2015.12.014.

[30] P. Regenfuss, A. Streek, L. Hartwig, S. Klötzer, T. Brabant, M. Horn, R. Ebert, and H. Exner. Principles of laser micro sintering. *Rapid Prototyping Journal*, 13(4):204–212, 2007. 10.1108/13552540710776151.

[31] Coherent. Lasers - Diamond J-Series, 2023. `https://www.coherent.com/lasers/co2/diamond-j-series`.

[32] Coherent. Lasers - Diamond 5 Micron CO Laser, 2023. `https://www.coherent.com/lasers/co2/diamond-5`.

[33] Pantec Biosolutions. Diode pumped solid state laser, 2023. `https://pantec-biosolutions.com/en/products/diode-pumped-solid-state-laser`.

[34] IPG Photonics. Mid Power CW Fiber Lasers, 2023. `https://www.ipgphotonics.com/en/products/lasers/mid-power-cw-fiber-lasers`.

[35] Azurlight Systems. 1064 nm High Power Fiber Lasers & Amplifiers, 2023. `https://azurlight-systems.com/portfolio_page/1064-nm-high-power-fiber-lasers-amplifiers-50w-single-mode-single-frequency/`.

[36] Astrum Laser Technologies. Semiconductor Laser Systems 1064-532nm, 2023. `https://astrum-lasers.com/technology-and-components/semiconductor-laser-systems-1064-532nm`.

[37] Pranalytica. High Power Laser System Model 1101-46-CW-XXXX, 2023. `http://www.pranalytica.com/products-services/1101-46-CW.php`.

[38] Pranalytica. OMNILUX™ Multiple Tunable QCL System, 2023. `http://www.pranalytica.com/products-services/omnilux.php`.

[39] Light Conversion. ORPHEUS-ONE Mid-IR Collinear OPA, 2023. `https://lightcon.com/product/orpheus-mid-ir-opa/`.

[40] F. Orsi, P. Arnone, W. Chen, and L. Zhang. High intensity focused ultrasound ablation: a new therapeutic option for solid tumors. *Journal of cancer research and therapeutics*, 6(4):414–420, 2010. 10.4103/0973-1482.77064.

[41] CNC Fandom. Command and Conquer Wiki - Harmonic resonance, 2023. `https://cnc.fandom.com/wiki/Harmonic_resonance`.

[42] C. Lobstein-Adams. *Development of a medical imaging-based technology for cancer treatment*. PhD thesis, University of Sussex, Brighton, 2015.

[43] Cleveland Clinic. Focal One® High-Intensity Focused Ultrasound, 2021. `https://www.youtube.com/watch?v=3d1GDfWlCWA`.

[44] K. Melde, E. Choi, Z. Wu, S. Palagi, T. Qiu, P. Fischer, K. Melde, E. Choi, Z. Wu, S. Palagi, T. Qiu, P. Fischer Micro, and P. Fischer. Acoustic Fabrication via the Assembly and Fusion of Particles. *Adv. Mater.*, 30(3):1704507, 2018. 10.1002/ADMA.201704507.

[45] K. Melde, H. Kremer, M. Shi, S. Seneca, C. Frey, I. Platzman, C. Degel, D. Schmitt, B. Schölkopf, and P. Fischer. Compact holographic sound fields enable rapid one-step assembly of matter in 3D. *Sci. Adv.*, 9(6):eadf6182, 2023. 10.1126/sciadv.adf6182.

[46] T. L. Starr, T. J. Gornet, and J. S. Usher. The effect of process conditions on mechanical properties of laser-sintered nylon. *Rapid Prototyp. J.*, 17(6):418–423, 2011. 10.1108/13552541111184143.

[47] J. P. Kruth, G. Levy, R. Schindel, T. Craeghs, and E. Yasa. Consolidation of polymer powders by selective laser sintering. In *Proceedings of the 3rd international conference on polymers and moulds innovations*, 2008.

[48] M. Vasquez, B. Haworth, and N. Hopkinson. Methods for quantifying the stable sintering region in laser sintered polyamide-12. *Polym. Eng. Sci.*, 53(6):1230–1240, 2013. 10.1002/PEN.23386.

[49] J. C. Nelson, S. Xue, J. W. Barlow, J. J. Beaman, H. L. Marcus, and D. L. Bourell. Model of the Selective Laser Sintering of Bisphenol-A Polycarbonate. *Industrial and Engineering Chemistry Research*, 32(10): 2305–2317, 1993. 10.1021/ie00022a014.

[50] J. C. Nelson, N. K. Vail, J. W. Barlow, J. J. Beaman, D. L. Bourell, and H. L. Marcus. Selective Laser Sintering of Polymer-Coated Silicon Carbide Powders. *Ind. Eng. Chem. Res*, 34(5):1641–1651, 1995.

[51] B. Caulfield, P. E. McHugh, and S. Lohfeld. Dependence of mechanical properties of polyamide components on build parameters in the SLS process. *Journal of Materials Processing Technology*, 182(1-3): 477–488, 2007. 10.1016/J.JMATPROTEC.2006.09.007.

[52] D. L. Bourell, T. J. Watt, D. K. Leigh, and B. Fulcher. Performance limitations in polymer laser sintering. *Phys. Procedia*, 56(C):147–156, 2014. 10.1016/J.PHPRO.2014.08.157.

[53] C. Bierwisch, S. Mohseni-Mofidi, B. Dietemann, M. Grünewald, J. Rudloff, and M. Lang. Universal process diagrams for laser sintering of polymers. *Mater. Des.*, 199, 2021. 10.1016/j.matdes.2020.109432.

[54] C. Majewski, H. Zarringhalam, and N. Hopkinson. Effect of the degree of particle melt on mechanical properties in selective laser-sintered Nylon-12 parts. *Proceedings of the Institution of Mechanical Engineers, Part B: Journal of Engineering Manufacture*, 222(9):1055–1064, 2008. 10.1243/09544054JEM1122.

[55] S. Singh, A. Sachdeva, and V. S. Sharma. Optimization of selective laser sintering process parameters to achieve the maximum density and hardness in polyamide parts. *Progress in Additive Manufacturing*, 2(1-2):19–30, 2017. 10.1007/s40964-017-0020-4.

[56] Optris. Optris PIX Connect. Retrieved January 18, 2023, from. *https://www.optris.global/optris-pix-connect*, 2023.

[57] Edmund Optics. Potassium Bromide Window, 2021. `https://www.edmundoptics.com/p/50mm-dia-x-3mm-thickness-uncoated-potassium-bromide-window/23423/`.

[58] Gentec. UP19K-30H-H5-D0 - Thermopile laser power detector, 2023. `https://www.gentec-eo.com/products/up19k-30h-h5-d0`.

[59] F. Yang, N. Zobeiry, R. Mamidala, and X. Chen. A review of aging, degradation, and reusability of PA12 powders in selective laser sintering additive manufacturing. *Materials Today Communications*, 34: 105279, 2023. 10.1016/J.MTCOMM.2022.105279.

[60] A. Ranellucci. Slic3r - Open source 3D printing toolbox, 2019. `https://slic3r.org/`.

[61] A. Pilipović, I. Drstvenšek, and M. Šercer. Mathematical Model for the Selection of Processing Parameters in Selective Laser Sintering of Polymer Products. *https://doi.org/10.1155/2014/648562*, 2014, 2014. 10.1155/2014/648562.

[62] R. Vande Ryse, M. Edeleva, A. Patoor, F. Pille, D. R. D'hooge, and L. Cardon. Upgrading analytical models to predict the onset of degradation in selective laser sintering. *Virtual and Physical Prototyping*, 19(1), 2024. 10.1080/17452759.2023.2285414.

[63] F. Lupone, E. Padovano, M. Pietroluongo, S. Giudice, O. Ostrovskaya, and C. Badini. Optimization of selective laser sintering process conditions using stable sintering region approach. *Express Polymer Letters*, 15(2):177–192, 2021. 10.3144/expresspolymlett.2021.9.

[64] R. Landauer. Electrical conductivity in inhomogeneous media. *AIP Conference Proceedings*, 40(1):2–45, 1978. 10.1063/1.31150.

[65] D. S. McLachlan. Measurement and analysis of a model dual-conductivity medium using a generalised effective-medium theory. *Journal of Physics C: Solid State Physics*, 21(8):1521, 1988. 10.1088/0022-3719/21/8/025.

[66] T. J. Coutts. Percolation conduction in mixed insulator-conductor systems. *Thin Solid Films*, 38(3): 313–321, 1976. 10.1016/0040-6090(76)90009-2.

[67] M. A. Dubson and J. C. Garland. Measurement of the conductivity exponent in two-dimensional percolating networks: square lattice versus random-void continuum. *Physical review. B, Condensed matter*, 32(11):7621–7623, 1985. 10.1103/PHYSREVB.32.7621.

[68] D. Stauffer and A. Aharony. *Introduction To Percolation Theory*. Taylor & Francis, second edition edition, 1992. 10.1201/9781315274386.

[69] F. Ternero, L. G. Rosa, P. Urban, J. M. Montes, and F. G. Cuevas. Influence of the Total Porosity on the Properties of Sintered Materials—A Review. *Metals 2021, Vol. 11, Page 730*, 11(5):730, 2021. 10.3390/MET11050730.

[70] J. P. Straley. Critical phenomena in resistor networks. *Journal of Physics C: Solid State Physics*, 9(5): 783, 1976. 10.1088/0022-3719/9/5/017.

[71] P. M. Davis and L. Knopoff. The elastic modulus, percolation, and disaggregation of strongly interacting, intersecting antiplane cracks. *Proceedings of the National Academy of Sciences*, 106(31):12634–12639, 2009. 10.1073/pnas.0903014106.

[72] M. Sahimi. *Applications of Percolation Theory*, volume 213 of *Applied Mathematical Sciences*. Springer International Publishing, Cham, 2 edition, 2023. 10.1007/978-3-031-20386-2.

[73] I. Balberg and N. Binenbaum. Direct determination of the conductivity exponent in directed percolation. *Physical review. B, Condensed matter*, 33(3):2017–2019, 1986. 10.1103/PHYSREVB.33.2017.

[74] J. Kováčik. Correlation between Young's modulus and porosity in porous materials. *Journal of Materials Science Letters*, 18(13):1007–1010, 1999. 10.1023/A:1006669914946.

[75] K. K. Phani and S. K. Niyogi. Young's modulus of porous brittle solids. *Journal of Materials Science 1987 22:1*, 22(1):257–263, 1987. 10.1007/BF01160581.

[76] I. Gibson and D. Shi. Material properties and fabrication parameters in selective laser sintering process. *Rapid Prototyping Journal*, 3(4):129–136, 1997. 10.1108/13552549710191836.

[77] A. Pilipović, T. Brajlih, and I. Drstvenšek. Influence of processing parameters on tensile properties of SLS polymer product. *Polymers*, 10(11), 2018. 10.3390/polym10111208.

[78] S. Ziegelmeier, F. Wöllecke, C. Tuck, R. Goodridge, and R. Hague. Characterizing the Bulk & Flow Behaviour of LS Polymer Powders. In *International Solid Freeform Fabrication Symposium*. University of Texas at Austin, 2013. 10.26153/tsw/15437.

[79] S. Rüsenberg, L. Schmidt, and H.-J. Schmid. *Mechanical and Physical Properties-A Way to assess quality of Laser Sintered Parts*. PhD thesis, University of Paderborn, Paderborn, 2011.

[80] J. Patel and P. J. Phillips. The young's modulus of polyethylene. *Journal of Polymer Science: Polymer Letters Edition*, 11(12):771–776, 1973. 10.1002/POL.1973.130111208.

[81] R. J. Young. A dislocation model for yield in polyethylene. *Philosophical Magazine*, 30(1):85–94, 1974. 10.1080/14786439808206535.

[82] A. J. Peacock and L. Mandelkern. The mechanical properties of random copolymers of ethylene: Force-elongation relations. *Journal of Polymer Science Part B: Polymer Physics*, 28(11):1917–1941, 1990. 10.1002/POLB.1990.090281104.

[83] T. B. Van Erp, D. Cavallo, G. W. M. Peters, and L. E. Govaert. Rate-, temperature-, and structure-dependent yield kinetics of isotactic polypropylene. *Journal of Polymer Science, Part B: Polymer Physics*, 50(20):1438–1451, 2012. 10.1002/polb.23150.

[84] H. J. M. Caelers, L. E. Govaert, and G. W. M. Peters. The prediction of mechanical performance of isotactic polypropylene on the basis of processing conditions. *Polymer*, 83:116–128, 2016. 10.1016/j.polymer.2015.12.001.

[85] E. Parodi, G. W. Peters, and L. E. Govaert. Structure–Properties Relations for Polyamide 6, Part 1: Influence of the Thermal History during Compression Moulding on Deformation and Failure Kinetics. *Polymers 2018, Vol. 10, Page 710*, 10(7):710, 2018. 10.3390/POLYM10070710.

[86] E. Parodi, G. W. Peters, and L. E. Govaert. Structure-Properties Relations for Polyamide 6, Part 2: Influence of Processing Conditions during Injection Moulding on Deformation and Failure Kinetics. *Polymers 2018, Vol. 10, Page 779*, 10(7):779, 2018. 10.3390/POLYM10070779.

[87] M. Heinl, T. Laumer, F. Bayer, and T. Hausotte. Temperature-dependent optical material properties of polymer powders regarding in-situ measurement techniques in additive manufacturing. *Polymer Testing*, 71:378–383, 2018. 10.1016/j.polymertesting.2018.09.016.

[88] T. Ree and H. Eyring. Theory of Non-Newtonian Flow. I. Solid Plastic System. *Journal of Applied Physics*, 26(7):793–800, 1955. 10.1063/1.1722098.

[89] Z. Hashin and S. Shtrikman. A Variational approach to the theory of the effective magnetic permeability of multiphase materials. *Journal of Applied Physics*, 33(10):3125–3131, 1962. 10.1063/1.1728579.

[90] R. Le Goff, G. Poutot, D. Delaunay, R. Fulchiron, and E. Koscher. Study and modeling of heat transfer during the solidification of semi-crystalline polymers. *International Journal of Heat and Mass Transfer*, 48(25-26):5417–5430, 2005. 10.1016/j.ijheatmasstransfer.2005.06.015.

[91] A. Mokrane, M. Boutaous, and S. Xin. Process of selective laser sintering of polymer powders: Modeling, simulation, and validation. *Comptes Rendus - Mecanique*, 346(11):1087–1103, 2018. 10.1016/j.crme.2018.08.002.

[92] J. Li, S. Yuan, J. Zhu, S. Li, and W. Zhang. Numerical model and experimental validation for laser sinterable semi-crystalline polymer: Shrinkage and warping. *Polymers*, 12(6), 2020. 10.3390/POLYM12061373.

[93] C. Balemans. *Computational analysis of polymer powder sintering for 3D printing*. PhD thesis, Technische Universiteit Eindhoven, Eindhoven, 2019.

[94] S. Yuan, J. Bai, C. K. Chua, J. Wei, and K. Zhou. Material evaluation and process optimization of CNT-coated polymer powders for selective laser sintering. *Polymers*, 8(10), 2016. 10.3390/polym8100370.

[95] F. Shen, W. Zhu, K. Zhou, and L. L. Ke. Modeling the temperature, crystallization, and residual stress for selective laser sintering of polymeric powder. *Acta Mechanica*, 232(9):3635–3653, 2021. 10.1007/s00707-021-03020-6.

[96] J. Hilsenrath. *Tables of Thermal Properties of Gases*, volume 564. U.S. Department of Commerce, National Bureau of Standards, Washington, 1955.

[97] E. W. Lemmon and R. T. Jacobsen. Viscosity and thermal conductivity equations for nitrogen, oxygen, argon, and air. *International Journal of Thermophysics*, 25(1):21–69, 2004. 10.1023/B:IJOT.0000022327.04529.F3.

[98] D. Riedlbauer, M. Drexler, D. Drummer, P. Steinmann, and J. Mergheim. Modelling, simulation and experimental validation of heat transfer in selective laser melting of the polymeric material PA12. *Computational Materials Science*, 93:239–248, 2014. 10.1016/j.commatsci.2014.06.046.

[99] S. Dadbakhsh, L. Verbelen, O. Verkinderen, D. Strobbe, P. Van Puyvelde, and J. P. Kruth. Effect of PA12 powder reuse on coalescence behaviour and microstructure of SLS parts. *European Polymer Journal*, 92(May):250–262, 2017. 10.1016/j.eurpolymj.2017.05.014.

[100] D. Drummer, M. Drexler, and F. Kühnlein. Effects on the Density Distribution of SLS-Parts. *Physics Procedia*, 39:500–508, 2012. 10.1016/J.PHPRO.2012.10.066.

[101] C. T. Bellehumeur, M. Kontopoulou, and J. Vlachopoulos. The role of viscoelasticity in polymer sintering. *Rheologica Acta*, 37(3):270–278, 1998. 10.1007/s003970050114.

[102] O. Pokluda, C. T. Bellehumeur, and J. Vlachopoulos. Modification of Frenkel's model for sintering. *AIChE Journal*, 43(12):3253–3256, 1997. 10.1002/AIC.690431213.

[103] G. W. Scherer. Viscous Sintering of a Bimodal Pore-Size Distribution. *Journal of the American Ceramic Society*, 67(11):709–715, 1984. 10.1111/j.1151-2916.1984.tb19506.x.

[104] T. H. C. C. Childs and A. E. Tontowi. Selective laser sintering of a crystalline and a glass-filled crystalline polymer: Experiments and simulations. *Proceedings of the Institution of Mechanical Engineers, Part B: Journal of Engineering Manufacture*, 215(11):1481–1495, 2001. 10.1243/0954405011519330.

[105] K. Wudy, D. Drummer, and M. Drexler. Characterization of polymer materials and powders for selective laser melting. In *AIP Conference Proceedings*, volume 1593, pages 702–707. American Institute of Physics Inc., 2014. 10.1063/1.4873875.

[106] M. Avrami. Kinetics of phase change. I: General theory. *The Journal of Chemical Physics*, 7(12): 1103–1112, 1939. 10.1063/1.1750380.

[107] M. Avrami. Kinetics of phase change. II Transformation-time relations for random distribution of nuclei. *The Journal of Chemical Physics*, 8(2):212–224, 1940. 10.1063/1.1750631.

[108] M. Avrami. Granulation, phase change, and microstructure kinetics of phase change. III. *The Journal of Chemical Physics*, 9(2):177–184, 1941. 10.1063/1.1750872.

[109] F. Neugebauer, V. Ploshikhin, J. Ambrosy, and G. Witt. Isothermal and non-isothermal crystallization kinetics of polyamide 12 used in laser sintering. *Journal of Thermal Analysis and Calorimetry*, 124(2): 925–933, 2016. 10.1007/s10973-015-5214-8.

[110] K. Nakamura, T. Watanabe, K. Katayama, and T. Amano. Some aspects of nonisothermal crystallization of polymers. I. Relationship between crystallization temperature, crystallinity, and cooling conditions. *Journal of Applied Polymer Science*, 16(5):1077–1091, 1972. 10.1002/app.1972.070160503.

[111] K. Nakamura, K. Katayama, and T. Amano. Some aspects of nonisothermal crystallization of polymers. II. Consideration of the isokinetic condition. *Journal of Applied Polymer Science*, 17(4):1031–1041, 1973. 10.1002/app.1973.070170404.

[112] R. M. Patel and J. E. Spruiell. Crystallization kinetics during polymer processing—Analysis of available approaches for process modeling. *Polymer Engineering & Science*, 31(10):730–738, 1991. 10.1002/pen.760311008.

[113] A. Ziabicki. *Fundamentals of fibre formation : the science of fibre spinning and drawing*. Wiley, 1976.

[114] C. J. G. Plummer, J.-E. Zanetto, P.-E. Bourban, and J.-A. E. Månson. The crystallization kinetics of polyamide-12. *Colloid & Polymer Science*, 279(4):312–322, 2001. 10.1007/s003960000425.

[115] O. Verkinderen, D. Baeten, P. Van Puyvelde, and B. Goderis. The crystallization of PA11, PA12, and their random copolymers at increasing supercooling: From eutectic segregation to mesomorphic solid solutions. *Polymer Crystallization*, 4(6), 2021. 10.1002/pcr2.10216.

[116] J. I. Lauritzen and J. D. Hoffman. Extension of theory of growth of chain-folded polymer crystals to large undercoolings. *Journal of Applied Physics*, 44(10):4340–4352, 1973. 10.1063/1.1661962.

[117] J. D. Hoffman and J. J. Weeks. Melting process and the equilibrium melting temperature of poly-chlorotrifluoroethylene. *Journal of Research of the National Bureau of Standards Section A: Physics and Chemistry*, 66A(1):13, 1962. 10.6028/jres.066A.003.

[118] J. D. Hoffman, G. T. Davis, and J. I. Lauritzen. The Rate of Crystallization of Linear Polymers with Chain Folding. *Treatise on Solid State Chemistry*, pages 497–614, 1976. 10.1007/978-1-4684-2664-9_7.

[119] W. Thomson. On the equilibrium of vapour at a curved surface of liquid. *Philosophical Magazine Series 1*, 42:448–452, 1871. 10.1080/14786447108640606.

[120] H. Berghmans. Thermal transitions and gelation in polymer solutions. In V. B. F. Mathot, editor, *Calorimetry and thermal analysis of polymers*, pages 207–230. Hanser, Munich, 1994.

[121] L. Telen, P. Van Puyvelde, and B. Goderis. Random Copolymers from Polyamide 11 and Polyamide 12 by Reactive Extrusion: Synthesis, Eutectic Phase Behavior, and Polymorphism. *Macromolecules*, 49(3): 876–890, 2016. 10.1021/acs.macromol.5b00976.

[122] M. Zhao, K. Wudy, and D. Drummer. Crystallization kinetics of polyamide 12 during Selective laser sintering. *Polymers*, 10(2), 2018. 10.3390/polym10020168.

[123] A. Toda, M. Hikosaka, and K. Yamada. Superheating of the melting kinetics in polymer crystals: a possible nucleation mechanism. *Polymer*, 43(5):1667–1679, 2002. 10.1016/S0032-3861(01)00733-9.

[124] T. Laumer, K. Wudy, M. Drexler, P. Amend, S. Roth, D. Drummer, and M. Schmidt. Fundamental investigation of laser beam melting of polymers for additive manufacture. *Journal of Laser Applications*, 26(4):42003, 2014. 10.2351/1.4892848.

[125] E. Moeskops, N. Kamperman, B. Van De Vorst, and R. Knoppers. CREEP BEHAVIOUR OF POLYAMIDE IN SELECTIVE LASER SINTERING. In *International Solid Freeform Fabrication Symposium*, pages 60–67, 2004.

[126] T. Diller, R. Sreenivasan, J. Beaman, D. Bourell, and J. Larocco. Thermal model of the build environment for polyamide powder selective laser sintering. In *International Solid Freeform Fabrication Symposium*, 2010.

[127] M. A. Hulsen. TFEM A toolkit for the finite element method User's Guide, 2004.

[128] HSL. The HSL Mathematics Software Library, 2011. https://www.hsl.rl.ac.uk/.

[129] S. Dan-Andrei. Viscoplastic Behaviour of Polyamides. In M. F. El-Amin, editor, *Viscoelastic and Viscoplastic Materials*, chapter 9. IntechOpen, Rijeka, 2016. 10.5772/64563.

[130] L. Li, M. H. J. Koch, and W. H. De Jeu. Crystalline structure and morphology in nylon-12: A small- and wide-angle X-ray scattering study. *Macromolecules*, 36(5):1626–1632, 2003. 10.1021/ma025732l.

[131] I. Gibson, D. W. Rosen, and B. Stucker. Direct Digital Manufacturing. In *Additive Manufacturing Technologies*, pages 378–399. Springer, Boston, MA, Boston, MA, 2010. 10.1007/978-1-4419-1120-9_14.

[132] J. R. Tumbleston, D. Shirvanyants, N. Ermoshkin, R. Janusziewicz, A. R. Johnson, D. Kelly, K. Chen, R. Pinschmidt, J. P. Rolland, A. Ermoshkin, E. T. Samulski, and J. M. DeSimone. Continuous liquid interface production of 3D objects. *Science*, 347(6228):1349–1352, 2015. 10.1126/science.aaa2397.

[133] D. L. Miller, N. B. Smith, M. R. Bailey, G. J. Czarnota, K. Hynynen, and I. R. S. Makin. Overview of Therapeutic Ultrasound Applications and Safety Considerations. *J. Ultrasound. Med.*, 31(4):623–634, 2012. 10.7863/JUM.2012.31.4.623.

[134] Y.-F. Zhou. High intensity focused ultrasound in clinical tumor ablation. *World J. Clin. Oncol.*, 2(1): 8–22, 2011. 10.5306/WJCO.V2.I1.8.

[135] D. White. Ultrasonic object consolidation. *United States patent*, US6519500B1, 2000.

[136] D. R. White. Ultrasonic Consolidation of Aluminum Tooling. *Adv. Mater. Process.*, 161(1):64–65, 2003.

[137] K. F. Graff, M. Short, and M. Norfolk. Very high power ultrasonic additive manufacturing (VHP UAM) for advanced materials. In *Int. Solid Freeform Fabr. Symp.*, pages 82–89, Austin, Texas, 2010. 10.26153/tsw/15165.

[138] M. Habibi, S. Foroughi, V. Karamzadeh, and M. Packirisamy. Direct sound printing. *Nat. Commun.*, 13(1):1800, 2022. 10.1038/s41467-022-29395-1.

[139] G. Moagăr-Poladian. Quick manufacturing process using focused ultrasound beam (Procedeu de manufacturare rapidă folosind fascicul focalizat de ultrasunete). *Romanian patent*, RO130409, 2013.

[140] P. B. Neibecker, H. Ceeh, and J. A. Weber. Method and device for producing a three-dimensional object (Verfahren und Vorrichtung zum Herstellen eines dreidimensionalen Objekts). *European patent*, EP3059074, 2015.

[141] H. Claussen, L. Dalloro, and J. S. Mcconkey. Systems and methods of volumetric 3D printing. *United States patent*, US10500640, 2017.

[142] M. Asad. 3D Printing and Bioprinting Process Using High Intensity Focused Ultrasound (HIFU) Technology. *Australian patent*, AU2018201765, 2018.

[143] H. M. Kim, K. J. Pahk, B. C. Lee, and I. Youn. Method for 3d printing and 3d printer using ultrasound. *Korean patent*, KR102140967, 2018.

[144] F. P. A. van Berlo, L. C. A. van Breemen, and P. D. Anderson. Apparatus and method for producing an object by means of additive manufacturing. *Worldwide patent*, WO2023234771A1, 2023.

[145] F. P. A. van Berlo, L. C. A. van Breemen, P. D. Anderson, and P. J. F. M. Janssen. Methods and an apparatus for producing an object by means of selective acoustic sintering. *Dutch patent filed*, P100198NL, 2024.

[146] R. Anastasio, W. Peerbooms, R. Cardinaels, and L. C. A. Van Breemen. Characterization of Ultraviolet-Cured Methacrylate Networks: From Photopolymerization to Ultimate Mechanical Properties. *Macromolecules*, 52(23):9220–9231, 2019. 10.1021/ACS.MACROMOL.9B01439.

[147] P. Hejmady, L. C. van Breemen, D. Hermida-Merino, P. D. Anderson, and R. Cardinaels. Laser sintering of PA12 particles studied by in-situ optical, thermal and X-ray characterization. *Additive Manufacturing*, 52:102624, 2022. 10.1016/J.ADDMA.2022.102624.

[148] F. P. A. van Berlo, P. D. Anderson, and Breemen. L C A. Selective Laser Sintering: Predictive Analysis of Process Parameters Impact on Intrinsic Material Properties. *[Manuscript submitted for publication]*, 2024.

[149] H. T. O'Neil. Theory of Focusing Radiators. *J. Acoust. Soc. Am.*, 21(5):516–526, 1949. 10.1121/1.1906542.

[150] H. Goldenberg. A problem in radial heat flow. *Br. J. Appl. Phys.*, 2(8):233–237, 1951. 10.1088/0508-3443/2/8/305.

[151] E. A. Zabolotskaya and R. V. Khokhlov. Quasi-plane waves in the nonlinear acoustics of confined beams. *Sov. Phys. Acoust.*, 15(1):35–40, 1969.

[152] V. P. Kuznetsov. Equations of nonlinear acoustics. *Sov. Phys. Acoust.*, 16:467–470, 1971.

[153] O. V. Bessonova, V. A. Khokhlova, M. R. Bailey, M. S. Canney, and L. A. Crum. Focusing of high power ultrasound beams and limiting values of shock wave parameters. *Acoust. Phys.*, 55(4-5):463–473, 2009. 10.1134/S1063771009040034.

[154] H. J. Gohari. Focusing of ultrasound beams. *M.S. thesis, University of Oslo, Oslo, Norway*, 1997.

[155] C. Tao, G. Guo, Q. Ma, J. Tu, D. Zhang, and J. Hu. Accurate acoustic power measurement for low-intensity focused ultrasound using focal axial vibration velocity. *J. Appl. Phys.*, 122(1):014901, 2017. 10.1063/1.4991641.

[156] A. Vary. Ultrasonic measurement of material properties. In R. S. Sharpe, editor, *Research Techniques in Nondestructive Testing*, volume 4, pages 159–204. Academic Press, New York, 1980.

[157] W. L. Nyborg and R. B. Steele. Temperature elevation in a beam of ultrasound. *Ultrasound Med. Biol.*, 9(6):611–620, 1983. 10.1016/0301-5629(83)90006-6.

[158] K. Ono. A comprehensive report on ultrasonic attenuation of engineering materials, including metals, ceramics, polymers, fiber-reinforced composites, wood, and rocks. *Appl. Sci.*, 10(7):2230, 2020. 10.3390/app10072230.

[159] K. Tsuji, T. Norisuye, H. Nakanishi, and Q. Tran-Cong-Miyata. Simultaneous measurements of ultrasound attenuation, phase velocity, thickness, and density spectra of polymeric sheets. *Ultrasonics*, 99: 105974, 2019. 10.1016/j.ultras.2019.105974.

[160] A.-T. Petit and P.-L. Dulong. Recherches sur quelques points importants de la Théorie de la Chaleur. *Annal. Chim. Phys.*, 10:395–413, 1819.

[161] Z. Huber and J. W. Wilkerson. Revisiting the first Sandia Fracture Challenge with transient deformation heating and strain localization considerations. *Int. J. Fract.*, 226(2):197–217, 2020. 10.1007/S10704-020-00487-7.

[162] Edupack C. Materials selection software from Granta Design by M. Ashby, 2009.

[163] X. Chen, K. Q. Schwarz, and K. J. Parker. Radiation pattern of a focused transducer: A numerically convergent solution. *J. Acoust. Soc. Am.*, 94(5):2979–2991, 1993. 10.1121/1.407329.

[164] W. M. Madigosky, I. Rosenbaum, and R. Lucas. Sound velocities and B/A in fluorocarbon fluids and in several low density solids. *J. Acoust. Soc. Am.*, 69(6):1639–1643, 1981. 10.1121/1.385941.

[165] S. Saito and Y. Motohashi. Nonlinearity Parameter Measurement for Polymer Plates Using Focused Ultrasound. *Jpn. J. Appl. Phys.*, 47(9):7380–7385, 2008. 10.1143/JJAP.47.7380.

[166] A. Panfilova, R. J. G. van Sloun, H. Wijkstra, O. A. Sapozhnikov, and M. Mischi. A review on B/A measurement methods with a clinical perspective. *J. Acoust. Soc. Am.*, 149(4):2200–2237, 2021. 10.1121/10.0003627.

[167] K. Ono. Dynamic viscosity and transverse ultrasonic attenuation of engineering materials. *Appl. Sci.*, 10(15):5265, 2020. 10.3390/APP10155265.

[168] K. Ono. Ultrasonic Attenuation of Ceramic and Inorganic Materials Using the Through-Transmission Method. *Appl. Sci.*, 12(24):13026, 2022. 10.3390/app122413026.

[169] J. Carlson, J. van Deventer, A. Scolan, and C. Carlander. Frequency and temperature dependence of acoustic properties of polymers used in pulse-echo systems. In *IEEE Ultrason. Symp.*, pages 885–888. IEEE, 2003. 10.1109/ULTSYM.2003.1293541.

[170] P. E. Bloomfield. Experimental study of the acoustical properties of polymers utilized to construct PVDF ultrasonic transducers and the acousto-electric properties of PVDF and P(VDF/TrFE) films. *IEEE Trans. Ultrason. Ferroelectr. Freq. Control.*, 47(6):1397–1405, 2000. 10.1109/58.883528.

[171] A. E. Pylaev, E. A. Kostikova, A. L. Yurkov, D. I. Kalugin, A. P. Malakho, V. V. Avdeev, V. N. Lepin, L. V. Oktyabr'skaya, and S. V. Minchuk. Velocity and Attenuation of Acoustic Waves in Polymers and Polymer Composites. *Polym. Sci.*, 11(3):272–276, 2018. 10.1134/S1995421218030152.

[172] J. Min, J. Kim, H. Jung, J. Kim, S. Noh, and H. Choi. Study on Changes in Shape of Denatured Area in Skull-mimicking Materials Using Focused Ultrasound Sonication. *IEIE Trans. Smart Process. Comput.*, 3(1):28–34, 2014. 10.5573/IEIESPC.2014.3.1.28.

[173] J.-C. Chen, C.-M. Su, G.-S. Chen, C.-C. Lai, C.-Y. Chen, K. M.-C. Lin, F.-H. Lin, and G.-C. Dong. Enhancement of Neurite Outgrowth by Warming Biomaterial Ultrasound Treatment. *Int. J. Mol. Sci.*, 21(6):2236, 2020. 10.3390/ijms21062236.

[174] M. S. A. Fathi. Ultrasonic Investigation Of Thermoplastic Polymers. *Int. J. Sci. Technol. Res.*, 8(11): 3260–3264, 2019.

[175] Matweb. Matweb Material property data, 2023. http://www.matweb.com/.

[176] W. P. Mason and H. J. McSkimin. Attenuation and Scattering of High Frequency Sound Waves in Metals and Glasses. *The Journal of the Acoustical Society of America*, 19(3):464–473, 1947. 10.1121/1.1916504.

[177] B. Liu, H. Xia, G. Fei, G. Li, and W. Fan. High-Intensity Focused Ultrasound-Induced Thermal Effect for Solid Polymer Materials. *Macromol. Chem. Phys.*, 214(22):2519–2527, 2013. 10.1002/macp.201300320.

[178] K. Sastry, L. Froyen, J. Vleugels, E. H. Bentefour, and C. Glorieux. Effect of Porosity on Thermal Conductivity of Al-Si-Fe-X Alloy Powder Compacts. *Int. J. Thermophys.*, 25(5):1611–1622, 2004. 10.1007/s10765-004-5762-9.

[179] B. Z. Djordjević, C. Benedetti, C. B. Schroeder, E. Esarey, and W. P. Leemans. Filtering higher-order laser modes using leaky plasma channels. *Phys. Plasmas*, 25(1):013103, 2018. 10.1063/1.5006198.

[180] H. H. Pennes. Analysis of Tissue and Arterial Blood Temperatures in the Resting Human Forearm. *J. Appl. Physiol.*, 1(2):93–122, 1948. 10.1152/JAPPL.1948.1.2.93.

[181] J. Wu and G. Du. Temperature elevation generated by a focused gaussian beam of ultrasound. *Ultrasound Med. Biol.*, 16(5):489–498, 1990. 10.1016/0301-5629(90)90171-8.

[182] F. P. A. van Berlo, P. J. F. M. Janssen, P. D. Anderson, and L. C. A. van Breemen. Selective Acoustic Sintering: a Framework to Study Focused Ultrasound 3D Printing. *Ultrasonics*, 2024.

[183] J. D. Mollon. The origins of the concept of interference. *Philosophical Transactions of the Royal Society of London. Series A: Mathematical, Physical and Engineering Sciences*, 360(1794):807–819, 2002. 10.1098/rsta.2001.0968.

[184] J. C. Somer. The history of real time ultrasound. *International Congress Series*, 1274(C):3–13, 2004. 10.1016/j.ics.2004.07.037.

[185] Olympus. *Phased Array Testing Basic Theory for Industrial Applications*. Olympus Scientific Solutions Americas, Waltham, USA, 3 edition, 2014.

[186] D. Pajek and K. Hynynen. Applications of Transcranial Focused Ultrasound Surgery. *Acoustics Today*, 8(4):8, 2012. 10.1121/1.4788651.

[187] M. T. Tan, C. M. Chu, and S. Chauhan. High intensity ultrasound phased array for surgical applications. In *Int. J. Pharm. Biomed. Res.*, pages 564–568, 2006. 10.1109/ICBPE.2006.348658.

[188] G. T. Clement, J. Sun, T. Giesecke, and K. Hynynen. A hemisphere array for non-invasive ultrasound brain therapy and surgery. *Physics in Medicine and Biology*, 45(12):3707–3719, 2000. 10.1088/0031-9155/45/12/314.

[189] V. Chaplin, M. A. Phipps, and C. F. Caskey. A random phased-array for MR-guided transcranial ultrasound neuromodulation in non-human primates. *Physics in Medicine & Biology*, 63(10):105016, 2018. 10.1088/1361-6560/aabeff.

[190] M. Pernot, J.-F. Aubry, M. Tanter, J.-L. Thomas, and M. Fink. High power transcranial beam steering for ultrasonic brain therapy. *Physics in Medicine and Biology*, 48(16):2577–2589, 2003. 10.1088/0031-9155/48/16/301.

[191] L. Deng, M. A. O'Reilly, R. M. Jones, R. An, and K. Hynynen. A multi-frequency sparse hemispherical ultrasound phased array for microbubble-mediated transcranial therapy and simultaneous cavitation mapping. *Physics in Medicine and Biology*, 61(24):8476–8501, 2016. 10.1088/0031-9155/61/24/8476.

[192] L. R. Gavrilov. The possibility of generating focal regions of complex configurations in application to the problems of stimulation of human receptor structures by focused ultrasound. *Acoustical Physics*, 54 (2):269–278, 2008. 10.1134/S1063771008020152.

[193] J. W. Hand, A. Shaw, N. Sadhoo, S. Rajagopal, R. J. Dickinson, and L. R. Gavrilov. A random phased array device for delivery of high intensity focused ultrasound. *Physics in Medicine and Biology*, 54(19): 5675–5693, 2009. 10.1088/0031-9155/54/19/002.

[194] B. E. Treeby and B. T. Cox. k-Wave: MATLAB toolbox for the simulation and reconstruction of photoacoustic wave fields. *Journal of biomedical optics*, 15(2):021314, 2010. 10.1117/1.3360308.

[195] B. E. Treeby, J. Jaros, A. P. Rendell, and B. T. Cox. Modeling nonlinear ultrasound propagation in heterogeneous media with power law absorption using a k-space pseudospectral method. *The Journal of the Acoustical Society of America*, 131(6):4324–4336, 2012. 10.1121/1.4712021.

[196] K. R. Waters, J. Mobley, and J. G. Miller. Causality-imposed (Kramers-Kronig) relationships between attenuation and dispersion. *IEEE Transactions on Ultrasonics, Ferroelectrics, and Frequency Control*, 52(5):822–833, 2005. 10.1109/TUFFC.2005.1503968.

[197] W. Chen and S. Holm. Fractional Laplacian time-space models for linear and nonlinear lossy media exhibiting arbitrary frequency power-law dependency. *The Journal of the Acoustical Society of America*, 115(4):1424–1430, 2004. 10.1121/1.1646399.

[198] B. E. Treeby and B. T. Cox. Modeling power law absorption and dispersion for acoustic propagation using the fractional Laplacian. *The Journal of the Acoustical Society of America*, 127(5):2741–2748, 2010. 10.1121/1.3377056.

[199] B. E. Treeby, . B. T. Cox, and B. T. Cox. Modeling power law absorption and dispersion in viscoelastic solids using a split-field and the fractional Laplacian. *The Journal of the Acoustical Society of America*, 136(4):1499–1510, 2014. 10.1121/1.4894790.

[200] B. E. Treeby, . B. T. Cox, and B. T. Cox. A k-space Green's function solution for acoustic initial value problems in homogeneous media with power law absorption. *The Journal of the Acoustical Society of America*, 129(6):3652–3660, 2011. 10.1121/1.3583537.

[201] B. E. Treeby, M. Tumen, and B. T. Cox. Time Domain Simulation of Harmonic Ultrasound Images and Beam Patterns in 3D Using the k-space Pseudospectral Method. *Lecture Notes in Computer Science (including subseries Lecture Notes in Artificial Intelligence and Lecture Notes in Bioinformatics)*, 6891 LNCS(PART 1):363–370, 2011. 10.1007/978-3-642-23623-5_46.

[202] M. Tabei, . T. Douglas, R. C. Waag, and T. D. Mast. A k-space method for coupled first-order acoustic propagation equations. *The Journal of the Acoustical Society of America*, 111(1):53–63, 2002. 10.1121/1.1421344.

[203] B. T. Cox, S. Kara, S. R. Arridge, and P. C. Beard. k-space propagation models for acoustically heterogeneous media: application to biomedical photoacoustics. *The Journal of the Acoustical Society of America*, 121(6):3453–3464, 2007. 10.1121/1.2717409.

[204] B. Fornberg. High-Order Finite Differences and the Pseudospectral Method on Staggered Grids. *SIAM Journal on Numerical Analysis*, 27(4):904–918, 1990. 10.1137/0727052.

[205] J. Jaros, A. P. Rendell, and B. E. Treeby. Full-wave nonlinear ultrasound simulation on distributed clusters with applications in high-intensity focused ultrasound. *The International Journal of High Performance Computing Applications*, 30(2):137–155, 2016. 10.1177/1094342015581024.

[206] J. P. Berenger. A perfectly matched layer for the absorption of electromagnetic waves. *Journal of Computational Physics*, 114(2):185–200, 1994. 10.1006/JCPH.1994.1159.

[207] X. Yuan, D. Borup, J. W. Wiskin, M. Berggren, R. Eidens, and S. A. Johnson. Formulation and validation of berenger's pml absorbing boundary for the fdtd simulation of acoustic scattering. *IEEE Transactions on Ultrasonics, Ferroelectrics, and Frequency Control*, 44(4):816–822, 1997. 10.1109/58.655197.

[208] J. P. Berenger. Three-Dimensional Perfectly Matched Layer for the Absorption of Electromagnetic Waves. *Journal of Computational Physics*, 127(2):363–379, 1996. 10.1006/JCPH.1996.0181.

[209] X. Yuan, D. Borup, J. Wiskin, M. Berggren, and S. A. Johnson. Simulation of acoustic wave propagation in dispersive media with relaxation losses by using FDTD method with PML absorbing boundary

condition. *IEEE Transactions on Ultrasonics, Ferroelectrics, and Frequency Control*, 46(1):14–23, 1999. 10.1109/58.741419.

[210] E. S. Wise, B. T. Cox, J. Jaros, and B. E. Treeby. Representing arbitrary acoustic source and sensor distributions in Fourier collocation methods. *The Journal of the Acoustical Society of America*, 146(1): 278–288, 2019. 10.1121/1.5116132.

[211] B. E. Treeby, E. S. Wise, F. Kuklis, J. Jaros, and B. T. Cox. Nonlinear ultrasound simulation in an axisymmetric coordinate system using a k-space pseudospectral method. *The Journal of the Acoustical Society of America*, 148(4):2288–2300, 2020. 10.1121/10.0002177.

[212] B. D. Steinberg. *Principles of aperture and array system design : including random and adaptive arrays*. Wiley, New York, 1976.

[213] M. L. Hentschel and N. W. Page. Elastic properties of powders during compaction. Part 2: Elastic anisotropy. *Journal of Materials Science*, 42(4):1269–1278, 2007. 10.1007/S10853-006-1394-8.

[214] A. Amado-Becker, J. Ramos-Grez, M. José Yañez, Y. Vargas, and L. Gaete. Elastic tensor stiffness coefficients for SLS Nylon 12 under different degrees of densification as measured by ultrasonic technique. *Rapid Prototyping Journal*, 14(5):260–270, 2008. 10.1108/13552540810907929.

[215] R. Ali, A. V. Telichko, H. Wang, U. K. Sukumar, J. G. Vilches-Moure, R. Paulmurugan, and J. J. Dahl. Local Sound Speed Estimation for Pulse-Echo Ultrasound in Layered Media. *IEEE Transactions on Ultrasonics, Ferroelectrics, and Frequency Control*, 69(2):500–511, 2022. 10.1109/TUFFC.2021.3124479.

[216] B. Pal. Fourier Spectrum Pulse-Echo for Acoustic Characterization. *Journal of Nondestructive Evaluation*, 37(4), 2018. 10.1007/S10921-018-0533-X.

[217] S. G. Lee, D. Oh, and J. H. Woo. The effect of high glass fiber content and reinforcement combination on pulse-echo ultrasonic measurement of composite ship structures. *Journal of Marine Science and Engineering*, 9(4), 2021. 10.3390/JMSE9040379.

[218] T. Q. Santos, A. V. Alvarenga, D. P. Oliveira, and R. P. Costa-Felix. Metrological Validation of a Measurement Procedure for the Characterization of a Biological Ultrasound Tissue-Mimicking Material. *Ultrasound in Medicine & Biology*, 43(1):323–331, 2017. 10.1016/J.ULTRASMEDBIO.2016.09.007.

[219] P. He and J. Zheng. Acoustic dispersion and attenuation measurement using both transmitted and reflected pulses. *Ultrasonics*, 39(1):27–32, 2001. 10.1016/S0041-624X(00)00037-8.

[220] B. Pal. Pulse-echo method cannot measure wave attenuation accurately. *Ultrasonics*, 61:6–9, 2015. 10.1016/J.ULTRAS.2015.03.005.

[221] U. A. Hofmann, S. Pérez-López, H. Estrada, and D. Razansky. High-Order Pulse-Echo Ultrasound. *Physical Review Applied*, 17(5):054024, 2022. 10.1103/PhysRevApplied.17.054024.

[222] W. Xu and J. J. Kaufman. Diffraction Correction Methods for Insertion Ultrasound Attenuation Estimation. *IEEE Transactions on Biomedical Engineering*, 40(6):563 – 570, 1993. 10.1109/10.237676.

[223] P. Droin, G. Berger, and P. Laugier. Velocity dispersion of acoustic waves in cancellous bone. *IEEE transactions on ultrasonics, ferroelectrics, and frequency control*, 45(3):581–592, 1998. 10.1109/58.677603.

[224] R. Martinez, L. Leija, and A. Vera. Ultrasonic attenuation in pure water: Comparison between through-transmission and pulse-echo techniques. *Pan American Health Care Exchanges, PAHCE 2010*, pages 81–84, 2010. 10.1109/PAHCE.2010.5474593.

[225] J. C. Adamowski, F. Buiochi, and R. T. Higuti. Ultrasonic material characterization using large-aperture PVDF receivers. *Ultrasonics*, 50(2):110–115, 2010. 10.1016/J.ULTRAS.2009.09.018.

[226] N. V. Smagin, L. M. Krutyansky, A. P. Brysev, and F. V. Bunkin. Measurement of acoustic absorption coefficient with phase-conjugate ultrasonic waves. *Acoustical Physics 2011 57:4*, 57(4):482–489, 2011. 10.1134/S1063771011030195.

[227] G. Xing, P. Yang, and L. He. Estimation of diffraction effect in ultrasonic attenuation by through-transmission substitution technique. *Ultrasonics*, 53(4):825–830, 2013. 10.1016/J.ULTRAS.2012.12.001.

[228] L. M. D. de Castro and F. P. Capote. *Techniques and Instrumentation in Analytical Chemistry*, volume 26 of *Techniques and Instrumentation in Analytical Chemistry*. Elsevier, 2007. 10.1016/S0167-9244(07)80026-6.

[229] IEC TS 63081:2019. Ultrasonics - Methods for the characterization of the ultrasonic properties of, 2019. `https://standards.iteh.ai/catalog/standards/iec/91be19e2-f9c1-4617-b7e9-d5c269b7e254/iec-ts-63081-2019`.

[230] B. Zeqiri, W. Scholl, and S. P. Robinson. Measurement and testing of the acoustic properties of materials: a review. *Metrologia*, 47(2):S156, 2010. 10.1088/0026-1394/47/2/S13.

[231] J. Bustillo, J. Fortineau, G. Gautier, and M. Lethiecq. Ultrasonic characterization of electrochemically etched porous silicon. *Japanese Journal of Applied Physics*, 53(6):060308, 2014. 10.7567/JJAP.53.060308/XML.

[232] T. C. Dourado, A. V. Alvarenga, F. C. Peters, W. J. Mansur, and R. P. Costa-Félix. Simultaneous use of pulse-echo and through-transmission methods in determining a combined reflection coefficient. *Applied Acoustics*, 192:108700, 2022. 10.1016/J.APACOUST.2022.108700.

[233] H. Towsyfyan, Biguri Ander, R. Boardman, and T. Bluemensath. Successes and challenges in non-destructive testing of aircraft composite structures. *Chinese Journal of Aeronautics*, 33(3):771–791, 2020. 10.1016/j.cja.2019.09.017.

[234] A. Panfilova, P. Chen, R. J. van Sloun, H. Wijkstra, M. Postema, A. T. Poortinga, and M. Mischi. Experimental acoustic characterization of an endoskeletal antibubble contrast agent: First results. *Medical Physics*, 48(11):6765–6780, 2021. 10.1002/MP.15242.

[235] G. S. Kino. *Acoustic Waves: Devices, Imaging, and Analog Signal Processing*, volume 100. Prentice Hall, Englewood Cliffs, 1987.

[236] J. Krautkrämer and H. Krautkrämer. *Ultrasonic Testing of Materials.* Springer Science & Business Media, Berlin, Heidelberg, 4 edition, 2013. 10.1007/978-3-662-10680-8.

[237] R. K. Miller and P. McIntire. *Nondestructive Testing Handbook: Acoustic Emission Testing.* ASM International, 2 edition, 1987.

[238] L. E. Kinsler, A. Frey, A. B. Coppens, and J. V. Sanders. *Fundamentals of Acoustics.* John Wiley & Sons, 4 edition, 2000.

[239] A. N. Kalashnikov and R. E. Challis. Errors and uncertainties in the measurement of ultrasonic wave attenuation and phase velocity. *IEEE Transactions on Ultrasonics, Ferroelectrics, and Frequency Control*, 52(10):1754–1768, 2005. 10.1109/TUFFC.2005.1561630.

[240] R. Challis. The Effect of Transducer-Reflector Angulation on Echoes Received from Targets Using Ultrasonic Pulse-Echo Equipment. *Acta Acoustica united with Acustica*, 50(3):221–232, 1982.

[241] R. Queiros, P. S. Girao, and A. C. Serra. Cross-Correlation and Sine-Fitting Techniques for High Resolution Ultrasonic Ranging. In *IEEE Instrumentation and Measurement Technology Conference Proceedings*, pages 552–556. Institute of Electrical and Electronics Engineers (IEEE), 2006. 10.1109/IMTC.2006.328588.

[242] M. O. Khyam, S. S. Ge, X. Li, and M. R. Pickering. Highly Accurate Time-of-Flight Measurement Technique Based on Phase-Correlation for Ultrasonic Ranging. *IEEE Sensors Journal*, 17(2):434–443, 2017. 10.1109/JSEN.2016.2631244.

[243] K. Pahlavan, X. Li, and J. P. Mäkelä. Indoor geolocation science and technology. *IEEE Communications Magazine*, 40(2):112–118, 2002. 10.1109/35.983917.

[244] P. Misra, N. Kottege, B. Kusy, D. Ostry, and S. Jha. Acoustical ranging techniques in embedded wireless sensor networked devices. *ACM Transactions on Sensor Networks (TOSN)*, 10(1), 2013. 10.1145/2529981.

[245] L. Kinsler, A. Frey, A. Coppens, and J. Sanders. Fundamentals of Acoustics (4th Edition). *John Wiley and Sons Inc.*, page 560, 1999.

[246] V. A. Krasilnikov. *Sound and Ultrasound Waves in Air, Water and Solid Bodies.* Israel Program for Scientific Translations, Washington, 3 edition, 1960.

[247] W. Marczak. Water as a standard in the measurements of speed of sound in liquids. *The Journal of the Acoustical Society of America*, 102(5):2776–2779, 1997. 10.1121/1.420332.

[248] J. M. Pinkerton. The Absorption of Ultrasonic Waves in Liquids and its Relation to Molecular Constitution. *Proceedings of the Physical Society. Section B*, 62(2):129, 1949. 10.1088/0370-1301/62/2/307.

[249] Y. C. Eldar. Resampling. In *Sampling Theory*, chapter 9, pages 323–367. Cambridge University Press, 2015. 10.1017/CBO9780511762321.010.

[250] G. W. C. Kaye and T. H. Laby. *Tables of Physical and Chemical Constants and Some Mathematical Functions.* Longmans, Green and Company, London, 1911.

[251] P. V. Thanh, P. T. T. Nhung, L. T. M. Thuy, and N. H. Nhai. Effect of Temperature on Ultrasonic Velocities, Attenuations, Reflection and Transmission Coefficients between Motor Oil and Carbon Steel Estimated by Pulse-echo Technique of Ultrasonic Testing Method. *VNU Journal of Science: Mathematics - Physics*, 31(4):39–48, 2015.

[252] M. Sinha and D. J. Buckley. Acoustic Properties of Polymers. In J. E. Mark, editor, *Physical Properties of Polymers Handbook*, chapter 60, pages 1021–1031. Springer, New York, 2 edition, 2007. 10.1007/978-0-387-69002-5_60.

[253] A. Demčenko, R. Akkerman, P. B. Nagy, and R. Loendersloot. Non-collinear wave mixing for non-linear ultrasonic detection of physical ageing in PVC. *NDT & E International*, 49:34–39, 2012. 10.1016/J.NDTEINT.2012.03.005.

[254] A. Maynell, Coin. *Ultrasound propagation in the sodium borosilicate glass system*. PhD thesis, Univeristy of Durham, Durham City, 1972. `http://etheses.dur.ac.uk/8823/`.

[255] A. R. Selfridge. Approximate Material Properties in Isotropic Materials. *IEEE Transactions on Sonics and Ultrasonics*, 32(3):381–394, 1985. 10.1109/T-SU.1985.31608.

[256] C. Cadot, J.-F. Saillant, and B. Dulmet. Method for Acoustic Characterization of Materials in Temperature. In *19th World Conference on Non-Destructive Testing*, pages 1–9, 2016.

[257] E. Grinzel and R. Grinzel. Ultrasonic Properties of a New Low Attenuation Dry Couplant Elastomer. *e-Journal of Nondestructive Testing*, 1(2):1–10, 1996.

[258] S. F. Reis. *Characterisation of biological tissue: measurement of acoustic properties for ultrasound therapy*. PhD thesis, University of Lisbon, Lisbon, 2013. `http://hdl.handle.net/10451/9598`.

[259] P. S. Epstein and R. R. Carhart. The Absorption of Sound in Suspensions and Emulsions. I. Water Fog in Air. *The Journal of the Acoustical Society of America*, 25(3):553–565, 1953. 10.1121/1.1907107.

[260] J. R. Allegra and S. A. Hawley. Attenuation of Sound in Suspensions and Emulsions: Theory and Experiments. *The Journal of the Acoustical Society of America*, 51(5B):1545–1564, 1972. 10.1121/1.1912999.

[261] R. E. Challis, J. S. Tebbutt, and A. K. Holmes. Equivalence between three scattering formulations for ultrasonic wave propagation in particulate mixtures. *Journal of Physics D: Applied Physics*, 31(24):3481, 1998. 10.1088/0022-3727/31/24/012.

[262] M. M. Alam, V. J. Pinfield, and P. Maréchal. Scattering coefficients for a sphere in a visco-acoustic medium for arbitrary partial wave order. *Wave Motion*, 97:102589, 2020. 10.1016/J.WAVEMOTI.2020.102589.

[263] K. Tsuji, H. Nakanishi, and T. Norisuye. Viscoelastic ECAH: Scattering analysis of spherical particles in suspension with viscoelasticity. *Ultrasonics*, 115:106463, 2021. 10.1016/J.ULTRAS.2021.106463.

[264] C. F. Bohren and D. R. Huffman. *Absorption and Scattering of Light by Small Particles*. Wiley, New York, 1998. 10.1002/9783527618156.

[265] C. F. Ying and R. Truell. Scattering of a Plane Longitudinal Wave by a Spherical Obstacle in an Isotropically Elastic Solid. *Journal of Applied Physics*, 27(9):1086–1097, 1956. 10.1063/1.1722545.

[266] G. C. Gaunaurd, . H. Überall, and C. Gaunaurd. Resonance theory of bubbly liquids. *The Journal of the Acoustical Society of America*, 69(2):362–370, 1981. 10.1121/1.385462.

[267] B. J. Dorussen, M. G. Geers, and J. J. Remmers. A discrete element framework for the numerical analysis of particle bed-based additive manufacturing processes. *Engineering with Computers*, 38(6):4753–4768, 2022. 10.1007/S00366-021-01590-6.

[268] L. Lanzl, K. Wudy, M. Drexler, and D. Drummer. Laser-high-speed-DSC: Process-oriented Thermal Analysis of PA 12 in Selective Laser Sintering. *Physics Procedia*, 83:981–990, 2016. 10.1016/J.PHPRO.2016.08.103.

[269] A. Panfilova, X. Chen, C. Widdershoven, J. E. Freund, D. S. Heijink, P. Zondervan, R. J. van Sloun, O. A. Sapozhnikov, H. Wijkstra, and M. Mischi. B/A Measurement of Clear Cell Renal Cell Carcinoma versus Healthy Kidney Tissue. *Ultrasound in Medicine & Biology*, 48(7):1348–1355, 2022. 10.1016/J.ULTRASMEDBIO.2022.02.024.

[270] Dispersion Technology Inc. Model DT-100 with Temperature Control Option, 2024. `https://dispersion.com/product/particle-sizing/`.

[271] H. S. Carslaw and J. J. C. Jaeger. *Conduction of heat in solids*. Oxford University Press, London, 2 edition, 1959.

Samenvatting

Poedergebaseerde 3D print technieken, zoals Selective Laser Sintering (SLS), worden vaak gebruikt om producten kosteneffectief en efficiënt te produceren. Door de uitstekende eigenschappen van geproduceerde onderdelen zijn deze technieken het meest geschikt voor hoogwaardige toepassingen. Toch vormt het delicate samenspel tussen procesparameters, materiaaleigenschappen en temperatuurregeling bij conventionele poedergebaseerde printmethoden een uitdaging die onderzoek noodzakelijk maakt. Dit proefschrift onderzoekt het complexe samenspel tussen procesparameters en intrinsieke materiaaleigenschappen door nieuwe concepten te introduceren in de bestaande SLS printtechniek en in een nieuw ontwikkelde ultrasone 3D-printtechniek, genaamd Selective Acoustic Sintering (SAS).

In **Hoofdstuk 2** wordt de temperatuurregeling in SLS behandeld, gevolgd door een experimentele studie naar het voorspellen van materiaaleigenschappen op basis van verwerkingscondities. Het integreren van een infraroodcamera verbetert de temperatuurregeling van een commerciële SLS-printer. Procesparameters worden gedefinieerd door de verhouding van laserenergie tot de energie die nodig is voor smelten (AMR) te variëren door middel van een reeks bedtemperaturen, laserkrachten en scansnelheden. Een printbaarheidsgrafiek wordt geïntroduceerd en trekproeven tonen relaties tussen AMR, dichtheid, modulus, breukrek en vloeispanning. Er wordt geconcludeerd dat de AMR-relaties met dichtheidsafhankelijkheid, in combinatie met de printbaarheidsgrafiek, kunnen worden gebruikt als een algemeen instrument om de kwaliteit van SLS-geprinte onderdelen te voorspellen uit intrinsieke materiaaleigenschappen.

Een eindige-elementenmethode wordt gebruikt om verder onderzoek te doen naar de rol van procesparameters op de kwaliteit van onderdelen, zoals beschreven in **Hoofdstuk 3**. Er is een model ontwikkeld dat temperatuurafhankelijke thermische eigenschappen en porositeit-geïnduceerde krimp tijdens het smelten beschrijft. De thermische geschiedenis van een meerlaags onderdeel wordt gesimuleerd voor verschillende procescondities. Dit illustreert dat onnauwkeurige prints als gevolg van doorzakking van lagen gerelateerd zijn aan de combinatie van de initiële porositeit van het poederbed en het laservermogen. Bovendien wordt het gemiddelde-lamelldikte (ALT) kristallisatiemodel geïntroduceerd, dat de kristallisatie en smeltkinetiek beschrijft. Het gebruik van dit model biedt inzichten in evoluties van kristalgroei en smelt tijdens SLS-printen en uiteindelijk lamellaire dikteverdelingen, die gekoppeld zijn aan de vloeispanning van PA12 eindproducten.

In **Hoofdstuk 4** wordt de SAS 3D-printbenadering voor de verwerking van poedergebaseerde materialen bestudeerd. Eerst worden de voordelen besproken van het overschakelen van een laser naar een akoestische bron, waarbij met name in-volume 3D-printen en poedercompressie mogelijk worden gemaakt. Vervolgens wordt een wiskundig kader geïntroduceerd om de haalbaarheid van volumetrisch SAS 3D-printen in een bolvormig gevormd bouwvolume te bepalen. Het theoretische model toont aan dat selectieve temperatuurstijging in de

buurt van het centrum van de printer wordt beïnvloed door energie-invoer, energietoename door geometrische focussering en energieverlies door akoestische demping. Bovendien legt het model relaties tussen printergrootte, akoestische en thermische materiaaleigenschappen en transducereigenschappen ten opzichte van temperatuurstijging en focusafstanden. Voor toepassingsdoeleinden analyseert de studie een dataset van printbare materialen en wordt er geconcludeerd dat optimalisatie volumetrisch printen mogelijk maakt voor verschillende materialen, waaronder metalen, kunststoffen en keramieken.

Hoofdstuk 5 presenteert een uitbreiding van het SAS-model door het gebruik van numerieke simulaties. Hierin worden verschillende transducerconfiguraties en bouwvolumevormen gesimuleerd met behulp van de k-space pseudospectrale methode. Zowel tweedimensionale als driedimensionale simulaties worden uitgevoerd om het effect van transducerconfiguratie op temperatuursstijging en focusspotgrootte te bestuderen. Hierin worden de transducereigenschappen (aantal, grootte, posities en frequentie) gevarieerd om aan te tonen dat focussering op specifieke posities binnen het bouwvolume mogelijk is. Een tijdsinversiemethode wordt gepresenteerd om de vertragingen tussen transducers en amplitudes van de transducers die leiden tot de gewenste focuslocatie te voorspellen. Ten slotte wordt de akoestisch-thermische koppeling via eindige-differentie-simulaties van de energiebalans gebruikt om de ultrasone temperatuurstijging te bepalen.

Omdat gegevens over de akoestische eigenschappen van poeders die in het SAS-systeem worden gebruikt ontbreken, wordt een ultrasone opstelling voor het karakteriseren van poedercompacten ontworpen. In **Hoofdstuk 6** wordt het ontwerp van deze opstelling toegelicht. Via numerieke simulaties wordt aangetoond dat een gecombineerde echo- en transmissie opstelling met een gefocuste ultrasoontransducer kan worden gebruikt om verschillende materialen akoestisch te karakteriseren. Vervolgens wordt de realisatie van de opstelling getoond en worden akoestische snelheid- en dempingsmetingen uitgevoerd. Ten slotte worden nietgevulde en (met olie en kaarsvet) gevulde poeders samengedrukt om het effect van porositeit en volumefractie op de akoestische eigenschappen te bestuderen.

Dankwoord

Ondanks dat er in de afgelopen vier jaar van mijn PhD-traject veel is gebeurd (denk aan corona), zijn het vooral de leuke en leerzame momenten met collega's, kennissen en naasten die me zijn bijgebleven. Zij hebben ook het schrijven van deze thesis mogelijk gemaakt en daarom wil ik ze graag bedanken.

Allereerst wil ik mijn promotoren bedanken voor de mogelijkheid om onderzoek te verrichten in deze gezellige en vooruitstrevende onderzoeksgroep. **Lambèrt**, ik wil jou bedanken voor alles wat je me geleerd hebt in de afgelopen jaren. Zonder jou was dit werk nooit geworden wat het is. De onderzoeksvrijheid die je geeft kan soms wat frustrerend werken in het begin, maar zorgt er uiteindelijk wel voor dat we vele unieke inzichten hebben gecreëerd. Naast je wetenschappelijke kennis ben je vooral ook iemand die het welzijn van anderen vooropstelt en je biedt graag een luisterend oor. Dit waardeer ik enorm aan jou! Bedankt voor jouw steun en vertrouwen in mij en alle wetenschappelijke discussies en vooral ook leuke gesprekken die we hebben gevoerd.

Patrick, ik wil jou bedanken voor de fijne begeleiding en het mogelijk maken van mijn PhD. Van jou heb ik geleerd hoe ik de inhoud van mijn werk kan richten tot het publiek waarvoor ik presenteer op bijvoorbeeld conferenties. Dit heeft met name geleid tot veel positieve reacties op mijn presentatie bij Conference of the Polymer Processing Society (PPS). Daarnaast heb ik veel van je geleerd op het gebied van reologie en hebben we ook mooie (internationale) samenwerkingen met onder andere Prof. Amy Shen kunnen verwezenlijken. Ook ben ik je erg dankbaar voor de mogelijkheden die ik van je heb gekregen om (ondanks de corona-onderbreking) vele conferenties te kunnen bezoeken; ik heb ervan genoten!

Without my colleagues from the Processing and Performance of Materials group, the last four years would not have been nearly as great. Thank you for the memorable moments, including the conferences, MaTe and TU/e parties, our healthy pizza and RPK lunches, and office chatter.

In het bijzonder wil ik **Michelle** bedanken voor haar geduld bij mijn vragen over TFEM, **Paul H.** en **Rosa** voor het ondersteunen bij trekproeven en de leuke kantoormomenten en **Stan** en **Martin** voor het analyseren en uitvoeren van X-ray metingen.

Bovendien, **Thijs**, het was altijd kei leuk tijdens onze vooral bloedhete en luide ochtendgesprekken, waarin we onze (alcohol-gerelateerde) weekendplannen en voetbalzaken bespraken. Ik heb erg genoten van jouw gelach en gezelligheid. Het organiseren van de voetbalpoule, die ik uiteraard won, was ook een groot succes. Toekomstige ondernemer **Coen**, ik vond het altijd erg leuk om met je te discussiëren over onze startupplannen en cursussen hierover te volgen. Veel dank dat je dit proces samen met me hebt doorlopen. DJ **Hamid**, my funny, energetic and positive hardworking colleague - thank you for the unforgettable moments we

had together at conferences, your delicious dinners and the rooftop barbeques.

Daarnaast wil mijn dank uitspreken naar nog twee collega's. Wat heb ik een geluk gehad dat jij ineens verscheen tijdens mijn PhD, **Paul J.**. Jouw ontwerpkennis is van onschatbare waarde geweest in de ontwikkelingen van de meetopstellingen. Bedankt voor je enthousiasme en hulp bij het schrijven van de patenten en het opzetten van mijn startup. Ik hoop in de toekomst ons goede contact voort te kunnen zetten. **Lucien**, jou wil ik bedanken voor de uren werk die je verricht hebt om mijn meetopstellingen te verwezenlijken. Ook je gezelligheid tijdens het koffiedrinken en de activiteiten met collega's ga ik niet meer vergeten.

De samenwerkingen met bachelor- en masterstudenten en meerdere onderzoeksgroepen binnen de TU/e zijn ook heel waardevol gebleken. Ik wil een paar personen uitlichten die onderdelen van dit werk mede mogelijk hebben gemaakt.

Met name **Kylian**, **Kevin**, **Luuk**, **Max** en **Myrthe**, jullie inzet en kennis heeft een grote bijdrage geleverd aan dit proefschrift. Heel veel dank hiervoor.

Then, I would like to thank **Richard** and **Massimo** for allowing me to perform experiments in their labs, and **Jan-Willem** and **Anastasiia** for teaching me the basics of ultrasound and helping with numerical simulations and experiments thereof.

Verder wil ik graag mijn maten uit Lieshout en omstreken bedanken (you know who you are) voor de gezellige en gekke (kantine) avonden, de vele lekkere Bavaria biertjes en jullie oprechte interesse.

Natuurlijk kan ook mijn familie niet ontbreken (**Van Berlo** en **Brugmans**). Bedankt voor jullie belangstelling en hulp tijdens deze vierjarige periode van vele ups en downs. Met name bedankt dat jullie altijd voor mij klaarstonden, ongeacht wat er aan de hand was.

Lieve **Vera Schatje**, de laatste woorden zijn voor jou. De afgelopen tijd is in meerdere opzichten een stressvolle tijd geweest, waarin ik enorm veel steun van je heb gehad. Bedankt dat je altijd in mij gelooft, voor alle liefde die je me geeft en de onvoorwaardelijke, onuitputtelijke en positieve steun die ik van je ontvang. Dankjewel dat je, ongevraagd, mijn onbegrijpelijke hersenspinsels en onderzoeksplannen aan hebt willen horen. Zonder jou was dit allemaal nooit mogelijk geweest; je hebt me er doorheen gesleept. Ik hou van je.

Iedereen die heeft bijgedragen aan dit proefschrift, zowel wetenschappelijk als sociaal, nogmaals heel erg bedankt.

Curriculum Vitae

Frank van Berlo was born on June 9, 1996, in Lieshout (The Netherlands). After completing his secondary education at the Commanderij College in Gemert in 2014, he studied Mechanical Engineering at Eindhoven University of Technology (TU/e) and obtained his bachelor's degree in 2017. He continued to pursue his master's degree in Mechanical Engineering at Eindhoven University of Technology. To conclude his master's degree, he worked on numerical simulations of the flow and structure formation of polymers in a filament stretching extensional rheometer in the Processing and Performance of Materials group (formerly known as Polymer Technology) chaired by Prof. Dr. Ir. Patrick Anderson. After he obtained his master's degree in 2019, he started as a doctoral candidate in the same group under the supervision of Dr. Ir. Lambèrt van Breemen. During this period, he worked on the characterization of the mechanical properties of polymers and the development of 3D printing methods using polymer powders. His main focus was developing a new high-temperature powder-based 3D printer for high-performance polymer materials. The most relevant results of this research are presented in this thesis.
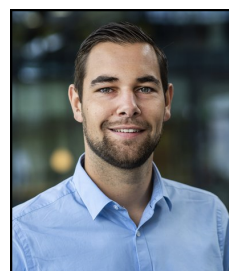
Frank van Berlo werd geboren op 9 juni 1996 in Lieshout (Nederland). Na het afronden van zijn middelbare schoolopleiding aan het Commanderij College in Gemert in 2014, is hij Werktuigbouwkunde gaan studeren aan de Technische Universiteit Eindhoven (TU/e). Hij behaalde zijn bachelordiploma in 2017. Hij vervolgde zijn studie met een masteropleiding Werktuigbouwkunde aan de Technische Universiteit Eindhoven. Om zijn masteropleiding af te ronden, werkte hij aan numerieke simulaties van de stroming en structuurvorming van polymeren in een filamentstrek-reometer in de groep Processing and Performance of Materials (voorheen bekend als Polymer Technology) onder leiding van Prof. Dr. Ir. Patrick Anderson. Nadat hij zijn masterdiploma in 2019 heeft behaald, begon hij in dezelfde groep aan zijn promotieonderzoek onder begeleiding van Dr. Ir. Lambèrt van Breemen. Gedurende deze periode werkte hij aan de karakterisering van de mechanische eigenschappen van polymeren en de ontwikkeling van 3D-printmethoden met polymeerpoeders. Zijn belangrijkste focus lag op het ontwikkelen van een nieuwe poeder-gebaseerde 3D-printer die kan werken bij hoge temperaturen voor het produceren van hoogwaardige polymeermaterialen. De belangrijkste resultaten van dit onderzoek staan beschreven in dit proefschrift.

List of publications

This thesis has resulted in the following publications:

- **F.P.A. van Berlo**, L.C.A van Breemen, P.D. Anderson, Apparatus and method for producing an object by means of additive manufacturing, *Worldwide patent*, WO2023234771A1, 2023.

- **F.P.A. van Berlo**, L.C.A. van Breemen, P.D. Anderson, and P.J.F.M. Janssen, Methods and an apparatus for producing an object by means of selective acoustic sintering, *Dutch patent filed*, P100198, 2024.

- **F.P.A. van Berlo**, P.J.F.M. Janssen, P.D. Anderson, and L.C.A. van Breemen, Selective Acoustic Sintering: a Framework to Study Focused Ultrasound 3D Printing, [Manuscript submitted for publication], 2024.

- **F.P.A. van Berlo**, P.D. Anderson, and L.C.A. van Breemen, Selective Laser Sintering: Predictive Analysis of Process Parameters Impact on Intrinsic Material Properties, [Manuscript submitted for publication], 2024.

- **F.P.A. van Berlo**, P.D. Anderson, L.C.A. van Breemen, Selective Laser Sintering: Numerical Modeling of Porosity and Crystallization Effects, [Manuscript submitted for publication], 2024.

Additionally, the author has contributed to the following publications outside this thesis:

- P.M.H. van Heugten, S.F.S.P. Looijmans, **F.P.A. van Berlo**, M. Rosenthal, P.D. Anderson, and L.C.A. van Breemen, Fiber-Induced Crystallization in Elongational Flows. *Macromolecules*, 57(5):2246–2259, 2024. `https://doi.org/10.1021/acs.macromol.3c02632`

- S.T. Chan, **F.P.A. van Berlo**, H.A. Faizi, A. Matsumoto, S.J. Haward, P.D. Anderson, A.Q. Shen, Torsional fracture of viscoelastic liquid bridges. *Proceedings of the National Academy of Sciences of the United States of America*, 118(24): e2104790118, 2021. `https://doi.org/10.1073/pnas.2104790118`

- **F.P.A. van Berlo**, R. Cardinaels, G.W.M. Peters, P.D. Anderson, Towards a universal shear correction factor in filament stretching rheometry, *Rheologica Acta*, 60:691–709, 2021. `https://doi.org/10.1007/s00397-021-01299-9`

- **F.P.A. van Berlo**, R. Cardinaels, G.W.M. Peters, P.D. Anderson, A numerical study of extensional flow-induced crystallization in filament stretching rheometry. *Polymer Crystallization*, 4:e10154, 2021. `https://doi.org/10.1002/pcr2.10154`